Maria Førde Møll

Solidification of Silicon

Macro- and Microstructure as Functions of Thermal History and Composition

Thesis for the degree of Philosophiae Doctor

Trondheim, January 2014

Norwegian University of Science and Technology
Faculty of Natural Sciences and Technology
Department of Materials Science and Engineering

NTNU – Trondheim
Norwegian University of
Science and Technology

NTNU
Norwegian University of Science and Technology

Thesis for the degree of Philosophiae Doctor

Faculty of Natural Sciences and Technology
Department of Materials Science and Engineering

ISBN 978-82-471-4952-2 (printed ver.)
ISBN 978-82-471-4953-9 (electronic ver.)
ISSN 1503-8181

Doctoral theses at NTNU, 2014:21

IMT-Report 2014:200

Printed by NTNU-trykk

Til pappa

Preface

This work has mainly been carried out at the Department of Material Science and Technology at the Norwegian University of Science and Technology, NTNU, and at Elkem Silicon Materials, Trondheim. Experiments have also been performed at two Elkem plants and at the Pilot facilities of Elkem Technology in Kristiansand. The work is part of an industrial PhD funded by the Research Council of Norway and Elkem Silicon Materials. Some experiments have also been supported by the KMB project ROMA-Raw material Optimization and energy recovery in the MAterials industry and eCAST-Energy and cost effective casting of ferroalloys. eCAST is funded by the Research Council of Norway and The Norwegian Ferroalloy Producers Research Association (FFF).

Acknowledgements

I would like to express a huge gratitude to my supervisor Professor Halvard Tveit who has guided me through my years as a PhD student. The progress during the last year of my PhD would not have been the same without the meetings together with Halvard Tveit and Kjell Håkon Berget, Elkem Silicon Materials, that have motivated me and increased my understanding of the industrial solidification process.

I would like to thank my co-supervisor Professor Merete Tangstad, Department of Material Science and Technology, NTNU, especially for including me in the SiManTi group. It has been an important social arena and has left me with friends such as Mari, Ida, Marit, Delphine, Stephen and Laila. I am also grateful to Professor Lars Arnberg, Department of Material Science and Technology, NTNU, for including me as a member of his Solidification group.

I have been fortunate and had a lot of support during my experimental work and there are several people that I would like to mention. The industrial experiments could not have been performed without the help of the staff at the plants. I would like to thank Kjartan Myklebust, Elin Stubhaug, Gabriel Ossenkamp, Bente Faanes, Tine Eikevik, Ole Jørgen Østensen, Hallgeir Ophaug and Leif Kristiansen for all their help. At Elkem Technology in Kristiansand I want to thank Karl Forwald, Terje Hansen, Stephen Leite, Frank Simonsen, Sigurd Simonsen, Ronny Nilsen, Tarjei Nordbøe, Helge Mathisen, Anne Grete Forwald, Kate Skarpeid, Bente Kroka, Pål Baggetun, Stein Arne Foss, Anders Hope Amundsen, Roger Sandvik, Astrid Storesund, Anette Toverød, Hege Teisrud and Kjell Blandhol. Ingvill Vikan Myhre and Erna Leco at Elkem Thamshavn for squeezing my samples into their already busy schedules. From NTNU, Delphine Leroy for facilitating my experiments, Yinga Yu for help with the SEM and Morten Raanes for all the work with the microprobe analysis. At the Department of Geology and Mineral Resources Engineering, NTNU, I would like to thank Arvid Rein, Erik Larsen and Odd Corneliussen. From SINTEF Materials and Chemistry I would like to thank Ove Darell, Tone Anzjøn, Sarina Bao, Svend Grådahl, Edith Thomassen and Wilhelm Dall. Also Martin Syvertsen and Halvor Dalaker for helping me with the Cyberstar experiment. The project leaders of the ROMA and eCAST projects, Eli Ringdalen, Morten

Onsøien and Freddy Syvertsen have been very helpful. From SINTEF Building and Infrastructure I want to thank Knut Lervik and Roger Leistad. I would like to thank Einar Andersen, Elkem Technology, and Professor Otto Lohne, Department of Material Science and Technology, NTNU, who both tipped me in the direction to investigate solidification layers in more detail. I am also grateful to Stewart Clark in the administration of NTNU for his assistance with the editing of this thesis. I also want to thank those who have been my Elkem colleagues at NTNU during this work: Viktor Myrvågnes, Jirang Cui, Edin Myrhaug, Nils Eivind Kamfjord, Ole Svein Klevan, Kurt Aasly and Vegar Andersen for their support and the good discussions we have had. Great colleagues have been important in order to maintain my motivation.

Among my non-material science friends I would like to thank Lise for always being there during my Kristiansand visits. And off course Stina, the years back in Trondheim would not have been the same without “Stina and Maria quality time”.

I would like to thank Nils Inge and Helga for making me feel appreciated and welcome in their home. I would also like to thank my aunt and my brother. I value the close relationship that we have. I want to give a special thanks to my mother. I admire your strength and the kindness you share with the people around you.

Finally I want to thank Stian. It has been easy to write and be focused having you as a good “distraction” in an otherwise monotone daily life. Thank you for all your patience and support.

Abstract

Silicon of purity 90 to ~100 wt % was cast at different cooling conditions. The temperature recordings from the experiments were used to validate a heat transfer model of the solidification. The model, thermal history and experimental observations were utilized to determine the factors that had the largest impact on the cast product.

Three experiments were performed in industrial scale. In addition a directional solidification experiment and casting onto a water cooled copper plate were performed for different silicon grades in order to study the effect of cooling rate.

These experiments have illustrated that several factors determined the silicon grain size. In addition to the well known effect of cooling rate - other factors were: inclusions present, amount of alloying elements, the temperature of the melt and the formation of solidification layers during casting. The layers acted as a barrier to further growth and may be more frequent in industrial castings. The layers were important to the overall silicon macro- and microstructure.

For the industrial MG-Si2 experiment it was observed that small silicon grains were often accompanied by an uneven distribution of intermetallic phases, while large silicon grains were found in combination with a more even distribution of intermetallic phases. This work supports that the cooling rate after the solidification of primary silicon had an effect on the size and form of the intermetallic phases. This may be utilized industrially to achieve a wanted intermetallic structure. The distribution of the intermetallic phases also depended on solidification layers, available space between the silicon grains and the amount of alloying elements.

All the investigated casts contained a varying degree of segregation. The segregation pattern was in good agreement with the heat transfer model. The model may be used to predict segregation patterns in different casting methods.

The main intermetallic phases observed in this work were consistent with former work on the same alloys.

The distribution of trace elements in the intermetallic phases was studied. Most intermetallic phases contained 10 to several hundred times more trace elements than the bulk analysis, reflecting the low distribution coefficients of the trace elements in question.

A few analyses of the silicon matrix indicated that an increased cooling rate, such as in the copper plate experiments, increased the incorporation of alloying and trace elements into the silicon matrix. This suggests that the trade off to obtain a smaller grain size due to an increased cooling rate was a less pure silicon matrix.

A mass balance was done and it indicated that some of the transition elements with a high diffusion coefficients, such as nickel and copper, could be found in the silicon grain boundaries and matrix due to solid state diffusion.

An abrasion test was performed on samples from all experiments. For the MG-Si2 material, a weak trend was seen where an increased cooling rate increased the abrasion strength. It was not possible to conclude when investigating other material, Alloy A, MG-Si1 and SoG-Si and this was believed to be a result of the inhomogeneity of the material. The micro hardness of the intermetallic phases was measured and it depended on the amount of cracks present in the phases before the measurement since the cracks influenced the length of the measured diagonals.

An initial test where MG-Si2 was purified by means of magnetic separation showed promising results. A grade of 4.9 wt % iron was obtained in the -53 µm fraction using the SLon 100 separator. The recovery in the fraction was 11 % illustrating that there is potential for further optimization of the separation.

Table of contents

Symbols and abbreviations

Symbol	**Description**
A	Area
A	Mass ratio of magnetic and non-magnetic fraction
α	Absorptiviy
C_L^*	Composition in liquid at the solid-liquid interface
C_o	Initial concentration
Cp	Heat capacity
C_s^*	Composition in solid at the solid-liquid interface
D_L	Diffusion coefficient in liquid
δ	Boundary layer thickness
d	Mean diagonal length of indentions Vickers hardness measurement
E	Emissive power for a non black body
E_b	Emissive power for a black body
ε	Emissivity
F	Force
F_c	Competing forces
F_i	Inter-particle forces
F_m	Magnetic force
f_l	Fraction liquid
f_s	Fraction solid
f(u)	Shape factor magnetic particle
ΔG	Gibbs free energy
ΔG_i	Gibbs free energy of cluster formation
ΔG^*_{ci}	Critical Gibbs free energy to form a cap on a substrate- heterogeneous nucleation
ΔG^*_i	Critical Gibbs free energy of cluster formation
G_{abs}	Absorbed irradiation
G_l	Thermal gradient in liquid
G_m	Grade of magnetic fraction
ΔH	Enthalpy
ΔH_f	Latent heat of fusion
H	Field strength
dH/dx	Field strength gradient
h	Heat transfer coefficient
J	Nucleation rate
J_0	Density of available nucleation sites
K	Proportionality constant
κ	Surface curvature
k	Boltzmann’s constant
k	Thermal conductivity
k_0	Equilibrium distribution coefficient
k_{eff}	Effective distribution coefficient

μ_o	Permeability in vacuum
μ_r	Relative permeability
ΔP	Change in pressure
N_{circle}	Number of grains within a circle
$N_{circumference}$	Number of grains that intersects the circle
P	Pressure
P	Load
$q\cdot$	Heat transfer rate
R_m	Recovery of magnetic fraction
R_{nm}	Recovery of non-magnetic fraction
r^*	Critical radii for nucleation
r	Equivalent grain size
ΔS	Entropy
σ	Stefan-Boltzmann's constant
σ^{sl}	Surface energy of the solid-liquid interface
ΔT	Undercooling
ΔT_p	Undercooling due to pressure
ΔT_r	Undercooling due to curvature
θ	Wetting angle
T_M	Transformations temperature liquid to solid
T_s	Surface temperature
T_{sur}	Temperature of surroundings
T_∞	Fluid temperature
ΔV	Change in volume
V	Growth rate of solid-liquid interface
Vs	Molar volume
x	Magnetic susceptibility

Abbreviations	**Description**
At %	Atomic percent
EG-Si	Electronic grade silicon
EPMA	Electron microprobe analysis
HES	Health, safety and environment
HV	Vickers hardness
ICP-OES	Inductively coupled plasma-optical emission
MCS	Dimethyl dichlorosilane
MG-Si	Metallurgical grade silicon
SCG	Screw dislocation growth
SEM	Scanning electron microscope
SoG-Si	Solar Grade silicon
TDN	Two dimensional nucleation
TPRE	Twin plane reentrant angle
TCS	Trichlorosilane
Wt %	Weight percent
XRF	X-ray fluorescence

1 Introduction

The use of silicon and silicon alloys play an important part in the daily life and well-being of the 7 billion habitants on Earth. Silicon constitutes an alloying element in aluminium and steel, it is the main building block in silicones and has an important role in the ever increasing use of electronic-based products.

Elemental silicon is not found in nature, but is bound to oxygen or other elements. The source of silicon is mainly SiO_2 which is found in quartz. The production process used requires a high temperature, a high energy input and the use of a carbon-based reducing agent. The process includes the solidification of liquid silicon to solid silicon and the transformation into usable form and size.

The solidification step is important when it comes to determining the quality and the yield of the cast product. Due to the high silicon temperature and high energy transformation the solidification process also may result in a negative health, environment and safety standard at a plant. For metallurgical grade silicon many of the casting procedures used at most silicon plants today are in principle the same as those developed decades ago and there is a need for improvement. The main reasons for a new and improved casting process are:

- Increasing the post taphole yield and hence reducing the total energy consumption
- Improving the product quality regarding customer value – this may include
    - Defined silicon grain size
    - Distribution of intermetallic phases
    - Trace elements
    - Homogeneity
- Meeting new requirements for working environment
- Reducing the cost for the solidification and silicon forming step

In this study silicon, ranging from 90 to ~100 wt % silicon was cast at different cooling conditions. By tracking the silicon from the furnace throughout the casting it was seen that several factors interacted and in combination gave the final product. The main focus was how grain size, type and distribution of intermetallic phases and abrasion strength were affected by a change in the cooling rate, chemical composition and direction of the heat extraction. A heat transfer model was developed to describe and understand the solidification process and the cast product.

1.1 The history of silicon

Silicon is the 14th element in the periodic table and belongs to the 4A group together with carbon, germanium, tin and lead. Elements within a group have some common chemical features due to the equal number of valence electrons. In most natural substances silicon or carbon are the building blocks, and **Zumdahl** (1998) describes that what carbon is to the biological world, silicon is to the geological world. Most rocks, sands and soils are silica and different silicates. Silicon has a great affinity for oxygen and forms chains and rings containing Si-O-Si bridges that are the basis in these substances. In carbon-based compounds the carbon-carbon bond is the most stable bond, while the Si-O bond gives the most stable silicon compounds. In Figure 1.1 the unit cell of silicon is illustrated.

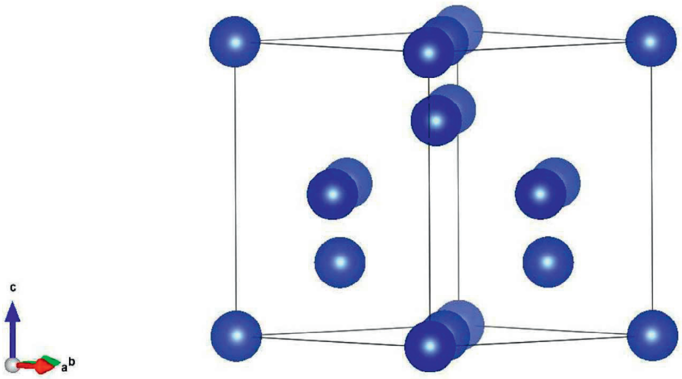

Figure 1.1: Unit cell of silicon, VESTA, **Momma and Izumi** (2011).

It is almost 200 years since the Swedish chemist Jöns Jakob Berzelius discovered silicon, but almost another 100 years passed before ferrosilicon was produced industrially in an electric arc furnace. Steel production was the original application of the electric arc furnace, but after the development of the Søderberg electrode the production of ferrosilicon became feasible. Ferrosilicon is an important additive to steel due to the good de-oxidation properties of silicon which improves the steel quality and yield. In the 1920s ferrosilicon also became an important part of the production of stainless steel, **Gabrielsen and Grue** (2012).

In Figure 1.2 the main applications of silicon are illustrated, not including ferrosilicon.

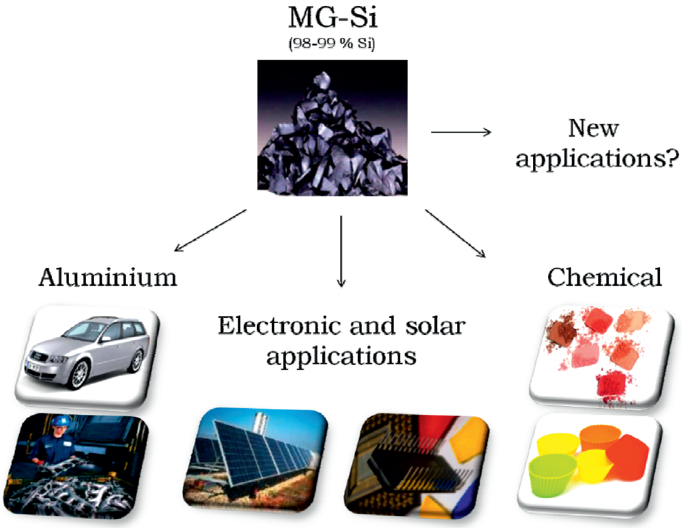

Figure 1.2: Main applications of silicon: aluminium alloys, electronic and solar applications and chemical use as a backbone element in silicones, (**Elkem internal**).

On a world basis around 50 % of the silicon is consumed by the aluminium industry, Table 1.1. Silicon is added to aluminium mainly to improve the viscosity of the alloy, the floatability and mechanical strength. The alloys are mainly used in the machinery and auto production.

The first quantities of silicones, which is the main chemical application of silicon, were produced in the 1930s. During the Second World War the need for improved sealing in airplanes and submarines intensified the research on silicones. The merge of the chemical company Dow and the metallurgical company Corning enabled a rapid development of silicones. Dr Eugene Rochow developed a direct method for synthesizing silicones on an industrial scale. The aimed product of the reaction is dimethyl dichlorosilane, MCS, (**Ceccaroli and Lohne**, 2003). This process is referred to as the direct synthesis or MCS production in this work. Dimethyl dichlorosilane, MCS, serves as a precursor to a vast number of different compounds, named silicones, which contain a Si-O-Si backbone. This backbone can be incorporated into rings and large chains. Parts of the chains and rings can contain different substitute groups such as -CH3, -COOH, -OH. This gives an enormous diversity when it comes to the properties of the different silicones. The silicones are an important part of our modern lifestyle. Products where silicones are frequently used are makeup, paint, water resistant clothing, medicines and baking moulds **Bluestar Silicones** (2013)

The development of the first usable computers occurred during the Second World War. In the 1950s the invention of the transistor and combined with the development and use of semiconductor silicon opened the era that could be referred to as the “silicon age”, **Gabrielsen and Grue** (2012).

Silicon is also essential in the development of renewable energy as the main constituent in solar cells. Both the negative impact fossil fuels have on the environment and the decrease in their deposits have led to increased research activity focusing on renewable energy.

There are stricter requirements to purity for silicon to be used for electronic and solar applications due to the detrimental effect some trace elements can have on the electrical properties. The purity of metallurgical grade silicon, MG-Si, used in aluminium alloys and the production of silicones, is typically 98.5 % and as seen from Table 1.2 impurities are present in the ppmw range. Silicon used in electronic devices and solar cells requires impurity levels in the ppb(a) and ppt(a) range. One common way to obtain this purity is by the distillation and thermal decomposition of volatile silicon compounds. The process where trichlorosilane, TCS, is decomposed, where the main process is the Siemens process, has a dominant position in the industry. It is however a process that consumes a high level of energy where 90% of the input power is lost. Other processes have been developed. Another method to produce Solar grade silicon, SoG-Si is to upgrade MG-Si. This can be done by slag refining, plasma refining, acid leaching, directional solidification or a combination of several methods, **Ceccaroli and Lohne** (2003). The upraded silicon may however not be as pure as silicon from the Siemens process.

Table 1.1 and Figure 1.3 give the amount of silicon consumed in 2002 and 2012 by the aluminium industry, MCS related industry, which is the silicone industry, and trichlorosilane related industry. The numbers are published by courtesy of **deLinde** (2013). In the aluminium segment minor miscellaneous uses are included in addition to some inventory movements. It is assumed that the bulk part of the TCS segment is for solar applications in 2012 but an exact number is not given.

The global production of silicon in 2012 was 2027 MT, and as can be seen from Figure 1.3, 947 MT was consumed by the aluminium industry, 705 MT by the MCS industry and 375 MT by the TCS related industry. This gives an increase from 2002 of 33 %, 83 % and 317 % respectively.

Table 1.1: Global demand for silicon 2002 and 2012 including.

	Si [MT] 2002	**Si [MT] 2012**	**Increase 2002-2012 [%]**
Silicon for aluminium	710	947	**33**
MCS related	385	705	**83**
TCS related	90	375	**317**
Total	1185	2027	**71**

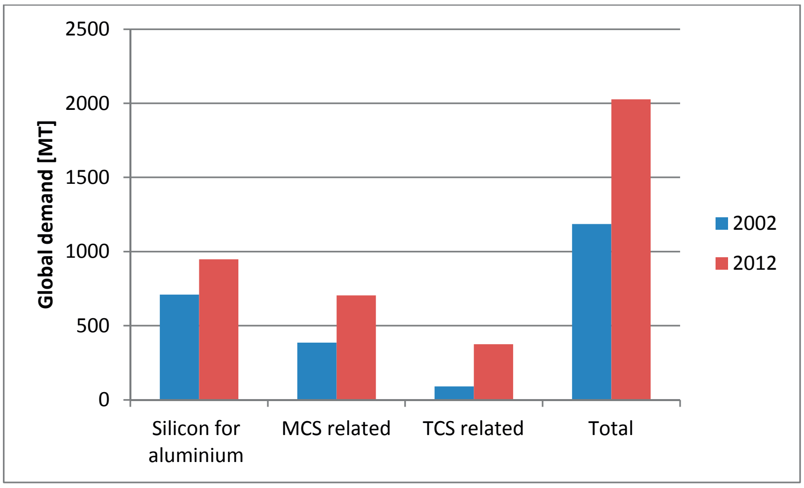

Figure 1.3: Global demand for silicon in 2002 vs. 2012, courtesy of **deLinde, CRU** (2013)

The increase in silicon consumption also means there will be an increased demand for metallurgical grade silicon. The silicon industry faces some main challenges. The industry will have to improve regarding cost, product quality, health, environment and safety (HES) and the access of energy and raw materials.

1.2 Production of silicon

The high stability of the Si-O bond has led to the formation of oxides such as quartz, olivine and feldspars. The main production route to elemental silicon is by carbothermal reduction between quartz, SiO_2, and carbonaceous materials in an electric arc furnace, as illustrated in Figure 1.4.

Figure 1.4: Illustration of the production of metallurgical grade silicon in an electric arc furnace from raw materials quartz, coal/coke and woodchips (**Elkem internal**).

A simplified equation for the production of silicon collected from the textbook by **Schei et al.** (1998) can be written as

$$SiO_2\ (s) + 2\ C\ (s) = Si\ (l) + 2\ CO\ (g) \tag{1.1}$$

The silicon melt is tapped from the furnace, usually into a ladle, and then poured into a mould for solidification. The quartz and carbonaceous materials used in production contain impurities and as a consequence impurities may be present in the silicon produced. Metallurgical grade silicon, MG-Si, is here defined as silicon produced from an electric arc furnace with purity around 98.5 %. The typical composition of MG-Si is listed in Table 1.2. As can be seen from the table the gap between the low value and high value is large for most elements and the obtained bulk purity will depend on the raw materials used and type of electrodes. The variation in purity within a cast will depend on the solidification

Table 1.2: Typical chemical composition of cast MG-Si (**Ceccaroli and Lohne,** 2003)

Element	**O**	**Fe**	**Al**	**Ca**	**C**	**Mg**	**Ti**	**Mn**
Low (ppm)	100	300	300	20	50	5	100	10
High (ppm)	5000	25000	5000	2000	1500	200	1000	300
Element	**V**	**B**	**P**	**Cu**	**Cr**	**Ni**	**Zr**	**Mo**
Low (ppm)	1	5	5	5	5	10	5	1
High (ppm)	300	70	100	100	150	100	300	10

In the work by **Myrhaug** (2003) the source of impurity elements in ferrosilicon is listed. For silicon as opposed to ferrosilicon no iron ore is added, and the Søderberg electrodes can be the main source of iron and give in the order of 1 % iron in the silicon. To produce silicon with MG-Si quality, electrodes are utilized that yield lower iron contamination in the silicon. Solid graphite electrodes are used in smaller furnaces – and composite electrodes are used in larger furnaces. The principles for the composite electrodes are extrusion of the electrode through a slow moving outer steel casing – or that parts the electrode are made from aluminium, **Tveit** (2013).

The different elements that originate from the raw materials and the electrodes will end up in the off gas, slag or the solidified product. According to the boiling point model by **Myrhaug and Tveit** (2000) elements with a low boiling point will evaporate at the furnace top while elements with a higher boiling point will follow the melt out of the furnace.

As the global resources of high purity quartz and carbonaceous material are limited it will be crucial to develop good refining techniques to be able to reduce the level of unwanted elements. This can be processes such as slag refining, leaching or directional solidification. Beneficiation techniques such as magnetic separation or flotation may also obtain an increased interest.

There are different specifications for silicon that are used in the chemical industry as opposed to silicon used in solar applications or in the production of aluminium alloys. It is important to be aware of the similarities and differences in specification in order to obtain a product and a production route that is suited for its application. From an industrial point of view the economics and emissions during production also need to be considered. It will be the combination of production cost, quality and environment that will predict what method that should be chosen in the future.

1.3 Publications

Parts of this work have published in the proceedings of the Silicon for the Chemical and Solar Cell Industry conference XI, **Møll et al.** (2012) and INFACON XIII, **Møll et al.** (2013).

1.4 Structure of the thesis

Chapter 2 introduces the theory that has been considered relevant during this work. A literature survey regarding silicon rich alloys has also been included. In Chapter 3 a basis for the materials and methods used during this work will be presented. In addition a discussion around uncertainties related to some of the experimental methods will be given. Chapter 4 describes the thermal history of the experiments. A heat transfer model in **COMSOL 4.3a** (2012) has been developed based on two of the experiments. The model has been used to predict important casting phenomena. The chemical segregation, distribution and size of silicon grains and intermetallic phases are given in Chapter 5. This is put in context of the thermal history presented in Chapter 4. A discussion regarding the partition of trace elements is given including a mass balance between the intermetallic phases and the silicon matrix. Some aspects regarding post processing of MG-Si are included in Chapter 6 and include a discussion about abrasion strength, micro hardness and fines generation. In Chapter 7 an introductory test of magnetic separation of crushed and milled metallurgical grade silicon is presented. The work is summarized in Chapter 8- conclusions. Finally a discussion regarding future work will be given in Chapter 9.

2 Theoretical Background

Solidification involves the transition from a liquid to a solid state. The process will have a substantial impact on the properties of the finished product. The main product characteristics that are influenced by the solidification process are grain size and grain size distribution, size and distribution of intermetallic phases, chemical segregation on micro and macro scales, product strength and product yield. The solidification process includes the transport of a high amount of thermal energy – and has a significant role in the health, environment and safety, HES, standard in the silicon plant.

This chapter describes a basis for important solidification phenomena. This includes an introduction to the thermodynamics of solidification, nucleation and growth, heat transfer, distribution of impurity elements and morphology. In addition an introduction to magnetic separation and a literature review regarding silicon rich alloys will be given. The main focus has been metallurgical grade silicon and silicon alloys intended for the production of silicones and hydrometallurgical leaching. If the subjects described in this chapter are to be studied in more detail the reader is referred to **Flemings** (1974), **Stølen et al.** (2004) and **Kurz and Fisher** (1998), **Geankoplis** (2003), **Gaskell** (2008) and **Incropera and DeWitt** (2002).

2.1 Thermodynamics of solidification

In thermodynamics a system is defined as the matter subjected to thermodynamic analysis. With a given set of conditions, such as temperature, pressure and composition, a system will always try to minimize its energy. At this minimum the system will be in equilibrium and the equilibrium states of a system can be represented by a phase diagram.

At equilibrium the change in free energy during solidification can be written as

$$\Delta G = \Delta H - T_M \Delta S = 0 \tag{2.1}$$

, ΔG is the change in free energy and ΔH and ΔS the changes in enthalpy and entropy at the equilibrium transformation temperature T_M.

At other temperatures the free energy change can be written as

$$\Delta G = \Delta H - T\Delta S \neq 0 \tag{2.2}$$

Assuming that the enthalpy and entropy are not dependent on small changes in temperature the two equations combined yields

$$\Delta G = \frac{\Delta H \Delta T}{T_M} \neq 0 \tag{2.3}$$

, where ΔT is the undercooling (T_M-T).

The driving force for solidification increases when the negative value of the free energy increases. Since ΔH is negative for solidification, increased undercooling will increases the driving force for solidification.

In Figure 2.1 free energy curves as a function of temperature are illustrated for a pure material (**Baker and Cahn,** 1971). At T >T_M the free energy is at a minimum for the liquid phase and the liquid will be the thermodynamically stable phase.

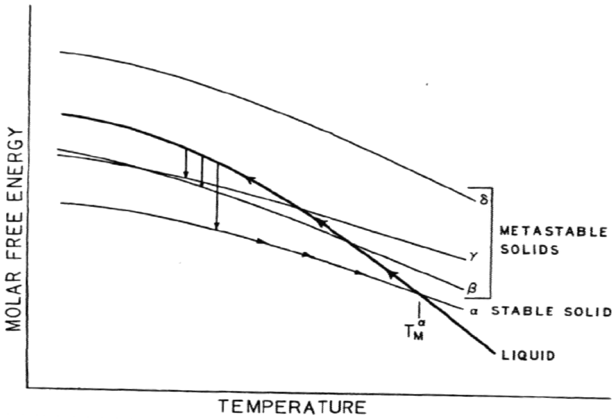

Figure 2.1: Free energy curves versus temperature for a pure material (**Baker and Cahn**, 1971).

At T =T_M, the liquid phase will be in equilibrium with the solid phase α and further cooling could lead to the solidification of this phase. If however nucleation is suppressed for some reason the liquid will continue to cool. The formation of the metastable phases β and γ may take place in subsequent order. The δ phase has no melting point and can therefore never form from the liquid. For a pure element the transition between liquid and solid will occur at a distinct temperature.

The equilibrium melting temperature will depend on the pressure in the system and is given by the Clapeyron equation.

$$\frac{\Delta T_P}{\Delta P} = -\frac{T_M \Delta V}{\Delta H} \tag{2.4}$$

Silicon expands during solidification and increased pressure would decrease T_M. (For most materials the density increase upon solidification and T_M would increase following a change in pressure).

The surface curvature of the particles formed will also affect equilibrium melting point as given in equation (2.5).

$$\Delta T_r = -\frac{2\sigma T_M V_S \kappa}{\Delta H} \tag{2.5}$$

, κ is the mean surface curvature and increases with decreasing radii, σ is the surface tension and Vs is the molar volume of the solid. The surface tension of liquids is usually lower than the surface tension of solids. This result in suppression of the liquidus and solidus lines as the radius of a particle decreases. This yields when the surface area is less than ~1 μm (**Stølen et al.**, 2004).

In Figure 2.2 a phase diagram for an ideal binary alloy is illustrated (middle figure) together with free energy curves at temperatures, $T_{M,}$ the melting temperature (left figure), and $T_1 < T_M$ (right figure). At the melting temperature, the free energy of the liquid is less than the free energy of the solid over the whole compositional range. As a result the liquid is the thermodynamically stable phase. At temperature T_1, the solid will be stable at low concentrations of B, while the liquid will be stable at high concentrations of B. Similar diagrams as shown to the left and right in Figure 2.2 can be calculated for all temperatures, and the loci of all these diagrams constitute the liquidus and solidus curves of the equilibrium phase diagram shown in the middle of Figure 2.2. The derivations of the equations constituting the diagrams are described by **Flemings** (1974).

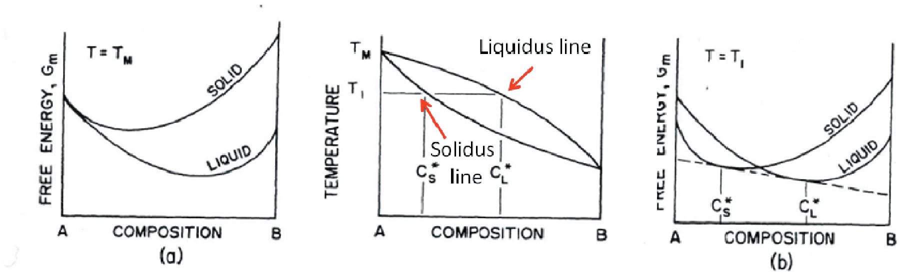

Figure 2.2: Free energy curves at temperatures $T=T_M$ and $T_1 <T_M$ for an ideal binary solution and resulting phase diagram (**Flemings**, 1974).

In a binary system the melting or solidification will occur over a range of temperatures given by the liquidus and solidus lines. The area between the liquidus and the solidus of the system is termed the mushy zone, and here liquid and solid will coexist, (**Flemings**, 1974). The micro structural characteristics such as shape, size and distribution of concentration variations, precipitates and pores are determined in this region (**Kurz and Fisher**, 1998).

All crystalline material will contain a various degree of imperfections and impurity atoms can be found in solid solutions where they are found as substitutional or interstitial point defects. The degree of dissolution of the solute will depend on factors such as, atomic size, the crystal structure, electro negativity and valences (**Callister and Rethwisch,** 2007). The crystal structure of silicon restricts dissolution of most elements and most elements will therefore have a lower solubility in solid silicon than in liquid silicon (**Trumbore**, 1960). This means that when a silicon alloy start to solidify the liquid will be enriched in alloying elements, while nearly pure silicon solidifies. When solidification phenomena are to be studied constrained, local equilibrium is assumed. This means that equilibrium is valid only at the solid-liquid interfaces. For other processes the rate is assumed to occur at a negligible rate. If complete diffusion in both solid and liquid are assumed a description of equilibrium solidification can be outlined.

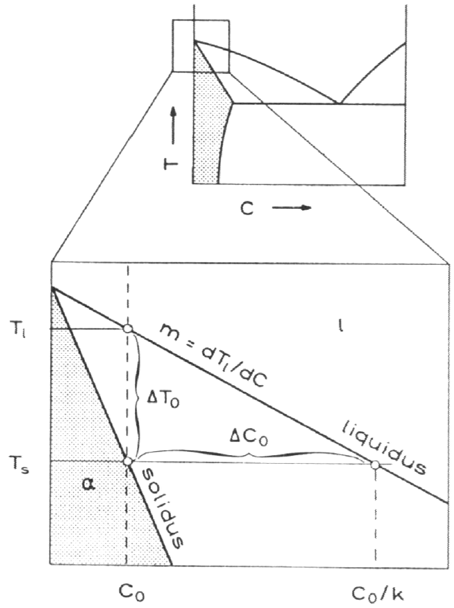

.

Figure 2.3: Binary phase diagram of a A-B system where the distribution coefficient is smaller than unity k<1 (**Kurz and Fisher,** 1998).

The solid and liquid compositions at the solid-liquid interface are temperature dependent as illustrated in the binary equilibrium phase diagram, Figure 2.3. The distribution of the solute between the solid and the liquid phases can be expressed by the equilibrium distribution coefficient, k.

$$k=\frac{C_s^*}{C_L^*} \tag{2.6}$$

, where C_s^* and C_L^* are the solid and liquid composition at the solid and liquid interface respectively (**Flemings**, 1974). For an initial concentration C_0, the liquid will be the only phase that exists above the liquidus temperature. When the liquidus line is crossed, assuming that nucleation is not suppressed, a solid phase will start to nucleate. The composition of the solid and liquid phases, C_s^* and C_l^* is given by the tie-line between the liquidus and the solidus at that specific temperature. A material balance for the system will be

$$C_s f_s + C_L f_L = C_0 \tag{2.7}$$

, where f_s and f_L are the solid and liquid fractions respectively. The remaining liquid disappears when the solidus line is crossed.

If it is assumed that diffusion in the solid is negligible, another expression for the solidification can be developed. Since the amount of solute rejected at the interface must be equal to the increase of solute in the liquid a material balance can be given when a small amount solidifies, df_s.

$$(C_L - C_s^*)df_s = (1 - f_s)dC_L \tag{2.8}$$

If we use the relationship from the phase diagram $k = C_{s^*}/C_{L^*}$ and integrate from $C_{s^*} = k{*}C_0$ at $f_s=0$ one obtains an expression for the concentration in the solid as a function of the fraction solid

$$C_s^* = kC_0(1 - f_s)^{(k-1)} \tag{2.9}$$

, or the relationship between solute in liquid as a function of fraction liquid.

$$C_L = C_0 f_L^{(k-1)} \tag{2.10}$$

The equations are termed the Scheil equation or the non-equilibrium lever rule. A practical application of this is directional solidification of silicon. For elements with a small distribution coefficient it is possible to purify an ingot in a way where the bulk part of the impurity elements ends up in the last part to solidify (given that the planar front does not become unstable). This is a good method to remove e.g. iron and aluminium, but for elements such as P and B that have a segregation coefficient close to unity, see Table 2.1, directional solidification is not as efficient.

Table 2.1: Distribution coefficients in silicon for a selection of elements.

Atom	**k (k_{eff})**	**Reference**	**Atom**	**k (k_{eff})**	**Reference**
Al	$2.0*10^{-3}$	1)	Ni	$8.0*10^{-6}$	4)
B	0.8	1)	O	0.25-1.25	4)
C	0.07	2)	P	0.36	1)
Ca	$1.6*10^{-3}$	3)	Sn	0.016	1)
Cr	$1.1*10^{-5}$	4)	Ti	$(2.0*10^{-6})$	4)
Cu	$4.0*10^{-4}$	1)	V	$(4.0*10^{-6})$	2)
Fe	$8.0*10^{-6}$	1)	Zn	$1.0*10^{-5}$	1)
Mg	$2.3*10^{-3}$	2)	Zr	$1.6\ 10^{-8}$	5)
Mn	$1.0*10^{-5}$	1)	N	$7.0*10^{-4}$	4)
Mo	$(4.5*10^{-8})$	2)	W	$1.7\ 10^{-8}$	5)

1)**Trumbore** (1960), 2)**Zulehner and Huber** (1982) 3)**Sigmund** (1982), 4)**Hull** (1999), 5) **Hopkins** (1985)

Table 2.2: Maximum solid solubilities for a selection of elements.

Atom	**Maximum Solid Solubility (at/cm^{-3})**	**Reference**	**Atom**	**Maximum Solid Solubility (at/cm^{-3})**	**Reference**
Al	$2.0*10^{19}$	1)	N	$4.5*10^{15}$	2)
B	$6.0*10^{20}$	1)	Ni	$8.0*10^{17}$	2)
C	$3.0*10^{17}$	2)	O	$3.0*10^{18}$	2)
Cu	$1.5*10^{18}$	1)	P	$1.3*10^{21}$	2)
Fe	$3.0*10^{16}$	1)	Sn	$5.0*10^{19}$	1)
Mn	$3.0*10^{16}$	1)	Zn	$6.0*10^{16}$	1)

1)**Trumbore** (1960), 2)**Hull** (1999)

At higher growth rates the distribution coefficient will not equal the equilibrium distribution coefficient but it will increase asymptotically towards 1 for k<1. The distribution coefficient can according to **Burton et al.** (1953) be expressed as:

$$k_{eff} = \frac{k_0}{k_0 + (1 - k_0)\exp(-\frac{V\delta}{D_L})} \tag{2.11}$$

,where V is the growth rate of the interface, δ thickness of the boundary layer and D_L the diffusion coefficient of the impurity in the melt. At higher growth rates more impurities will be incorporated into the silicon crystal.

2.2 Nucleation and growth

Even though thermodynamics predicts the phases that are stable at equilibrium, thermodynamics will not predict the time for equilibrium to be reached. Before a solid can start to grow the first solid nucleus needs to be formed. In a melt there are random fluctuations of atoms, and at a given moment there will be a certain amount of clusters due to these fluctuations. If a cluster is larger than a critical size a stable nucleus is formed and can continue to grow by adding atoms arriving at the nucleus. During the transformation from one phase to another the atoms must be arranged into new positions. This transition can only occur if the probability of the transfer of atoms from the parent phase to the product phase is higher than the opposite transfer (**Kurz and Fischer**, 1998).

2.2.1 Nucleation

In pure materials the solid is formed from its own melt without the help of foreign materials. In order to do so a large energy barrier must be surpassed. This process is named **homogeneous nucleation**. An expression for the free energy change involved in the transition between liquid and solid is given in the equation below.

$$\Delta G_i = -V\frac{\Delta G}{V_s} + A\sigma \qquad (2.12)$$

, where ΔG_i is the free energy of formation of one cluster with i atoms, V is the volume of the cluster, V_s is the molar volume, ΔG the driving for solidification, A the surface area and σ the surface tension between the liquid and the solid. For small particles the surface energy, the second term in the equation, plays a large role determining the total free energy of the particles. The bulk energy, the first term, dominates at a larger radius. A cluster needs to be larger than a critical radius in order to be stable and grow. This critical radius will decrease with the degree of undercooling, ΔT, as seen from Equation 2.13 below.

$$r^* = \frac{-2\sigma T_M V_S}{\Delta H \Delta T} \qquad (2.13)$$

The critical free energy of formation for the cluster is given in equation 2.14.

$$\Delta G_i^* = \frac{16}{3}\frac{\pi\sigma^3 T_M^2 V_s^2}{\Delta H^2 \Delta T^2} \tag{2.14}$$

The nucleation rate can be written as

$$J = J_0 \exp(\frac{-\Delta G_i^*}{kT}) \tag{2.15}$$

, where Jo is the density of available nucleation sites and k is Boltzmann's constant, **Cantor and Nabarro** (2003). The nucleation rate increase with increased undercooling. For metals the maximum undercooling attained around is 0.18 of the absolute melting point according to different studies (**Flemings**, 1974). The barrier to nucleation can be reduced when the nucleation starts at foreign particles and in practice most liquids start to crystallize only with a few degrees of undercooling. This is termed **heterogeneous nucleation.** The barrier to nucleation decreases when the wetting between the crystal and the substrate improves.

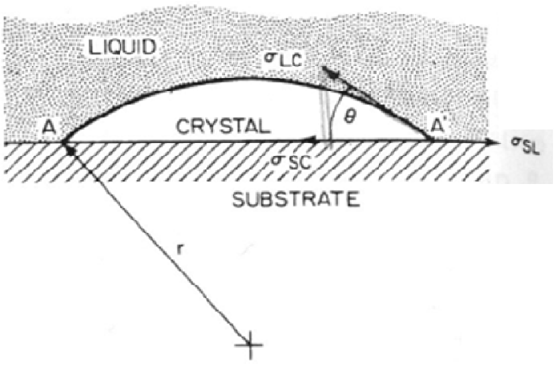

Figure 2.4: Formation of a cluster on a substrate (**Flemings**, 1974).

For complete wetting the wetting angle, θ, is zero, while for zero wetting, θ is 180°. The barrier to nucleation, can be reduced by the function f(θ), so when θ goes to zero the barrier to nucleation goes to a minimum as expressed in Equation 2.16

$$\Delta G_{ci}^* = \Delta G_i^* f(\theta) \tag{2.16}$$

In commercial practice inoculants/ grain refiners are added to many molten alloys to form fine-grained materials. The grain refiner increases the amount of stable nucleus formed in the initial stage and therefore gives a more fine-grained material.

2.2.2 Growth

When the barrier to nucleation is surpassed the nucleus can continue to grow. At the interface, atoms will be both attached and detached and the growth rate will be dependent on the rate of these processes. Diffusion in the liquid will influence the rate of attachment and the number of neighbours binding the atoms to the interface will influence the rate of detachment. The more neighbours binding an atom to the crystal, the higher the probability that it will remain. If an atom is to be incorporated in a position with few neighbours a large difference in the force binding it to the crystal and binding it to the melt must exist. A large undercooling is needed in order to create such a difference.

It is common to divide the interface structure into **non-faceted** and **faceted** interfaces. For most metals the atomic structure of the solid will be quite similar to the structure in the liquid and atoms are added easily to any position of the surface, a non-faceted morphology will be adapted. This is illustrated in point **a** to the left in Figure 2.5, and point **b** to the right in the right figure. In faceted crystals there is a greater difference between the structure and bonding in the solid to that in the liquid as compared to metals. Some atomic planes accept atoms readily. The faster growing planes will disappear, while the slower growing planes define the structure.

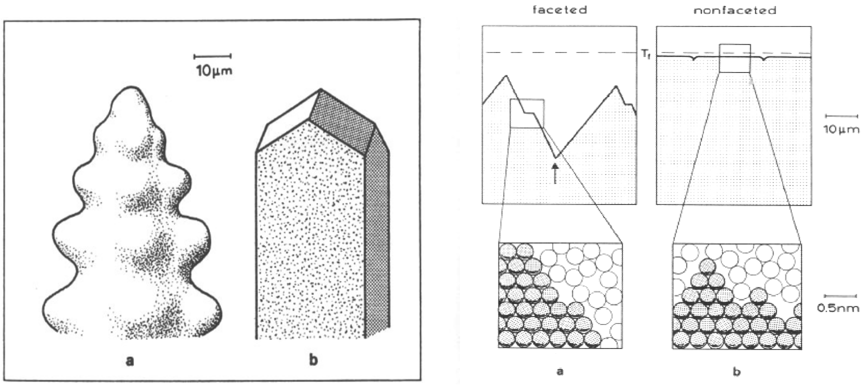

Figure 2.5: Non-faceted, **a**, and faceted, **b**, growth morphology, left, and the form of faceted, **a**, and non-faceted, **b** interfaces, right (**Kurz and Fisher,** 1998).

Generally one can look at the melting entropy in order to predict the morphology the crystal will adapt. When the dimensionless entropy, $\alpha=(\Delta S/R)$, is <2, a non-faceted growth morphology is predicted, while when $\alpha>2$, a faceted growth morphology is predicted. ΔS is the entropy related to the phase change and R is the gas constant. **Beatty and Jackson** (2000) describes that facets that develops in silicon are only of the {111} family. The growth in other planes is non-faceted and the interfaces are rough.

There are several mechanisms describing the growth of silicon. Two terrace-step kink, TSK, models, **Liaw** (1990), have been widely accepted in addition to the twin plane re-entrant edge model, TPRE. The TSK type models are, the two-dimensional nucleation model, TDN, and the screw dislocation growth model, SCG. In the TSK models, if there is a step present, the atom will diffuse towards and along it until it meets a kink where it can be incorporated, see Figure 2.6. In the TDN model a 2D nucleus must first form on top of a flat surface. When the nucleus reaches a critical size, it is stable and can continue to grow with a lateral step upon the surface. At the start of each new layer a two-dimensional nucleus must be formed once more. When the surface has a defect such as a screw dislocation, the SCG model, Figure 2.6c is applicable. New atoms arriving can diffuse to the steps of the dislocation and continue to grow. The dislocation will still be present when a new atomic layer is to be formed so the undercooling required for 2D nucleation is not called for. The TDM model requires a high degree of undercooling in the range of 3.7 to 9 K, while the SCG model ranges from 0.32 to 0.8 K according to **Abe** (1974) and **Chikawa and Sato** (1980)

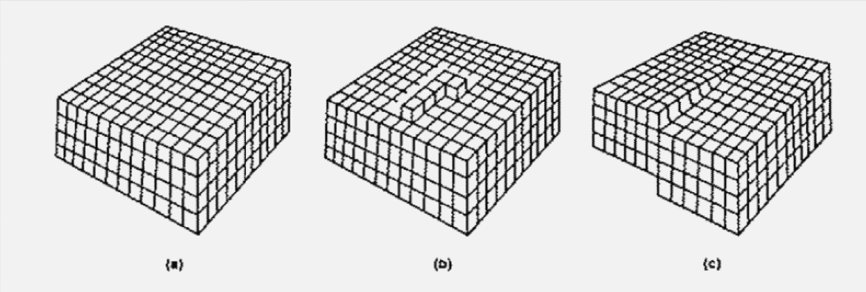

Figure 2.6: Growth mechanism in silicon- a) and b) representing the TDN model and c) the SCG model.

In the TPRE model new atoms can arrive at re-entrant edge which facilitates the bonding and leads to a more rapid growth. The defects introduce new bonds which will reduce the kinetic undercooling needed for growth to occur.

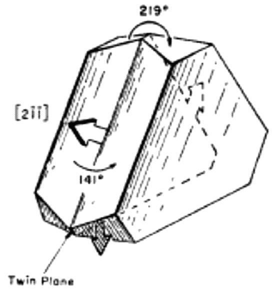

Figure 2.7: Illustration of a twin re-entrant angle (**Hamilton**, 1960).

The basis for the TPRE model is given by **Hamilton** (1960) and **Wagner** (1960). A summary of this growth mode is given by amongst others **Rong** (1992) and **Forwald** (1997).

Both the SCG and the TPRE models are the result of crystal defects. The growth mechanism will depend on factors like the growth rate, thermal gradient and undercooling. A review regarding crystal growth behaviours of silicon during melt growth processes can be found in the review article by **Fujiwara** (2012).

2.3 Microstructure

The material in this section is mainly collected from **Kurz and Fisher,** (1998) if nothing else is stated.

Figure 2.8 illustrates a typical representation of several structural zones in a casting. In usual castings one or more of these zones exists. The formation of these zones will be outlined below.

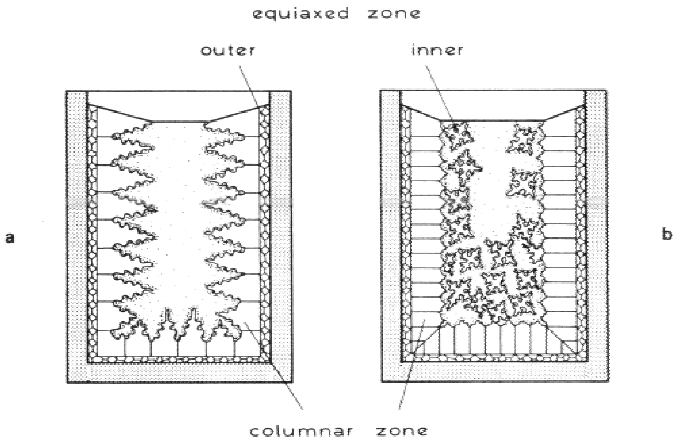

Figure 2.8: Structural zones in a casting (**Kurz and Fisher,** 1998).

The driving force towards nucleation is large close to the mould wall due to a large temperature difference. An outer equiaxed zone will develop consisting of many small equiaxed grains. When the temperature difference is reduced grains that remove heat efficiently, that is grains that grow opposite to the heat flow, will outgrow grains growing in other directions. A columnar zone is developed. If small branches of the columns become detached, the branches can continue to grow if they are in an undercooled region of the melt. The heat will be dissipated isotropically and an equiaxed shape will be attained i.e. an inner equiaxed zone is developed. The solid-liquid interface is said to be morphologically stable if a plane front is attained and unstable if cells and dendrites are developed.

For a pure element the solid-liquid interface will be stable as long as the thermal gradient at the interface is positive

$$G = \frac{dT_q}{dz} > 0 \tag{2.17}$$

For an alloy the situation is more complex due to variations in composition along the interface. When an alloy solidifies the solute will either be rejected at the solid liquid interface, k<1, or accumulated in the solid when k>1. In silicon most solutes will be rejected at the solid-liquid interface and this will be described further. Mass can neither be created nor destroyed, so the atoms rejected at the interface will pile up in a boundary layer as illustrated in Figure 2.9. Simplified the length of the boundary layer can be expressed as

$$\delta_c = \frac{2D_L}{V} \tag{2.18}$$

, where δ is the thickness of the boundary layer, D_L the diffusion coefficient of the impurity in the melt and V is the growth rate of the interface. Since the solute rejected needs to be removed from the interface by diffusion, a higher growth rate means that the solute will not have as much time to diffuse and the boundary layer thickness is reduced.

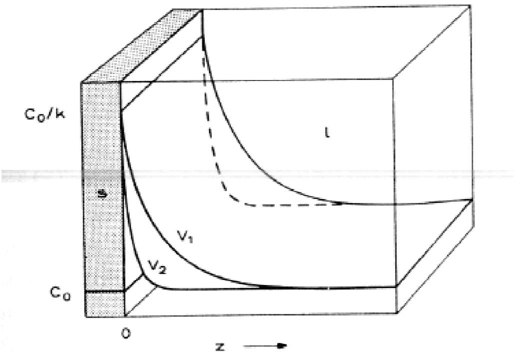

Figure 2.9: Steady state boundary layer at a planar solid-liquid interface. Growth rate V2>V1 (**Kurz and Fisher,** 1998).

From the phase diagram, Figure 2.10a, it is seen that the liquidus temperature will be affected by the amount of solute in the liquid. In Figure 2.10b the liquid composition as a function of distance from the solid-liquid interface is given. Since the amount of solute is higher close to the interface the liquidus temperature will be lower here then further away from the interface. If the temperature in the melt at all times is higher than the liquidus temperature a protuberance at the interface caused by an instability will be in a superheated environment and melt back, Figure 2.10c. However if the actual temperature is below the liquidus temperature a protuberance will find itself in undercooled region where it can grow Figure 2.10d. This is called constitutional undercooling.

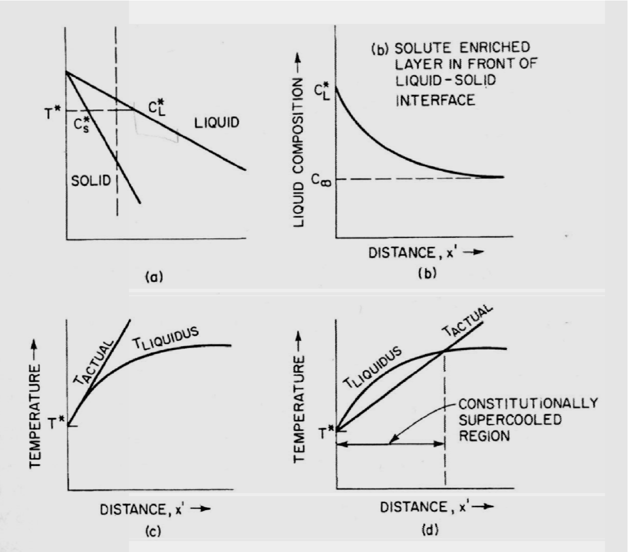

Figure 2.10: d) illustrate the condition for constitutional undercooling in alloys, where T_{actual} is less than $T_{liquidus}$ (**Flemings**, 1974).

For a binary alloy the front will be stable as long as the criterion below is fulfilled.

$$\frac{G_L}{V} \geq -\frac{m_L C_0 (1-k)}{k D_L} \tag{2.19}$$

If this criteria is not fulfilled cells will start to develop at the interface. The cells will grow perpendicular to the solid-liquid interface regardless of crystal orientation. Crystallographic features will be more important if the growth rate is increased and dendrites start to develop.

Kattamis et al. (1967) described the grain coarsening during isothermal holding which is similar to coarsening during dendritic solidification. The same models are also explained by **Flemings** (1974), where Figure 2.11 is from.

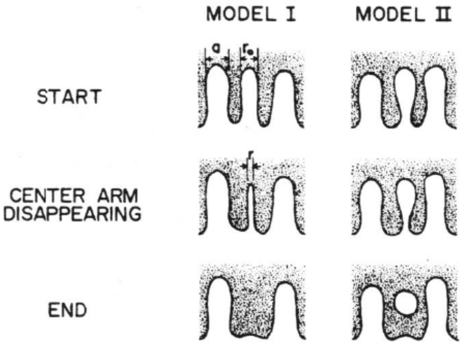

Figure 2.11: Model I (left) and II (right) explaining dendrite coarsening during isothermal holding (**Flemings**, 1974).

In the first model, model I, one of the dendrites has a smaller radius, $\mathbf{r_0}$, and will consequently have a lower melting point than the dendrite with the larger radius, as shown in Equation 2.5. The dendrite with radius $\mathbf{r_0}$ will melt since it is in a region above the melting temperature. The concentration in the liquid surrounding $\mathbf{r_0}$ will be higher than the liquid surrounding **a**, so the solute will diffuse to dendrite **a** and grows. In the second model the radius of the dendrite is smaller at the root so the arm melts. The effect of this phenomenon during solidification is that an increased coarsening time tc, that is the time the system is in the solid-liquid region, will result in a coarsening of the dendrites.

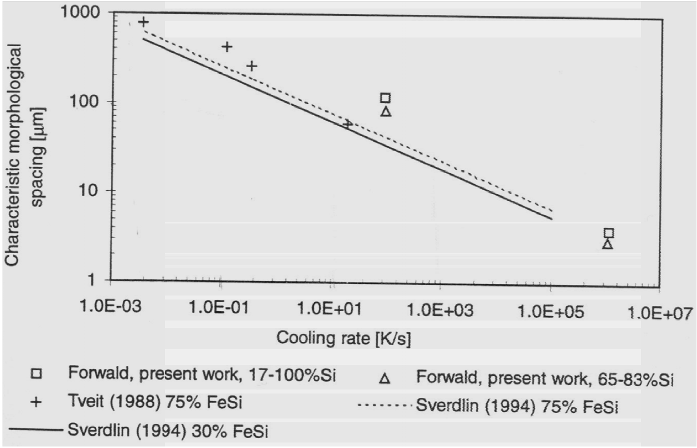

Figure 2.12: Morphological spacing vs. cooling rate for some silicon rich alloys (**Forwald**, 1997)

Forwald (1997) illustrated how the morphological spacing in some silicon rich alloys is affected by the cooling rate. Values for **Tveit** (1988) and **Sverdlin** (1994) are also illustrated in Figure 2.12. Decreasing the cooling rate increases the morphological spacing in agreement with the model by **Kattamis et al.** (1967).

2.4 Heat transport during solidification

Solidification of a material involves the extraction of heat from the melt to ambient temperature. As the heat is extracted there will be a change in the enthalpy of the material due to cooling; $\Delta H=\int c_p dT$, and due to the transition from liquid to solid; $\Delta_f H$, which is the latent heat of the material. In Figure 2.13 ΔH is represented as a function of temperature for several ferro-silicon alloys with increasing silicon content. It is seen that the latent heat, which in the figure is represented as a jump in ΔH at the melting temperature, increases with increasing silicon content. The latent heat is a material property and for silicon the latent heat is about 5 times larger than for most metals. ΔH_f is 50 kJ/mol for silicon while it is only 14 kJ/ mol and 11 kJ/mol for iron and aluminium respectively, (**Aylward and Findlay**, 2008).

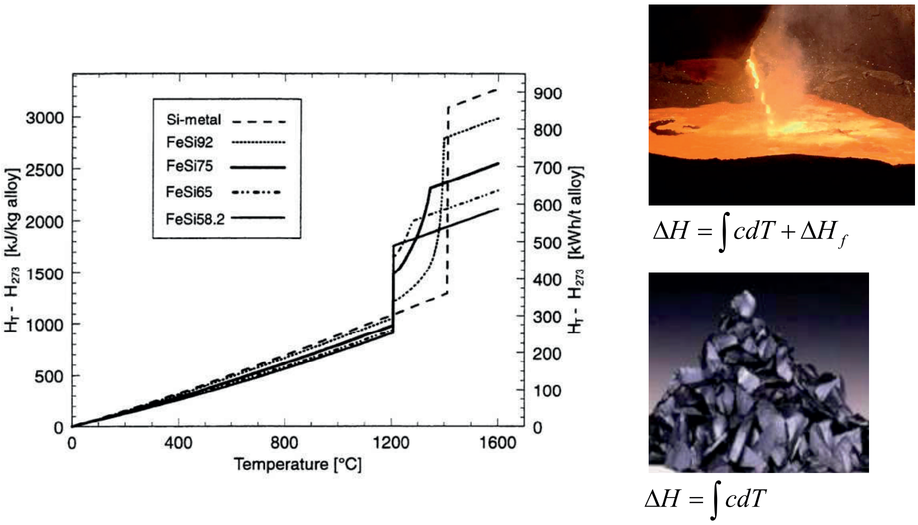

Figure 2.13: Enthalpy in Fe-Si alloys in the range of 0-1600 °C (**Tveit,**1988 adapted by **Klevan**, 1997),

2.4.1 Mechanisms of heat transfer

The three main mechanisms of heat transfer are; conduction, convection and radiation (**Incropera and DeWitt**, 2002).

Conduction involves the transport of heat though molecular movements in a solid, gas or liquid. There is no bulk movement, but heat can be conducted by an energy transfer between adjacent molecules due to lattice vibrational waves and migration of free electrons. Higher temperatures involve higher molecular energies and when particles with a high level of energy collide with particles with less energy there will be a transfer of energy between the particles. The net flux of the heat is towards lower temperature region. An example of heat conduction can be dipping a metal spoon into a glass of cold water. Even though the whole spoon is not in contact with the water, the metal will reach the same temperature as the water after a while. The rate of heat transfer by conduction can be expressed by Fourier´s law.

$$\dot{q} = -k\frac{dT}{dx} \tag{2.20}$$

, in (W/m^2) where k is the thermal conductivity of the material. Metals typically have high thermal conductivity while isolating materials have a low thermal conductivity.

Convection involves heat transfer by bulk motion and mixing (**Geankoplis**, 2003). It describes the energy transfer between a moving fluid and a surface. Close to the surface the mechanism will be by the diffusion of heat while further away the mechanism is usually by bulk motion of fluid particles. A boundary layer and temperature and velocity profiles develops at the surface. An example of convection is blowing air over a hot cup of chocolate to make it cool faster. This is named forced convection. Convection can also be natural such as flow due to temperature differences in a fluid. At different temperatures the density will differ and a low density liquid will rise while high density liquid will sink. The rate of the convective heat transfer can be written as Newton´s law of cooling

$$\dot{q} = h(T_s - T_\infty) \tag{2.21}$$

, in (W/m^2), where h is the convective heat transfer coefficient and T_s and T_∞, the surface and fluid temperature respectively. The conductive heat transfer coefficient depends on the conditions at the boundary layer between the surface and the fluid. Using Equation (2.21) convective heat transfer is set to be positive if heat is transferred from the surface, $T_s > T_\infty$, and negative if heat is transferred to the surface, $T_\infty > T_s$ (**Incropera and DeWitt**, 2002).

Energy can also be transferred by means of electromagnetic waves. This form of energy transfer is termed radiation. An example is the heat emitted from the sun. The rate at which the energy is emitted from a surface is called the emissive power, E. The upper limit to radiation occurs for an ideal surface named a perfect black body. The emissive power is then

$$E_b = \sigma T_s^4 \tag{2.22}$$

, given in (W/m^2). T_s is the absolute temperature at the surface and σ is the Stefan Boltzmann constant.

The emissivity, ε, of a perfect black body equals 1. For a body that is not a black body ε<1. The emissive power can then be written as

$$E = \sigma \varepsilon T_s^4 \tag{2.23}$$

The surface will also absorb some radiation from the surroundings and this can be described as

$$G_{abs} = \alpha G = \alpha \sigma T_{sur}^4 \tag{2.24}$$

,α is the absorptiviy and has a value between 1 and 0. Assuming that α and ε are equal, the net heat transfer due to radiation can then be written as the combination of Equations 2.23 and 2.24.

$$\dot{q} = \sigma \varepsilon (T_s^4 - T_{sur}^4) \tag{2.25}$$

The radiative and the convective heat transfer can be combined into one equation describing the heat transfer from a surface.

$$\dot{q} = h(T_s - T_\infty) + \sigma \varepsilon (T_s^4 - T_{sur}^4) \tag{2.26}$$

At temperatures where $T_s>>>T_{sur}$ the radiative term will dominate while at lower temperatures the convective term will dominate.

2.4.2 Solidification in an industrial sized mould

In the following section solidification in a mould covered in fines will be used as an example of heat transfer during solidification. The energy that needs to be transported in order for the melt to cool to ambient temperature is the energy related to the reduction in enthalpy during cooling, $\Delta H=\int C_p dT$ and the energy related to the phase transfer from liquid to solid $\Delta_f H$.

With the cooling rates used in industrial casting of silicon and ferrosilicon the rate of heat removal will mainly depend on the resistance to heat transfer to the surroundings. It seems that the conductivity in silicon/ ferrosilicon is only decisive at very high cooling rates. This means that the cooling rate can be altered by changing the mould material. This is illustrated in the thesis by **Tveit** (1988). A sketch of the solidification of silicon in a mould covered in fines is given in Figure 2.14 at different snapshots into the solidification.

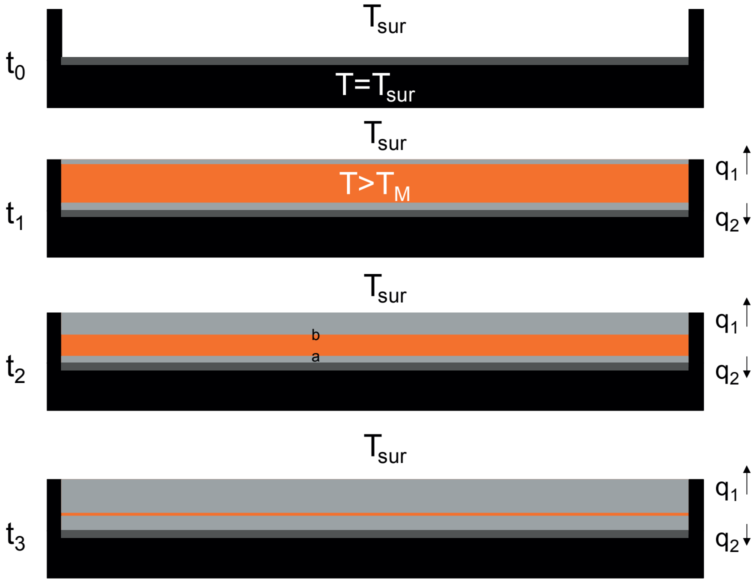

Figure 2.14: Heat flow during solidification, time t_0, t_1, t_2, t_3. The mould is illustrated in black, the fines in dark grey, liquid silicon in orange and solid silicon in light grey.

t_0 is a snapshot prior to filling the mould. The mould-fines layer has a temperature equal to the surroundings.

t_1 is straight after filing of the mould. T_{melt}-T_{mould} is large and the solidification starts instantly close to the mould wall. From the top surface, heat will be lost in a combination of radiation and convection and can be given by Equation 2.26 at a given moment. Assuming a low over temperature in the melt, the surface solidifies rapidly. The radiative term will dominate when the surface temperature is much higher than the surrounding temperature. Through the solid silicon, mould-fines layer, heat will be transported by conduction, Equation 2.20. As described above heat removal will mainly depend on the resistance to heat transfer to the surroundings, which for the lower part will be the mould-fines. At the solid- liquid interface latent heat will be generated and this heat also needs to be removed. In liquid silicon there will be flow due to density differences which will result in convective heat transfer. Solid silicon has a lower density compared to liquid silicon and this density difference is enhanced due to the enrichment of alloying elements in the liquid during solidification. In the case of solidification from the top surface this leads to low density silicon floating at the top, while higher density liquid enriched in impurity elements will sink.

t_2- For a given position the heat will be transported in the direction where there is least resistance to heat transport. That is where the temperature gradient is largest. Depending on the mould material and the size of the fines heat will preferentially be transported upwards or downwards. In Figure 2.14 the positions **a** and **b** at time t_2 are examined. For point **a,** the temperature above, that is in the liquid, is higher than the temperature below, so the heat will be removed in the direction where the temperature gradient is negative; towards the mould. For point **b**, the temperature below, that is in the liquid, is higher than above, so the heat will be removed toward the top surface. Two solidification fronts will develop, one moving downwards and one moving upwards and the rate of their movement will depend on how fast the heat is removed from the top and bottom.

t_3- Since there has been an accumulation of alloying elements in the liquid during solidification, the area where the two fronts meet is enriched in alloying elements. If the heat has been removed faster from the top than the bottom the fronts meet closer to the mould than the top surface.

2.5 Magnetic separation

According to **Oberteuffer** (1974) magnetic separation is conventionally used for two general purposes:

1) Purification of feeds with magnetic components
2) Concentration of magnetic materials.

For silicon that contains a certain amount of intermetallic phases the objective is to separate the intermetallic phases from silicon in order to obtain a purified product. The degree of purification will depend on several factors, such as design of the separation device, magnetic field, particle size and magnetic susceptibility of the intermetallic phases. The susceptibility is a measure of how much a material will affect an electric field. The following presents an introduction to magnetism and magnetic separation. The theory is collected from **Oberteuffer** (1974), **Xiong et al**. (1998), **Sandvik et al.** (1999), **Sherrell and Dunn** (2012) and **Zumdahl** (1998).

2.5.1 Magnetism

In Bohr`s atomic model the atom is built up by a positively charged core surrounded by negatively charged electrons positioned in different orbitals. In the molecular orbital theory the atomic orbitals bond which results in orbitals with energy levels both higher and lower than the original orbitals. The orbitals are filled with electrons in subsequent order starting with the lowest lying orbital. The electrons are usually arranged in pairs with opposite spins that will cancel the magnetic momentum. When a sample of a non-magnetic material is put into a magnetic field two types of magnetism are induced. If the material is attracted to the inducing magnetic field it is a paramagnetic material- not all electrons are paired, as for O_2. If the material is repelled by the magnetic field it is a diamagnetic material- all electrons are paired, this is the case for N_2 (**Zumdahl**, 1998). Elements that are close to iron in the periodic table have a lot of unpaired electrons and spontaneously magnetize, they are named ferromagnetic materials. In an induced field ferromagnetic substances will order parallel to the field and the total field can be strong.

A measure often used when talking about magnetism is the magnetic susceptibility of a material, x. For a paramagnetic material $x>0$, while for a diamagnetic material $x<0$. For paramagnetic substances the magnetic susceptibility decreases with temperature. For ferromagnetic substances it is dependent on both temperature and field strength, while for a diamagnetic material it is always negative no matter the temperature and field strength.

The magnetic force acting on a particle in a magnetic field can be expressed in the simplified equation below (**Sandvik et al.**, 1999)

$$F_m = VH\frac{dH}{dx}f(u)\mu_0(\mu_r - 1) \tag{2.27}$$

V is the volume of the particle, f(u) the shape factor, H the field strength, dH/dx the gradient of the field strength, μ_r and μ_o, the relative permeability and the permeability in vacuum respectively. The absolute permeability dependent on the material and the relative permeability can be related to the susceptibility in the equation below

$$\mu_r = 1 + \chi \tag{2.28}$$

From this it is seen, as given above, that F_m will be negative for a diamagnetic material and positive for paramagnetic materials.

When a material is to be separated there will be a competition between several forces, as illustrated in Figure 2.15. The magnetic force F_M binds the magnetic particle to the magnetized wire, while the competing forces F_c, such as gravity and hydrodynamic drag force, pulls the particle away from the magnetized wire. Attraction between the particles F_i, such as electrostatics and surface chemical double layer forces, will decide how many non-magnetic particles that will join the magnetic fraction.

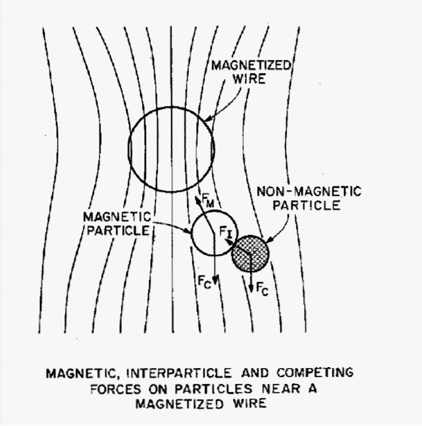

Figure 2.15: Forces acting on a particle attracted to a magnetized wire by a force F_M, **(Oberteuffer,** 1974).

The efficiency of the magnetic separation can be reported as:

Recovery, R_m: ratio of magnetic material in the magnetic fraction relative to that in the feed.

Grade, G_m: the fraction of magnetic materials in the magnetic fraction.

The grade can be defined as

$$G_m = \frac{R_m}{R_m + AR_{nm}} = \frac{1}{1 + A\frac{R_{nm}}{R_m}} \tag{2.29}$$

, where A is the mass ratio between the non magnetic and magnetic particles in the feed, and R_{nm} is the recovery of non magnetic particles in the magnetic fraction.

The recovery of magnetic particles is given in the equation below.

$$R_m = K\frac{F_m}{F_c} \tag{2.30}$$

, where K is proportionality constant.

The recovery of the non-magnetic particles will depend on the inter particle forces and the competing forces as shown below.

$$R_{nm} = K'R_m\frac{F_i}{F_c} \tag{2.31}$$

Inserting this into Equation 2.29 the following expression is given for the grade.

$$G_m = \frac{1}{1 + AK' \frac{F_i}{F_c}} \tag{2.32}$$

It is seen that R_m increases when the competing forces decrease and the magnetic force increases. However as the competing forces decrease the grade will be reduced. Increased inter-particle force will also reduce the grade.

2.6 Micro hardness

Hardness is a measure of the resistance of a material to localized plastic deformation. The lower the hardness index number, the larger and deeper the indention is, that is, the softer the material is (**Callister and Rethwisch,** 2007). A material that is soft is usually ductile, while a hard material is brittle.

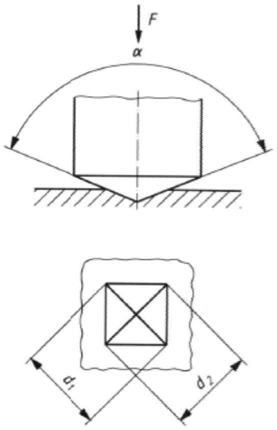

Figure 2.16: Principle of Vickers hardness measurements (**ISO 6507-1**, 2005)

The hardness can be calculated from the equation below.

$$HV = 1.854 \frac{P}{d^2} \tag{2.33}$$

, where P is the load in kg and d the mean diagonal in mm (**Callister and Rethwisch,** 2007). The equation can also be written as

$$HV = 0.1891 \frac{F}{d^2} \tag{2.34}$$

, where 0.0191 is the conversion factor from mass to force, F is the force in N and d the mean diagonal in mm, (**ISO 6507-1,** 2005).

2.7 Solidification of MG-Si and its alloys - literature study

The production of metallurgical grade silicon was outlined in Chapter 1. Iron, aluminium, calcium and titanium are usually the main impurities and will in this work be referred to as alloying elements. Other elements are referred to as trace elements. During the 1990s much of the research regarding solidification of MG-Si focused on how the solidification would influence the direct synthesis. The bulk part of this literature is published in connection with the conference Silicon for the Chemical and Solar Cell Industry. The International Ferro Alloy conference, INFACON, has also been represented with contributions from the industry. For metallurgical grade silicon several of these publications have described the microstructure of metallurgical grade silicon and the effect of cooling rate. Examples are the publications by **Anglezio et al**. (1990), **Dubrous and Anglezio** (1990), **Rong** (1992), **Schei et al.** (1992), **Margaria** (1994), **Margaria** (1996), and **Meteleva-Fischer et al.** (2012). The publications give a thorough description of the intermetallic phases found in MG-Si and emphasise the effect of cooling rate on the degree of grain coarsening of primary silicon. Amongst others **Margaria** (1994) studied the influence of cooling rate on the distribution of intermetallic phases and described that the distribution of the intermetallic phases was determined by the silicon grain size. It was therefore dependent on the cooling rate in the region the grain size of primary silicon was defined. **Rong** (1992) on the other hand noted that the shape of the intermetallic phases changed when the cooling rate in the region after solidification of primary silicon decreased. This was attributed to minimizing the surface energy.

In addition to MG-Si, research on hydrometallurgical leaching of alloyed silicon has also been an area of interest. This includes the development of the Silgrain process®. The last decades the research on silicon for solar and electronic applications has increased.

As can be seen from Figure 1.3 the demand for high purity silicon has increased dramatically over the last 10 years. The increase has been highest for silicon for solar applications, listed as TCS in the figure, where the main process is the Siemens process. Numbers given by

Tranell et al. (2012) state that the Siemens process uses 180 kWh/kg silicon produced as opposed to 40-60 kWh/ kg for silicon produced by the metallurgical route. From an energy perspective the metallurgical route is to be preferred. The silicon from the metallurgical route will however contain more impurities than the silicon from the Siemens process. This can reduce the efficiency of the solar cell. Since the deposits of pure raw materials for the production of MG-Si is reduced it can be expected that the purity of MG-Si will decrease in the following years. If refining of MG-Si is to be cost efficient the refining techniques must be improved or new techniques must be developed.

2.7.1 Binary systems

The binary system of greatest interest in this work has been the binary **Fe-Si** system. The phase diagram is given in Figure 2.17.

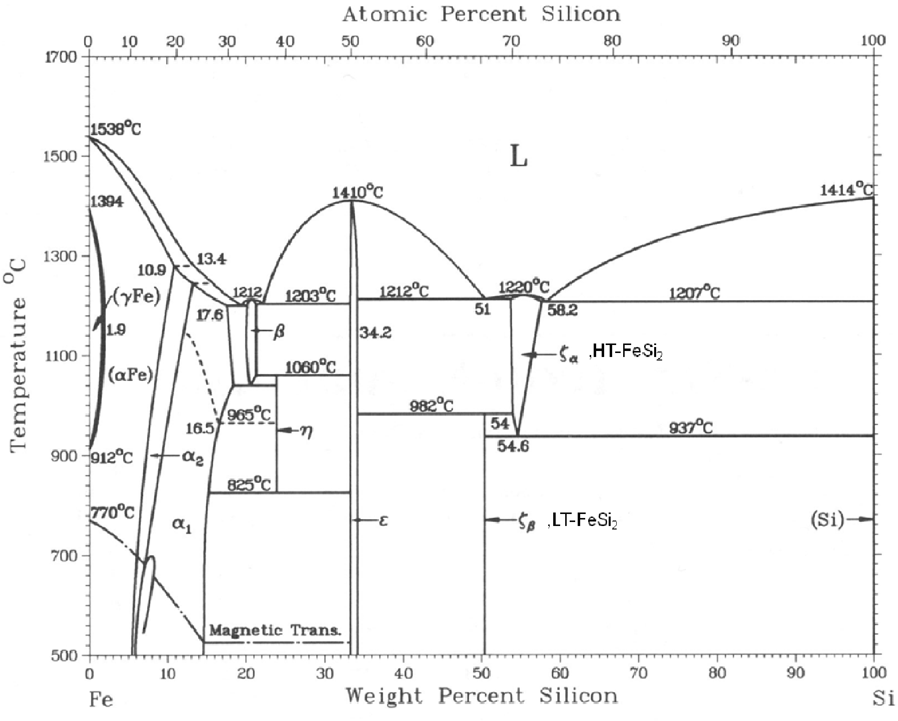

Figure 2.17: Binary phase diagram Fe-Si, **Massalski** (1990). Superimposed on the diagram is the labelling used in this work, HT-FeSi$_2$ and LT-FeSi$_2$.

For the purpose of this study only the Si-rich corner of the phase diagram is studied. For compositions above 58.2 wt % Si, Si will be the first phase to solidify. In the two-phase region between the liquidus temperature and the solidus temperature at 1220 °C, pure silicon crystals will solidify while the melt will be enriched in iron. At 1220 °C the high temperature phase, HT-$FeSi_2$ will solidify with a structural formula is close to $FeSi_{2.4}$. At around 927 °C an eutectoid reaction is predicted from the phase diagram. HT-$FeSi_2$, the high temperature version should transform into LT-$FeSi_2$, the low temperature version. Examinations of MG-Si have indicated that this transformation does not take place to a great extent. **de Huff** (1969), reported the minimum time for this transformation to be completed is 3h at 700 °C. This means that the cooling rate in the conventional casting used in industry is too rapid for the transformation to be complete. It is also reported that the phase can contain a varying degree of aluminium. According to **Anglezio et al**. (1990), the maximum amount is 3 wt % Al. Al will substitute for silicon in the structure. According to **Margaria** (1996) the maximum content of Al can be up to 8 at % and the aluminium stabilizes the high temperature version.

The **Al-Si** system is a simple eutectic system with an eutectic point at 577 °C and 12.6 wt % silicon, (**Massalski**, 1990). The solubility of Al in Si is limited, but Si has some solubility in the Al phase. For the **Ca-Si** system the only phase relevant for metallurgical grade silicon is the $CaSi_2$ phase, which is observed in MG-Si with high concentrations of calcium, see Figure 2.19. The eutectic point is at 1030 °C and 61.4 wt %Si. (**Massalski**, 1990). Si_2Ti is observed in silicon with a high content of titanium and the eutectic temperature is 1330 °C **(Massalski**, 1990).

2.7.2 Ternary systems

The Al-Fe-Si system has been investigated by several authors, ranging from early studies by **Takeda and Mutuzaki** (1940), **Rivlin and Raynor** (1981), to the more recent work by **Liu** (1999), **Krendelsberger et al.** (2007) **Raghavan**, (2009) and **Raghavan** (2010). The regions with high concentrations of either Al or Fe have attained most of the focus, due to their importance in aluminium and iron alloys. A complete study of the whole compositional range was performed by **Takeda and Mutuzaki** (1940). In the literature the different Al-Fe-Si phases have been designated letters and numbers which are not always consistent. In Table 2.3 different ternary phases are designated with the letters τ collected from the review by **Raghavan** (2009).

Table 2.3: Stable phases in the Al-Fe-Si ternary system, **Raghavan** (2009).

Phase	**Designation**	**Composition at %**		
		Al	**Fe**	**Si**
$Al_2Fe_3Si_3$	τ_1 or τ_9	21.5-44.5	~37	18.5-41.5
Al_3FeSi	τ_2 or γ	54.4-64.8	~20	15.2-25.6
Al_2FeSi	T_3	53.5-55-5	~24	20.5-22.5
Al_3FeSi_2	τ_4 or δ	46-53.5	~16	30.5-38
$Al_{7.4}Fe_2Si$	τ_5	68.75-71.25	~18.75	10-12.5
$Al_{4.5}FeSi$	τ_6 or β	65-67	~16	17-19
$Al_3Fe_2Si_3$	τ_7	39.7-48.2	~24	27.8-36.3
$Al_2Fe_3Si_4$	τ_8	24.6-28.1	~32.4	39.5-43
$Al_9Fe_4Si_3$	T_{10}	57.5-58.5	~24.5	17-18
Al_5Fe_2Si	τ_{11}	64.5-66	24.5	9.5-11

Some of the phases are reported to have a large homogeneity range, like τ_4, while others have a more restricted range, as for τ_{10}. It can be seen from the table that the iron content is relatively stable, while the aluminium and silicon content varies. This is due to the ease these elements substitute each other. When it comes to MG-Si, there have been several studies regarding the structure of intermetallic phases found in the material. **Anglezio et al.** (1990) listed Al_3FeSi_2 and $Al_8Fe_5Si_7$ phase as common phases in MG-Si. According to **Liu** (1999) the group later modified the stoichiometry of this phase to $Al_6Fe_4Si_6$, which is equal to τ_7 in Table 2.3. The two Al-Fe-Si phases were also reported by **Schei** (1992), **Rong** (1992), and **Margaria et al.** (1992). A liquidus projection for Al-Fe-Si, as given by **Krendelsberger et al.** (2007) is illustrated in Figure 2. 18.

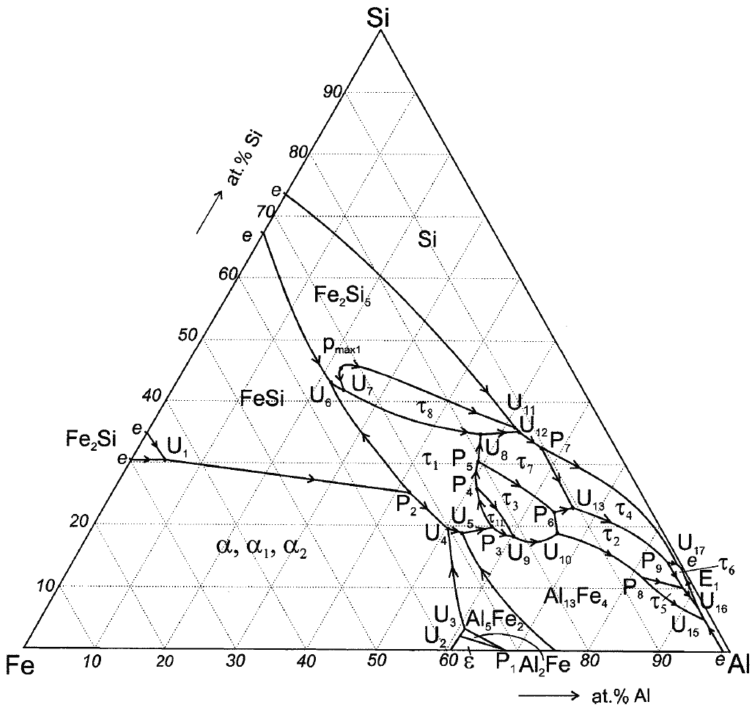

Figure 2. 18: Liquidus projection for Al-Fe-Si, **Krendelsberger et al.** (2007)

In the publication by **Anglezio et al.** (1994**a**), a review of the literature regarding the binary and ternary, Al, Ca, Fe and Si systems relevant for MG-Si was given. For silicon rich alloys the relevant ternary phase in the **Al-Ca-Si** system is Al_2CaSi_2. It melts congruently below 975 °C according to **Anglezio et al.** (1990).

The ternary Fe-Si Ti system was amongst others studied by **Weitzer et al.** (2008). Nine ternary phases were observed, where the $FeSi_2Ti$ phase is the phase normally observed in MG-Si. From the ternary phase diagram listed it can be seen that for high concentrations of titanium the binary Si_2Ti phase is formed.

The quaternary phase of highest importance in the Al-Ca-Fe-Si system is the $Al_6CaFe_4Si_8$ phase. This phase is studied in detail by **Anglezio et al**. (1990).

2.7.3 Intermetallic phases in MG-Si

There is a consensus between authors describing MG-Si when it comes to which intermetallic phases that are usually found in silicon after industrial casting. These phases include HT-(Al)$FeSi_2$, Si_2Ti, Al_3FeSi_2, (Al)$FeSi_2Ti$, Al_2CaSi_2, $Al_6CaFe_4Si_8$, $CaSi_2$ and $Al_6Fe_4Si_6$. The solidification starts with the solidification of almost pure silicon below 1414 °C. As the temperature is reduced more silicon solidifies while the melt is enriched in alloying/trace elements. Calculation done by the programme Sistruc13, described by **Dons et al**. (2009) gave a solidification range of the subsequent solidification of the intermetallic phases from ~1100 °C to ~600 °C depending on the composition.
The crystal structures of the most common phases in MG-Si are given in Table 2.4.

Table 2.4: Crystal structure of common intermetallic phases in MG-Si

Phase	**Crystal structure**
HT-(Al)$Fesi_2$	Tetragonal 1)
$CaSi_2$	Hexagonal2)
Si_2Ti	Orthorhombic 3)
Al_3FeSi_2	Orthorhombic 4)
$Al_6Fe_4Si_6$	Monoclinic 5)
Al_2CaSi_2	Hexagonal 6)
(Al)$FeSi_2Ti$	Orthorhombic 3)
$Al_6CaFe_4Si_8$	Triclinic7)

1)**Maex and van Rossum** (1995), 2) **Massalski** (1990) 3)**Weitzer et al.** (2008) 4)**Gueneau**, (1995a), 5)**Gueneau**, (1995b), 6) **Anglezio et al.** (1994**a**). 7)**Anglezio et al.** (1990)

In the study by **Dubrous and Anglezio** (1990) 30 samples within the Al-Ca-Fe-Si-Ti system were examined. They varied the content of Ca and Al in the samples while the iron content was kept constant at 0.4 wt %. In Figure 2.19 the areas of existence of the main intermetallic phases in MG-Si developed from their study is illustrated. In the samples titanium was always present as $FeSi_2Ti$.

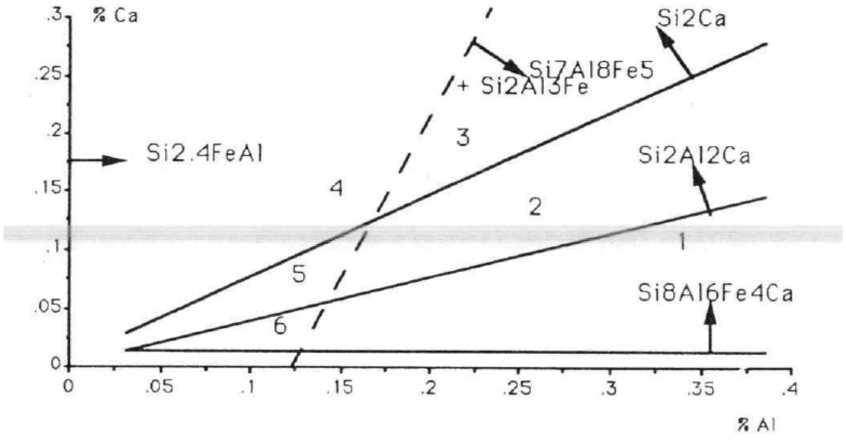

Figure 2.19: Area of existence for intermetallic phases in MG-Si containing 0.4 wt % Fe and a varying amount of Ca and Al. (**Dubrous and Anglezio**, 1990)

In this figure, $Si_{2.4}FeAl$ and $Si_7Al_8Fe_5$ equals the phases designated HT-(Al)$FeSi_2$ and $Al_6Fe_4Si_6$ in this work respectively. The figure illustrates that HT-(Al)$FeSi_2$ was found in all the MG-Si alloys and when the Al content increases the ternary Al-Fe-Si phases starts to form as well. The quaternary calcium phase was found in all the alloys except when the calcium content was very low. Increasing the calcium content led to the subsequent formation of the ternary and the secondary calcium phases.

2.7.4 Impact of the MG-Si quality on the downstream consumer

As mentioned in the introduction there are different specifications to metallurgical grade silicon depending on the application. In this section silicon for the aluminium industry, the direct process and hydrometallurgical leaching is discussed.

2.7.4.1 Silicon for aluminium industry

In aluminium alloys silicon is added to improve amongst other things the viscosity of the alloy, the floatability and mechanical strength. A high and constant silicon yield and a low level of fines are preferred. Low iron, calcium and phosphorus contents in silicon are critical for this application (**Ceccaroli and Lohne**, 2003). The size distribution of the silicon is also vital to the alloying process. Small sized material will flout and end up in the slag causing material loss and a reduced control of the alloy composition. In addition it is more energy demanding to melt small sized particles compared to larger particles.

An example of the impact impurities have on the system is in near eutectic Al-Si alloys. When phosphorus is present AlP can form and these particles nucleate fine silicon grains. This effect can however be poisoned by sodium or calcium since $(Ca_{n-x}Na_x)P_m$ or CaSiP compounds that are more stable than AlP are formed. Then AlP can no longer work as a nucleating agent. **Lui et al.** (2005) describe that the calcium level in the alloy they have studied was directly related to the purity of the commercial silicon, which was MG-Si. From this it was seen that it is important to control amongst others the level of P and the level of Ca.

2.7.4.2 Silicon for direct syntheses, MCS related

The first step in producing silicones involves the production of dimethyl dichlorosilane.

$$Si\,(s) + 2\,CH_3Cl\,(g) \rightarrow (CH3)_2SiCl_2\,(g) \quad \text{(Cu catalyst, 260 to 370 °C)}$$

The reaction is carried out in a fluidized bed reactor. To obtain a good fluidization of the bed particles, a size of 20-300 µm is preferred (**Ceccaroli and Lohne**, 2003). If particles are too small they can be blown out of the reactor, leading to silicon loss, or if they are too large they can accumulate in the reactor. Important parameters for the reaction are the reactivity, the amount of $(CH_3)_2SiCl_2$ produced per tonne silicon, and the selectivity, the amount of the $(CH_3)_2SiCl_2$ produced versus the total amount of products (**Margaria et al.,** 1992). The direct synthesis is complex and not fully understood. Different design and operating conditions of the fluidized bed reactor affect the reactivity and selectivity. The same yields for the catalyst chosen and the intermetallic phases present in silicon. Owing to the fact that the reactivity and selectivity are dependent on many factors it is difficult to give a strict specification when it comes to MG-Si. There have been several attempts to describe the effect of the different intermetallic phases, but so far there is not a complete consensus. It can however be concluded that homogeneity in the material, a given grain size and minimum level of some elements are important. **Rong** (1992) lists several elements that can act as promoters, inhibitors or auxiliaries in the synthesis. It is stated that the process is sensitive to the presence of impurities.

2.7.4.3 Hydrometallurgical leaching

For some purposes the silicon is alloyed with a higher amount of e.g. iron, calcium and aluminium, in order to facilitate a process such as leaching. This is done in the Silgrain process, where a 90-94 % silicon alloy is leached. In 1971 Aas described the technology for the Silgrain process, **Aas** (1971). He described how silicon alloyed with Fe, Al, Ca and Ti was solidified, crushed and leached in a solution of hot acidic of $FeCl_3$. The bulk part of the alloying elements was found as intermetallic phases that were leachable to a varying extent, while the silicon was not leached. The result was therefore a purified material consisting of purified silicon grains. Table 2.5 is collected from **Aas** (1971), and it is seen that the calcium containing phases were easiest attacked by the Silgrain acid, followed by the Al-Fe-Si phases. The Fe_2Si_5, which equals the HT-$FeSi_2$, was not leachable in Silgrain acid. A chemical composition and solidification procedure that suppress the Fe_2Si_5, that is the HT-$FeSi_2$, phase should be chosen.

Table 2.5: Solubility of intermetallic phases in silicon (**Aas**, 1971) with designations of solubility, A: Not soluble, B: Slightly soluble, C: soluble, ® solution used in Silgrain

Phase	**Analysis %**				**Relative solubility**					
	Fe	**Si**	**Al**	**Ca**	**$FeCl_3$**	**$FeCl_3$ + HCl®**	**HCl**	**HF**	**HF + HNO_3**	**HNO_3**
Fe_2Si_5	42-47	53-58			A	A	A	C	C	-
Fe-Al-Si	28-38	30-39	28-37		A	B	B	C	-	-
Fe-Al-Ca-Si	32-39	31-34	22-24	3-13	B	C	C	C	-	-
"Ca Al_2Si_2"		37.4	35.9	26.7	C	C	C	C	C	B

Queiroz et al. (2001) came to the same conclusion. In their work several Si alloys were leached in both HCl and a mixture of HCl and $FeCl_3$*6 H_20. The relative reactivities for the phases were listed as follows: Ca-Si > $CaAl_2Si_{1.5}$> Fe-Al-Si-Ca, Al-Fe-Si >>> $FeSi_{2.}$

It is assumed that the $CaAl_2Si_{1.5}$ was the same as the $CaAl_2Si_2$ notation used by Aas, and that the quaternary and $FeSi_2$ phases were the $Al_6CaFe_4Si_8$ and HT-(Al)$FeSi_2$ phases respectively.

Other factors that are important for the leaching are solidification time and distribution of phases. Even if the cast contains leachable intermetallic phases they must be located such that the acid can attack them. All the phases contain silicon so this means that removal is associated with a silicon loss that should be kept to a minimum. Dissolution time in the acid, temperature of the acid and pressure can also affect the leaching.

Due to the low solubility of most elements in solid silicon, as seen from Table 2.2 there will usually be an accumulation of trace elements in the intermetallic phases. This means that purification is achieved not only by removing the main constituents in the intermetallic phases, but also trace elements that following the intermetallic phases will be removed.

2.7.5 Industrial method for solidification of MG-Si

A summary of the casting processes used for silicon aimed for chemical industry, is given by **Nygaard** (2006). This includes mould casting, granulation and casting on a copper plate. In the silicon plants located in Norway, casting in a bed of fines, casting onto cast iron moulds and layer casting are common practices for silicon alloys ranging for 54-99 wt % Si. In addition granulation has been tested, but mainly due to explosions this is not in use in Norway today. Granulation may also yield a product that is not applicable for aluminium customers due to its small grain size. In recent years casting onto cooled copper plates has gained increased attention and the basis for this is described by **Bullon** (2007) and **Boisvert et al.** (2004). When a casting method is to be chosen, it is important to define the qualities the producer aims for in the product. In the next chapters the effect the casting method has on the product will be elucidated.

3 Experimental Work

3.1 Introduction

In Figure 3.1 images from the main casting experiments in this thesis are shown with respect to the order they were conducted.

Figure 3.1: Experiments included in this work left to right: A1-A2-MGSi2 Industrial, Cyberstar furnace experiment –Copper plate experiments.

The experiments were designed using a 90-94 wt % silicon alloy, **alloy A**, and standard metallurgical grade silicon, **MG-Si 1** and **MG-Si2**. Alloy A and MG-Si2 were collected from industrial experiments, while MG-Si 1 was collected from a cast without exact knowledge of the thermal history. MG-Si 1 and MG-Si2 were re-melted and used in two new solidification experiments: Solidification on a copper plate, carried out at the Elkem Pilot Plant in Kristiansand, and a directional solidification experiment in the "Cyberstar" furnace at NTNU. In addition Solar Grade Silicon, **SoG-Si**, was used for two of the copper plate experiments and one of the four crucibles in the Cyberstar furnace was filled with Electronic Grade Silicon, **EG-Si**. Comprehensive temperature measurement and alloy sampling were performed in all the experiments.

The collected samples were used for chemical and metallographic analysis. As an alternative to purifying metallurgical grade silicon, an initial test run with magnetic separation was carried out. Furthermore the abrasion strength of the materials was determined by a tumbler test and the micro hardness of selected intermetallic phases was investigated.

3.2 Industrial experiments

3.2.1 Alloy A

The silicon alloy was produced in an electric arc furnace from raw materials, quartz, coke, coal and woodchips. Al, Fe and Ca rich material were added in order to obtain the required alloy composition.

The alloy was continuously tapped from the furnace into moulds placed on a railway that surrounded the furnace. The moulds used were cast iron moulds. To prevent the mould from experiencing a “thermal shock” and to avoid iron contamination of the alloy, the mould was covered in a fines layer of the silicon alloy, size 0-2 mm. On average it takes 15 minutes to fill a mould, but the flow during tapping will depend on the ease of draining the silicon from the taphole. Two experiments were performed using alloy A.

A1: Solidification in an industrial sized mould covered in a layer of fines (0-2 mm) of the same material, Figure 3.2 (left).

A2: Solidification in an aluminium box (500x300x195mm) insulated with the ceramic fibre Kaowool, Figure 3.2 (right)

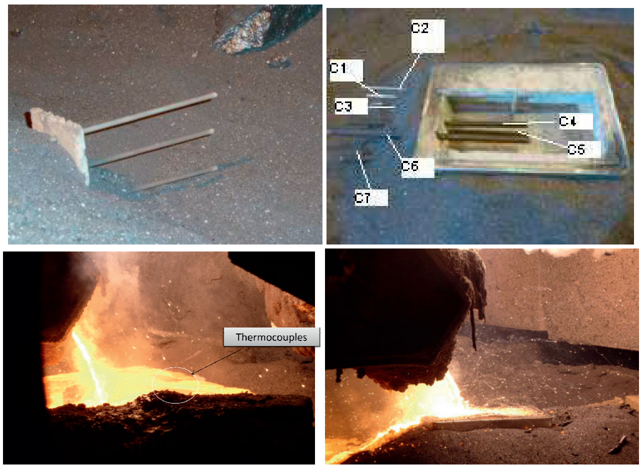

Figure 3.2: Pictures taken before and during experiment A1 (to the left top and bottom) and experiment A2 (to the right top and bottom).

In experiment A1, 3 C-type thermocouples, (W5%Re-W26%Re, 0.1 diameter wire, 125 x 600mm molybdenum sheath, where 500 mm was coated with tungsten, hafnia insulation, ungrounded junction with ultra high temperature ceramic plug) in quartz protection tubes were used to record the temperature in different positions in the cast as shown in Figure 3.3. In addition one K-type element recorded the temperature increase in the fines.

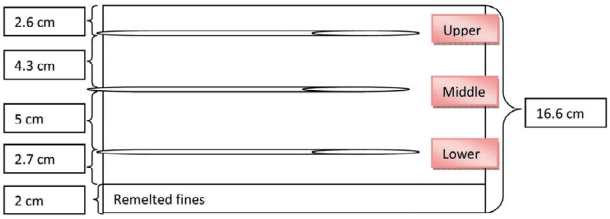

Figure 3.3: Placement of the thermocouples as taken with respect to sample A1.

In experiment A2, 7 C-type thermocouples of same specification were positioned in different positions in the box. Three of the thermocouples were protected by quartz tubes while four of the thermocouples were protected by graphite and quartz tubes. The temperature increase in the fines was recorded in this experiment as well with a K-type thermocouple. A DT80 Datataker was used to collect the temperature data in both experiments. After pouring the melt from the ladle into the mould the casts were left to cool to ambient temperature.

For experiment A1 samples were collected in the proximity of the thermocouples where the thermal history was exactly known. The box from experiment A2 was cut in half and the half that contained the thermocouples was divided in to seven samples, 2.1-2.7. Thermocouples C1 to C3 were part of sample 2.2, thermocouples C4 and C5 were part of 2.4 and thermocouples C6 and C7 were part of sample 2.6. The samples were cut at SINTEF Building and Infrastructure and Elkem Technology, Materials Characterization.

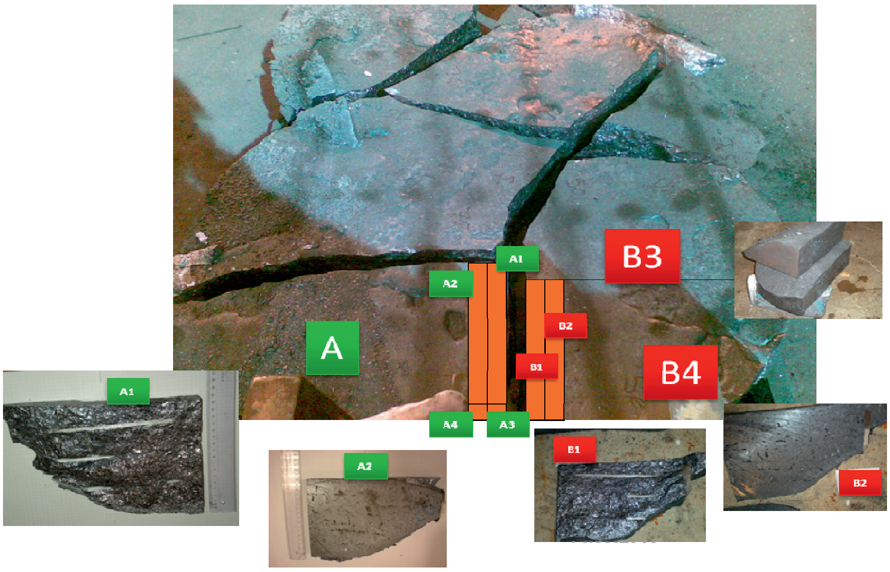

Figure 3.4: Extraction of samples in experiment A1.

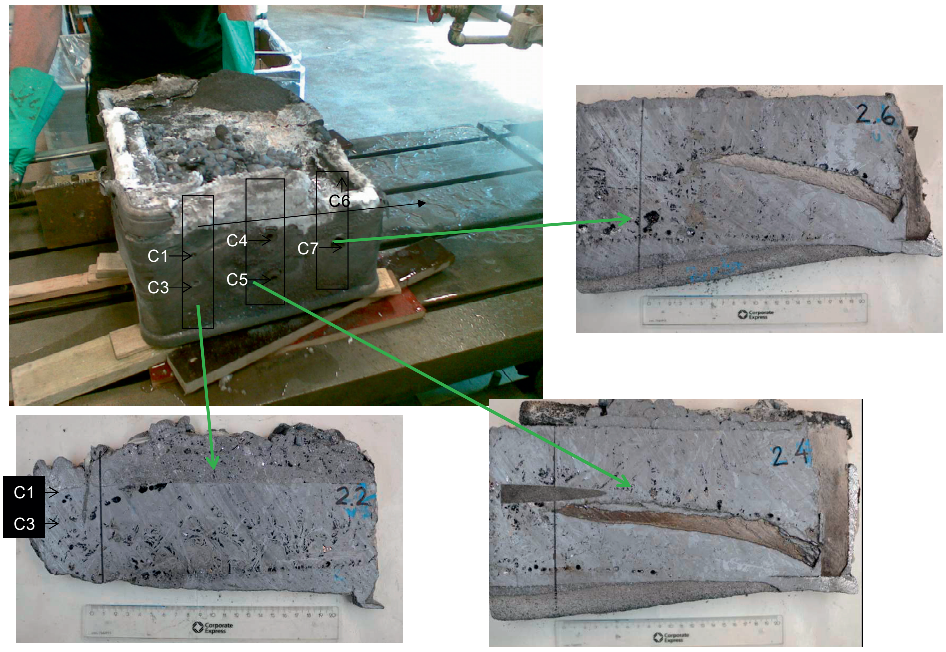

Figure 3.5: Extraction of samples in experiment A2.

3.2.2 MG-Si 2

A cast iron mould (2100 x 2100 cm, outer dimensions) was prepared for the experiment: 8 holes were drilled through the cast iron mould walls to fit the thermocouples. To avoid movement of the thermocouples during casting two steel plates were mounted to the bottom of the mould. Kaowool plates were attached to the steel plates and the C-type thermocouples were supported by this. To protect the mould a 15 mm layer of silicon gravel of size 10-15 mm covered the mould. Metallurgical grade silicon, MG-Si, of purity 99 wt % silicon produced in an electric arc furnace was tapped from the furnace and refined in a ladle. After refining the melt was poured from the ladle into the mould, as shown in Figure 3.6.

Figure 3.6: Picture taken during the industrial experiment, MG-Si2.

The temperature in the melt/cast was recorded by 6 C-type thermocouples of same quality as for experiments A1 and A2. Two K-type thermocouples recorded the temperature under the layer of silicon gravel and one K-type thermocouple logged the temperature underneath the mould. A DT80 Datataker was used to collect the temperature data in both experiments. After pouring the melt from the ladle into the mould the cast was left to cool to ambient temperature.

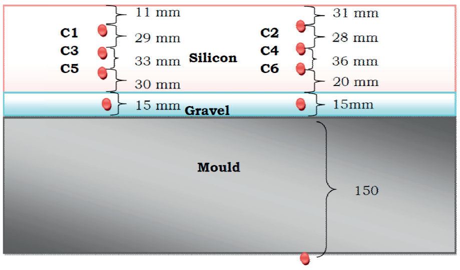

Figure 3.7: Placement of the thermocouple after the experiment.

After the experiment samples were collected in the proximity of thermocouples C1, C3, C5 and C2, C4, C6, samples B and D respectively. In addition a sample from another location was collected, sample G, and a sample from another cast that had been left to cool underneath another cast, sample H. The samples were cut at SINTEF Building and Infrastructure and SINTEF Materials and Chemistry.

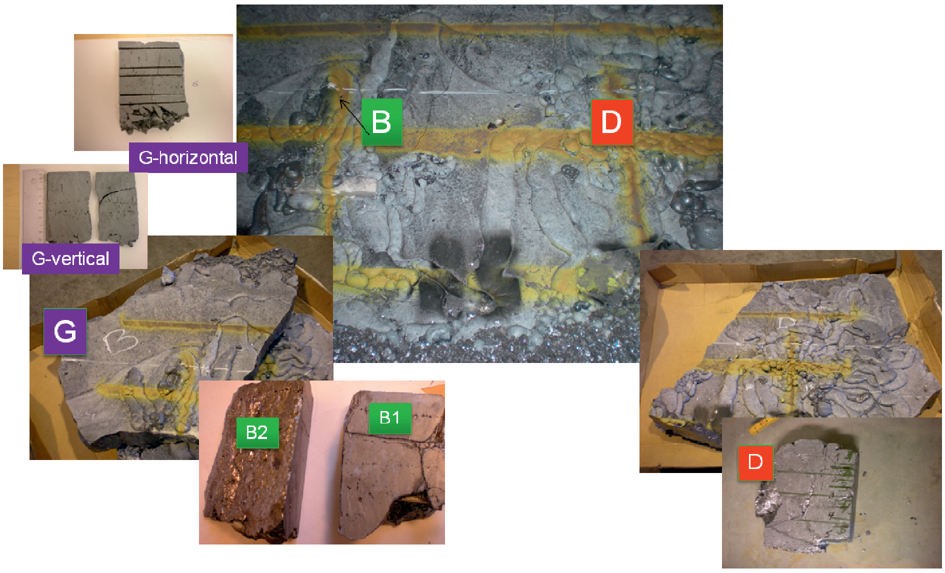

Figure 3.8: Extraction of samples in experiment MG-Si2.

3.3 Lab scale solidification experiments

3.3.1 Solidification on a cooled cooper plate

Figure 3.9: Experimental setup for the copper plate experiment.

The casting experiments onto a cooled copper plate were performed in Kristiansand at Elkem Technology. The experimental setup used for the experiments are shown in Figure 3.9. As seen from the photo, a graphite frame was mounted on top of the copper plate. This gave a cast with dimensions 19 cm * 39 cm. At the middle of the plate, thermocouples were mounted symmetrically. Three qualities of silicon were used in this experimental campaign comprising of 10 experiments. Table 3.1 lists some conditions used in the experiments. The silicon was melted in a 75 KW induction furnace with argon atmosphere. The casting was initiated at a melt temperature in the furnace of 1480 °C. The furnace was tipped so that the melt flowed to the runner, into a graphite cup and then onto the copper plate. The temperature in the melt/cast was recorded by B type thermocouples (Pt6Rh, Pt30 Rh). In addition 2 K type thermocouples measured the temperature at the inn and outlet of the water stream. When the temperature in the cast reached 400 °C the cast was moved to a nearby location. The thermocouples were located 0.5 and 1 cm from the copper plate in the 1.5 cm casts, 1 and 2 cm and 1.25, 2.5 and 3.75 cm from the copper plate in the 3 and 5 cm casts respectively.

Table 3.1: Experimental parameters copper plate experiments.

Experiment	Material	Height [cm]	Weight of the cast [kg]
1.1	SoG-Si	3	6.5
1.2	SoG-Si	5	9.3
2.1	MG-Si1	1.5	3.5
2.2	MG-Si1	3	6.3
2.3	MG-Si1	3	7.1
3.1	MG-Si2	1.5	3.6
3.2	MG-Si2	3	5.7
3.3	MG-Si2	3	5.6
3.4	MG-Si2	5	9.2
3.5	MG-Si2	5	10.2

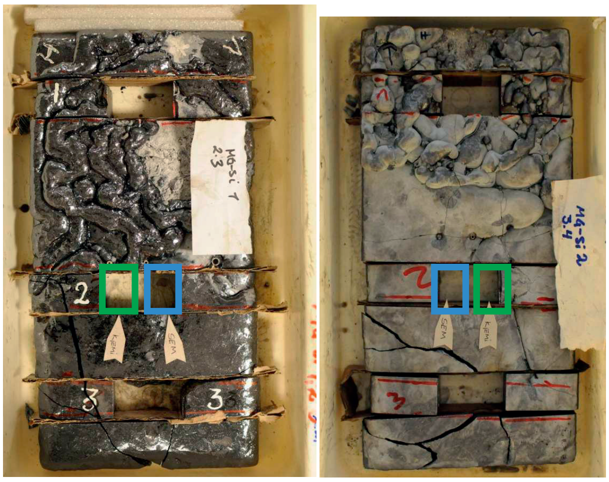

Figure 3.10: Extraction of samples for SEM and chemical analysis Experiment 2.3 and 3.4.

In Figure 3.10 the extraction of samples for **SEM** and **chemical analysis** are illustrated for experiment 2.3 and 3.4. For the other experiments the samples were extracted in the manner of either 2.3 or 3.4 depending on the amount of cracks in the sample. The sample that was least fractured was chosen for the SEM. The sample for chemical analysis was divided in 2, 3 and 5 pieces from top to bottom for the 1.5 cm, 3 cm and 5 cm casts respectively. It can be seen from Figure 3.10 that the surface of the cast was not plane, but for simplicity the pieces were said to be 0.75 cm for the 1.5 cm cast and 1 cm for the 3 and 5 cm cast when they are referred to in figures representing the chemical analysis, Chapter 5 and Appendix A.

3.3.2 Directional solidification- Cyberstar furnace experiment

The Cyberstar furnace experiment was performed at NTNU with the aid of Halvor Dalaker and Martin Syvertsen from SINTEF Materials and Chemistry. The description of the Cyberstar furnace is reproduced from **Dalaker et al**. (2010). *The Cyberstar furnace,* Figure 3.11*, is a 250 kg Cyberstar unidirectional furnace. It is equipped with two independently controlled susceptors, each powered by a 100 kW generator. The two susceptors are placed immediately above and below the crucible, causing a unidirectional heat flow from the hot (top) to the cool (bottom) susceptor. The ability to control each susceptor independently gives good control of the vertical temperature gradients of the system. Each susceptor is controlled by a type C thermocouple and a Eurotherm 3504 controller.*

Four quartz crucibles of inner dimensions 0.225x0.225 (l x w) were stacked with the given quality of silicon. Sandblasted quartz tubes coated in silicon nitride, Si_3N_4, were placed in the centre of each ingot. In addition one quartz tube was placed in the centre of the furnace, see Figure 3.11. C-type wires (W5%Re-W26%Re) protected in alsint tubes were positioned at different heights inside each quartz tube, as seen in Table 3.2. A molybdenum wire was twisted around the quartz tubes to hinder them from falling. Graphite insulation was mounted outside the crucibles as shown in Figure 3.11.

Table 3.2: Placement of thermocouples Cyberstar furnace experiment.

Placement of thermocouple	Material	Thermo couple	Time the thermocouple functioned [h]	Position from crucible bottom [cm]
Crucible 1	MG-Si 2 14.9 kg	**T.1.1**	31.3	5
		T.1.2	no signal	8.5
		T.1.3	31.4	10.5
Crucible 2	MG-Si 1 15.0 kg	**T.2.1**	34.9	5
		T.2.2-	no signal	8.5
Crucible 3	MG-Si 2 14.7 kg	**T.3.1**	29.6	5
		T.3.2	29.6	8.5
Crucible 4	EG-Si 1 15.0 kg	**T.4.1**	room temp	5
		T.4.2	whole exp	8.5
Centre of furnace		**T.M.1**	no signal	5
		T.M.2	whole exp	8.5

Figure 3.11: The Cyberstar furnace, left, and stacking of the ingots, right.

A temperature program was initiated for the upper and lower susceptors and their set points are illustrated in Figure 3.12 together with the power of the suscpetors.

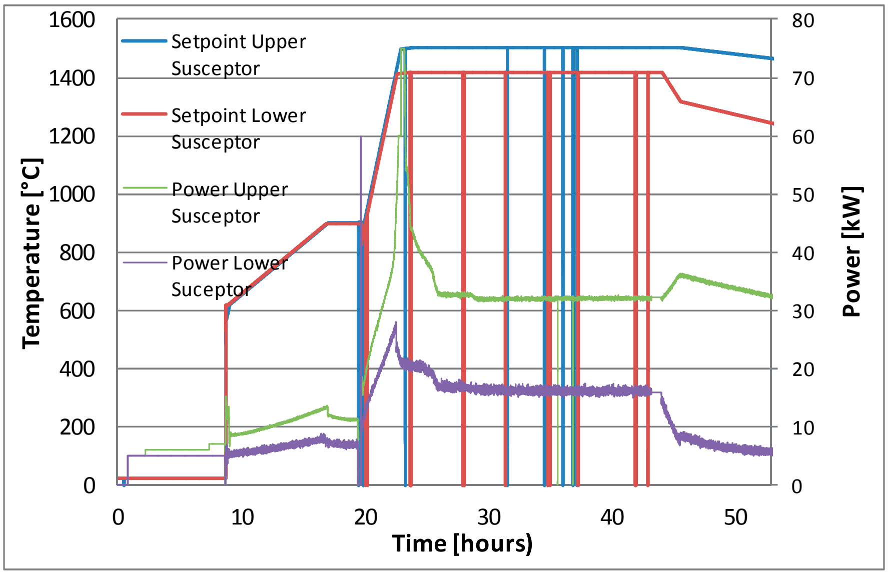

Figure 3.12: Temperature settings and power for the upper and lower susceptor.

Figure 3.13: Extraction of samples for SEM and chemical analysis Ingot 1-4. Samples divided in to 5 small pieces are for the chemical analysis. The picture to the right illustrates how samples for SEM were cut prior to encapsulation in epoxy, and the red rectangles samples for additional chemical analysis.

As shown in Figure 3.13, a slice of each ingot was cut for chemical analysis and SEM. The samples for chemical analysis were divided into 5 equal parts from top to bottom. For the metallographic analysis, 3 samples, T (top), M (middle) and B (bottom) were cut from each of the large SEM samples extracted from each ingot. These were encapsulated in epoxy before they were ground and polished.

3.4 Differential thermal analysis-DTA

A Setaram SetSys 2400 DTA/TGA with a W5%Re/W26%Re DTA/TGA rod, were used for the tests. Two alumina crucibles were utilized, one filled with the sample and one empty reference crucible. The difference in temperature between the sample and a reference (DTA signal), weight change (TGA signal) and sample temperature were measured during heating of the sample and the reference. In a curve illustrating the DTA signal a dip will indicate an endothermic reaction. This can be a phase change or a reaction. A temperature calibration was done prior to the test and compared to known values a maximum of 5 °C deviation was measured. Copper and Iron were used for the calibration. Milled samples from experiments A1 and A2 were tested. The DTA analyses were performed by Sarina Bao, SINTEF Materials and Chemistry.

3.5 Mechanical properties

3.5.1 Abrasion strength

Samples from all experiments were crushed down to a size of +3.36-9.52 mm by Odd Corneliussen at the Department of Geology and Mineral Resources Engineering, NTNU. A Hannover drum was used to test the abrasion strength. The tests were run by Edith Thomassen and Wilhelm Dall at SINTEF Materials and Chemistry. Figure 3.14 is a photo and a sketch of the Hannover drum. The experimental procedure for the abrasion test was based on the work of **Tangstad et al.** (2010), except that a different set of sieving fractions were chosen.

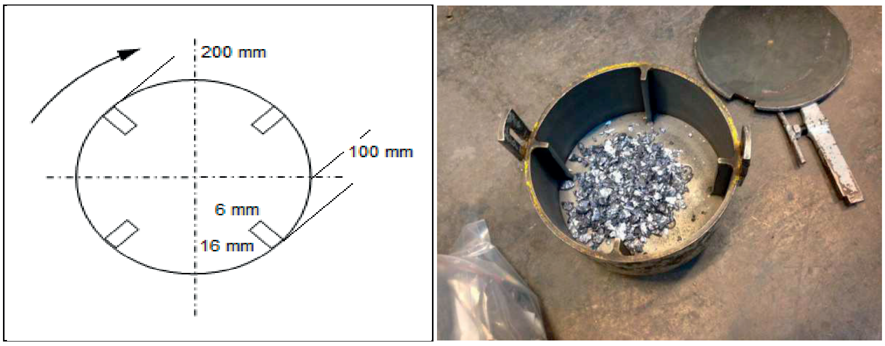

Figure 3.14: Sketch and photo of the Hannover drum.

All samples were split into 250 g fractions and the sample was sieved at 8, 6.3, 4, 2 and 1 mm before each fraction was weighed. The sample was tumbled for 30 min at a speed of 40 rpm. After the test the sample was sieved and weighed again.
To study the variation of elements as a function of size several of the crushed and sieved samples were analysed by XRF. The samples analysed were -3.36, 3.36-9.52, +9.52. The sample –3.36 mm was sieved into fractions –53 µm, 53-180 µm, 180-300 µm, 300-900 µm, 0.9-2 mm, 2-3 mm. In addition the samples of size +1 mm and –1 mm from after the abrasion test were analysed.

3.5.2 Vickers hardness test

A sample from the MG-Si2 industrial experiment was used to test the micro hardness of the different intermetallic phases. The micro hardness test was performed using a DuraScan 70 from Stures with a load of 25 g. This equals 0.025 kg*9.81m/s^2=0.245 N. The dwell time was 10 s and the speed: 0,8 mm/s. The micro hardness was measured on intermetallic phases that had been characterized by electron microprobe analysis, EPMA, prior to indentions. The tests were run by Tone Anzjøn, SINTEF Materials and Chemistry.

3.6 Magnetic separation of MG-Si2

Two methods of magnetic separation were tested, a dry and a wet separation method: The Permroll separator and the SLon 100 separator respectively. The basis for the SLON separator can be collected from **Xiong et al.** (1998), **Sherrell and Dunn** (2012), and **Chen et al.** (2013) and the basis for the Permroll can be collected in **Sandvik et al.** (1999).

Sample G for experiment MG-Si2 was used for the separation. The sample was crushed down to a size of 4 mm by a large and small jaw crusher with FeMn jaws. The sieve analysis after crushing is given in Table 3.3.

Table 3.3: Sieve analysis after crushing of sample G- MG-Si2.

Fraction	Weight [g]
-53 µm	93
53-150 µm	164
150-300 µm	202
+300 µm	81
Total weight	540

The different fractions were divided in two parts, one for the Permroll separator and one for the SLon 100 separator. The experimental conditions for the separation are given in Table 3.4 and Table 3.5.

Table 3.4: Experimental conditions SLon 100 separation.

Experiment	Fraction	Matrix	Water (l/h)	Pulse (rpm)	Field(T)
01	-53 µm	2 mm	10	250	1.1
02	53-150 µm	2 mm	10	250	1.1

Table 3.5: Experimental conditions Permroll separation.

Experiment	Fraction	Field (T)
01	-53 µm	0.9
02	53-150 µm	0.9
03	150-300 µm	0.9
04	+300 µm	0.9

After the separation the sample >10 g were analysed with an XRF while sample < 10 g were analysed with ICP-OES.

3.7 Characterization and microstructural analysis

3.7.1 X-ray fluorescence spectroscopy (XRF)

The chemical analysis of all samples of size > 10 g and analysis < 99.5 wt % Si were analysed by means of an XRF. The XRF analysis was performed at Elkem Thamshavn and Elkem Technology Lab in Kristiansand. The instrument at Thamshavn was of the type Panalytical Axios. The instrument is calibrated on a daily basis with a sample of silicon reference material. The lower detection limit for the standard program used is shown in Table 3.6.

Table 3.6: Lower detection limits, LDL, Panalytical Axios XRF, Elkem Thamshavn.

Element	LDL wt %	Element	LDL ppmw	Element	LDL ppmw
Al	0.002	**Pb**	10	**Cr**	10
Ca	0.002	**Bi**	10	**V**	5
Ti	0.001	**As**	10	**Ba**	20
Fe	0.005	**Zn**	10	**Mo**	15
Mg	20$^{\text{ppmw}}$	**Cu**	10	**Sb**	10
Zr	20$^{*\text{ppmw}}$	**Ni**	5	**Sn**	10
Sr	5$^{*\text{ppmw}}$	**Mn**	5	**P**	3

The instrument used in Kristiansand was of Panalytical PW 2404.

All samples were prepared by first reducing the size <1mm. The material was then split into 10 g fractions and 0.6 g Polyethylene (PE tablets) was added. A wolfram carbide mill was used to grind the sample for 90 seconds. The milled sample was then pressed by a force of 200 kN for 20 seconds. The finished tablet was subsequently analysed by means of X-ray Diffraction.

3.7.2 Inductively coupled plasma – Optical Emission, ICP-OES

The chemical analysis of the samples that were less than 10 g was determined by Inductively Coupled Plasma-Optical Emission Spectrometry (ICP-OES). The instrument used was of type: Spectro Arcos. The solutions used were prepared by dissolving ground material of size < 0.5 mm in HF and HNO_3 in a platinum cup. The dissolved samples were heated in a sand bed until all liquid had evaporated. This removed the remaining acids and silicon in the form of H_2SiF_6. After heating a 10 % HCl solution was added until the salts were dissolved. Finally the sample was poured into a volumetric flask and dissolved to 50 ml. The analyses were performed at the chemical lab of Elkem Technology in Kristiansand.

3.7.3 Grinding and polishing

For samples for metallographic analysis the samples were mechanically ground using SiC paper in the order 120, 320, 500, 1200 and 2400. They were then polished using DP-mol 3µm and DP-Nap 1µm. Except for the samples from experiments A1 and A2, samples were prepared by Tone Anzjøn, SINTEF Materials and Chemistry, Trondheim. Samples from experiments A1 and A2 were prepared at the Materials Characterization lab at Elkem Technology in Kristiansand.

3.7.4 Etching

To reveal the grain structure the samples were etched in a stirred solution of 20 g/100 ml NaOH at 70-80 °C for 5 minutes.

3.7.5 Scanning electron microscopy

Investigation of the microstructure was performed by a LV-FE- SEM (Zeiss Supra 55 VP) and a FE-SEM (Zeiss Ultra 55 LE). Most micrographs were imaged with a back scatter electron detector, BSE-detector. The fraction of backscattered electrons, η, is defined as number of electrons backscattered, η_{BS} divided by number of electrons in the primary beam, η_B (**Hjelen** ,1989)

$$\eta = \frac{\eta_{BS}}{\eta_B} \tag{3.1}$$

With the same settings for voltage, electrons will penetrate deeper into a material with a low atomic number than a material with a higher atomic number yielding more backscattered electrons for a material with a high atomic number. In the micrograph the effect was seen as a difference in contrast depending on the atomic number of the material. The lower the mean atomic number, the darker the phase appeared in the micrograph.

3.7.6 EPMA

An electron probe micro-analyzer, EPMA, (JEOL JXA-8500F) was used to determine the composition of the intermetallic phases observed. The work was performed by Morten Raanes at the Department of Material Science and Technology at NTNU.

3.7.7 Light microscopy

A Leica MEF4M was used to for the optical observations of the samples.

3.7.8 Grain size determination

The circular intercept method described in **ASTM E112-96** (2004) was used to determine the average grain size with the exception that the circumference of the circles was not kept constant in all samples as described by the standard. The circles were imposed on the sample in **Image Pro- Analyzer** (2005-2009).

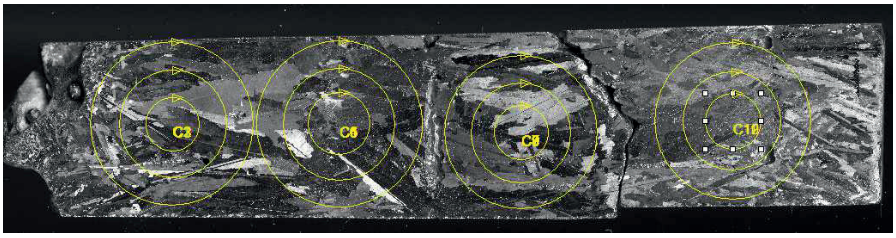

Figure 3.15: Example of grain size measurement sample B.

For two of the samples the average surface area of the grains was determined by imposing a circle onto the sample and counting the grains within the circle and grains that intersect the circle. The number of grains, N, was accounted for as given in the equation below.

$$N = N_{circle} + N_{circumference}/2 \qquad (3.2)$$

,where N_{circle} is the number of grains within the circle and $N_{circumference}/2$ the number of grains that intersects the circumference of the circle.

Since the area of the circle, A, was known, the number of grains in the circle was used to find the average grain size.

$$\overline{A}_{grain} = \frac{A}{N} \qquad (3.3)$$

The equivalent grain size was then calculated by the equation below.

$$r = \sqrt{\frac{A_{grain}}{2\pi}} \qquad (3.4)$$

The grain size measurement was performed by Bente Kroka at Elkem Technology Materials Characterization Lab in Kristiansand.

An EBSD scan was performed on a small part of sample B by Yingda Yu, Department of Material Science and Technology, NTNU, in order to obtain a grain size measurement. The basis for the EBSD technique can be found in **Goldstein et al**. (2003).

3.8 Evaluation of uncertainties related to the experimental results

In the following some of the uncertainties related to the experimental work are presented.

3.8.1 Temperature measurements

As the cooling rate increased, the deviation between the recorded temperature and the actual temperature increased due to a prolonged response time. From the thesis of Tveit (1988) it was seen that 90 % of the maximum temperature recorded was recorded 17 seconds after the melt hit the thermocouple. For the copper plate experiments, the rapid heat removal of the copper plate/water cooling and a low flow rate of the melt contributed to that the correct temperature in melt was not measured. For some of the experiments the maximum recorded temperature was only 1200 °C.

In Chapter 4 the cooling rates in the experiments were calculated. Since the long response time led to a lower recorded temperature than the actual temperature, the time the melt solidified had to be estimated in some of the calculations which led to an uncertainty in the calculated value.

Calibration data from the manufacturer of the C-type thermocouples gave a departure from the **ASTM-E230/E230M** (2012) standard curve of -4 °C at 1400 °C. For the B-type thermocouples no deviation was presented.

In the COMSOL model of the water cooled copper plate, the heat flux from the bottom was based on T_{inlet} and T_{outlet} in the water stream. The calculation used $\frac{q}{A} = Cp_{water} * massflow * \Delta T$

Since this ΔT is only a couple of degrees, a small uncertainty in the temperature can have a large impact on the calculated heat flux.

3.8.2 Chemical analysis

The material that was analysed was inhomogeneous due the segregation of alloying and impurity elements. This resulted in a variation in the analysis depending on the area the sample has been extracted from.
For the bulk part of the XRF analysis two parallels were run. A sample was mixed and split into two equal sized samples. This reduced the inhomogeneity between the parallels.

During sample preparation impurity elements could be introduced during crushing of the samples. Since the material in question was impure it was not assumed to affect the analysis significantly. The instruments used for analysis had calibrated against a reference material similar to the material analysed. The sample used for XRF was 10 g and would give a good representation of the analysis in the area where the sample was extracted.

The XRF signal will account for the total amount of the alloying elements present in oxides and intermetallic phases. It does not distinguish between the two. It was observed that most samples were slag free except that some of the samples of alloy A that might have contained small amounts of slag inclusions.

A few samples from the magnetic separation were too small to be analysed by XRF and were thus analysed by ICP-OES. The samples were dissolved in HF and HNO_3. In two of the samples it was observed that the solubility limit of Al, Fe and Mg was reached thus leading to the precipitation of the respective salts. Since the instrument only detects dissolved elements, the levels of Al, Fe and Mg will be lower than the actual value. Some elements were above the calibration range for the instrument, but for the instrument used the calibration curves are assumed to be linear so the reported values should be quite accurate.

3.8.3 EPMA

The electron beam used for the analysis will penetrate the surface. This means that in some cases the beam will penetrate through an intermetallic phase and also knock out electrons from the phase below. The beam will also have a circumference which means that the beam can touch the area of a neighbouring phase. For MG-Si 2, the low contrast between the phases means that in some cases a point where the circumference includes two or more phases could have been chosen. This gives an analysis that will have an influence from several phases. From the study of **Rong** (1992) approximately 10 % of the analyses performed were a combination of two or more intermetallic phases. This could be the reason for the relatively high standard deviation of the mean atomic % given in Appendix C. In the calculation of the mean atomic %, oxygen and carbon were removed from the original data set and the amount of the remaining elements was normalized.

3.8.4 Grain size determinations

For silicon it is difficult to define a good value of the grain size because of the large variation in grain size and shape of the grains. In some areas grains are columnar and in other areas more equiaxed. An automatic measurement was attempted, but not achieved due to the following reasons:

1) For SEM micrographs the intermetallic phases do not cover all grain boundaries so it was not possible to define a grain.

2) Etched samples gave different contrast between the grains, but the contrast was not good enough for the image processing program **Image J** (2013) to distinguish between them. Also in most grains twins were seen and it was not always possible to say if a boundary was a twin boundary or a grain boundary.

The standard deviations of the average grain size are listed in Table 5.3. The table illustrates the large variation in the grain size in the samples. The grain size of a part of sample B was measured with EBSD and an automatic intercept method. This gave an average grain size several 100 microns smaller than what observed from the circular intercept method indicating a weakness in the methods used. Grain size measurements have not been the main focus during this work, but it was clearly seen that there is a need for a better definition of the grain size in industrially cast silicon.

3.8.5 Abrasion strength

The material used for the abrasion test was inhomogeneous with regard to factors such as grain size, distribution of intermetallic phases, layers, crack and porosity. Even though a given sample was mixed and spilt prior to the tumbler test these variations leads to large standard deviations in the obtained results.

4 Thermal History

In Sections 4.1 to 4.4 the thermal history of the different experiments will be given. One of the main objectives with the temperature recordings was to correlate the microstructure of the cast to the thermal history. The result of this will be given in Chapter 5. In addition, casting experiments can serve as a basis for heat transfer models of the casting. Two mathematical simulation models was developed in **COMSOL 4.3a** (2012), one describing the industrial experiment with MG-Si2 and the other describing the copper plate experiments. Both models will be outlined in Section 4.6. Together with temperature recordings and observations during the experiment, the models gave an increased understanding about the solidification process and the cast product.

4.1 Alloy A

Two experiments were performed utilizing Alloy A as outlined in Chapter 3. In the first experiment, A1, the alloy was tapped directly into the mould from the furnace and in the second experiment, A2, it was filled into an insulated box.

4.1.1 Experiment A1

The thermal history of experiment A1 is given in Figure 4.1. The curves in the figure represent temperature recordings from three thermocouples positioned in the cast. Their positions can be read from Figure 3.3. The thermal history was mainly explained by Figure 2.14, but in practical silicon casting some exceptions were observed. The flow of silicon out of the taphole was slow. This caused the melt to solidify stepwise and several solidified layers were formed before the casting process ended.

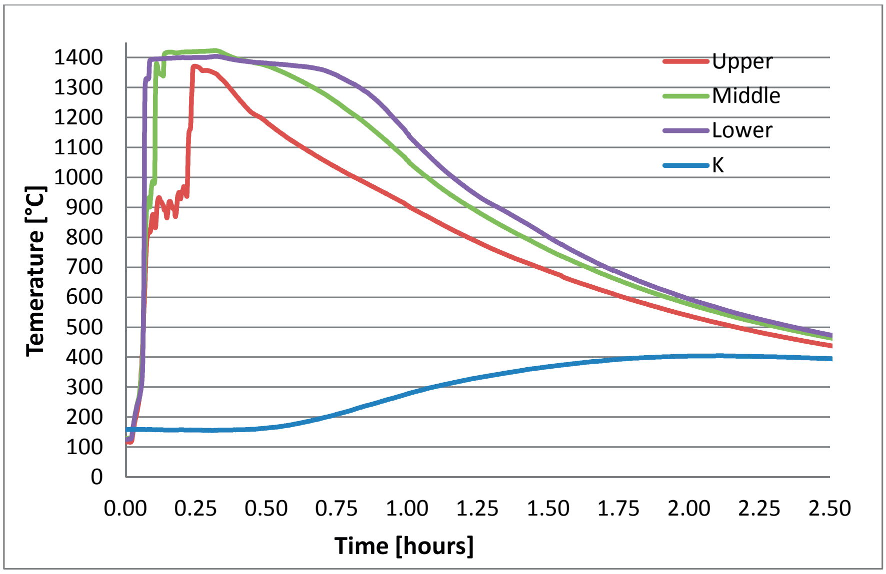

Figure 4.1: Temperature -time curve for experiment A1.

4.1.1.1 Surface temperature during solidification

In Figure 4.2 several images shot between 2 minutes and 77 minutes after the mould was full are given. IR images were shot simultaneously and the images were processed by the **ThermoCAM™ Researcher Pro 2.10** (2007-2010) software. Average surface temperatures were calculated by the program utilizing a set emissivity of 0.75. The results are illustrated in Figure 4.2 for 2, 12, 28, 45 and 77 minutes after the mould was full. From Equation 2.25, the radiative heat transfer, q·(W/m^2) was calculated. It can be seen from the figure that the emissive power was high initially, but decreased.

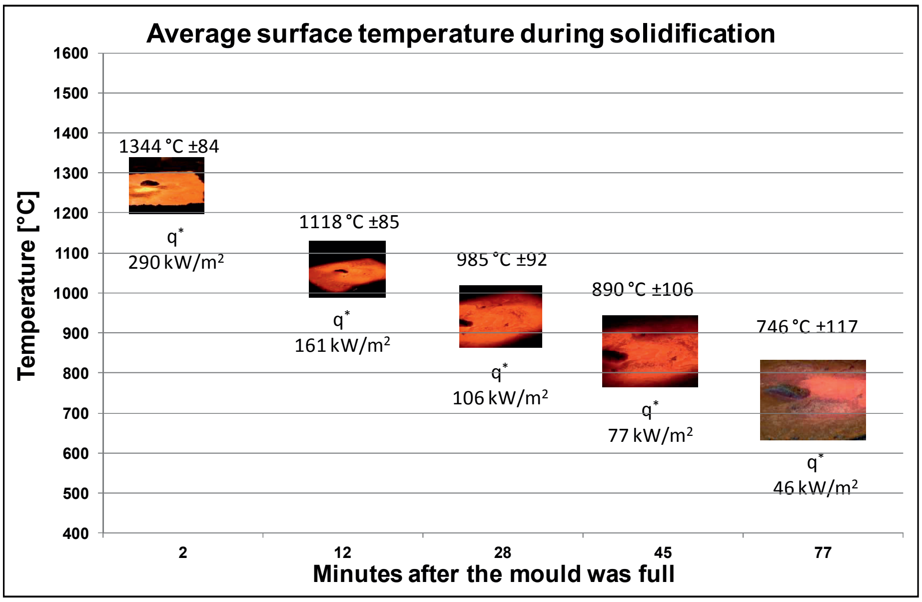

Figure 4.2: Average surface temperature during solidification. The emissive heat flux from the surface is also given.

Figure 4.3 illustrates an IR image shot 12 minutes after the mould was full. It can be seen that the surface temperature varied with position. Even though most of the heat flowed in the vertical directions, some heat was extracted horizontally, as illustrated by the lower temperature close to the sides of the mould.

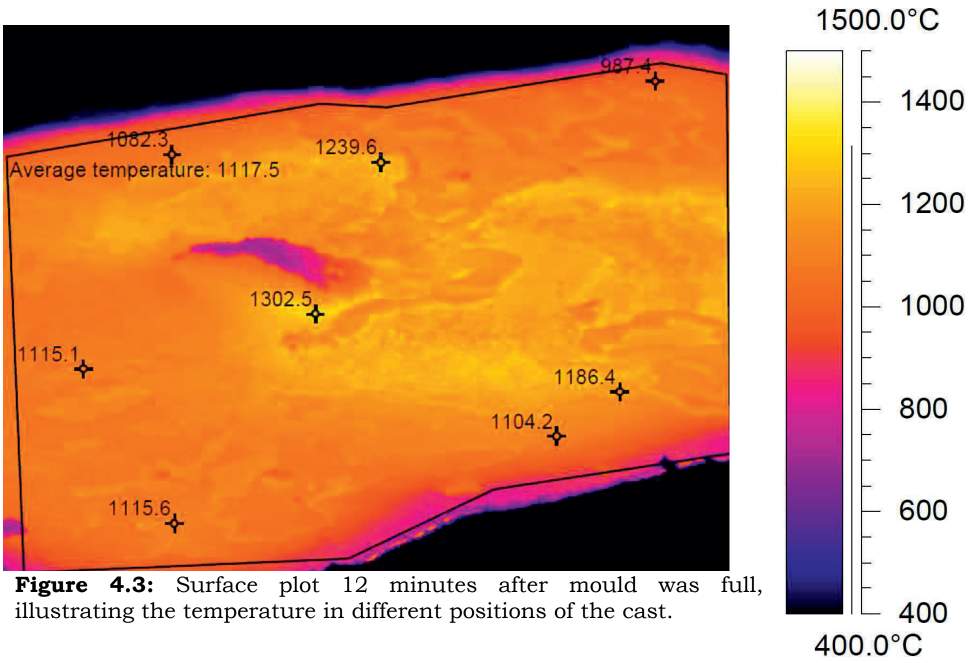

Figure 4.3: Surface plot 12 minutes after mould was full, illustrating the temperature in different positions of the cast.

After casting it was observed that the surface was oxidized in addition to that some areas consisted of slag. A surface covered in slag will be less reflective than a surface of pure silicon. In the textbook by **Incropera and DeWitt** (2002) emissivity values are listed for some metallic and non-metallic materials. Highly oxidized stainless steel has an emissivity of 0.76 at 1200 K, while polished stainless steel has an emissivity of 0.3 and 0.17 at 1000K and 300K respectively. This illustrates that emissivity is dependent on the temperature and the surface finish. Since the silicon surface was oxidized the emissivity value of 0.75 was considered to be a good average fit.

4.1.2 Experiment A2

As explained in the experimental section an aluminium box insulated in Kaowool was used as a mould in order to reduce the cooling rate during solidification. The box was placed onto a mould of industrial size that followed the railway around the furnace. In Figure 4.4 the cooling curve for thermocouple C3 is shown. Cooling from liquid to ambient temperature can be divided into several domains, as delineated in the figure. The basis for separation is outlined in Table 4.1. The same reasoning was used by **Schei et al**. (1998) and **Tveit** (1988) for silicon and FeSi respectively.

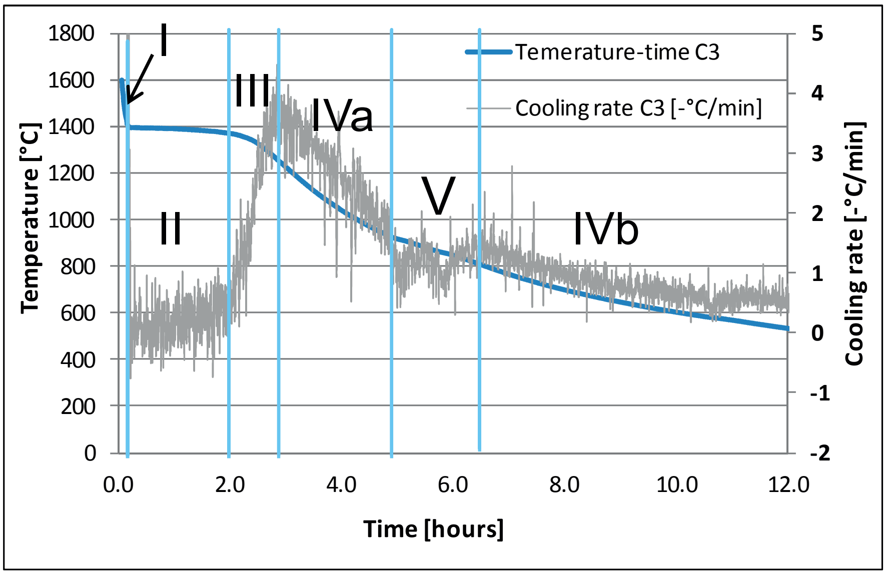

Figure 4.4: Temperature and cooling rate curves for thermocouple C3, experiment A2. Roman letters signifying different cooling domains given in Table 4.1

Table 4.1: Descriptions of different cooling domains during casting.

Cooling domain	Silicon status	Description
I	Liquid	Low heat capacity – very high heat loss
II	Solidification near thermocouple	High heat loss – evolution of latent heat
III	Parts of the cast not solidified	Increased thermal gradient – some liquid silicon below or above the thermocouple
IV a and b	Bulk part of silicon has solidified	Low heat capacity – heat loss high but abating
V	Solidification of intermetallic phases	Release of latent heat – lowers the cooling rate

Two local minimums were seen in the cooling rate around 900-800 ° C. The same peaks were observed in a few samples that were delivered for DTA analysis. Analysing the area around thermocouple C3 by EPMA, it was seen, as will be shown in Chapter 5, that Al_2CaSi_2 and Al_3FeSi_2 were the main phases observed in experiment A2 as opposed to Al_2CaSi_2, $Al_6CaFe_4Si_2$ and Al_3FeSi_2 in experiment A1. The observed peaks were assumed to be a result of the solidification of the intermetallic phases.

Figure 4.5 illustrates melting point measurements obtained by DTA from samples extracted from experiments A1 and A2. The melting point is given as a function of the total amount of alloying elements. A sample extracted close to C3 had a melting point close 1395 °C, as indicated by the temperature curve in Figure 4.4. The DTA results are illustrated together with a calculation of the melting point utilizing Sistruc13. Sistruc13 is a computer program that calculates temperature, precipitation of phases and purity of silicon during the solidification of MG-Si. The basis of the program has been described in the SINTEF report by **Dons et al**. (2009).

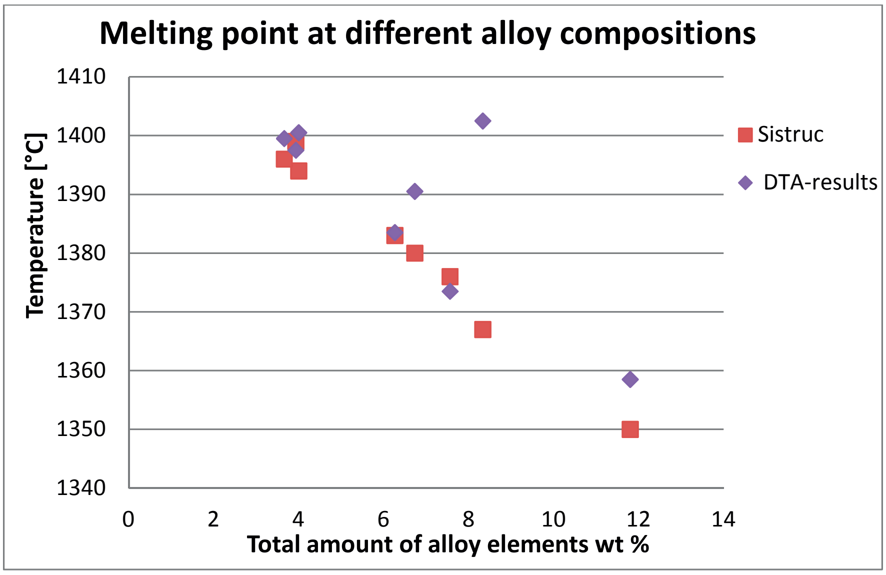

Figure 4.5: Comparison of melting temperatures from DTA results and by Sistruc calculation.

As seen from the figure the DTA results gave the same trend for most data points as the Sistruc values; alloy addition resulted in a melting point depression. The outliers from the trend were assumed to be a result of the analytical method used to determine the composition of the samples, XRF. The XRF signal will account for the total amount of the alloying elements but the method does not distinguish between elements in intermetallic phases or elements present as an oxide, such as aluminium. Al present as an oxide would not contribute to the melting point depression and the amount of Al used in the Sistruc calculation would then be too high compared to the result obtained by DTA. The DTA temperature in the figure was adjusted with respect to the calibration performed with iron and copper.

4.2 MG-Si2- Industrial experiment

In the second industrial experiment, 99 wt % metallurgical grade silicon was cast.

4.2.1 Thermal history

The recorded temperature as a function of time during the experiment is illustrated together with the COMSOL model in Figure 4.16 and Figure 4.17. In the figures it can be seen that the temperature increased for elements C1 and C2 after 12-15 minutes. During this period it was observed that liquid silicon erupted from the surface of the cast. The reason for the eruption is that silicon expands during solidification and pushes the remaining melt upwards. The temperature rise was larger for C2 and occurred prior to the temperature rise of C1. This indicates that the flow of the melt pushing its way up to the surface started closer to thermocouple C2 and had a more pronounced effect here. Examinations of the top surface revealed that the top part close to C2 had the typical structure of silicon pushed to the surface- it looked like a “worm”.

Figure 4.6 shows the main cooling domains for metallurgical grade silicon – ref Table 4.1.

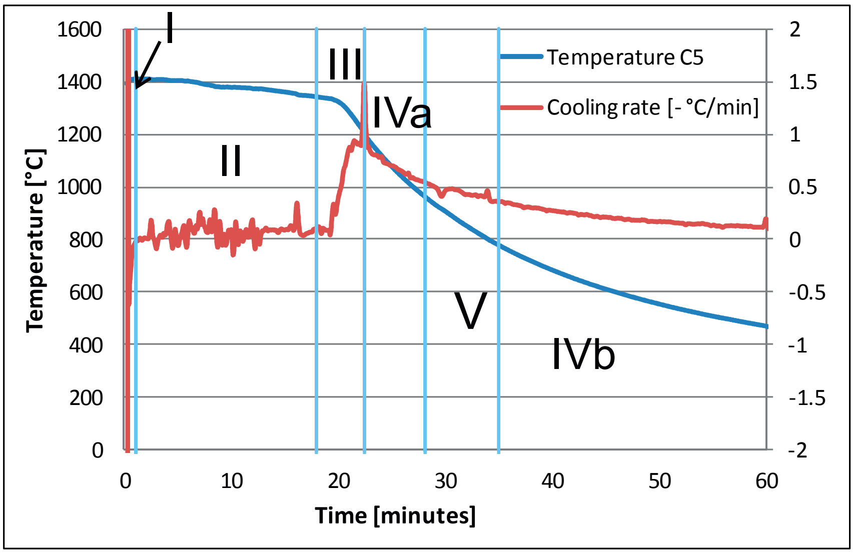

Figure 4.6: Temperature and cooling rate for thermocouple C5, 3 cm from gravel.

4.2.2 Emissions during casting

Health, safety and environment, HSE, are important issues when a given casting process is to be evaluated. In the textbook by **Tangstad et al.** (2013), *Metal production in Norway*, Tveit, discuss the health, safety and environmental issues regarding metal production.

The main environmental issues in the casting and screening area are emission of silica fume during casting and dust generated during handling, transport and crushing /sizing of the cast. Several measures have been made over the last few decades to improve the HSE standards at the Elkem plants such as **Næss** (2013), **Kamfjord** (2012).

Figure 4.7: Industrial casting at an Elkem plant.

Figure 4.7 presents a picture taken during casting. During casting it was observed that the emissions of fume ceased after around 20 seconds. This was in good agreement with the COMSOL model of the industrial mould, Figure 4.18. In the model a casting temperature of 1427 °C resulted in a surface that solidified within 20 seconds. As clearly seen from Figure 4.7 the silica fume mainly developed at liquid or near liquid surfaces. In the figure this would be the liquid surface in the ladle, the beam from the ladle to the cast and the surface of the cast while liquid.

Removal of the silica fume has to be done close to the ladle and the silicon surface until it has solidified. A stationary point where the moulds could be filled within the reach of a powerful suction would collect most of the silica fume generated in the casting area.

4.3 Copper plate experiments

As seen from Table 3.1, Chapter 3, 10 experiments were conducted on the cooled cooper plate. Three qualities were used, Solar Grade Silicon (SoG-Si), Metallurgical Grade Silicon Type 1 (MG-Si1) and Metallurgical grade silicon type 2 (MG-Si2). In Figure 4.8 to Figure 4.10 temperature time plots for three of the experiments are illustrated.

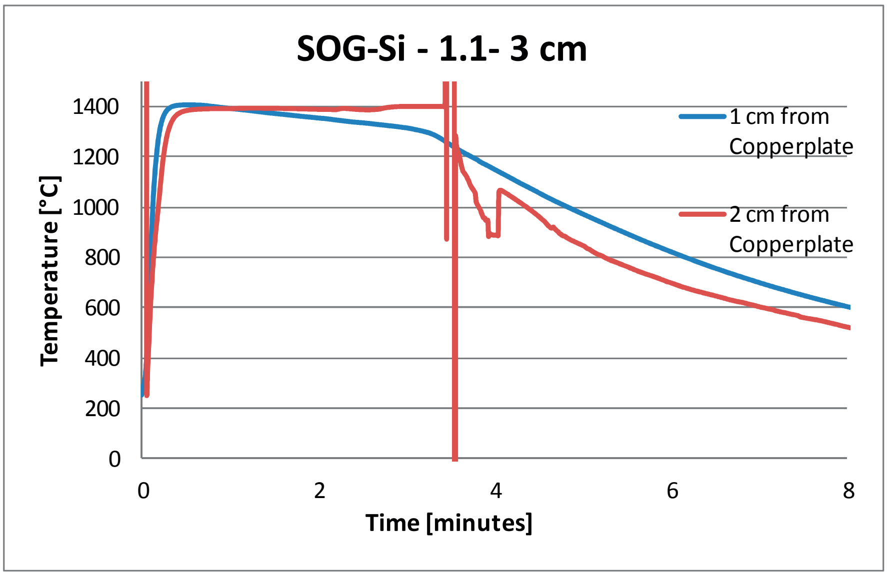

Figure 4.8: Temperature-time curve for experiment 1.1.

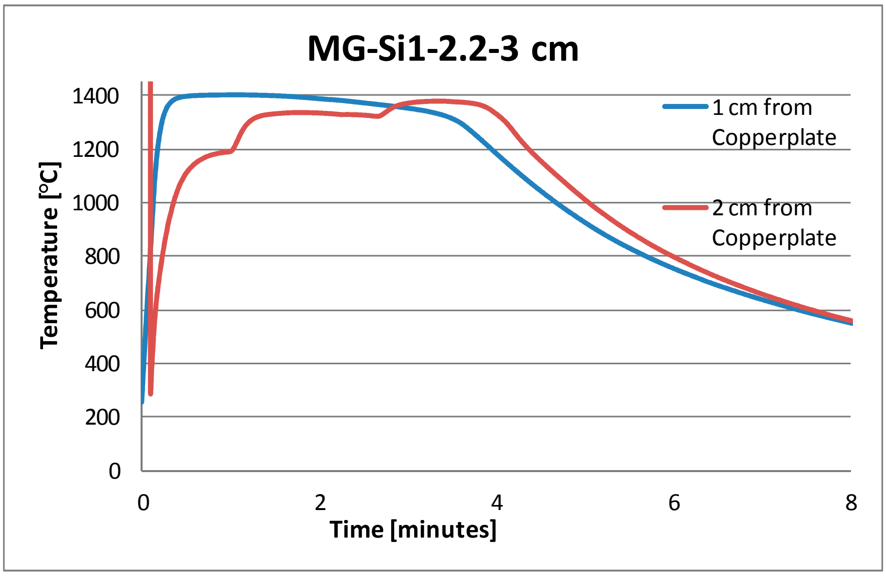

Figure 4.9: Temperature-time curve for experiment 2.2.

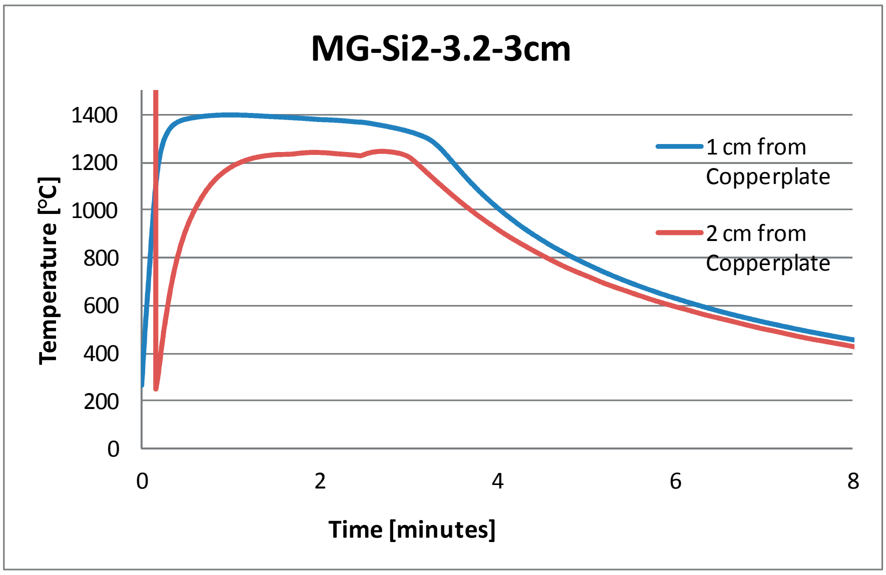

Figure 4.10: Temperature-time curve for experiment 3.2.

Due to a long response time there was an uncertainty connected to the recorded temperatures as explained in Section 3.8. From the 10 experiments conducted it was seen that the flow pattern had an impact on the thermal history. Solidification occurred with two fronts evolving from top and the bottom- or as observed in most cast solidification layers formed during casting because of a poor flow, as seen from Figure 5.12. This had an impact on both the distribution of intermetallic phases and the silicon grain size.

4.4 Directional Solidification- Cyberstar furnace experiment

Several experiments have been conducted in the Cyberstar furnace prior to this experiment and the general trend in the temperature profile, Figure 4.11, was consistent with that explained by **Dalaker** (2009), **Dalaker et al**. (2010) and **Dalaker and Syvertsen**, (2013).

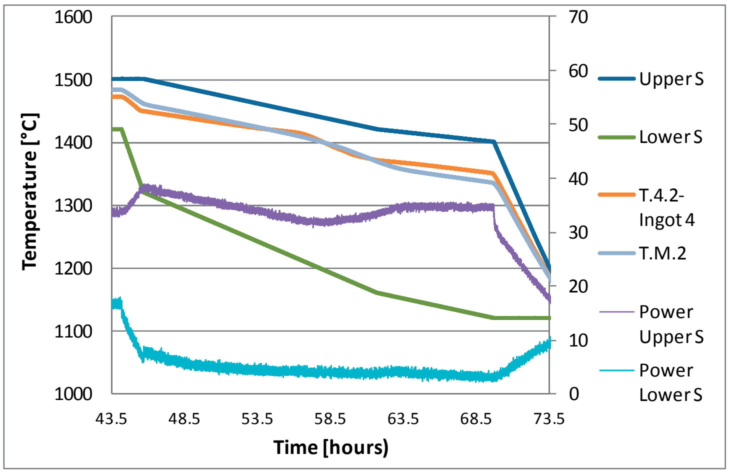

Figure 4.11: Temperature and power input during the casting.

In Figure 4.11 the temperature and power during solidification is illustrated. A program for the solidification was initiated after complete melting, as presented in the experimental part. As a consequence of the program initiated, the power of the lower susceptor was reduced. The upper susceptor started to compensate in order to keep a stable temperature at the top. This was seen as an increase in the power of the upper susceptor. When the solidification started, heat evolved and the upper susceptor no longer needed to increase its power. The solidification was assumed to occur when the power of the upper susceptor was at maximum, which was around 45.63 hours. For thermocouple T.4.2, which was placed in ingot 4 a lower cooling rate was observed after 54.5 hours. This was assumed to be the time the front starts moving close to the thermocouple and it felt the release of the latent heat. After 55.56 hours the temperature tipped below 1414 °C and the solidification occurred at this position. When the solidification was almost complete, the upper susceptor needed to increase its power in order to maintain the temperature of the set point. This was due to a reduction in the latent heat evolved and was observed after 59 hours. Thermocouples, T.4.2 and T.M.2 should both have been placed 8.5 cm from the crucible bottom. It can however be seen that the temperature was somewhat lower for T.4.2 which indicated that it was positioned a bit closer to the crucible bottom or that the temperature profile in the furnace was not equal in all horizontal positions. The height of the solid ingot was approximately 12.7 cm compared to an initial melt height of 11.5 cm. It took around 13.4 hours to complete the solidification. This yielded an average solidification velocity of 0.95 cm/hr or 2.6 µm/s. Not all thermocouples lasted the whole experimental run. The thermocouples might have been destroyed in the MG-Si cases due to a reaction between the Ca in the melt and the quartz tubes. **Martin et al**. (2009) have showed that alkaline impurities can have a detrimental effect on fused silica crucibles during multi-crystalline ingot growth.

A 1D- heat flow model describing directional solidification was developed by **Mjøs** (2006). This model has been further developed for the Cyberstar by **Dalaker et al.** (2010) and **Dalaker and Syvertsen** (2013). The reader is referred to these references if further details concerning the basis for this model are of interest.

Data from the experiment was put into this 1D model and the result is illustrated in Figure 4.12 . The modelled temperature is illustrated together with the measured temperature curves 8.5 cm from the bottom of ingot 4 and the 8.5 cm from the bottom in the middle of the furnace. It can be seen that the correlation between the model and the thermocouple in the melt was good, ingot 4. In Figure 4.13 modelled values of front velocity and front position are shown together with front positions obtained from the experimental data.

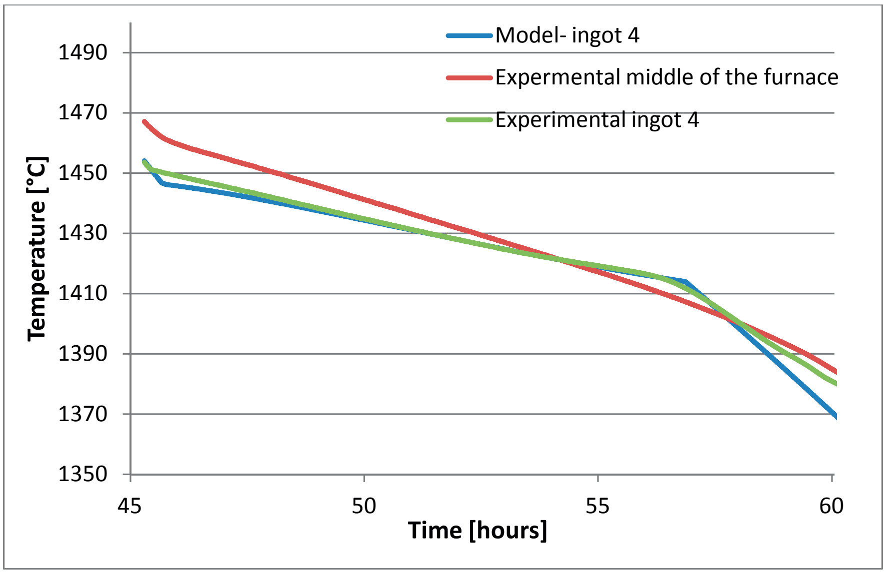

Figure 4.12: Measured and modelled temperature 8.5 cm from the crucible bottom in ingot 4, and the middle of the furnace.

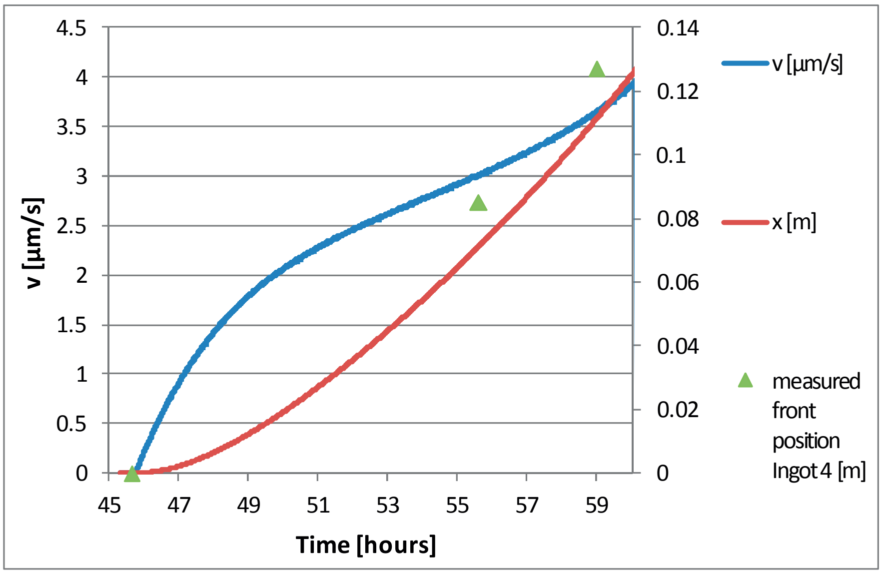

Figure 4.13: Modelled solidification speed, v (µm/s) and modelled and measured front position, x (m),

4.5 Comparison of the cooling rates

As described in the theoretical section factors such as the cooling rate and direction of heat flow will affect the microstructure of the solidified product. To see how the grain size varied with the cooling rate, the local solidification time and cooling rate was estimated in the temperature interval where silicon grains were able to grow. The fraction solid, fs, at 1396 ° C was 0.95 according to calculations in FactSage by **Kai Tang** (2013). It was assumed that after this point, no grain coarsening would occur so that the interval where the grain size was determined was between 1412.8 °C (start solidification calculated by **Kai Tang** (2013) for a composition close to MG-Si1, Fe= 0.3 wt %, Ca = 0.01 wt % and Al= 0.1 wt %. Ti not included in the calculation) and 1396 °C. **Kinoshita and Champier** (1981) illustrated that recrystallization of silicon after annealing at 1396 °C was a very slow phenomenon. This was taken as a confirmation that with the considerably higher cooling rates in these experiments no grain coarsening occurred below 1396 °C. The cooling rates from a selection of the experiments are presented in Table 4.2

Table 4.2: Cooling rate of selected experiments.

Experiment	**Thermocouple**	**Interval (°C)**	**Cooling rate (-°C/minute)**
MG-Si2 Industrial			
	C1	1413-1396	4.7
	C2	1413-1396	10.2
	C3	1413-1396	4.3
	C4	1413-1396	1.4
	C5	1413-1396	2.6
	C6	1413-1396	3.0
A1			
	A1-lower	1395-1360	1.8
	A1 middle	1395-1360	4.2
	A1-upper	1395-1360	17.5
A2			
	A2	1395-1360	0.3
Copper plate experiments			
1.2	1 cm from plate	1413-1396	21.0
1.2	1.25 cm from plate	1413-1396	9.2
2.1	0.5 cm from plate	1413-1396	32.4
2.2	1 cm from plate	1413-1396	10.6
2.3	1.25 cm from plate	1413-1396	8.9
3.2	1 cm from plate	1413-1396	15.0
3.3	1 cm from plate	1413-1396	8.9
3.4	1.25 cm from plate	1413-1396	7.2

Due to the long response time of the thermocouples temperatures around the solidification temperature were usually not recorded. In the calculation, the time solidification started was estimated. The estimation was based on the position of the thermocouples and the time it took to fill the mould under the assumption of a constant flow rate.

Based on the DTA analysis it was assumed that alloy A on average started to solidify at 1395 °C disregarding macrosegregation in the cast which would give different chemical composition at different locations. The fraction solid as a function of temperature was not known, but 35 °C was used in these calculations.

It can be seen from the table that the cooling rate for the upper thermocouple in the MG-Si2 industrial experiment, C1, was 4.7 °C/min compared to 17.5 °C/min in experiment A1, even though C1 was positioned closer to the surface. During casting in experiment A1 the low flow during filling caused a lot of heat to be lost from the surface during the 15 minutes before the mould was full. For the MG-Si2 case the filling was complete in only two minutes and the heat had to be transported through the cast where only a small part of the melt/cast was in contact with the ambient. The heat transport would therefore be slower initially for the upper thermocouples in the MG-Si2 experiment. However as more silicon solidified, less heat due to over temperature and latent heat needed to be removed. It was easier to transport the remaining heat since the MG-Si cast was thinner and the gravel size larger which increased the transport from the bottom, hence MG-Si2 reached ambient temperature faster than cast A1.

For the copper plate experiments it can be seen that the cooling rates of the thermocouples placed 1.25 cm from the bottom were similar, while there was a larger span of the cooling rates 1 cm from the plate. All experiments were started when the temperature in the furnace was 1480 °C/min, but the flow from the furnace to the plate and the flow at the plate differed. This may be the reason for the variation.

4.6 Modelling of the casting

Two models was developed using **COMSOL Multiphysics 4.3a** (2012), a model describing the industrial experiment MG-Si2 and a model describing the copper plate experiments. COMSOL Multiphysics uses the finite element method (FEM. The models gave a flexibility to calculate the consequence of changing certain parameters without the need to conduct new experiments.

4.6.1 Basis of the model

During the development of the model it was assumed that many of the thermo-physical properties of metallurgical grade silicon were close to the properties of pure silicon. Literature values describing pure silicon have been used for the latent heat, heat conductivity, emissivity and heat capacity of silicon, **Mills and Courtney** (2000).

COMSOL has a user friendly interface and allows the user to build the model stepwise. First the heat transfer module was chosen and for the case of solidification, the heat transfer in solids module was used. The geometry also needed to be defined and in Figure 4.14a and Figure 4.15 the geometry of the industrial experiments and one of the copper plate experiments are illustrated. When building a model the user defines the mechanisms of heat transfer at the boundaries and in the different domains. The equations used to solve the model are given in the COMSOL user guide included in the **COMSOL Multiphysics 4.3a** (2012) software. As described in the theory the main mechanisms for heat transfer are radiation, conduction and convection. The basis for the calculation was the principle of conservation of energy. Over a time interval the energy into the system + the energy generated (latent heat in the solidification case) must equal be to the energy out of the system – the accumulated energy. In the domains, silicon, gravel and mould, heat was transported by conduction and the latent heat generated was accounted for in the expression for heat capacity. At the boundaries a heat flux was defined, such as a radiative heat flux at the silicon surface. Values, boundary conditions and assumptions used in the models can be collected from Table 4.3 and Table 4.4.

Figure 4.14a: Sketch of the 2D geometry of the industrial mould 1560 mm horizontal, 150 mm vertical. Fines 15 mm vertical and Silicon 100 mm vertical.

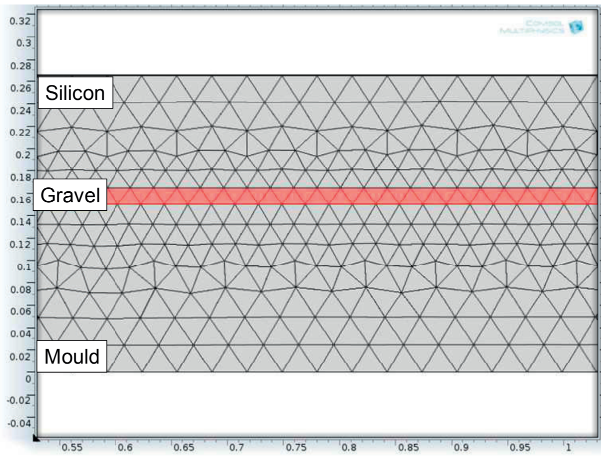

Figure 4.14b: Mesh used in the model. The sequence type used was physics controlled mesh and the element size extra fine.

Figure 4.15: Sketch of the 2D geometry of the 30 mm cast from copper plate experiments. Mould dimension: 10 mm vertical and 400 mm horizontal. Silicon dimensions: 30 mm vertical and 390 mm horizontal. Graphite: 5 mm horizontal.

Table 4.3: Properties used for the COMSOL model. Heat was transported by conduction in silicon, gravel and moulds. The boundary conditions at the different surfaces are also given.

Silicon	**MG-Si2- Industrial**	**Copper plate**
Heat capacity [J/kg*K]	Cp(T) 1)	Cp(T) 1)
Thermal conductivity [,W/m*K],	k(T) 1)	k(T) 1)
Latent heat [J/kg*K]	$(Cp(T)+((0.1*\Delta H_{fus})*((T>1675\ K)*(T<1685K))$ 1),2)	$(Cp(T)+((0.1*\Delta H_{fus})*((T>1675\ K)*(T<1685K))$ 1),2)
ε_l	0.15 1)	0.15 1)
ε_s	0.75 3),4)	0.75 3),4)
Silicon gravel	**MG-Si2- Industrial**	
Heat capacity [J/kg*K]	Cp(T) 1)	
Thermal conductivity [W/(m*K)]	k=1.4 ,extrapolated from 5)	
Latent heat [J/kg*K]	$(Cp(T)+((0.1*\Delta H_{fus})*((T>1675\ K)*(T<1685K))$ 1),2)	
Density	$0.6*\rho_{Si}$ 6)	
Mould	**Industrial MG-Si2**	**Copper plate**
Heat capacity [J/kg*K]	Cp=465 3)	Cp=385 3),6)
Thermal conductivity [W/(m*K)]	Cp=52 at 100 °C 3)	Cp=400 3),6)
Boundaries		
Heat flux mould air $[W/m^2*K]$	A total convective and radiative heat of 50. Tuned to model.	A total convective and radiative heat flux, 10. Tuned to model.
Heat flux silicon air $[W/m^2*K]$	A convective heat flux, 13 4)7)	A convective heat flux, 13 4)7)
Radiative heat flux $[W/m^2*K]$	ε (T) was used to calculate the heat flux at the silicon surface.	ε (T) was used to calculate the heat flux at the silicon surface.
Heat flux sides	Assumed to be insulated	
Heat flux graphite air $[W/m^2*K]$		A total convective and radiative heat flux 10. Tuned to model.
Thin Thermally Resistive Layer silicon/copper		$d=1e^{-3}$[m], k=0.4 [W/(m*K)] Tuned to model.
Heat flux in the water stream		Based on T_{in}, T_{out} and flow [l/s] of water cooling.

1) **Mills and Courtney**, (2000), 2) **Aylward and Findlay,** (2008), 3) **Geankoplis**, (2003), 4) **Tveit,** (1988), 5) **Ksiazek**, (2012), 6) **COMSOL 4.3a** (2012) 7) **Bakken** (2000)

Table 4.4: Assumptions used in the models.

Parameter	**Model**	**Experimental**
t_0	The mould was full	Solidification started when the melt hit the mould bottom.
ε	0.15 > 1412 °C for liquid silicon 0.75 < 1412 °C for solid silicon	Temperature dependent
Flow	Assumes no liquid flow. This was corrected by using a higher "heat conductivity" in the liquid zone.	Convection in the liquid silicon assumed to increase heat transfer
Direction of the heat flow industrial cast	Since the length of the cast was much larger than the height, the heat was assumed to be transported mainly in y direction, sides were set to be insulated.	Heat flow in vertical directions, but also some in horizontal directions.
Planarity top surface	Assumed that the top surface was plane and that the height of the cast was equal throughout the cast.	The surface was not plane-Worms covered some areas.
Gravel industrial experiment	Assumed a constant layer of gravel with a uniform size and constant height.	The height of the layer of gravel varied and as did the size which affected the heat flow in the lower part of the cast.

4.6.2 Comparison of model and industrial experiment

In Figure 4.16 and Figure 4.17 the temperatures recorded during the experiment are illustrated together with the model. Figure 3.7 illustrated the placement of the thermocouples.

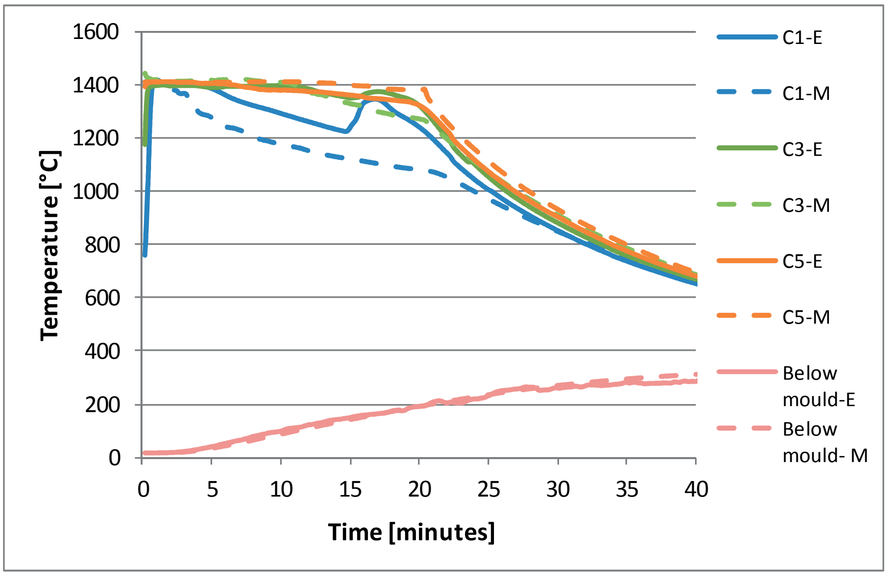

Figure 4.16: Temperature - time curve for thermocouple C1, C3, C5 and the thermocouple below the mould. E- denotes temperature recorded during the experiment and M- denotes the modelled value.

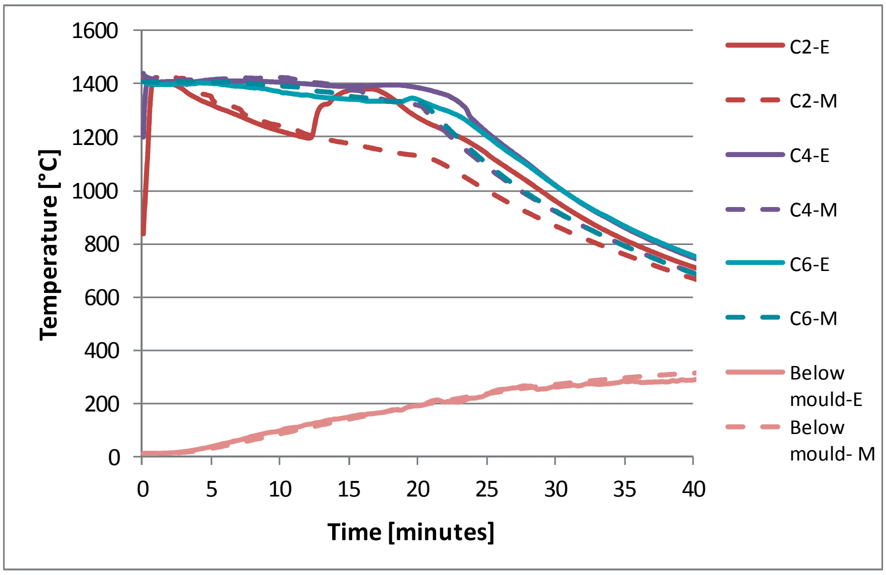

Figure 4.17: Temperature - time curve for thermocouple C2, C4, C6 thermocouple below the mould. E- denotes temperature recorded during the experiment and M- denotes the modelled value.

As mentioned in Section 4.2, liquid silicon erupted from the surface of the cast during the experiment in the same time period as a temperature increase was observed for the thermocouples. This increase was not accounted for in the model and led to a deviation between the experimental and modelled values in this time range. The reason for the eruption was that silicon expanded during solidification and pushed the remaining melt upwards. Comparing the experiential and modelled temperatures it is seen that the model gives a good description of the thermal history during the casting.

4.6.3 Parameter study

As mentioned at the start of this chapter a model can be a useful tool to see the effect of changing one parameter in the system. Below, a few examples are given that illustrated the effect of a change in melt temperature, fines size and height.

4.6.3.1 Changing over temperature in the melt

During the experiment it was observed that the silica fume formation ceased soon after the mould was full. The fuming was a result of the oxidation of silicon. Figure 4.18 shows that an increased casting temperature increased the time before the fume formation ceased. The calculations were performed by changing initial temperature of the melt in the industrial MG-Si2 model and extracting the time the surface temperature reached 1413 °C.

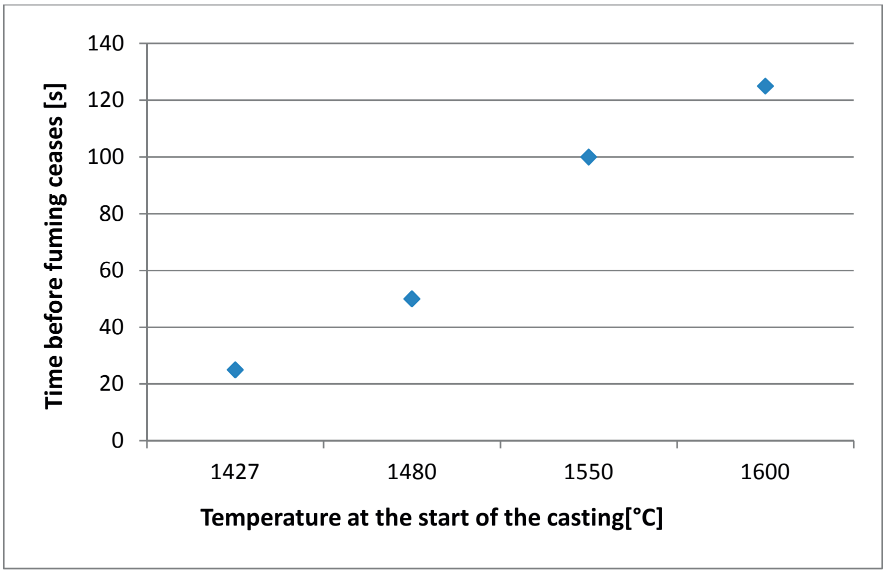

Figure 4.18: Time before the fuming ceases as a function of start temperature in the melt.

4.6.3.2 Changing the size of the gravel

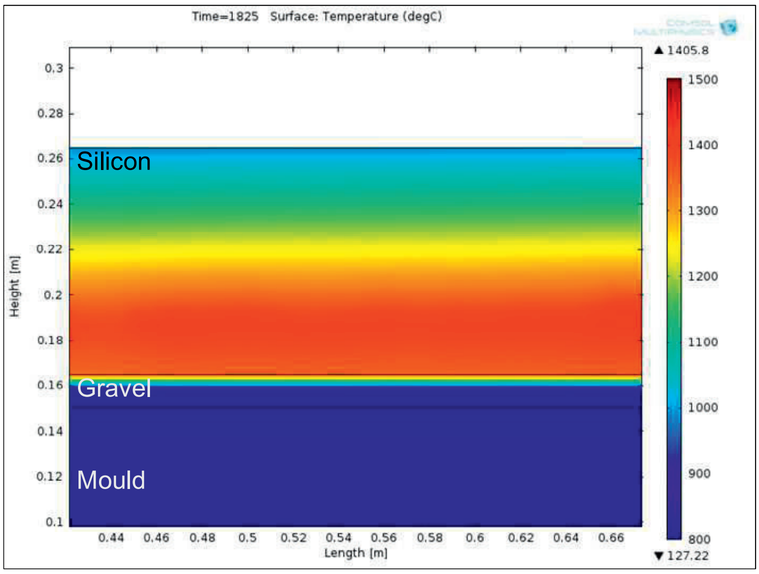

Figure 4.19: Surface plot 1825 seconds after casting- model based on the industrial case, but with thermal conductivity 0.5 [W/m*K]. Regions with temperatures below 800 ° C are illustrated in dark blue.

To illustrate the sensitivity of thermal conductivity the thermal conductivity was set to 0.5 [W/m*K]. A resulting surface plot is shown in Figure 4.19. (Surface plot with a thermal conductivity of 1.4 [W/m*K] is given in Figure 5.5.) Since the driving force to heat transport has been reduced at the bottom, more heat must be to be transported through the top part of the cast. The two solidifying fronts meet closer to the bottom as a result of the changed thermal conductivity. The lower part would be liquid for a longer time than in the industrial experiment.

4.6.3.3 Changing the height of the cast

Since the heat that needs to be removed per m^2 increases when the height of the cast increases this will affect the thermal history of the cast. To investigate this further the temperature 1 cm from the fines layer was modelled for casts of height 1.5, 3, 5 and 10 cm and the result is given in Figure 4.20

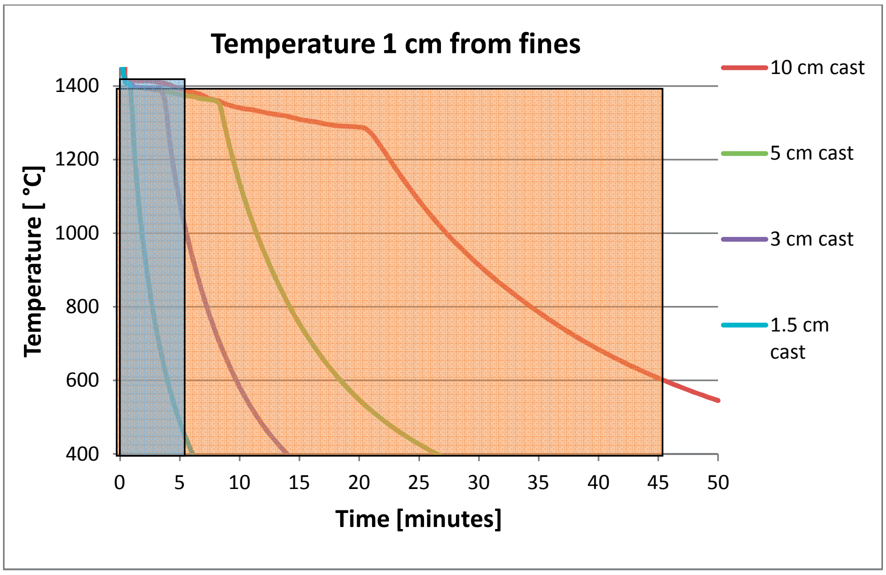

Figure 4.20: Temperature 1 cm from fines layer in 1.5, 3, 5 and 10 cm cast. Note the large variation in the time length from 1396 °C to 600 °C for the different casts.

As mentioned earlier, the FactSage modelling by **Kai Tang** (2013) gave a solid fraction of 95 % at 1396 °C and it was assumed that the primary silicon grain size was given at this temperature based on the recrystallization experiments by **Kinoshita and Champier** (1981). It can be seen that the cooling rate through the temperature range where the silicon grain size was determined was quite similar for the different casts, indicated by the blue rectangle. For the cooling rate in the subsequent cooling the difference was larger, given by the orange rectangle. The position 1 cm from the fines maintained a temperature in the region between 1396° C and 600° C for 3.3 minutes for the 1.5 cm cast. In the 10 cm cast a temperature in this region will be maintained for 40 minutes. If the remaining melt can rearrange in this temperature range, as suggested by **Rong** (1992), one would expect a difference in the distribution of the intermetallic phases between the cast. However if the distribution was determined by the cooling rate in the region where the primary silicon solidifies, **Margaria** (1994), the distribution is assumed to be quite similar. This is looked into in chapter 5.

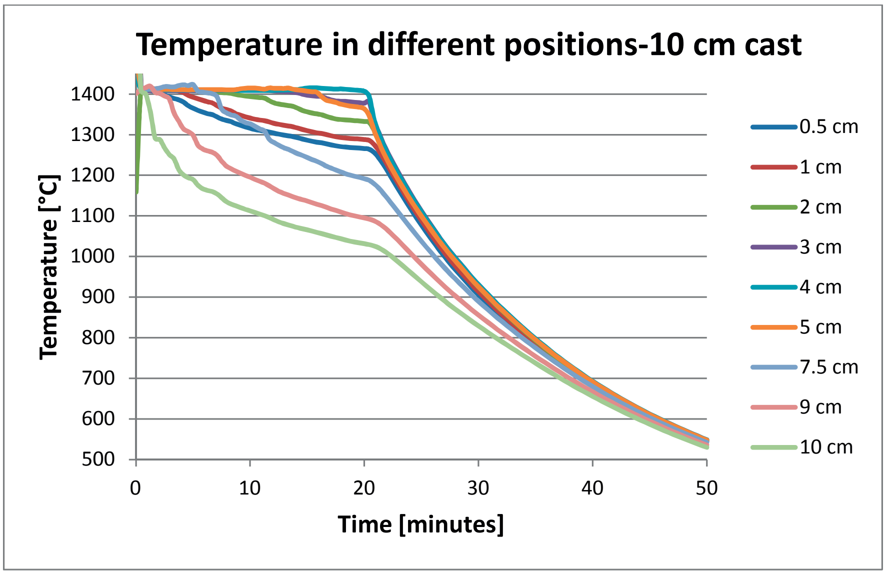

Figure 4.21: Temperature in different <u>positions from the bottom</u> of the 10 cm modelled cast. It is seen that when the position was close to the top or bottom surface the temperature decrease is fast initially, but slow subsequently due to the heat from other areas that must be transported through the surfaces.

Figure 4.21 illustrated that positions close to the top and bottom surfaces cooled fast initially, but the subsequent cooling was slow since the heat from the rest of the cast was transported through these areas. The opposite was observed for positions close to the area where the solidifying fronts meet, e.g. 4 cm from the bottom. The initial cooling was slow, while the subsequent cooling was rapid.

For most positions in a thicker cast, the remaining melt will have a longer time to rearrange before solidification. In industry several casts are often moved from the mould and stored on top of each other. This will retain the heat for a longer time and could have an effect on the microstructure of the intermetallic phases.

4.6.4 Modelling of the copper plate experiments

From the copper plate model it was shown that for the 3 cm and the 5 cm cases the solidifying fronts met closer to the upper surface since the resistance to heat transfer was less from the bottom than from the top of the cast. This is illustrated as a surface plot 180 seconds after start solidification for the 3 cm cast, experiment 3.3.

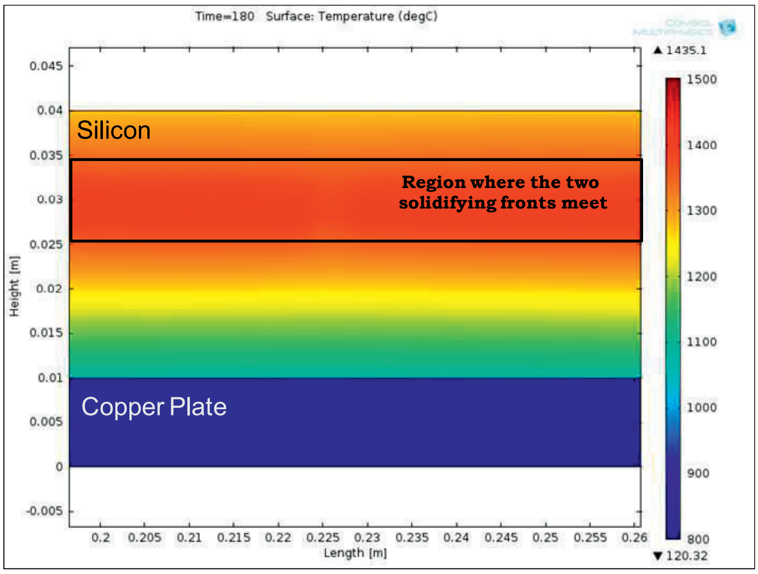

Figure 4.22: Surface plot 180 seconds after casting- model based on copper plate experiment 3.3, 3 cm. Regions with temperatures below 800 ° C are illustrated in dark blue.

For the 1.5 cm cast it was observed that the model calculates a more homogeneous temperature profile than for the 3 and 5 cm casts, seen from the surface plot given in Figure 4.23. A sample extracted from cast 3.1 was superimposed on the surface plot. It can be seen that the area were the two fronts have met in the sample was equal to the area where the melt solidifies last; that is where the fronts met. Examining the segregation pattern in the extracted samples with the model there was a good fit between where the highest amount of alloying elements were found and where the model predicted the liquid to solidify last. This supports the idea that the model was able to predict the solidification.

The model indicated that the heat transport have been significant also in horizontal directions, not only in vertical directions. (The whole cross section was not included in the figure so this cannot be seen from figure).

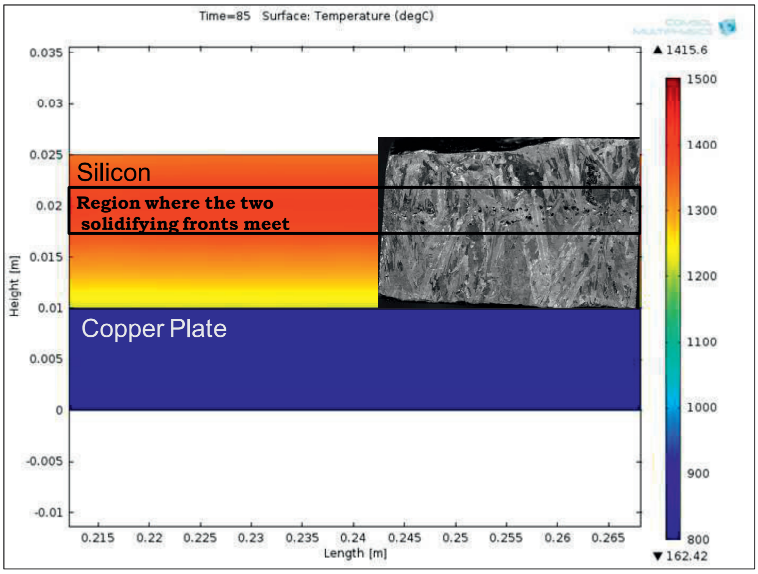

Figure 4.23: Surface plot 85 seconds after casting- model based on copper plate experiment 3.1, 1.5 cm. A sample cut from the cast is superimposed in the plot. Regions with temperatures below 800 ° C are illustrated in dark blue.

5 Investigation of the Macro- and Microstructures

To facilitate the reading of this chapter a set of colour codes was assigned to the chemical species and intermetallic phases encountered in the experiments. An overview is given in the table below. The colouring assigned to the chemical elements is used in figures describing the segregation pattern, while the colours assigned to the intermetallic phases are in general used in all aspects relating to a given intermetallic phase.

Table 5.1: Colouring assigned to elements and intermetallic phases encountered in the thesis.

Chemical elements:	Intermetallic phases:
Silicon- Si	**$Al_6CaFe_4Si_8$**
Iron- Fe	**Al_2CaSi_2**
Aluminium- Al	**HT- (Al)$FeSi_2$**
Calcium- Ca	**Al_3FeSi_2**
Titanium- Ti	**$Al_6Fe_4Si_6$**
Copper-Cu	**(Al)$FeSi_2Ti$**
Manganese-Mn	**Al-Fe-Si-Ti**
Magnesium-Mg	**(Al,Fe)$SiTi_2$**
Phosphorus –P	**(Al,Zr)$SiTi_2$**
Vanadium-V	**Al-Ba-Si**
Tin-Sn	**Al-Si**
	Al-Si (Ce,La,Nd)
	Si

In the following sections several micrographs will be presented. All the SEM micrographs are obtained using a SEM with a backscatter detector. The basis for the back scatter detector technique was outlined in the experimental section. A phase is imaged with a darker contrast when the mean atomic number is low compared to a phase with a higher mean atomic number. This means that the silicon matrix will be darker than the intermetallic phases with a higher mean atomic number. It is also possible to distinguish between some of the intermetallic phases based on contrast.

Samples from the experiments will be referred to frequently in the text and the origin of the samples is summarized in Table 5.2.

Table 5.2: Labelling of the samples extracted from the experiments.

Sample name	Experiment
A1	Alloy A, A1
A2-2.2,2.4 and 2.6	Alloy A, A2
B,D,G	MG-SI2 Industrial
1.1	Copper plate SoG-Si 3 cm
1.2	Copper plate SoG-Si 5 cm
2.1	Copper plate MG-Si1- 1.5 cm
2.2	Copper plate MG-Si1- 3 cm
2.3	Copper plate MG-Si1- 3 cm
3.1	Copper plate MG-Si2- 1.5 cm
3.2	Copper plate MG-Si2- 3 cm
3.3	Copper plate MG-Si2- 3 cm
3.4	Copper plate MG-Si2- 5 cm
3.5	Copper plate MG-Si2- 5 cm
Ingot 1	Cyberstar MG-Si2
Ingot 2	Cyberstar MG-Si1
Ingot 3	Cyberstar MG-Si2
Ingot 4	Cyberstar EG-Si

The segregation pattern in the samples extracted will be outlined in this chapter. Silicon grain size, distribution of intermetallic phases and the relationship to thermal history, casting procedure and alloy composition are also discussed. In addition the distribution of trace elements and their preferences for some of the intermetallic phases will be looked into. The objective is to elucidate how the solidified product was affected by a change in alloy composition, inclusions present, the solidification process including flow during filling of the mould and cooling rate.

5.1 Segregation pattern

Lower solubility of most elements in solid silicon as compared to liquid silicon result in an enrichment of the melt during solidification. There are multiple phenomena that can lead to segregation. On the micro scale there will be segregation between the relatively pure silicon and the intermetallic phases. Density differences between solid silicon and the melt can increase the segregation at a larger scale. Solid silicon has a lower density than liquid silicon and will therefore rise while remaining melt will descend. Temperature differences can also initiate density-related flow. These factors contribute to an inhomogeneous distribution of the elements in the cast. In this section the macrosegregation observed in the different experiments will be discussed.

5.1.1 Segregation pattern experiment A1

Two experiments were performed utilizing alloy A. For alloy A the chemical analysis is given in a relative scale. None the less the relative scale also provided useful insight into the segregation phenomena and gave an opportunity to compare the segregation pattern from all the experiments based on factors such as the cooling rate and direction of the heat flow.

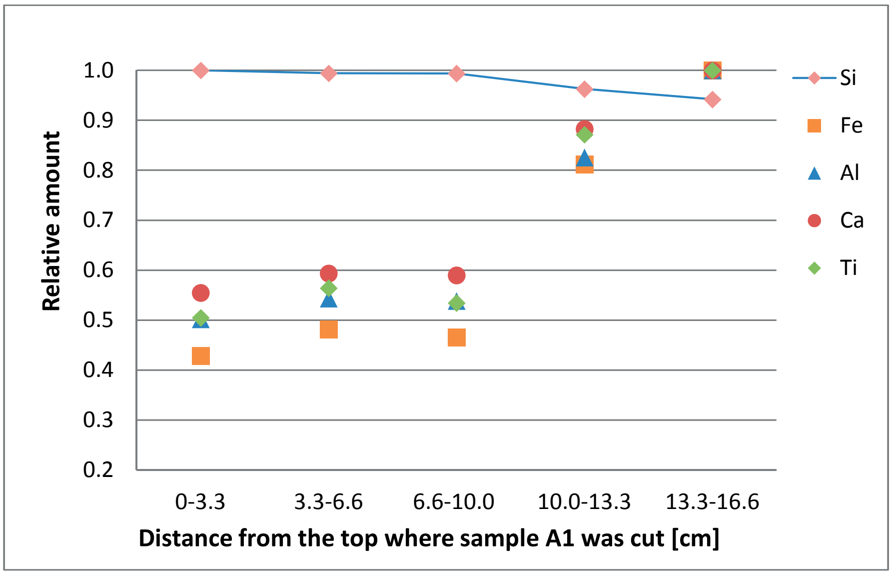

Figure 5.1: Relative analysis of sample A1.

The relative amount was calculated according to the formula below.

$$relative\ value = \frac{wt\ \%\ sample}{\max wt\ \%}$$

This means that the sample with the maximum amount was assigned a value of 1.

The conclusion to be drawn from the figure was that compared to the bulk analysis, the top part of the cast was deficient in alloying elements and the lower part was enriched in alloying elements. The silicon content in the top sample was approximately 5 wt % higher than in the bottom sample. In the case of solidification from the top surface this has lead to low density silicon floating at the top, while higher density liquid enriched in trace elements have descended. Solidification from the bottom will not give the same macrosegregation as expected with solidification from the top. Here grains that started to float melt back if they met melt with a temperature higher than the melting point of silicon. If however they arrived in an undercooled region equiaxed grains could start to grow. Equiaxed growth could also have been facilitated by impurity particles. The reason for the high amount of alloying elements in the sample between 13.3 and 16.6 cm from the top was remelted fines.

There was not a pronounced difference in alloying elements (or silicon) in the three top samples. This was attributed to the solidification layers in the cast, see Figure 5.12. The layers acted as barriers for the enriched melt and alloying elements solidified close to this boundary when their solidification temperature was reached. The enriched melt would therefore not sink all the way to the area where the two solidifying fronts met. The layers had a great impact on the silicon grain size and the distribution of the intermetallic phases.

Alloying elements that were not stopped by a layer accumulated in the remaining liquid and solidified in the area between 10 and 13.6 cm- which seemed to be where the solidifying fronts have met.

5.1.2 Segregation pattern experiment A2

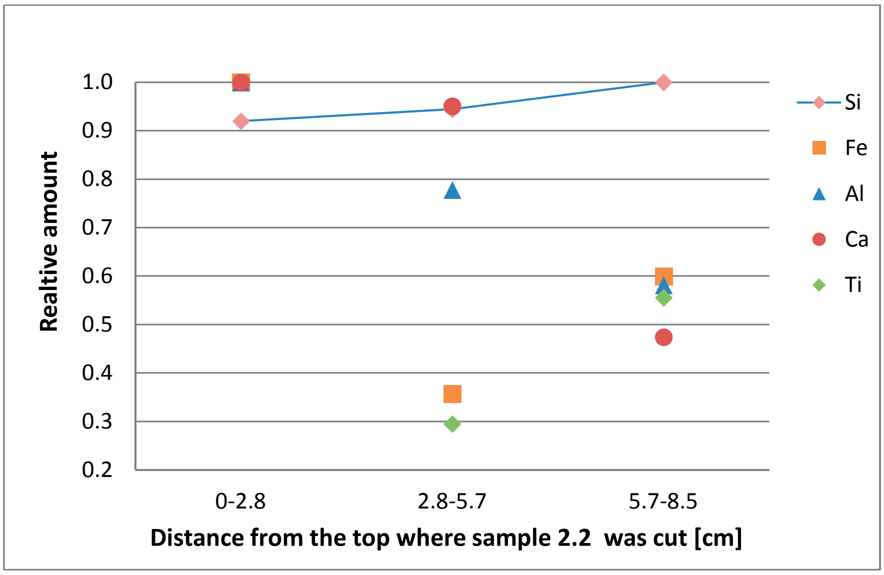

Figure 5.2: Relative analysis of sample 2.2 (A2).

In sample 2.2 the highest content of alloying elements was found in the top sample. This was explained by the density change of silicon during solidification. When silicon expanded, melt from the inside parts of the cast could have been pushed to the surface where there was more space. This melt was enriched in alloying elements because it solidified at a later stage.

5.1.3 Segregation pattern MG-Si2 industrial

Metallurgical grade silicon with a chemical composition applicable for the direct synthesis was chosen as the second industrial alloy. Prior to the casting the bulk composition of the ladle was measured. The content of the main alloying elements was: Fe = 0.42 wt %, Al = 0.26 wt %, Ca= 0.06 wt % and Ti = 0.03 wt %. A post refining took place in the ladle during casting as seen from the lower mean analysis of Al and Ca in the figure below.

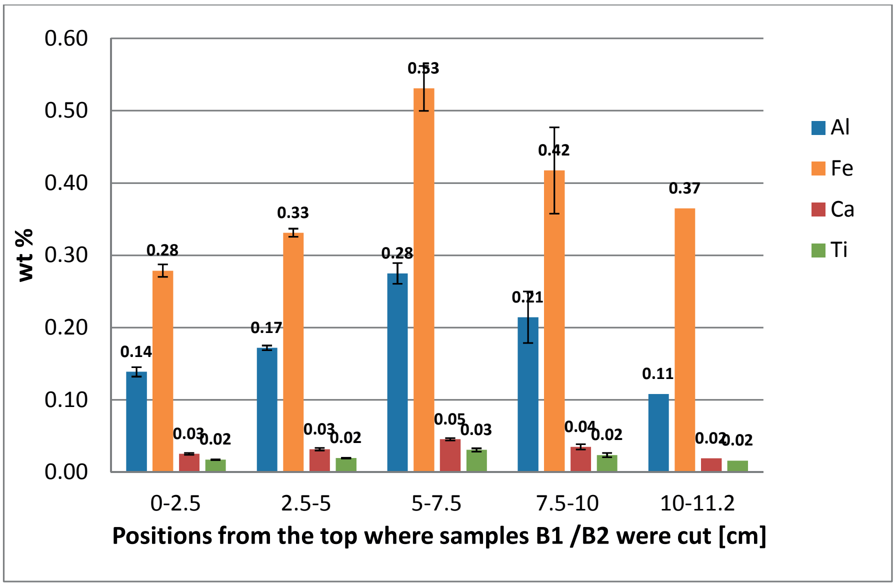

Figure 5.3: Chemical analysis of samples B1 and B2 in different positions from the top. The error bars give the standard deviation.

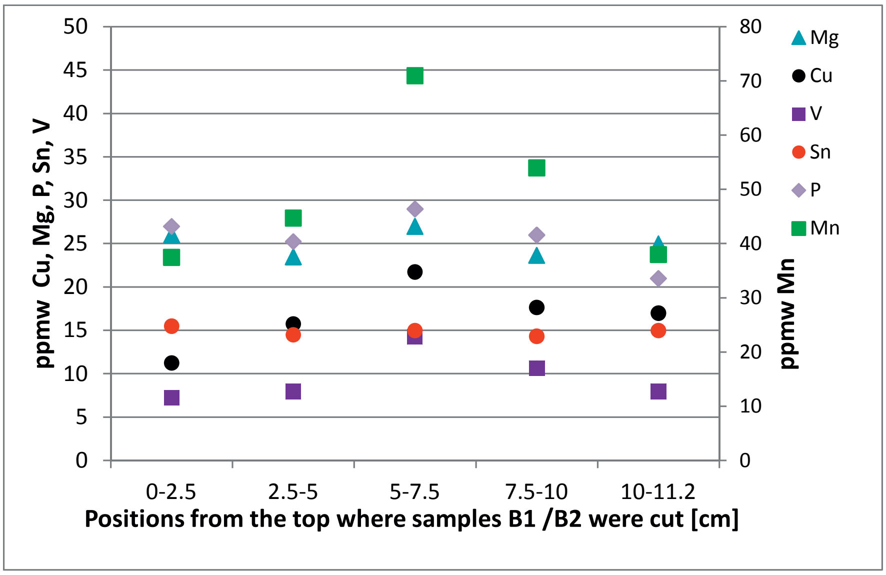

Figure 5.4: Segregation pattern of the main trace elements in sample B1/B2.

Figure 5.3 and Figure 5.4 present the mean chemical analysis of two vertical samples B1 and B2, cut in the proximity of thermocouples C1, C3 and C5. Sample B2 was slightly larger than B1 due to remelted gravel, so the sample from 10-11.2 only consisted of material from B2. The analysis revealed that there was a segregation of alloying elements from top to bottom of the cast. The amount of Al, Fe, Ca and Ti was at a minimum in the top sample, which was from 0-2.5 cm from the top. The maximum content of these elements was found in the sample from 5-7.5 cm from the top. The segregation can be explained by solidification from top and bottom as outlined in Section 2.4.2. This area was the last to solidify as shown in Figure 5.5b. The temperature curves from the experiment, the COMSOL model and the chemical analysis all indicate that the two fronts met in the area from 5-7.5 cm from the top.

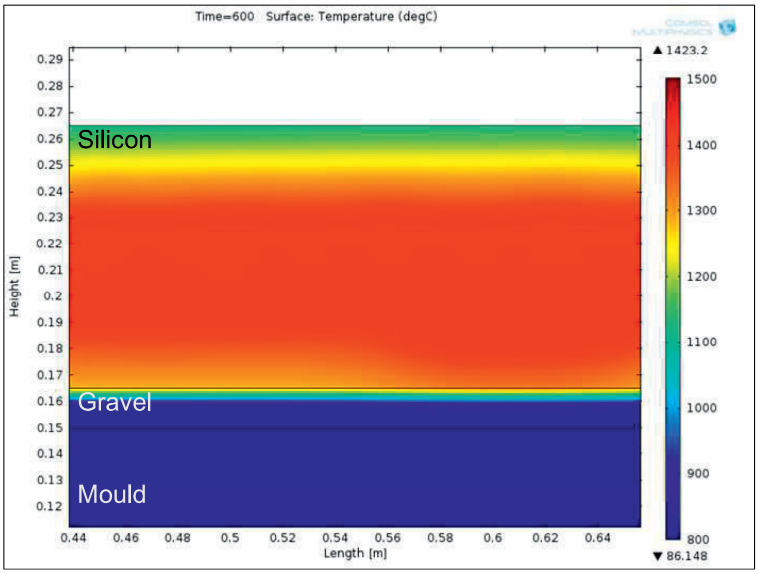

Figure 5.5a: Surface plot 600 seconds after start solidification obtained by the COMSOL model. The scale bar gives the temperature of the surface. Regions with temperatures below 800 ° C are illustrated in dark blue.

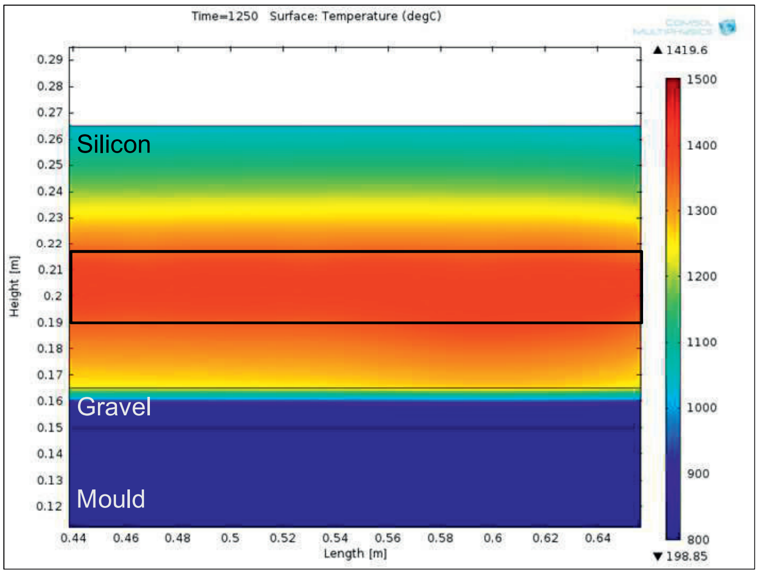

Figure 5.5b: Surface plot 1250 seconds after start solidification obtained by the COMSOL model. Regions with temperatures below 800 ° C are illustrated in dark blue. The area inside the rectangle corresponds to the sample extracted 5-7.5 cm from the top.

Sample D, extracted close to thermocouples C2, C4 and C6, and sample G, revealed another segregation pattern than sample B1/B2, Appendix A. The top part of sample D contained a worm which resulted in a high content of alloying elements in this sample.

The segregation pattern for trace elements Cu, Mg, Mn, P, Sn and V are illustrated in Figure 5.4. For MG-Si2 an analysis program that also could detect Pb, Bi, As, Zn, Ni, Cr, Ba, Mo, Sb, Sn, Y, Se, La and Ce was utilized, but the concentration of these elements was generally below the detection limit of the instrument. An exception was the sample that contained the maximum amount of Al, Ca, Fe and Ti. When comparing the segregation of the trace elements with the main alloying elements it was easy to see a similar trend for Cu, Mn and V.

The distribution coefficients of tin and phosphorus are high compared to those of vanadium, copper and manganese, as seen from Table 2.1 Magnesium, phosphorus and especially tin did not have a pronounced segregation pattern, Figure 5.4. In some cases it was opposite to the other trace elements, that is; tin followed the pattern of silicon.

The conclusion from the chemical analysis is that there were large variations in the composition throughout the cast. A general trend was that the area that contained the remaining melt had the highest concentration of alloying elements. This area may be found where the solidifying fronts met as well as in “worms”.

5.1.4 Segregation pattern copper plate experiments

For the copper plate experiments MG-Si2 industrial was remelted in addition to MG-Si1 and a SoG-Si quality, as explained in Chapter 3.

The chemical analysis of experiments 3.1, 3.3 and 3.5, all conducted with MG-Si2, are illustrated in Figure 5.6 to Figure 5.8. The analyses of samples 2.1-2.3 and 3.2 and 3.4 are given in Appendix A. In the 1.5 cm samples, 2.1 and 3.1, it was observed that the two solidifying fronts met closer to the top then the bottom of the cast and that the lower front moved approximately 1.1 mm from the copper plate. This explains the increased amount of alloying elements in the top sample seen from Figure 5.6. It can be seen that both the calcium and aluminium content in the samples were lower than for the starting material. The vapour pressures of calcium and aluminium are higher than of silicon which means calcium can easily evaporate from a silicon melt (**Safarian and Tangstad**, 2012). As described in the experimental part, the different grades of silicon were re-melted in a furnace under an argon flow prior to casting. Ca and Al may have evaporated during this process. Slag was observed in the furnace and on top of some casts so Al and Ca could also have been be lost due to oxidation to their respective oxides.

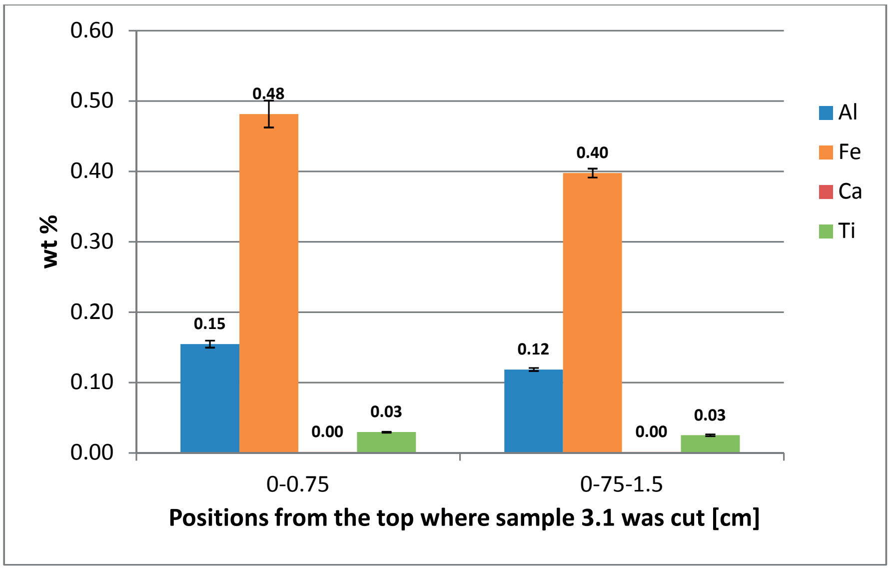

Figure 5.6: Chemical analysis of sample 3.1 in different positions from the top. The error bars give the standard deviation.

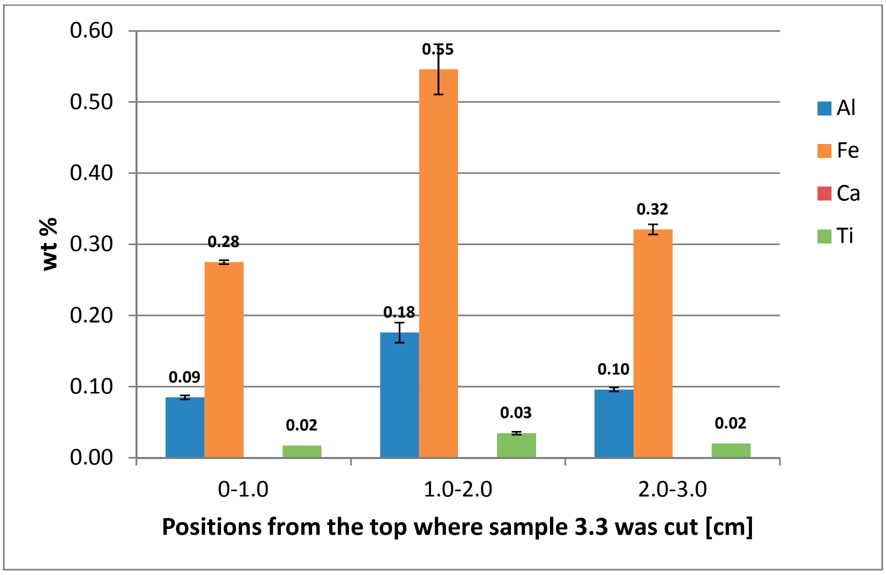

Figure 5.7: Chemical analysis of sample 3.3 in different positions from the top. The error bars give the standard deviation.

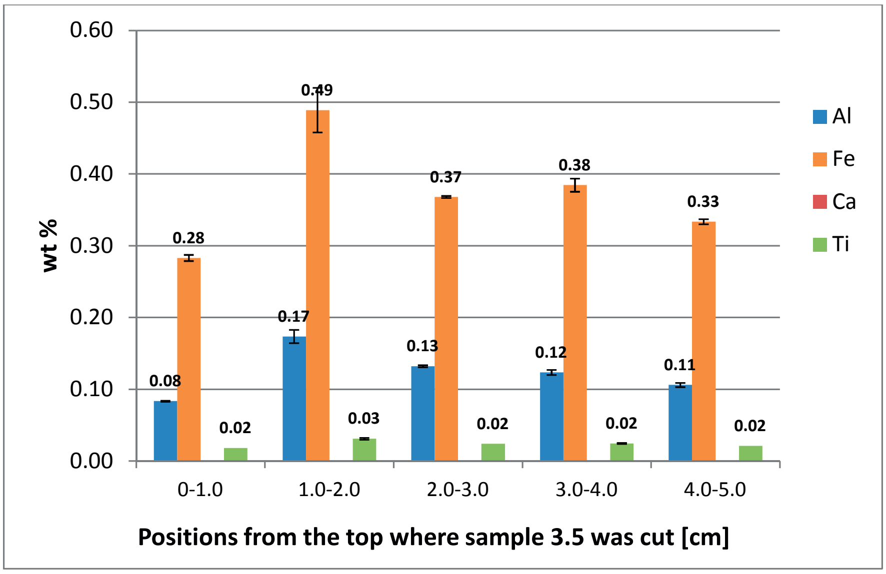

Figure 5.8: Chemical analysis of sample 3.5 in different positions from the top. The error bars give the standard deviation.

For samples 3.3 and 3.5 the maximum level of Fe, Al and Ti was found in the sample 1-2 cm from the top. Examining sample 3.3 this was the area where the two fronts met. For sample 3.5 a layer was seen in the area between 1 to 2 cm from the top. Mapping of the area adjacent to the layer in sample 3.5 illustrated that this area contained oxygen, see Figure 5.29. This is confirmation that the layer was due to low flow rate and that the surface of the layer solidified and oxidized before new melt covered the surface.

Examining the segregation pattern of a selection of trace elements, Appendix A, a similar trend as observed for MG-Si2 was seen. Except for Mg, P and Sn the segregation pattern resembled the pattern of the alloying elements. As seen before, the segregation was not as pronounced for P and Mg. When it came to Sn, if segregation was observed it usually followed the silicon analysis.

5.1.5 Segregation pattern Cyberstar furnace experiment

Analysis for Ingot 1, 2 and 3 are given in Appendix A. The segregation pattern for Ingot 2, MG-Si1, is illustrated in Figure 5.9.

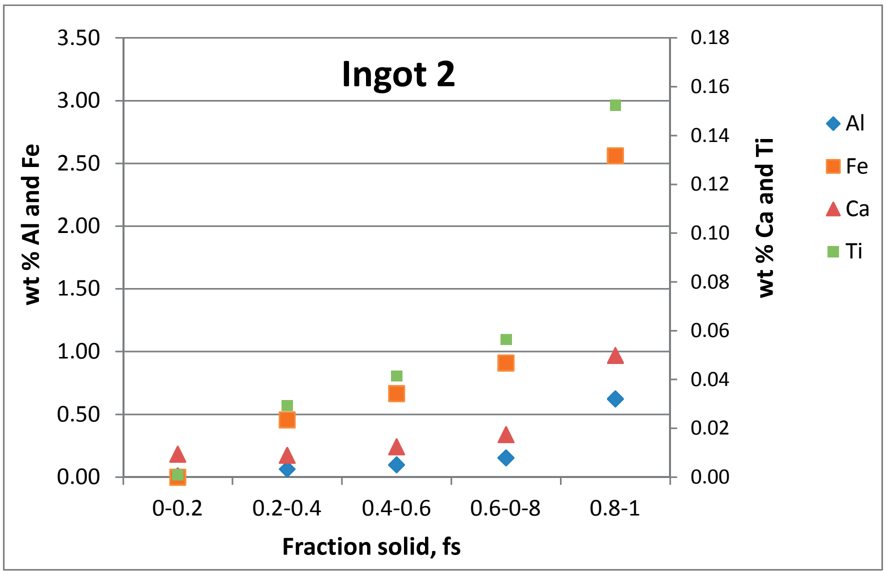

Figure 5.9: Segregation pattern main impurities, Ingot 2, MG-Si1, Cyberstar furnace experiment.

Constitutional undercooled regions developed during solidification due to the enrichment of the liquid. This resulted in the breakdown of the plane front, probably when the solid fraction was between 0.2 and 0.4. This was supported by SEM examinations of the samples. In the lower region of ingots 1, 2 and 3, no intermetallic phases were found. In the middle and the top sample they were found more frequently.

A comparison with the Scheil equation was done, Figure 5.10. It was seen that the concentration of alloying elements throughout the ingot was larger than predicted from the Scheil equation.

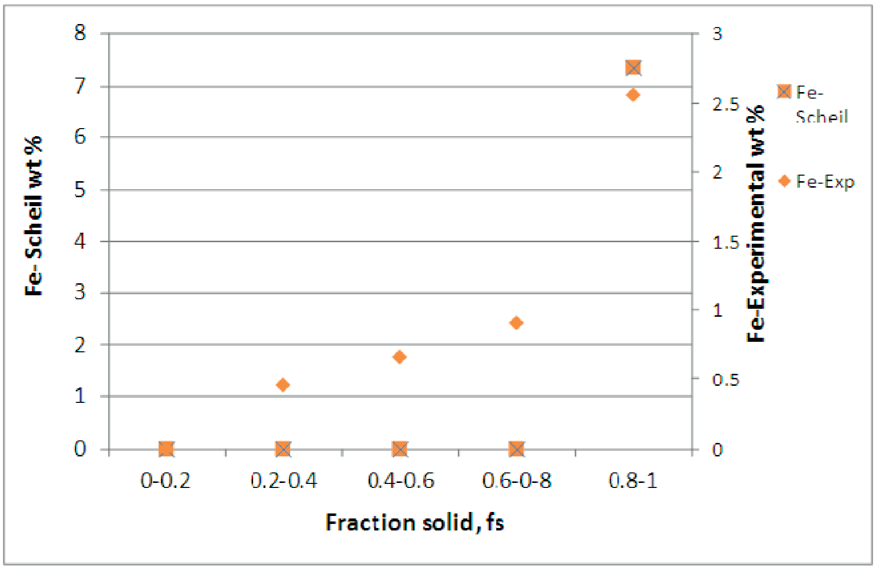

Figure 5.10: Experimental and Scheil values for iron as a function of fraction solid, Ingot 2, MG-Si1, Cyberstar furnace experiment. For the Scheil calculation, kFe= 8.0*10^{-6} and fs = 0.2, 0.4, 0.6, 0.8 and 0.999999 have been used.

It was not attempted to find an effective distribution coefficient that corresponded to the observed segregation pattern, since the XRF analysis gave the combined amount of trace elements in silicon matrix and intermetallic phases. Investigating the effective distribution coefficient, the concentration in the silicon matrix should be used to see if more trace elements have been incorporated into the matrix than what predicted using the equilibrium distribution coefficient.

As in the prior experiments no segregation was observed for tin, while other elements showed a pattern similar to the main elements. A lower concentration of calcium was observed in this experiment as well, indicating that it evaporated.

When comparing samples from several locations in the furnace it was observed that the analysis was higher towards the centre of the furnace compared to close to the mould wall. An explanation can be that a temperature gradient existed with decreasing temperature towards the mould wall. The result would be that the solidifying front bended towards the middle of the furnace. When alloying elements were rejected at the interface they would be pushed towards the liquid regions causing a melting point depression. This would reduce the planarity of the front.

5.2 Grain size

In Table 5.3 the average grain size obtained by the circular intercept method, mm, and equivalent grain size, mm, is listed for a selection of samples extracted after the experiments. It can be seen from the table that the standard deviations in the measurements were large, indicating a heterogeneous distribution of grain size. In Section 3.8 a discussion around the uncertainty relating to the grain size measurements was given. In Figure B.1-B.8, Appendix B, four magnified areas of samples A1, 2.2(A2), B, 1.1, 1.2, 2.1, 2.3 and 3.5 are illustrated. The individual squares in the figures all correspond to a real size of 1 cm x 1 cm.

Table 5.3: Average and equivalent grain size [mm] for a selection of samples. The average cooling rate is the average of the values calculated for a given experiment in Table 4.2. E.g. for sample A1, Alloy A this is the average of the upper, lower and middle thermocouple.

Sample	Mean [mm]	Std [mm]	Measured grain boundaries	Average cooling rate [-°C/s]	Equivalent grain size [mm]	Average grain area [mm²]
A1	0.63	0.49	523	0.13		
2.2 (A2)	1.35	0.95	240	0.005		
B	0.89	0.76	546	0.07	0.73	3.3
H	0.91	0.73	455			
2-1	0.52	0.36	328	0.54	0.41	1.1
2-3	0.53	0.44	342	0.15		
3-1	0.52	0.32	340			
3-3	0.53	0.34	348	0.15		
3-5	0.58	0.48	574	0.12		

5.2.1 Comparison of grain size

Sample A1 is illustrated in Figure 5.11 together with a selection of SEM micrographs. Figure 5.11 and the images in Figure B.1, Appendix B, illustrate that there were large variations in the grain size throughout the cast. Some grains were more than 1 cm in length while others were only a few mm.

Layers that have been formed during solidification were present in some of the casts. The layers were a result of low flow rate of silicon into the mould during the experiment. In Figure 5.12 there is an illustration explaining how the layers were formed.

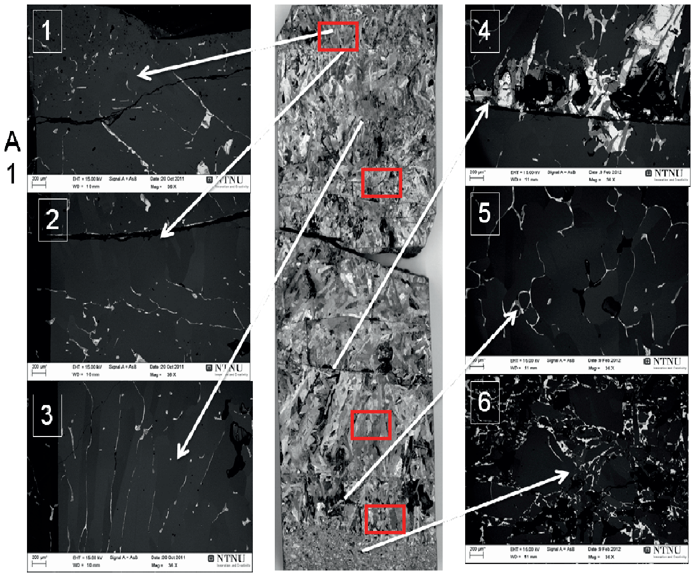

Figure 5.11: Selected SEM micrographs illustrating the distribution of intermetallic phases in sample A1. Red squares contain areas that have been magnified in Figure B.1. Micrograph 2 and 4 illustrate layers and micrograph 6 remelted fines.

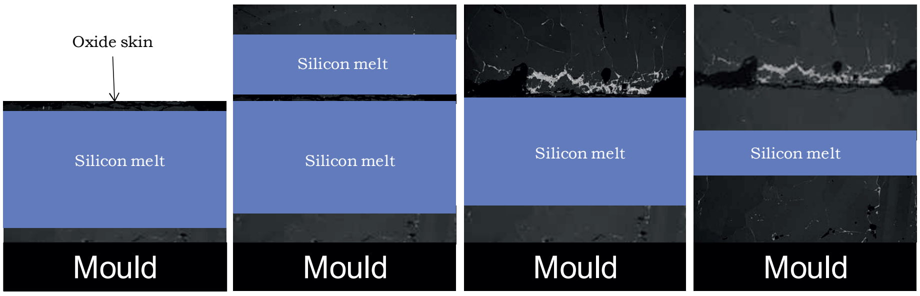

Figure 5.12: Illustration of the formation of a layer during casting. Left to right, SEM micrographs collected from copper plate experiment 3.5.

1) The silicon starts to solidify from the bottom once the melt touches the mould. Due to the low flow, a silicon skin forms at the surface before new melt arrives, illustration to the left Figure 5.12. This skin consists of an oxidized layer of silicon.

2) New melt arrives on top of the skin, and when the mould is filled the melt also start to solidify from the top surface.

3) The solidifying front from the top surface acts as a “snow shovel” where alloying elements are pushed together with the front due to a higher solubility in the melt. When the front reaches the oxide skin the alloying elements are not able to pass and will precipitate along the oxide skin. This is also illustrated in micrographs 2 and 4, Figure 5.11.

4) New grains will nucleate and start to grow in the direction opposite to the heat flow. Below the layer depicted in Figure 5.12 the silicon melt will be depleted on alloying elements compared to above the layer since the enriched melt was stopped by the layer.

The observed layers reduced the average grain size in the cast since new grains started to grow on the other side of a layer. The layer also reduced the amount of alloying/trace elements in the area where the solidifying fronts met since they could not cross the layer boundary. A new enrichment of the liquid started below the layer (or above depending on the direction of the heat flow).

In the upper picture to the right in Figure B.1, an area between two layers is seen. This was the area with the smallest distance between two layers and the effect was numerous small sized grains. In the lower left picture the grains were much larger. This was from the area where the distance between two layers was largest. This area was also filled with melt at an early stage in the casting, and it was the last to solidify due to poor heat conduction through the bottom part and the long distance to the top.

Comparing the grain distribution from experiment A1 to that of sample B, MG-Si2, where no pronounced layers were formed, it was seen that the grains in general were longer in MG-Si2 when no layers were present to act as a barrier to growth, Figure B.2. Another distinction between the two casts, A1 and MG-Si2, was the refining step prior to casting for MG-Si2. During a reefing step impurity particles such as silicon carbide can be captured by the slag phase or stick to the ladle walls as described by **Klevan** (1997). Also potential slag from the furnace can be retained in the ladle. This means that a casting procedure with no prior refining would have a melt containing more impurity particles. This was confirmed from the carbon analysis given in Section 5.6, Alloy A contained more carbon than MG-Si2. The SiC particles can act as a source for heterogeneous nucleation and stabilize the growth of equiaxed grains and thus yield a finer grain distribution. This was observed by **Mangelinck- Noêl and Duffar** (2008) who registered a large number of equiaxed grains in a polycrystalline silicon wafer. SEM observations correlated this to the presence of SiC in equiaxed regions.

Prior to examining the thermal history and the grain size of the two casts it was assumed that A1, due to an increased height (approximately 16.6 cm vs. 10 cm) and a smaller size of fines (0-2 mm vs. 10- 15 mm), would have a lower cooling rate and that this would yield a larger average grain size compared to MG-Si2. It seems however that time to fill the mould (15 minutes vs. 2 minutes) and the lack of a refining step decreased the grain size in portions of the cast. For the MG-Si cast a rapid filling of the mould led to a situation where less heat was removed during filling and more superheat and latent heat had to be removed after filling. For alloy A, a low flow rate reduced the temperature of the melt and in the regions where layers were thin, the distance to the top surface of the layer was short, which facilitated the heat transport. For a layer to form, the temperature in the melt must have been low so that the surface could solidify before new melt arrived on top. **Hunt** (1984) describes that in small castings low poring temperature is often used to promote equiaxed growth.

Another distinction between the two casts was the increased amount of alloying elements in alloy A compared to MG-Si2. The melt contained around 8 % alloying elements and if a silicon grain was detached from its parent crystal and found itself in a constitutionally undercooled region an equiaxed grain could grow. The effect was illustrated by the Cyberstar furnace experiment. All ingots had the same thermal history, but only Ingot 4, containing EG-Si consisted of mainly columnar grains. In the ingots that contained MG-Si the concentration of alloying elements at the interface increased so much that constitutionally undercooled regions developed which facilitated equiaxed growth. It was observed that columnar grains advanced further close to the furnace wall than close to the middle of the furnace. This supports the observations from the chemical analysis; the front was not been planar during solidification.

For the copper plate experiments when no layers were present the grains were more or less able to grow until the two fronts met. The effect of the layers was a reduction in the average grain length. This was seen for the 3 cm and 5 cm samples that were examined, there was not a distinct difference in grain size/grain length between these copper plate experiments as a consequence of the layers, as seen from Table 5.3 and Figure B.4 to Figure B.8.

Correlating the thermal history obtained from the COMSOL model of the industrial cast, illustrated in Figure 4.21, to the grain size in the industrial cast, it was observed that in areas where the heat was removed rapid initially, grains were smaller, Figure B.3. These were the areas close to the top and bottom surfaces. As seen from Figure 4.21 the subsequent cooling was slower since heat from the rest of the cast had to be transported through these areas. In areas where the initial cooling was slow, while the subsequent cooling was rapid grain coarsening was observed. This supports the assumption that the grain coarsening of the silicon grains took place at temperatures close to the melting point of silicon.

When observing etched silicon samples, numerous twin boundaries were revealed illustrating that growth by twinning was a common growth mechanism in the samples. Some of these boundaries can easily be seen from Figure B.1 to Figure B.8. Twin boundaries were also observed in samples cut normal to the growth direction.

In Table 5.3, both average grain size and average cooling rate in the region where the silicon grain size was determined, was presented for a selection of the experiments. The values for A1, 2.2 (A2), B and 2.1 are superimposed on the results collected from **Forwald** (1997) in Figure 5.13.

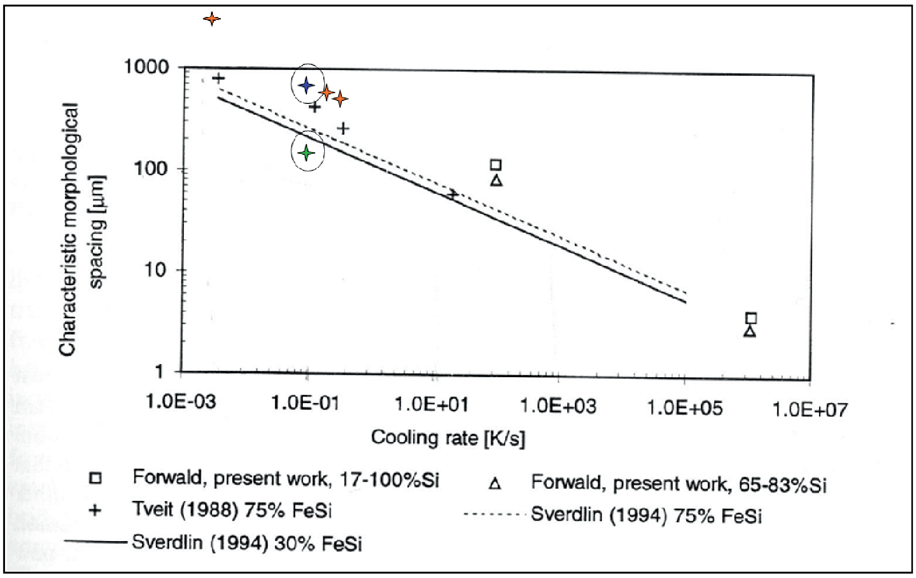

Figure 5.13: Data collected from **Forwald** (1997) and superimposed data from a few of the experiments in this work, B, A2, A1, 2.1. Stars in circles are both of sample B, MG-Si2 Industrial, but the grain size in the lower circle was determined by EBSD, electron backscatter diffraction. Note the large deviation between the methods.

It can be seen from the figure that the calculated values from the circular intercept method were larger than the given from earlier work. The average grain size of a part of sample B obtained from electron backscatter diffraction, EBSD, was compared to the grain size obtained by the circular intercept method: 185 ± 292 µm vs. 890 ± 760 µm. The EBSD value was obtained with the linear intercept method. The results from the EBSD are given in Table B.1, Appendix B. Some of the limitations concerning the determination of grain size and cooling rate were discussed in Chapter 3, and these uncertainties might have contributed to the deviation from earlier work. In addition, as seen from among others experiment A1 and Cyberstar furnace experiment, several factors contributed to the final grain distribution, not only the cooling rate. This means that a simple linear relationship between cooling rate and grain size will not be able give the whole picture. The factors that were considered to be of highest importance and their effect are listed in Table 5.4. The final grain distribution was a result of interplay between the factors listed in the table. If a given grain distribution is the aim, these factors must be controlled.

Table 5.4: Main factors that determined the grain size of the castings.

	High	**Low**
Cooling rate	A large grain population was able to grow- the **average grains size was reduced**.	Grains that removed heat most efficiently outgrew other grains. A grain coarsening took place and **average grain size increased.**
Particles in the melt, such as SiC	Inclusions could have reduced the barrier to nucleation - more grains nucleated -**grain refinement.**	Less heterogeneous nucleation.
Layers	Layers acted as a barrier to growth. **Average grain size reduced.**	Disregarding equiaxed growth. Grains grew until the solidifying fronts met– result was **increased grain length.**
Alloying elements	Constitutional cooling- created undercooled regions where detached silicon grains were stable to grow with the result **of more equiaxed grains.** Breakdown of a planar front in directional solidification.	If the temperature gradient at the interface was positive a plane front would be stable for pure materials.
Temperature in melt	Silicon grains that were detached from their parent crystal would melt back in contact with the liquid when $T>T_M$. The result was an **increase in average** grain size.	Low melt temperature increased the possibility that a detached silicon grain could grow. Less heat needed to be removed. Result- **Decreased average grain size.**

The basis for the theory concerning the factors given in the table was given in Chapter 2. It can be seen that the cooling rate, heterogeneous nucleation, constitutional undercooling and temperature in the melt are all factors that are well described in the literature. Layer casting is also a method that has been used in industry for a while to obtain a smaller grain size. However in the literature search no study has been found describing how the layers act as a boundary for inclusions and intermetallic phases. This is an important aspect when considering the segregation and distribution of intermetallic phases in the cast.

5.3 Distribution and identification of the intermetallic phases

In the following it will be described how the distribution of intermetallic phases and the type of intermetallic phases formed differs in the experiments as a result of the composition, thermal history and casting method.

5.3.1 Distribution of intermetallic phases

The distribution of intermetallic phases changed with the cooling rate and affected the structure of the cast silicon. This was observed by comparing SEM micrographs of MG-Si2 industrial and MG-Si2 copper plate 1.5 cm, Appendix B, Figure B.11 and B.14. More grain boundaries were covered with intermetallic phases in the 1.5 copper plate case, Figure B.14. This observation has also been done by authors such as **Margaria** (1996), **Bullon** (2007) for silicon cast onto a water cooled copper plate.

When grains are small, the total surface area of the grains will be larger and the intermetallic phases can distribute over a larger surface. In the direct synthesis, the number of sites attacked is determined by the length of the grains associated with intermetallics according to **Baud and Margaria** (1995).

One reason for the increased surface area in contact with silicon effect can be found considering surface energy. Simplified it can be said that the surface energy is a result of an imbalance in the intermolecular forces that act on the molecules in the boundary between two phases. In the bulk there would be no such imbalance and the sum of the forces acting on the molecules is zero. For molecules at the surface this imbalance causes the molecules to be drawn towards the bulk, **Mørk** (1997). For a remaining melt it will be preferential that the ratio surface area in contact with silicon matrix, A, and the bulk volume, V, is low, assuming that the contact angle, θ, is larger than 0 °. The result would be that at low cooling rates A/V is low, while at higher cooling rates were the molecules will not have time to rearrange, A/V increases. In this work it was assumed that the rearrangement stops when the intermetallic phases have solidified, which was assumed to be 600 ° C.

Observing the 1.5 cm, 3 and 5 cm casts, Figure 5.14, it was seen that compared to the industrial cast, utilizing a copper plate with water cooling only changed the distribution of intermetallic phases significantly if the height of the cast was reduced to 1.5 cm. This can also be seen from B.12-B.14, Appendix B. The COMSOL model compared casts of height 1.5, 3, 5 and 10 cm, cast in an industrial mould. It was seen that with increased thickness the time before the intermetallic phases (assumed to be 600 °) have solidified would increase from 4.2 minutes for the 1.5 cm cast to 10, 18 and 45 minutes for a 3, 5 and 10 cm cast respectively, Figure 4.20. This implies that an increased thickness of the cast increased the time the remaining melt had to rearrange.

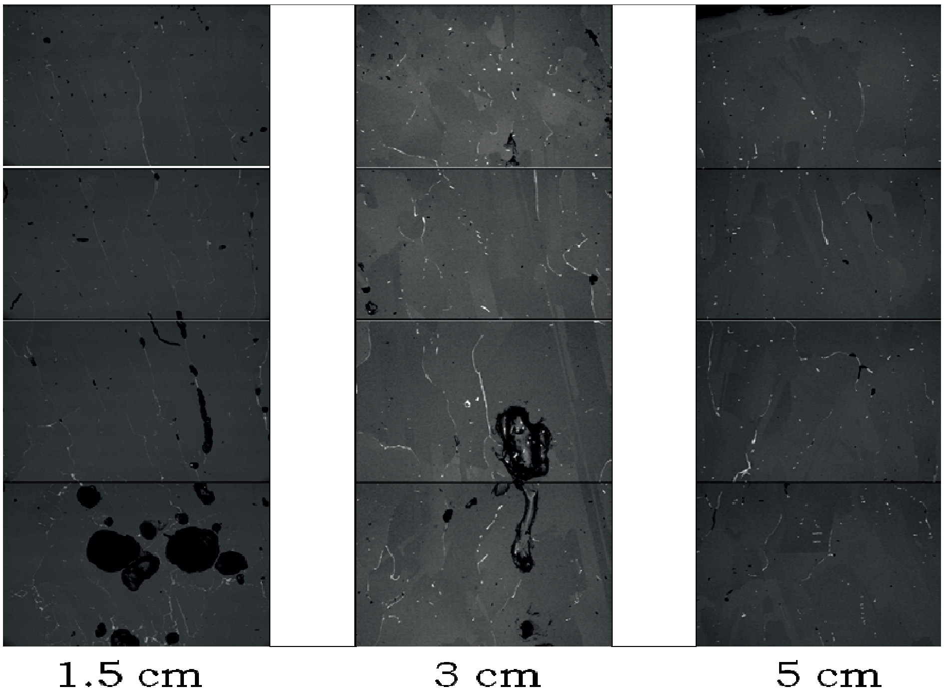

Figure 5.14: Comparison of SEM micrographs, copper plate experiments, 3.1 (1.5 cm), 3.3 (3 cm) and 3.5 (5 cm). A faster cooling combined with a more homogeneous temperature profile for the 1.5 cm cast resulted in a more homogeneous distribution of intermetallic phases for the 1.5 cm cast compared to the 3 and 5 cm casts. The black spots in the micrographs are pores and intermetallic phases that were removed during sample preparation.

The COMSOL model was used to compare different positions in the 10 cm industrial MG-Si2 cast, Figure 4.21. It was observed that in areas where the heat initially was removed fast, the subsequent cooling was slow since heat from the rest of the cast was transported through these areas. In these areas the intermetallic phases were rounder due to a longer time to rearrange. In areas where the initial cooling was slow and the subsequent cooling was rapid the intermetallic phases are more evenly distributed in the grain boundaries, see Figure 5.15.

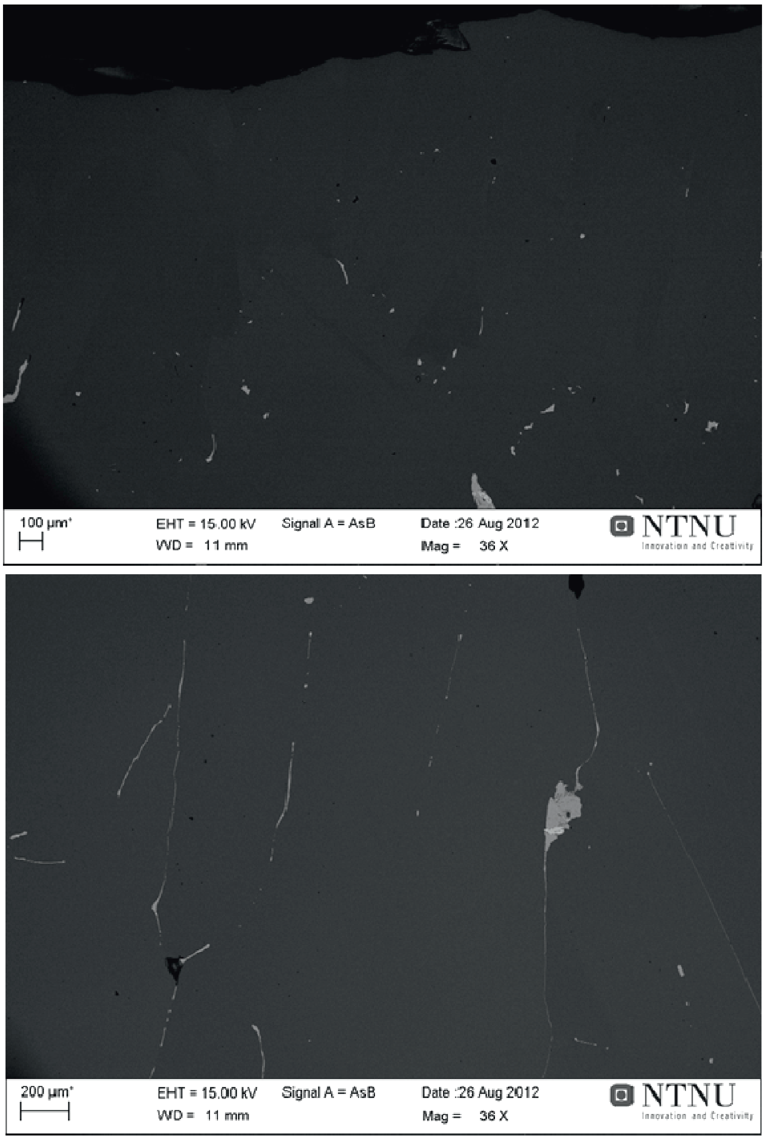

Figure 5.15: Microstructure top part, upper micrograph, and 6 cm from top, lower micrograph, sample B, MG-Si2- Industrial.

The results support the observations done by **Rong** (1992): the distribution of the intermetallic phases can be altered below the temperature were primary silicon solidifies and not the hypothesis by **Margaria** (1994): the distribution of the intermetallic phases is dependent on the cooling rate where the primary silicon grain size is defined.

The shape will also depend on the amount of alloying elements. In Figure B.9 and Figure B.10 micrographs from A1 and A2 are compared. A2 reached 600 °C around 8 hours later than A1. However all intermetallic phases were not found as round particles. The phases were larger, but the area they could distribute themselves might have been limited by the already solidified primary silicon grains. This implies that the shape with the lowest A/V ratio was not possible.

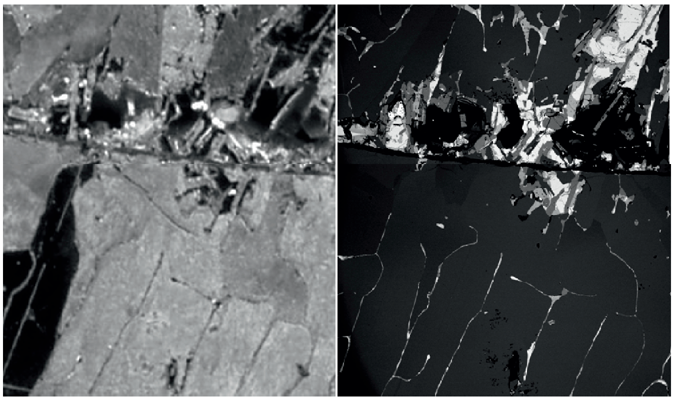

Figure 5.16: Etched sample, left, and SEM micrographs, right, of the same area, sample A1. It is seen that the intermetallics mainly are found in the silicon grain boundaries and not in the silicon matrix. An accumulation of intermetallic phases is seen above the layer.

In Figure 5.16 a segment of sample (3 mm x 1.5mm) of A1 after etching is illustrated together with SEM micrographs from the same area. From the figure it is seen that the intermetallic phases generally were found in the grain boundaries and not in the silicon matrix. In the figure a layer is also seen, and above the layer there have been an accumulation of intermetallic phases where it was not possible to pass thorough the layer. SEM micrographs from the other experiments have also been compared to etched samples and the intermetallic phases were in general found in the grain boundaries.

5.3.2 Identification of the intermetallic phases

In Table 5.5 an overview of the different intermetallic phases observed in the experiments is illustrated. For MG-Si2 and MG-Si1 **Image J**

1.46r (2013) was utilized to determine the amount of each intermetallic phase. However the contrast of several phases was similar so it was not possible to separate them by contrast in a reproducible manner. A more qualitative approach was applied which described the major and minor intermetallic phases based on coupled SEM/EPMA observations.

Table 5.5: Intermetallic phases in the different experiments. **X**, x, (x), indicating a major phase- a minor phase- or an observed, but rare phase, respectively. The labelling of the experiments was given in Table 5.2.

Phase	**Experiment**							
	A1	**A2**	**MG-Si2**	**2.1-2.3**	**3.1-3.5**	**C1**	**C2**	**C3**
$Al_6CaFe_4Si_8$	**X**		**X**	(x)	(x)	x	x	x
Al_2CaSi_2	**X**	**X**	(x)					
HT-(Al)$FeSi_2$			**X**	**X**	**X**	x	x	x
Al_3FeSi_2	**X**	**X**	x	x	x	x	x	x
$Al_6Fe_4Si_6$			x	x	**X**	x	x	x
(Al)$FeSi_{2.4}Ti$			x	**X**	**X**	x	x	x
Al-Fe-Si-Ti	x	(x)	(x)			(x)		(x)
(Al,Fe)$SiTi_2$						(x)	(x)	(x)
(Al,Zr)$SiTi_2$	(x)	x						
Al-Si-Ba	x	x						
Al phase	x	x						
(Ce,La,Nd)Al-Si		(x)						

Samples from all experiments were investigated by electron probe micro analysis, EPMA. In total, more than 700 point analysis were performed, and in Appendix C the mean composition of the main intermetallic phases observed in all the experiments is given. The basis for the EPMA was given in Section 3.7.6 and some of the uncertainties with the method were discussed in Section 3.8. Most of the intermetallic phases observed are well documented in the literature and were listed in Chapter 2. This yields for the HT-(Al)$FeSi_2$ phase the ternary Al-Fe-Si phases, Al_3FeSi_2 $Al_6Fe_4Si_6$, the calcium phases Al_2CaSi_2 and $Al_6CaFe_4Si_8$, and also the titanium phases (Al)$FeSi_2Ti$ and Si_2Ti.

Examining the intermetallic phases in Appendix C, it was seen that there was a variation from experiment to experiment. Besides measurement uncertainty, the reason could be that some elements occupied the same lattice positions. This could be the case for aluminium and silicon and this led to dissolution of aluminium in all phases. It has been noted that the Al_3FeSi_2 phase has a larger compositional range than the $Al_6Fe_4Si_6$ phase, e.g. **Dubrous and Anglezio** (1990). This is also seen from Appendix C, the standard deviation was larger for the Al_3FeSi_2 phase than the $Al_6Fe_4Si_6$ phase. When the average composition of the intermetallic phases from each experiment was compared, it was noted that the aluminium content in the Al_3FeSi_2 phase for alloy A was higher than in the metallurgical grade silicon. In experiments A1 and A2 the average amount was 48.9 and 51.7 at % respectively, while for MG-Si2 industrial the average amount was 44.5 at %. A higher amount of aluminium in alloy A was probably the reason for this.

Figure 5.17 to Figure 5.21 present SEM micrographs of intermetallic phases frequently observed in the experiments.

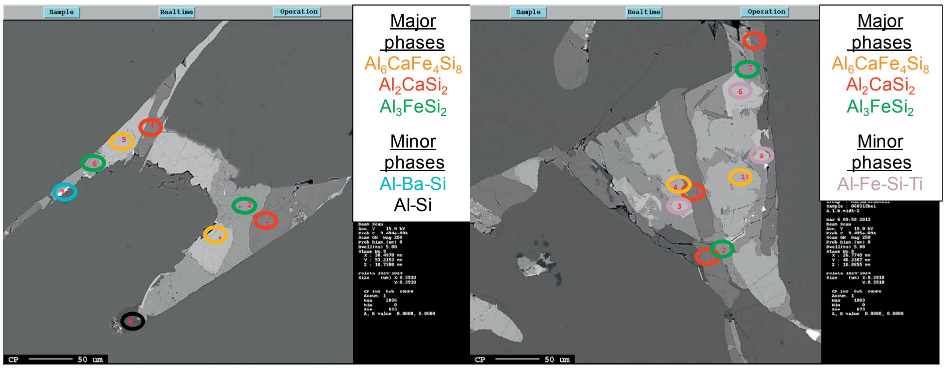

Figure 5.17: SEM micrographs sample A1.

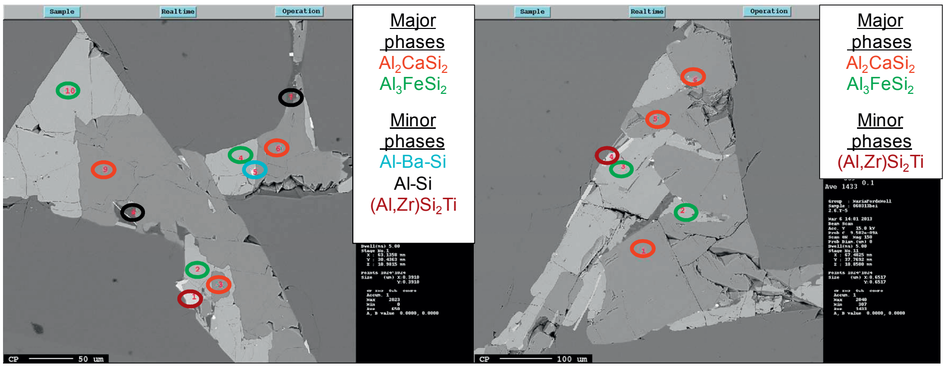

Figure 5.18: SEM micrographs sample 2.6, experiment A2.

For sample A1 three phases dominated. These were the phases containing Ca, $Al_6CaFe_4Si_8$ and Al_2CaSi_2, and one Al-Fe-Si phase, namely Al_3FeSi_2. However in the samples examined from experiment A2, 2.2 and 2.6, the quaternary phase was absent. (Figure 3.5 illustrated where the samples were extracted). Sample 2.4 was not analysed by EPMA, but observing the contrast in the micrographs one phase appeared to be missing here as well. When the cooling rate was reduced for alloy A, experiment A2, more Al_2CaSi_2 was found. This experiment indicated that the alloy was in a compositional range where the ternary phase was the thermodynamically stable phase. In the Cyberstar furnace experiment, the reduced cooling rate did not yield the same effect, no Al_2CaSi_2 was observed. In this compositional range $Al_6CaFe_4Si_8$ was the stable phase with both a high and low cooling rate, as described by **Margaria** (1994).

The main phases observed for the metallurgical grade silicon were HT-$(Al)FeSi_2$, $Al_6CaFe_4Si_8$, $Al_6Fe_4Si_6$, Al_3FeSi_2 and $(Al)FeSi_2Ti$. According to **Krendelsberger** (2007), the ternary phases present in the Al-Fe-Si phases are formed by peritectic reactions. This was also mentioned by **Margaria** (1994) who described that equilibrium calculations of a MG-Si system give the solidification route $Si \rightarrow HT\text{-}(Al)FeSi_2 \rightarrow Al_6Fe_4Si_6$. In addition Al_3FeSi_2 phase was observed in experimental samples, which was attributed to incomplete peritectic reactions. The phases observed in the MG-Si system are in accordance with Figure 2.19, given in **Dubrous and Anglezio** (1990).

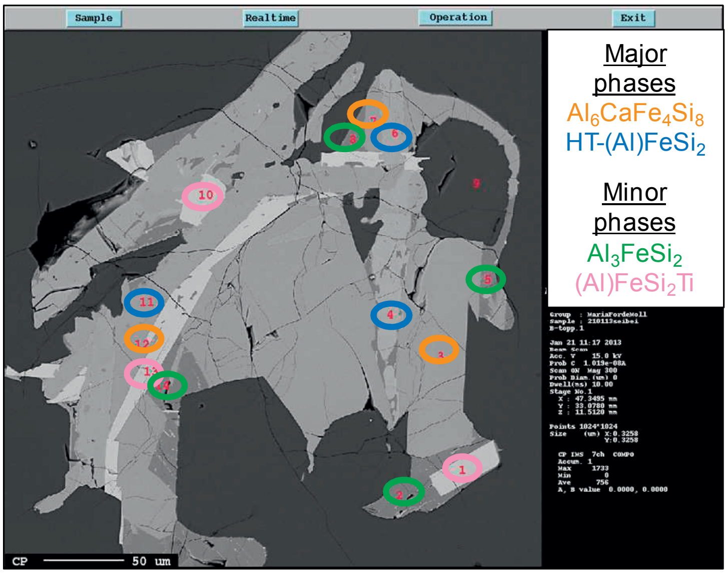

Figure 5.19: SEM micrograph sample B, experiment MG-Si2.

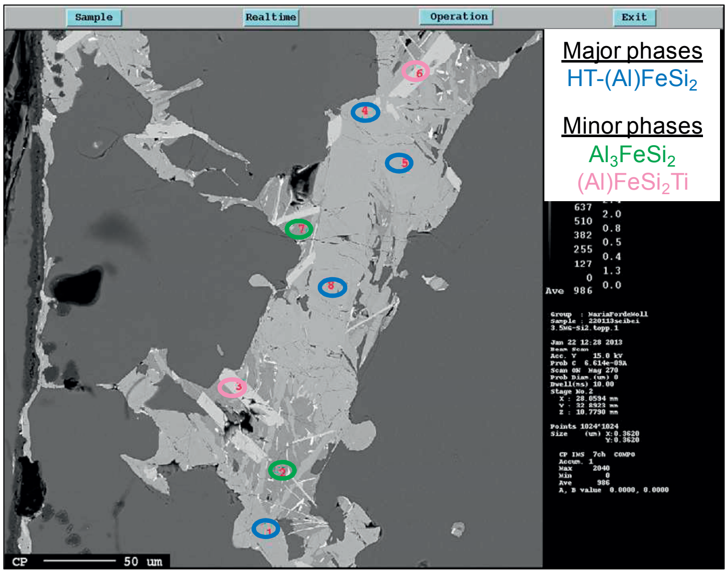

Figure 5.20: SEM micrographs sample 3.5, experiment 3.5, MG-Si2.

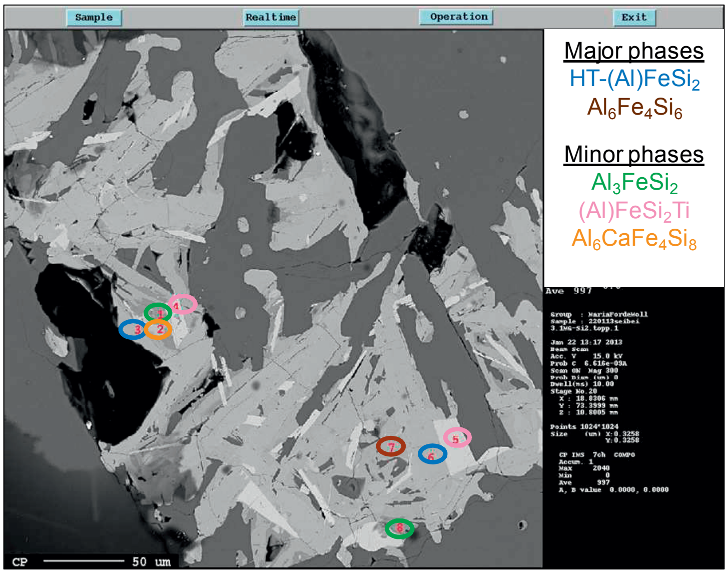

```
Ave  997

Group  : MariaFordeMoll
Sample : 220113seibei
3.1MG-Si2.topp.1

Jan 22 13:17 2013
Beam Scan
Acc. V    15.0 kV
Prob C  6.616e-09A
Scan ON  Mag 300
Prob Diam.(um) 0
Dwell(ms) 10.00
Stage No.20
  X : 18.8306 mm
  Y : 73.3999 mm
  Z : 10.8005 mm

Points 1024*1024
Size    (um) X:0.3258
             Y:0.3258

  CP IMS  7ch  COMPO
  Accum. 1
  Max     2040
  Min        0
  Ave      997
  A, B value  0.0000, 0.0000
```

Figure 5.21: SEM micrographs sample 3.3, experiment 3.3, MG-Si2.

The main distinction between the phases observed in the industrial experiment, MG-Si2 and the copper plate experiments, was the deficiency of calcium phases. As described in Section 5.1.4 calcium evaporated due to a high vapour pressure. The amount of aluminium was also reduced and this reduced the amount of the ternary aluminium phases. From the chemical analysis it was seen that the Al content (and the Al/Fe ratio) increased in the order MG-Si1< MG-Si2 copper plate < MG-Si2 Industrial. MG-Si2 industrial contained the highest amount of Al_3FeSi_2 which was the phase richest in aluminium, while copper plate MG-Si1 contained the least.

For the Cyberstar furnace experiments all the phases observed in the parent material were observed here as well except for the ternary calcium phase. The segregation from bottom to top of the ingot was significant, as seen from Figure 5.9. The bottom samples, extracted as illustrated in Figure 3.13, contained no particles. The Al_3FeSi_2 phase was hardly observed in the middle samples, but frequently in the top samples. There were also more trace elements in the phases at top than in the middle samples.

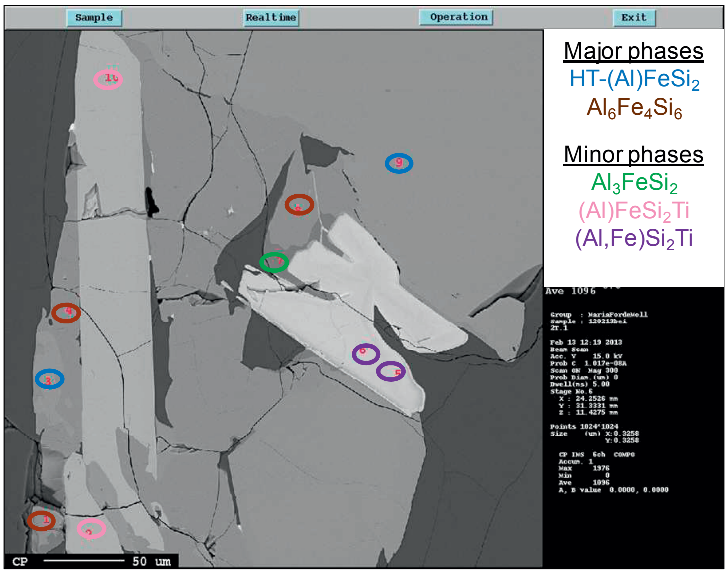

```
Ave  1096

Group  : MariaFordeMoll
Sample : 120213bei
2T.1

Feb 13 12:19 2013
Beam Scan
Acc. V    15.0 kV
Prob C  1.017e-08A
Scan ON  Mag 300
Prob Diam.(um) 0
Dwell(ms) 5.00
Stage No.6
  X : 24.2526 mm
  Y : 31.3331 mm
  Z : 11.4275 mm

Points 1024*1024
Size    (um) X:0.3258
             Y:0.3258

  CP IMS  6ch  COMPO
  Accum. 1
  Max     1976
  Min        0
  Ave     1096
  A, B value  0.0000, 0.0000
```

Figure 5.22: SEM micrographs sample 2T-Ingot 2, MG-Si1, Cyberstar furnace experiment.

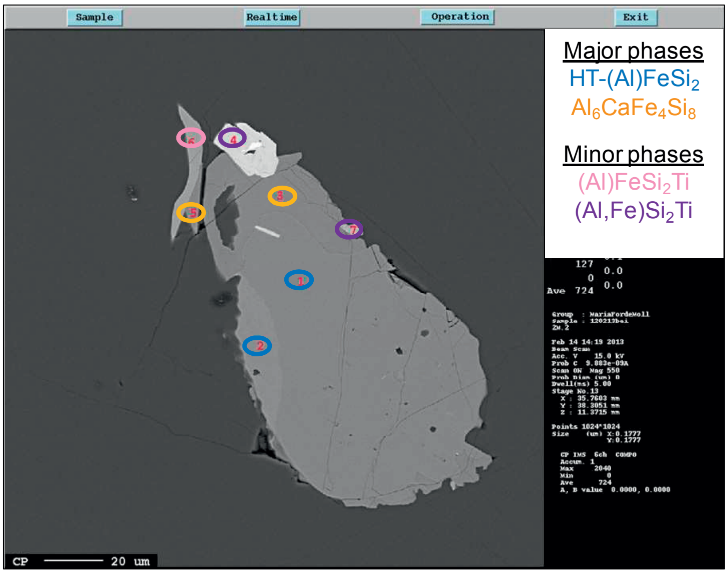

```
    127  0.0
      0  0.0
Ave  724

Group  : MariaFordeMoll
Sample : 120213bei
2M.2

Feb 14 14:19 2013
Beam Scan
Acc. V    15.0 kV
Prob C  9.883e-09A
Scan ON  Mag 550
Prob Diam.(um) 0
Dwell(ms) 5.00
Stage No.13
  X : 35.7603 mm
  Y : 38.3051 mm
  Z : 11.3715 mm

Points 1024*1024
Size    (um) X:0.1777
             Y:0.1777

  CP IMS  6ch  COMPO
  Accum. 1
  Max     2040
  Min        0
  Ave      724
  A, B value  0.0000, 0.0000
```

Figure 5.23: SEM micrographs sample 2M, MG-Si1, Cyberstar furnace experiment.

The type of intermetallic that forms mainly depended on the chemistry, but as noted an increased cooling rate could give incomplete reactions causing the intermetallic phases observed to differ from the equilibrium phases. When starting at a low aluminium content only the HT-(Al)FeSi$_2$

phase was formed. Increasing the Al/Fe ratio more Al_6FeSi_6 is formed in addition to Al_3FeSi_2. This was in accordance with the phase diagram given in Figure 2.18 and Figure 2.19 for iron content 0.4 wt % which is a typical MG Silicon level. At a low Ca/Al content only the $Al_6CaFe_4Si_8$ was observed, but with increasing the Ca/Al ratio Al_2CaSi_2 also formed.

In the slowly cooled samples, A2 and Cyberstar, an increased amount of titanium rich phases were observed, see Appendix C. These phases also contained an increased amount of trace elements, such as vanadium, zircon and chromium. This indicated that the decreased cooling rate led to a better purification of the silicon matrix consistent with equation 2.11.

It was observed that the final distribution and shape of the intermetallic phases depended on the time the remaining melt/ intermetallic phases had to rearrange, solidification layers present, available space between the silicon grains and amount of alloying elements

5.4 Distribution of trace elements in the intermetallic phases

The mean atomic % of the main intermetallic phases is presented in Appendix C. In addition to the main constituents of the intermetallic phases, Al, Ca, Fe, Si and Ti, a few minor elements were present in low concentrations in these phases. A trend predicting the intermetallic phase a given trace element preferred was observed from these data. In Appendix C, Figure C.1 to Figure C.6, the amount of trace element, ppmw, in the main intermetallic phases is presented. A summary of the results from Appendix C will be given below for a selection of trace elements. In the discussion regarding trace elements the three intermetallic phases that contained the highest average concentration of a given trace element are tabulated. Since the average differs in the experiments, the experiment where the intermetallic phase contained the highest average value is also listed.

The micro probe analysis, EPMA, of the intermetallic phase confirmed that most elements had a preference for the intermetallic phases and not the bulk matrix. As will be seen in the following, most trace elements were present in a concentration range of 10 times to several 100 times higher in the intermetallic phases.

Based on a few simple assumptions a material balance was done predicting the amount of each intermetallic phase formed in the MG-Si2 industrial. Two things were known from the EPMA analysis of this system:

1) All the calcium went into the quaternary $Al_6CaFe_4Si_8$ (assumed that only a negligible amount of Al_2CaSi_2 was formed).
2) All the titanium went into the $FeSi_2Ti$ phase.

Based on SEM micrographs it was assumed that the remaining aluminium divided itself between the ternary Al-Fe-Si phases, Al_3FeSi_2 and Al_6FeSi_6 in a 1 to 1 ratio, disregarding the fact that aluminium was also found in small portions in the HT-(Al)$FeSi_2$ phase and the $FeSi_2Ti$. Based on the average composition of MG-Si2 industrial, drawn from sample G and B1/B2, Al=0.18 wt %, Ca = 0.03 wt %, Fe= 0.4 wt % and Ti = 0.02 wt %, a mole balance was calculated as presented in Table 5.6.

Table 5.6: Amount Al, Ca, Fe, Si and Ti, mol, found in the intermetallic phases, per 100 g MG-Si2.

	Al (mol)	**Ca** (mol)	**Fe** (mol)	**Si** (mol)	**Ti** (mol)
$Al_6CaFe_4Si_8$	0.0047	**0.0008**	0.0032	0.0063	
Al_3FeSi_2	**0.0010**		0.0003	0.0007	
HT-(Al)$FeSi_2$			0.0025	0.0060	
(Al) $FeSi_2Ti$			0.0005	0.0009	**0.0005**
$Al_6Fe_4Si_6$	**0.0010**		0.0007	0.0010	

The amount of the element in question that went into a given phase was calculated from the EPMA results. The partition in % between the five main intermetallic phases in MG-Si2 industrial was presented in Figure 5.24. The figure will be discussed in connection with the trace elements.

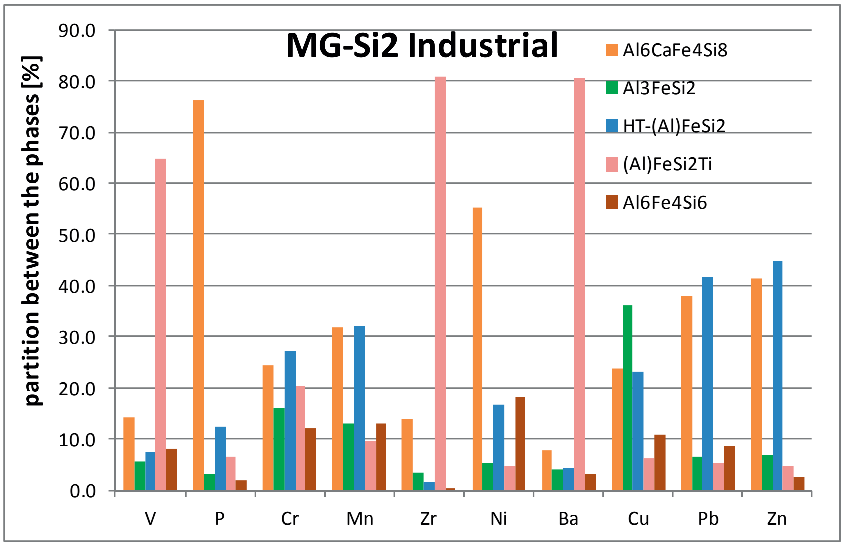

Figure 5.24: Partition of trace elements between the main intermetallic phases. Bulk analysis: Al=0.18 wt %, Ca = 0.03 wt %, Fe= 0.4 wt % and Ti = 0.02 wt %.

By comparing the total amount of trace elements calculated from the EPMA results with the amount attained from the XRF analysis a partition between the silicon matrix and the intermetallic was calculated, Figure 5.25.

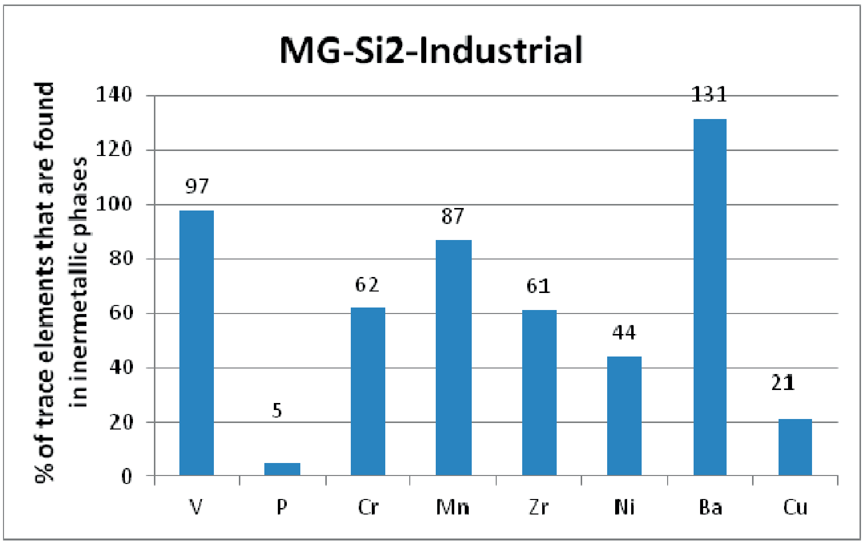

Figure 5.25: % of trace elements found in the intermetallic phases compared to bulk composition. Due to uncertainty in EPMA and the bulk analysis the mass balance gave more than 100 % for barium. Loss during sample preparation and solid state diffusion could have been reasons for to low values.

From the segregation pattern given in Section 5.1 one would expect that most of the elements with low distribution coefficients would be removed efficiently from the matrix. It was seen that of the elements listed in Figure 5.25, phosphorus did not segregate to the same extent as the main alloying elements, but still some segregation was seen. The low removal of phosphorus could be a result of a higher distribution coefficient, but probably also a result of loss during sample preparation. This is explained in Section 5.5.2.

Transition elements, especially the 3d elements, are known to have high diffusion coefficients in silicon **Ceccaroli and Lohne** (2003) and increase with an increasing atomic number. In silicon the high diffusions coefficients of the 3d elements are explained by an interstitial diffusion mechanism. In most metal alloys diffusion occurs by interstitial diffusion and due to their small size the transition elements are able to diffuse rapidly even in solid silicon. The diffusion will be a function of temperature, decreasing with decreasing temperature. Solid state diffusion could explain why the mass balance did not add up for the transition elements. In order to confirm if copper or other elements were found in the matrix or grain boundaries more investigations should be done. An alternative would be to investigate if secondary ion mass spectrometry, SIMS is applicable. The basis for the method is outlined on the website of EAG, Secondary Ion Mass Spectrometry, **SIMS** (2013). Another alternative could be a concentration profile with the EPMA.

Several analyses were performed by EPMA of the silicon matrix. Several transition elements were observed, such as Cu, Fe, Mn and V, in addition to P and Al. Large elements like wolfram, barium, lead were not found in the silicon matrix. The highest concentration was seen for iron. It was noted that the concentration in the matrix was less for the Cyberstar furnace experiments, indicating a better segregation in this experiment, while for the copper plate experiments the average iron content in the positions analysed was 1000 ppmw. This was in agreement with Equation 2.11. That states that with an increasing growth rate, the incorporation of other molecules into the matrix will increase. This indicated that “the trade-off” to obtain a smaller silicon grain size was an increased content of trace elements in the silicon matrix. Figure 5.25 revealed that the uncertainty in the EPMA analysis, the XRF analysis and the coarse assumptions in the model gave results over 100 % for barium. The barium content in the MG-Si2- industrial samples was below the detection limit of the XRF instrument and this of course affects the uncertainty of the average bulk analysis obtained. If a lower average bulk analysis than the actual value was used in the calculation, this explains why the calculation predicts more barium to be present in the intermetallic phases than what was available. The uncertainty in the XRF analysis, EPMA analysis and loss during sample preparation means that it was not possible to pin-point the partition, but based on the fact that it related well to segregation and diffusion coefficients is a good illustration of the trend.

The assumptions used in the mass balance cannot be used as general assumptions for all MG-Si systems. When using the same assumptions for sample H, MG-Si2, which was taken from another cast where the calcium content was higher, the material balance fails. When all the calcium was put into the quaternary phase in this system there was no aluminium left for other phases. From the EPMA analysis of sample H, Al_3FeSi_2, $Al_6Fe_4Si_6$ and HT-(Al)$FeSi_2$ were observed in addition to the Al_2CaSi_2 phase. This was consistent with Figure 2.19, collected from **Dubrous and Anglezio** (1990); starting from the set point of sample B/G, MG-Si2 of Al = 0.18 wt % and Ca = 0.03 wt %, increasing the Ca/Al ratio leads to the formation if Al_2CaSi_2 in addition to the quaternary phase.

5.4.1 Vanadium

From the chemical analysis of MG-Si1 and MG-Si2 it was seen that vanadium was present in around 10 – 15 ppmw in the bulk material. Of all the phases examined, the highest amount of vanadium was always found in correlation with a high level of titanium. This is seen from Figure C.1 to C.6, Appendix C. The top three vanadium containing phases found are given Table 5.7. For the copper plate experiments, MG-Si2 industrial and MG-Si1 before re-melting, the only titanium phase observed was (Al)$FeSi_2Ti$. The amount of V in this phase was several hundred per cent larger than for the bulk material. The preference for the titanium phases were also seen from the material balances presented in Figure 5.24.

Table 5.7: The top three intermetallic phases containing vanadium.

Phase	**(Al,Fe)$SiTi_2$>**	**(Al,Zr) Si_2Ti >**	**(Al)$FeSi_2Ti$ >**
Maximum (experiment)	32940 ppmw (3.3 wt %) (Cyb MG -Si2/1	10700 ppmw (1.1 wt %) (Alloy A)	9400 ppmw (0.94 wt %) (Cop MG -Si2)

The effective distribution coefficient of vanadium is $4.0*10^{-6}$, Table 2.1, which means that vanadium was expected to be found in the intermetallic phases. Vanadium and titanium are neighbours in the periodic table and their similar size allows vanadium to substitute for titanium in the structure. **Callister and Rethwisch** (2007), list that a solute is allowed to substitute another atom if the difference in their atomic radii is less than about ±15 %. High vanadium content in the titanium rich phases have been described by authors such as **Margaria et al.** (1992). Vanadium, chromium, zirconium, wolfram all form stable silicides and when the Si_2Ti phase was found it was often accompanied by the presence of these elements.

5.4.2 Phosphorus

Due to its importance in solar cells several studies have been performed with the focus on removal of phosphorus from silicon.

The phosphorus content was found to be maximum in the ternary calcium phase, Al_2CaSi_2. For sample A1, the average content was 0.15 wt %, see Table 5.8. In MG-Si2 the highest content was also observed in this phase, but since this phase was hardly ever observed, in total only a negligible quantity of the total phosphorus will be found in this phase.

Table 5.8: The top three intermetallic phases containing phosphorus.

Phase	**Al_2CaSi_2 >**	**Al_2CaSi_2 >**	**$Al_6CaFe_4Si_8$>**
Maximum ppmw (experiment)	1770 ppmw (MG-Si2 Industrial)*	1550 ppmw (A1)	640 ppmw (Cyb MG-Si2)

*Only one observation

Ludwig et al. (2013) described an enrichment of phosphorus in the Al_2CaSi_2 phase when studying an Al-7 wt % Si alloy. According to **Lui et al**. (2005) phosphorus forms stable compounds with calcium and silicon but was difficult to give an exact quantitative analysis due to the reaction

$$Ca_xSi_yP_z + 6H_2O \rightarrow Ca_{x-3}Si_yP_{z-2} + 2H_3P\uparrow + 3Ca(OH)_2 \qquad (5.1)$$

The reaction can result in loss of phosphorus during the sample preparation for EPMA. This means that the amount of phosphorus in the intermetallic phase was probably higher than measured by the EPMA.

Shimpo et al. (2004) reported that alloying of calcium and subsequent leaching increased the removal of phosphorus from silicon. In total 80.4 % of the phosphorus was removed with an addition of 5 at % calcium. The main calcium phase was $CaSi_2$, and phosphorus was thought to be found as CaP_3 precipitates in correlation with the $CaSi_2$ phase. Alloying of metallurgical grade silicon was also performed by **Meteleva-Fischer et al.** (2012). They found an increased level of phosphorus in the $FeSi_2Ti$ phase after alloying, up to 0.2-0.4 wt %. No phosphorus was detected in this phase in the source MG-Si before alloying. The amount of P in the $CaSi_2$ phase did not increase and they suggested that $CaSi_2$ had an intermediate role in the removal of phosphorus from MG-Si. In this work the average content of phosphorus was quite similar in the titanium and the quaternary calcium phase for the MG-Si2 industrial case, ranging from 100 to 200 ppma. Based on the mass balance, more $Al_6CaFe_4Si_8$ was formed compared to the titanium phase, as seen in Figure 5.19. This means that in total more phosphorus will be found in this calcium phase than in the titanium phase. For the copper plate and the Cyberstar furnace experiments it was clear from the chemical analysis that calcium had evaporated prior to and during casting which led to less $Al_6CaFe_4Si_8$ in the casts. The statement above was therefore not valid here. It seems that if no additional alloying elements were added it was difficult to accumulate phosphorus to a great extent in the intermetallic phases.

5.4.3 Chromium

As much as 1.2 wt % Cr was observed for the titanium rich phase $(Al,Fe)SiTi_2$ found in Cyberstar MG-Si2 and MG-Si1 samples. For the metallurgical type silicon used the main titanium phase was $(Al)FeSi_2Ti$, and an average of 0.2 wt % Cr was observed in this phase in MG-Si2 copper plate experiments. The ternary aluminium phase Al_3FeSi_2 also contained up to 0.13 wt % Cr. In general all intermetallic phases in the metallurgical grade silicon used contained 20 to 1200 X more Cr than the bulk. For alloy A the bulk concentration was not known and the amount of Cr was lower in the intermetallic phases. This could have been due to the formation of some chromium rich phases, which would have reduced the amount available for the other phases.

Table 5.9: The top three intermetallic phases containing chromium.

Phase	**$(Al,Fe)SiTi_2$>**	**$(Al)FeSi_2Ti$ >**	**Al_3FeSi_2**
Maximum (experiment)	12060 ppmw (Cyb MG -Si2/1)	2090 ppmw (Cop MG -Si2)	1340ppmw (Cop MG -Si2)

5.4.4 Manganese

Table 5.10: The top three intermetallic phases containing manganese.

Phase	**Al_3FeSi_2>**	**(Al)$FeSi_2Ti$ >**	**$Al_6Fe_4Si_6$**
Maximum (experiment)	117200 ppmw (Cyb MG –Si1)	7790 ppmw (Cyb MG -Si2)	6820 ppmw (Cop MG -Si21

Except for the industrial MG-Si2 experiment, the highest content of manganese was always found in connection with the ternary Al_3FeSi_2 phase. The bulk material, MG-Si2, contained around 50 ppmw Mn, which made it the main trace element. Manganese easily substitutes for iron and this led to its presence in all iron rich phases. In the phases that contained only minor amounts of iron such as Al_2CaSi_2, Al-Si, Al-Si (Ce,La,Nd) and Al-Ba-Si, manganese was hardly present, see Appendix C. In total, based on the material balance outlined for MG-Si, almost equal amounts of manganese went into the quaternary calcium phase and the HT-(Al)$FeSi_2$ phase, while due to a lower frequency of the Al_3FeSi_2 phase, in total less manganese was found here.

5.4.5 Zirconium

Table 5.11: The top three intermetallic phases containing zirconium.

Phase	**(Al,Zr) Si_2Ti>**	**(Al)$FeSi_2Ti$ >**	**Al-Fe-Si-Ti**
Maximum (experiment)	77763 ppmw (Alloy A)	13914 ppmw (Cyb MG-Si2)	7595 ppmw A1/A2

As for vanadium the maximum content of zirconium was found in the titanium rich phases. Both Si_2Ti and Si_2Zr are stable silicides with an orthorhombic crystal structure (**Maex and van Rossum**, 1995). This could explain the ease of substitution between Ti and Zr in the structure. There was almost no zirconium related to the phases that only contained Al, Fe and Si, see Appendix C. Zr is close to titanium in the periodic table and based on atomic size considerations it could substitute for titanium.

5.4.6 Nickel

The maximum content of nickel alternated in the experiments between the quaternary calcium phase, $Al_6CaFe_4Si_8$ and the two ternary aluminium phases, Al_3FeSi_2 and $Al_6Fe_4Si_6$. From the mass balance between 44- 70 % nickel was removed from the matrix, but as stated earlier the mass balance only gave a trend. Considering the low distribution coefficient of nickel, Table 2.1, one should expect most of the nickel to be found in the intermetallic phases. Nickel is one of the 3d transition elements, with the high diffusion coefficient in solid silicon

(**Ceccaroli and Lohne**, 2003) and it was suspected that some nickel diffused into the silicon matrix or grain boundaries.

Table 5.12: The top three intermetallic phases containing nickel.

Phase	**$Al_6CaFe_4Si_8$>**	**Al_3FeSi_2>**	**$Al_6Fe_4Si_6$**
Maximum (experiment)	8282 ppmw (Cop-MG-Si2)	3533 ppmw (Cop-MG-Si1)	1837 ppmw (Cop-MG-Si1)

Rong (1992) described that an increase in nickel content can be seen in correlation with an increase in the vanadium content. This was not observed in this work.

5.4.7 Barium

What seemed to be a distinct barium phase was formed in the case of alloy A. A theoretical value of the distribution coefficient of barium was not found, but barium is a large element and it will have problems dissolving in the other intermetallic phases in high concentrations as well as in silicon. If the solubility limit in the intermetallic phases was reached a new barium phase would be formed. In the metallurgical grade silicon this Al-Ba-Si phase was not observed. Hardly any barium was found in correlation with other phases than titanium rich phases. The exceptions were the Al_2CaSi_2 and the Al_3FeSi_2 phases in alloy A, as seen from Appendix C. This was attributed to higher barium content in alloy A compared to MG-Si2, although this was just an assumption that has not been confirmed by chemical analysis.

Table 5.13: The top three intermetallic phases containing barium.

Phase	**Al-Ba-Si>**	**Al-Fe-Si-Ti>**	**(Al,Zr) Si_2Ti**
Maximum (experiment)	42 wt % (Alloy A)	48791 ppmw (Alloy A)	6524 ppmw (Alloy A)

The fact that barium was able to dissolve to some extent in the titanium rich phases implies that the crystal structure of these phases were more spacious, and that it would be easier here to either fill vacant sites or substitute for titanium in the lattice.

5.4.8 Copper

For the metallurgical grade silicon investigated the maximum amount of copper was always found in the ternary Al_3FeSi_2 phase, which was the phase richest in aluminium in the system. In alloy A copper was also found in the phase with the highest aluminium content, but here this was a Al-Si phase, not the Al_3FeSi_2. The copper content in the Al_3FeSi_2

was 20 to 40 x lower in alloy A compared to MG-Si2. An explanation to the reduced level in the Al_3FeSi_2 phase could be the increased amount of aluminium in alloy A, while the amount of copper did not increase. More aluminium containing intermetallic phases were formed and copper divided itself among more phases, which would reduce the average concentration in a given phase.

Table 5.14: The top three intermetallic phases containing copper.

Phase	**Al-Si>**	**Al_3FeSi_2>**	**$Al_6CaFe_4Si_8$**
Maximum (experiment)	4300 ppmw (Alloy A)	4584 ppmw (Cyb MG-Si2)	2097 ppmw Cyb MG-Si1)

According to the mass balance 21 % of the copper present in the bulk material was removed from the matrix. As explained, it was expected from the segregation pattern in Section 5.1 that Cu should be found in correlation with the intermetallic phases. But as for nickel a high diffusion coefficient could have led to more copper in the grain boundaries or in the silicon matrix. Copper was observed from EPMA analysis of the silicon matrix. Silicon grain boundaries were not examined.

5.4.9 Lead

Lead did not seem to have an affinity for a particular phase. The maximum content, usually around 300 ppmw, was found in different phases in almost all the experiments. Pb was below the lower detection limit of the XRF instrument, Table 3.6. The average Pb content was 0 ppmw for most samples and naturally Pb was not found in high content in the intermetallic phases either.

5.4.10 Zinc

Like lead, zinc does not seem to have an affinity for a particular phase, and was not present in a high concentration in the bulk material. The maximum concentration was found together with the (Al,Zr)Si_2Ti and Al_3FeSi_2, in the Cyberstar furnace experiment and in the Al –Ba-Si phase in alloy A.

Table 5.15: The top three intermetallic phases containing zinc.

Phase	**(Al,Fe)$SiTi_2$>**	**Al_3FeSi_2>**	**Al-Ba-Si>**
Maximum (experiment)	3056 ppmw (Cyb MG -Si2/1	500 ppmw (Cop-MG-Si1)	400 ppmw (Alloy A)

5.4.11 Magnesium

In the first EPMA runs that were performed magnesium was not one of the elements that were searched for. Only the analysis in the Cyberstar furnace experiments, A1 and A2 contained information about this element.

Table 5.16: The top three intermetallic phases containing magnesium.

Phase	**$(Al,Fe)SiTi_2$>**	**Al-Si>**	**$Al_6CaFe_4Si_8$**
Maximum (experiment)	9528 ppmw (Cyb MG -Si2/1	5465 ppmw (Alloy A)	1194 ppmw (Alloy A)

5.4.12 Wolfram

Wolfram was assumed to be present due to contamination from the wolfram rhenium thermocouples. Wolfram has a very small distribution coefficient, $1.7*10^{-8}$, Table 2.1, which means it would effectively segregate from the silicon matrix. This was confirmed from the analysis of the matrix, no wolfram was found. The maximum content was found in $(Al,Fe)Si_2Ti$, sample MG-Si2 from the Cyberstar furnace experiment.

5.4.13 Cerium, lanthanum and neodymium

For alloy A, one phase, that was observed only three times, contained considerable amounts of cerium, lanthanum and neodymium. In total the content was 10 wt %. These elements were not detected in the other intermetallic phases of alloy A. **Meteleva- Fischer et al**. (2013) alloyed MG-Si with lanthanum and neodymium and observed an increased amount of phosphorus in these phases. The same observation was made in phases containing La, Ce and Nd in the MG-Si before alloying, **Meteleva- Fischer et al.** (2012). This was not seen in the case of alloy A.

5.5 Porosity

All the examined samples, except the Cyberstar samples, contained a varying degree of porosity. In a publication by **Anglezio et al.** (1990) porosity was explained by gas bubbles trapped during refining. When silicon was cast on the copper plate no refining was done prior to the casting, but porosity was still present in the cast. The silicon was however melted prior to solidification in a furnace flushed with argon.

The pores in samples extracted from experiment A1 were larger than the pores seen for the metallurgical grade silicon. A possible explanation was the ease of nucleation due to the increased amount of inclusions, such as carbides in alloy A. In some cases it was observed that the pores are found in combination with an accumulation of intermetallic phases.

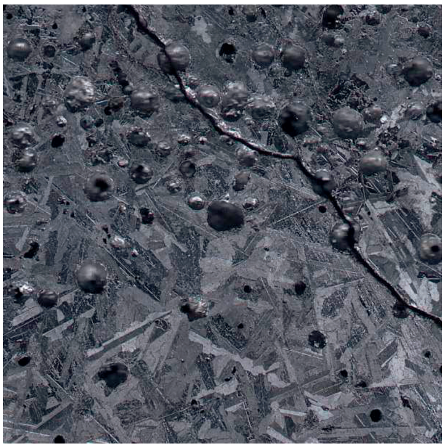

Figure 5.26: Horizontal cross-section sample G, illustrating porosity in the sample.

A cross section of a sample extracted from a porous layer of sample G is presented in Figure 5.26. Porous layers were found in regions where two solidification fronts met or close to a solidification layer where the gas could not penetrate.

The effect the pores will have in further processing steps such as leaching or the direct synthesis have not been studied, but at least for the direct synthesis which is a surface reaction, a porous material could behave differently in the process. In a leaching process, it is assumed that the acid would have a different contact with the intermetallic phases in a porous material than in a non-porous material.

5.6 Carbides

From examinations of the samples in the light microscope and SEM, it was observed that carbides were present at a much higher level in the A1 and A2 samples, alloy A, compared to MG-Si where carbides only were observed occasionally. In Section 5.2, carbides were mentioned as potential nucleation sites. The reason for the high carbide content was explained by the lack of a refining step for alloy A. The average carbon content in sample A1 was 70 ppmw compared to 11 ppmw for sample G /B. In sample A2 the content was much higher, 400 ppmw, but this was attributed to contamination by the carbon protection tubes used in the experiment and not seen as representative for the material. No bulk analysis of carbon was taken in the tapping beam so the carbon content prior to refining was not known.

In Figure 5.27 a belt of carbides that was observed 13 cm from the top in sample A1 is presented. Sample A1 contained several belts of carbides. Some of the SEM micrographs taken in areas with a high SiC content revealed that the carbides often were interconnected. **Ciftja** (2009) mentioned that particles in the melt can form agglomerates that were either within a grain or in the grain boundary.

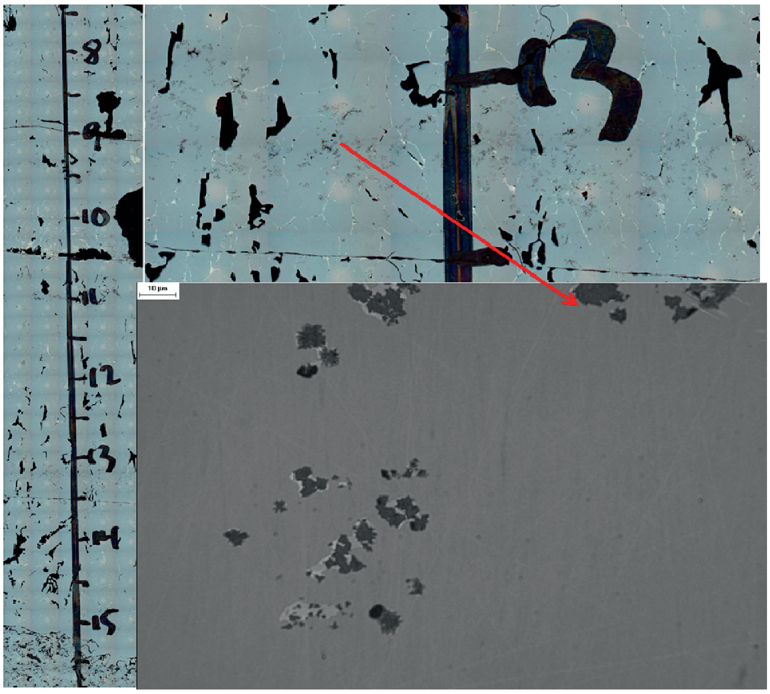

Figure 5.27: Belt of carbides found 13 cm from top surface**.**

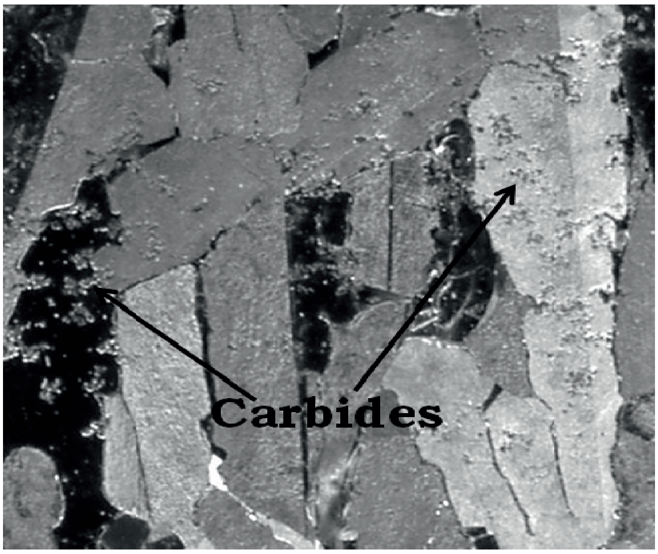

Figure 5.28: Section close to the belt around 13 cm corresponding to a 0.5 mm x 0.5 mm square on the sample.

From the two preceding figures it was observed that carbides were not only found in combination with intermetallic phases, but a substantial amount was present in the silicon matrix. During a process such as leaching, carbides present within the silicon matrix will not be removed, while carbides found in grain boundaries in connection with the intermetallic phases probably would be. According to **Margaria** (1994) SiC will modify surface properties of silicon and therefore affect the direct synthesis.

5.7 Oxygen

Oxygen was introduced in the samples where the surfaces that have been in contact with air or if slag was incorporated into the structure. Oxygen was seen in correlation with the layers, as confirmed by electron microprobe mapping, Figure 5.29.

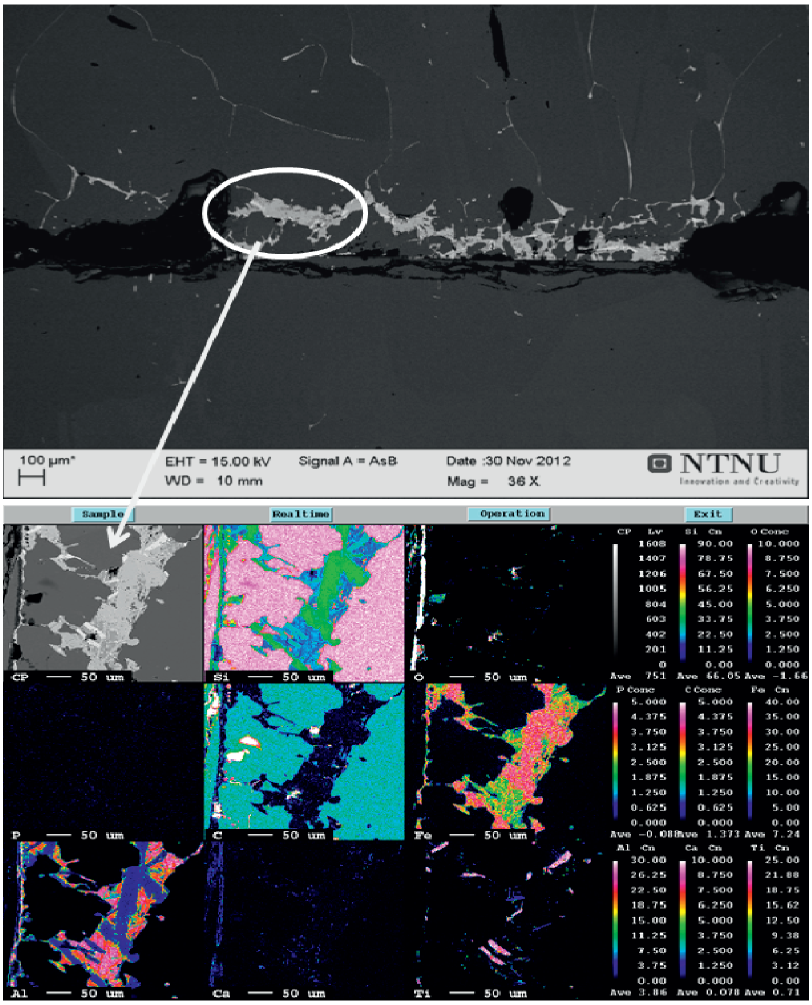

Figure 5.29: Mapping around a solidification layer, sample 3.5. The scale bar to the right indicates the amount of the different elements.

5.8 Silicon loss related to the intermetallic phases

It was seen from the above that silicon was one of the main constituents in all the intermetallic phases. This means that the formation of intermetallic phases represents a loss of silicon. In Section 5.4 a simple material balance for MG-Si was presented. From the material balance, for every iron atom present, approximately 2.4 silicon atoms were present. This means that the number of moles silicon bound in the intermetallic phases were more than twice the amount of moles iron in the cast. In weight per cent simplified this gave a ~1:1 ratio. For alloy A the main intermetallic phases were Al_3FeSi_2, $Al_6CaFe_4Si_8$ and Al_2CaSi_2 so at least twice as many moles silicon would lost compared to iron. In addition approximately an equal number of moles silicon compared to the moles aluminium was found in the Al_2CaSi_2, which gave an additional loss. Figure 5.30 illustrates the linear relationship between iron and silicon present in intermetallic phases in MG-Si. The silicon found in the ternary calcium phase was not considered. Neither was the fact that increasing the amount and ratio between certain alloying elements changes the ratio of the intermetallics formed, which can change the Fe:Si ratio in the phases.

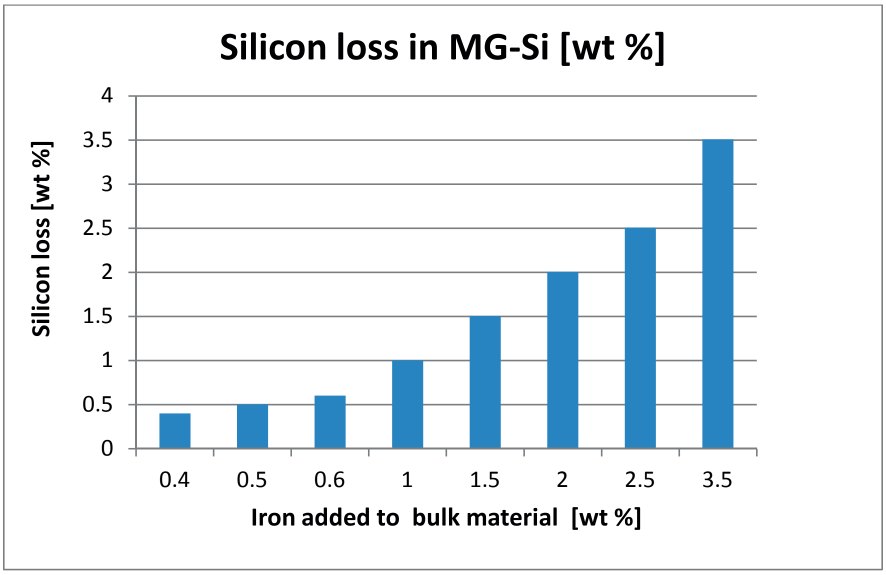

Figure 5.30: Silicon found in intermetallic phases as a function of wt % iron.

As an example of amount silicon bound to the phases, a MG-Si quality with 0.4 wt % iron content was considered. If the daily production of MG-Si is 80 tonnes at a plant, then annually 100 tonnes silicon will be bound to the intermetallic phases and may be lost.

Addition of other elements may be necessary, but will be accompanied by a silicon loss.

6 Post Processing of Silicon-Crushing and Screening

The sizing process of silicon from the casted silicon to a finished product includes several steps such as crushing and sieving. These processes involve several kinds of cost such as energy use, wear and losses.

If a material is to be crushed the sample needs to be exposed to a strain larger than the resistance to rupture. This is done by impact, pressure or abrasion. Industrially produced silicon is a heterogeneous material. According to **Sandvik et al.** (1999), needle shaped asbestos grains are said to be more difficult to crush than isometric grains. Transferred to silicon this means that zones in the cast with needle shaped grains will be harder to crush than the zones with a more equiaxed shape. In the screening process a needle shaped grain might pass if it enters parallel to the sieve, but it is stopped if it enters normal to it. This illustrates that there will be differences in the optimal sizing process within the same cast and between casts solidified under different conditions.

In a lecture by **Krogh** (1999), three main aspects of the crushing and screening are listed:

- To obtain a granulated product to the customer's specifications.
- To liberate phases in the material for separation or cleaning.
- To obtain products with size distributions optimal for further treatment.

For the silicon producer the aim is mainly to obtain a product with a size distribution corresponding to the customer's specifications. Material below the customer’s specification is considered as “fines” material. To get an impression of how the solidification effects the “fines” generation an abrasion test was conducted. This test was of indication on how much fines that would be generated during handling and transport of the material. A material with higher abrasion strength will generate less “fines” during handling and sizing. In this work “fines” were defined as material below 1 mm.

In Section 6.2 the micro hardness of the main intermetallic phases in the system has been investigated in order to see if this could be correlated to “fines” generation.

How the composition varied with size fraction after crushing/ grinding and sieving was also examined.

6.1 Abrasion strength

High abrasion strength can be an advantage if it means that less fines are generated during crushing, transport and handling.

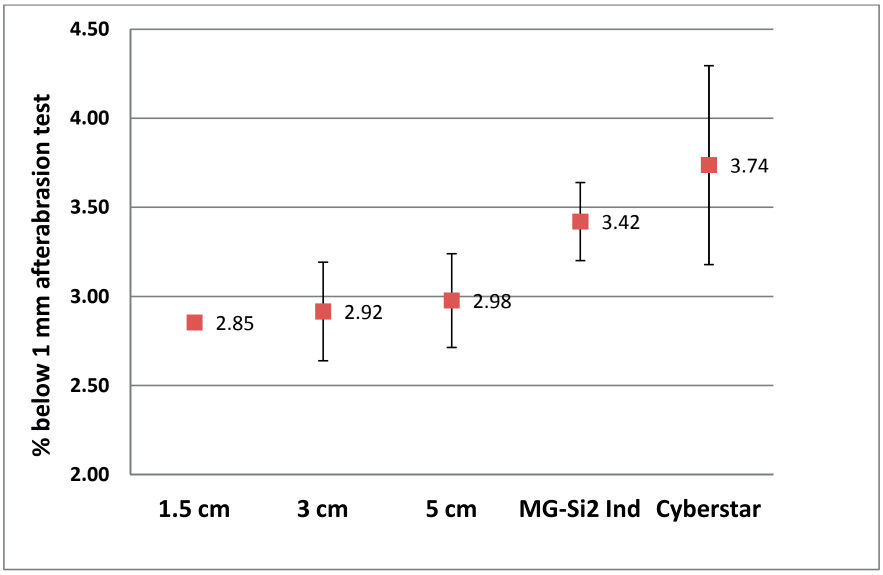

Figure 6.1: Results from the experiments where MG-Si2 have been used. Note the large variation in the results due to inhomogeneous materials. The cooling rate decreases from left to right.

In Figure 6.1 the abrasion strength is represented as amount, in wt %, material less than 1 mm after the abrasion test for MG-Si2 type silicon. The experiments compared are the 1.5, 3 and 5 cm copper plate experiments, MG-Si 2 industrial and the Cyberstar Ingots containing MG-Si2. The abrasion strength increased when the amount of sample below 1 mm after the abrasion test decreased. The standard deviations shown in the figure are large which illustrates that the material was inhomogeneous.

Prior to the abrasion test it was noted that the material especially from the copper plate experiment contained a lot of cracks, layers and "worms" in some regions. This could have caused zones in the material that were weaker and thus contributed to the inhomogeneity of the material. The figure indicated a weak trend - abrasion strength increased when the cooling rate was reduced for the MG-Si2 material. For the MG-Si1 and alloy A it was not possible to see this trend.

Schussler et al. (1992) described that silicon with a high content of Ca was more brittle. Experiment 3.1, – 1.5 cm copper plate, and the Cyberstar furnace experiment both had low calcium content, but they were at each end of the scale in the abrasion test. It was not possible to conclude if calcium content had an effect on the abrasion strength. There were too many variables in the system in order to conclude what was the most important contributor to the abrasion strength.

6.2 Vickers micro hardness measurements

The micro hardness measurements were performed on intermetallic phases that had been imaged with the SEM in combination with the EPMA prior to the measurements. After the measurements the same phases were imaged using a light microscope. Cracks already present in the material could then be distinguished from those made by the indention. In Table 6.1 the average micro hardness, HV is given for the four of the main intermetallic phases in the sample used, sample G from the industrial experiment, MG-Si2.

Table 6.1: Average micro hardness of the most common phases in MG-Si2.

	(Al)FeSi$_2$Ti	**Al$_6$CaFe$_4$Si$_8$**	**HT- (Al)FeSi$_2$**	**Al$_3$FeSi$_2$**
Mean	900	737	720	610
Max	1184	936	902	646
Min	512	485	573	557
STD	183	105	85	47
#	14	40	30	3

The table indicates that the titanium phase was the hardest phase while the Al$_3$FeSi$_2$ phase was the softest phase. It can be seen from the table that the difference between the maximum and minimum hardness observed for a given phase was large, in addition to a large standard deviation. It is described in **ISO 6507-1** (2005) that with a decreasing applied load there will be an increase in the scatter of the measurements. The determination of the diagonals was according to the standard unlikely to be better than ±0.001 mm with the load used in micro hardness testing. It was seen that the diagonals in these experiments vary from around 0.006 to 0.01 mm, and a small change in the measurement of the diagonals resulted in a large change in the micro hardness calculated. It was not possible to apply a higher load because then the phases shattered and no diagonals were left to measure.

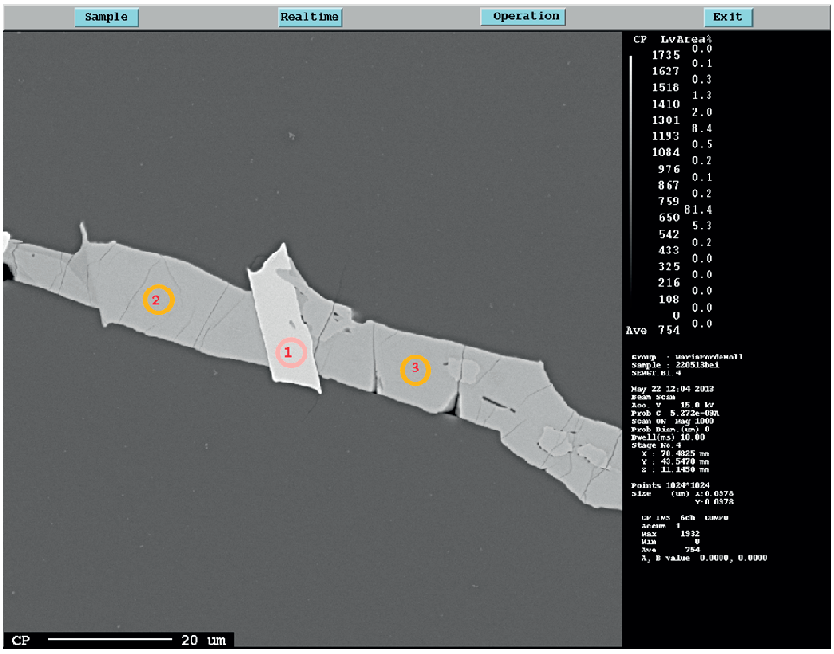

```
CP  LvArea%
          0.0
    1735
          0.1
    1627
          0.3
    1518
          1.3
    1410
          2.0
    1301
          8.4
    1193
          0.5
    1084
          0.2
     976
          0.1
     867
          0.2
     759
         81.4
     650
          5.3
     542
          0.2
     433
          0.0
     325
          0.0
     216
          0.0
     108
          0.0
       0
          0.0
Ave  754

Group  : MariaFordeMoll
Sample : 220513bei
SEM6I.B1.4

May 22 12:04 2013
Beam Scan
Acc. V     15.0 kV
Prob C  5.272e-09A
Scan ON   Mag 1000
Prob Diam.(um) 0
Dwell(ms) 10.00
Stage No.4
   X : 70.4825 mm
   Y : 43.5470 mm
   Z : 11.1450 mm

Points 1024*1024
Size     (um) X:0.0978
              Y:0.0978

  CP IMS   6ch   COMPO
  Accum. 1
  Max       1932
  Min          0
  Ave        754
  A, B value  0.0000, 0.0000
```

Figure 6.2: SEM micrograph prior to micro hardness measurement.

Figure 6.3: Light microscope image after micro hardness measurement.

Figure 6.2 and Figure 6.3 illustrate three of the points where the micro hardness was measured before and after the measurement. Points 2 and 3 were the $Al_6CaFe_4Si_8$ phase, while point 1 was the (Al)$FeSi_2Ti$ phase. The result gave a value of 485 and 811 for point 2 and 3 respectively and 902 for point 1. There was a large deviation between points 2 and 3 even though this was the same phase. It was observed that there were more cracks initially in the area where indention 2 was made compared to indention 3. Also it was seen that after indention 2 the area was more destroyed then after indention 3. This shows that the cracks initially present affected the value obtained. From the expression for Vickers micro hardness in Equation 2.33 it was seen that the larger the diagonals the lower the micro hardness. For a soft material the diagonals are long since the indenter is able to indent deep into the material, but for a hard material the diagonals are smaller. Since propagations of cracks could have led to longer diagonals, the hardness value could indicate that the phases were softer than what was actually the case. **Anglezio et al.** (1994b) reported a Vickers hardness of 1230 for the $Al_6CaFe_4Si_8$ phase measured with a load of 0.05 N.

6.3 Amount of alloying elements as a function of particle size

Figure 6.4 illustrates how the amount of alloying elements varied with size fraction of the sample. It can be seen that the composition was constant in all fractions above 0.180 mm. When the size was less than 0.180 mm, the amount started to increase. In the fraction - 0.053 mm, the amount of all elements was approximately doubled.

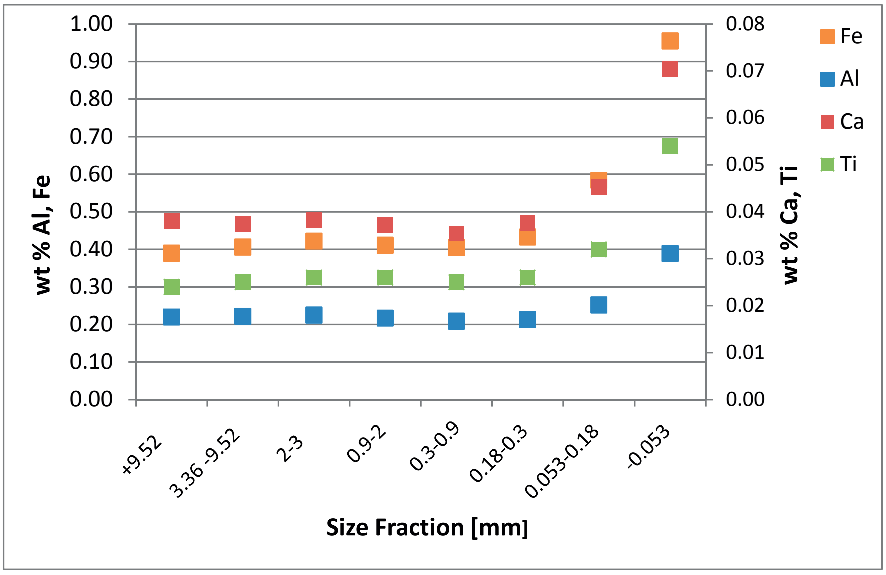

Figure 6.4: Chemical analysis of Al, Ca, Fe and Ti in the different size fractions after crushing and sieving.

The reason for the accumulation in the finer fractions was revealed by the SEM micrographs, there were several cracks in the intermetallic phases that divided each intermetallic phase into several cells, often with a diameter less than 0.053 mm, Figure 6.2. This has been noted by authors such as **Gueneau et al.** (1995c) and **Ott** (2003). Since there were already many cracks in the intermetallic phases the material would easily be crushed along their path. This was confirmed during the micro hardness measurement. When the material was crushed this caused the intermetallic phases to have a tendency to end up in the finer fractions, given that they were liberated. According to **Gueneau et al.** (1995c) the cracking in ferro-silicon was induced by thermo mechanical stressed due to the difference between dilation coefficients of silicon and HT-$FeSi_2$. This might have been the case for the intermetallic phases in silicon as well.

6.4 The consequences of the shape, size and strength of the intermetallic phases

The intermetallic phases show many different forms and sizes. As described in chapter 5, there was a strong indication that a lower cooling rate through the temperature region where the remaining melt could rearrange resulted in larger and more spherical intermetallic phases, that is a lower surface area/volume ratio. After crushing, given that the intermetallic phases break along the cracks, the probability of finding larger phases in the ground material is higher when the surface area/volume ratio has been low.

A higher cooling rate on the contrary seemed to give more "sheet"-formed intermetallic phases due to the higher surface area/volume ratio. This causes the intermetallic phases to break into smaller pieces.

This difference may be significant for the usage of the silicon in the different downstream processes.

7 Magnetic separation

The production of MG-Si today is based on the use of relative pure raw materials quartz and carbon. Lower quality raw materials may be a probable future scenario. For that reason other refining processes for raw materials and silicon may be needed. One alternative to purify metallurgical grade silicon is by means of magnetic separation of crushed/milled material. If the intermetallic phases in the MG-Si are ferro- or paramagnetic they could in principle be separated from the silicon matrix. In this work the aim was to carry out an initial test to explore if there is potential for purifying MG-Si by means of magnetic separation.

As outlined in Chapter 3, both a wet and a dry magnetic separator were used. For the wet separation fractions of -53 µm and 53-150 µm were utilized. For the dry separation fractions of -53 µm, 53-150 µm, 150-300 µm and +300 µm were utilized.

7.1 Recovery and Grade of the separated samples

In Chapter 2 two important terms describing the efficiency of the separation were listed as given by **Oberteuffer** (1974) – here adapted for silicon alloying elements:

Recovery, R_m: ratio of alloying elements in the magnetic fraction relative to that in the feed.

Grade, G_m: the amount of alloying elements in the in the magnetic fraction.

Grade, G_{nm}: the amount of alloying elements in the non-magnetic fraction.

In Figure 7.1 and Figure 7.2 histograms representing the wt % of Al, Ca, Fe and Ti in the magnetic and non-magnetic samples of fractions – 53 µm and -150+53 µm, are presented. From the figures it is seen that the highest grade of alloying elements was obtained in the magnetic fraction of size – 53 µm using the SLon separator. For the Permroll separation of size – 53 µm the amount of alloying elements were almost equal in the magnetic and non-magnetic samples.

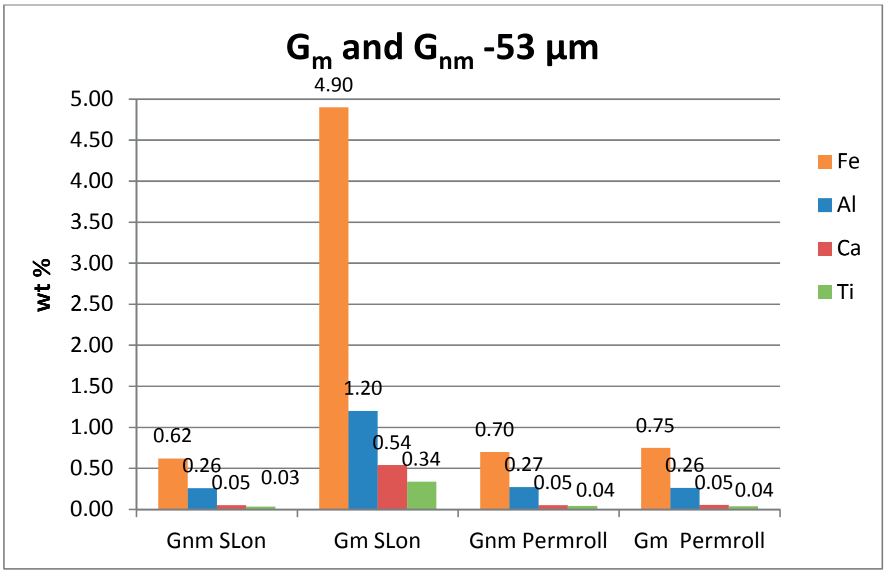

Figure 7.1: Chemical analysis wt % of alloying elements in the magnetic and non-magnetic fractions of size -53 µm. This equals the grade G_m and $G_{nm.}$ In sample G_mSLon, Al and Fe reached their solubility limits, indicating that their content could have been higher.

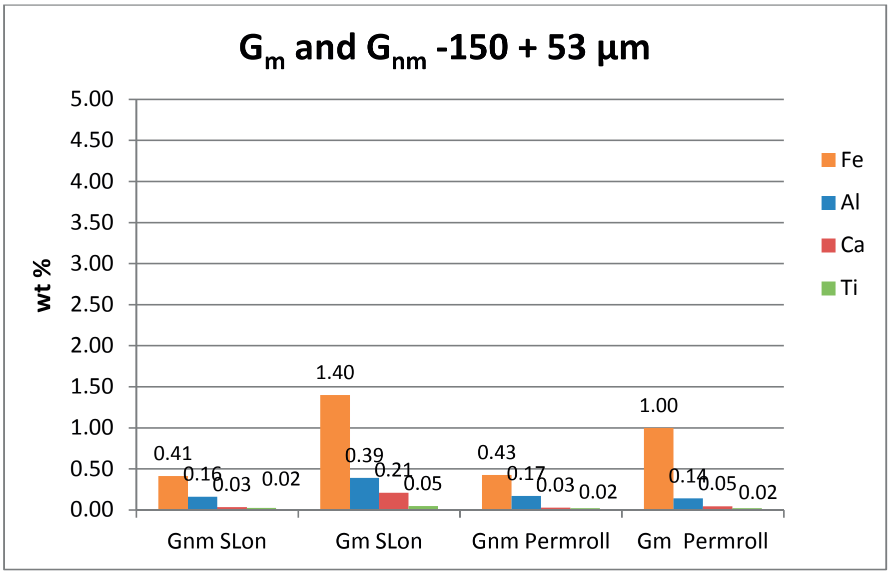

Figure 7.2: Chemical analysis of alloying elements in the magnetic and non-magnetic fractions of size -150+53 µm. This equals the grade G_m and G_{nm}.

In Figure 7.3 the percentage of alloying elements that end up in the magnetic fraction is given, that is the recovery of the alloying elements, R_m.

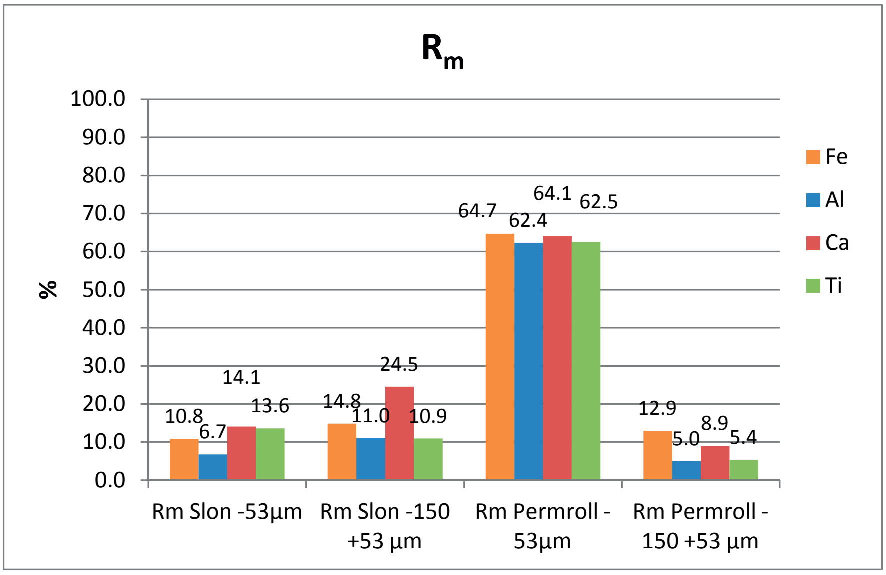

Figure 7.3: Recovery, R_m, of Fe, Al, Ca and Ti in the magnetic fractions.

The bulk composition before the separation of each fraction was calculated by summarizing the amount in the non-magnetic and magnetic samples. It was assumed that there was no loss during the experiment.

7.2 Size of the intermetallic phases

Figure 7.4 and Figure 7.5 illustrate concentration maps at different locations in the magnetic and non-magnetic samples from the SLon separation. The colour indicates the amount of a given element and the correlation between amount and colour is given by the scale bars to the right in the images.

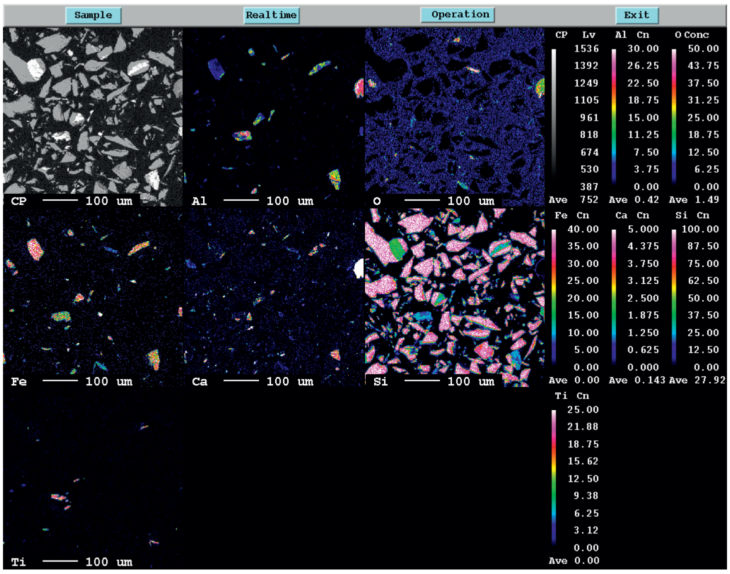

Figure 7.4 : Mapping of a part of the magnetic sample -53 µm from the SLon separation.

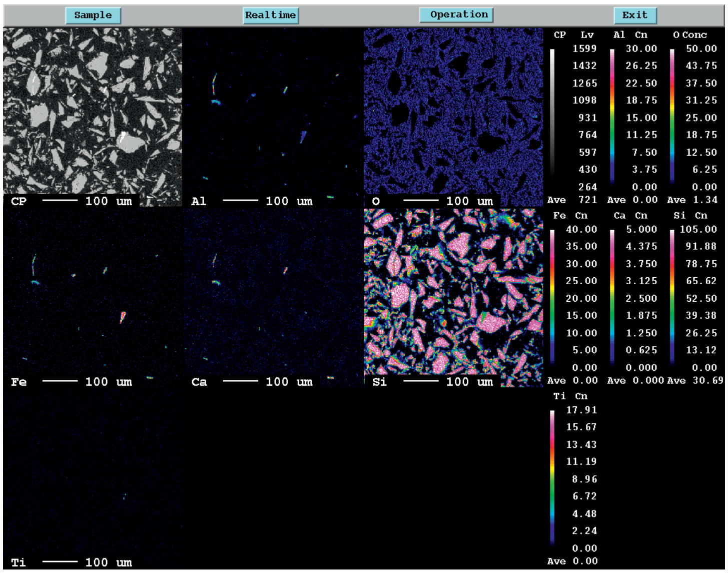

Figure 7.5: Mapping of a part of the non-magnetic sample -53 µm from the SLon separation.

Comparing the mapping of the magnetic and the non-magnetic samples in Figure 7.4 and Figure 7.5 it is seen that the average size of intermetallic phases was larger in the magnetic samples. From Equation 2.27, it is seen that the magnetic force F_m, will depend on both the volume and the size of the particle. When a particle is below a critical size the competing forces can exceed the magnetic forces and the magnetic particles will end up in the non-magnetic fraction. Examining the intermetallic phases in Figure 7.6 it was seen that there were several cracks in almost all of the intermetallic phases. Usually they do not extend far into the silicon matrix. It was assumed that the particle size of the intermetallic phase after crushing depended on the size given by the cracks before crushing, given that the phases were liberated. This means that many particles had a size less than 50 µm, as seen from Figure 7.6. The result could be that several particles were below the critical size needed for F_m to exceed the competing forces.

```
CP  LvArea%
          0.0
   1612
          0.0
   1511
          0.1
   1410
          1.5
   1309
          0.5
   1209
          2.2
   1108
          6.7
   1007
          1.0
    906
          2.1
    806
          0.3
    705
          0.3
    604
          6.4
    503
         77.5
    403
          0.8
    302
          0.1
    201
          0.1
    100
          0.3
      0
          0.0
Ave  560

Group  : MariaFordeMoll
Sample : 210113seibei
B-midt.3

Jan 21 11:29 2013
Beam Scan
Acc. V     15.0 kV
Prob C   1.020e-08A
Scan ON  Mag 300
Prob Diam.(um) 0
Dwell(ms) 10.00
Stage No.6
  X : 57.3909 mm
  Y : 67.5543 mm
  Z : 12.0185 mm

Points 1024*1024
Size     (um) X:0.3258
              Y:0.3258

  CP IMS  7ch  COMPO
  Accum. 1
  Max     1876
  Min        0
  Ave      560
  A, B value  0.0000, 0.0000
```

Figure 7.6: Backscatter micrograph of MG-Si2 material after industrial casting.

The micrographs in Figure 7.7 and Figure 7.8 also confirm that the average size of intermetallic phases was larger in the magnetic fractions.

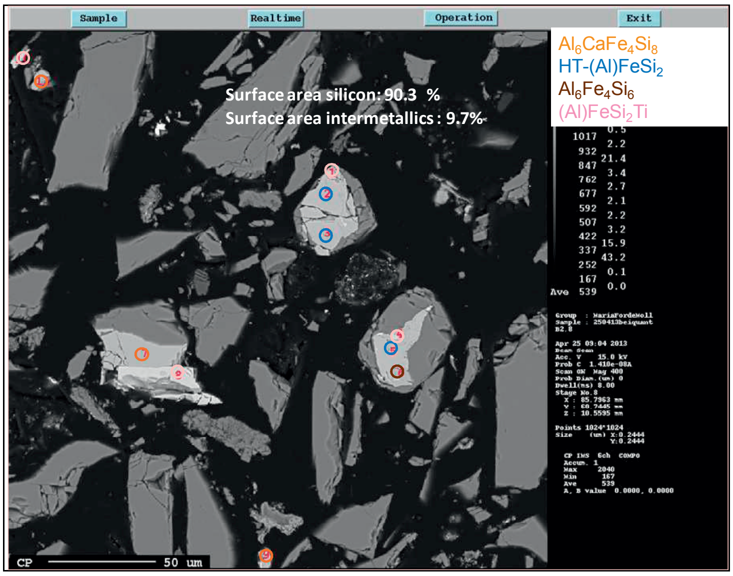

Figure 7.7: Backscatter micrograph of magnetic sample -53 µm from the SLon separation. Black background is epoxy and particles with the darkest grey contrast are silicon.

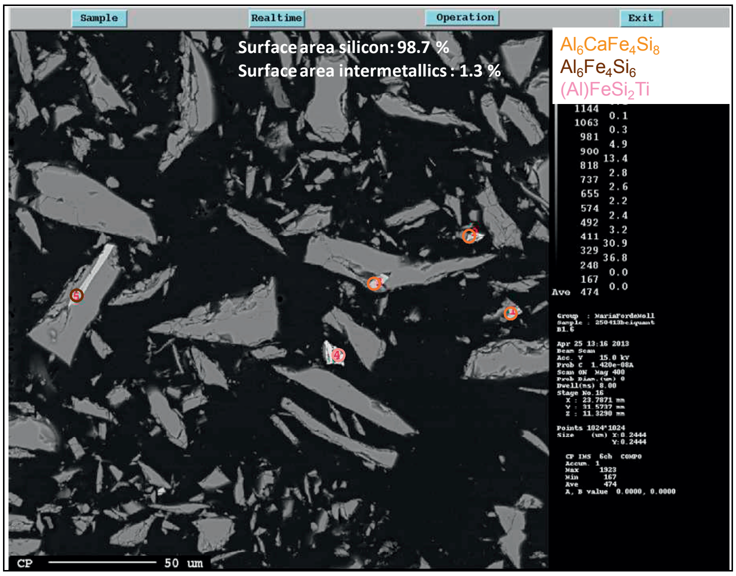

Figure 7.8: Backscatter micrograph of non-magnetic sample -53 µm from the SLon separation. Black background is epoxy and particles with the darkest grey contrast are silicon.

7.3 Evaluation of the experiment

According to **Nkosibomvu et al.** (1998) good magnetic properties for ferrosilicon are associated with a high content of iron and a low content of impurities. They tested ferrosilicon with an abundance of iron, with an analysis between 60 and 69 at % iron. The average iron content in the different intermetallic phases varied between average of 15 at % for the Al_3FeSi_2 to 29 at % for the HT-(Al)$FeSi_2$ and 21 at % for the $Al_6CaFe_4Si_8$ phase. **Kloc et al.** (1995) reported that LT-$FeSi_2$ (β-$FeSi_2$) and HT-$FeSi_2$ (α-$FeSi_2$) showed a small positive magnetic susceptibility. Literature describing other phases was not found. From the EPMA analysis of the magnetic and non-magnetic fractions HT-(Al)$FeSi_2$ and $Al_6CaFe_4Si_8$ were observed most frequently. These were also the phases most found frequently in the bulk material. From the chemical analysis an increase in all alloying and trace elements was found in the magnetic fractions compared to the calculated bulk analysis of a given fraction. For the -53 um fraction the bulk composition was calculated to be Fe = 0.7 wt%, Al =0.27 wt % Ca=0.06 wt % and Ti = 0.04 wt %. In Chapter 5 it was seen that the bulk part of trace elements were found in the intermetallic phases. It is therefore natural that their content increased together with the main alloying elements.

Examining the BSE micrographs it was seen that several intermetallic phases often were found together in the same particle. That means that a non-magnetic phase might end up in the magnetic fraction because it was connected to a phase with a positive magnetic susceptibility.

Evaluating the results from this initial test it was seen that the SLon separator gave the highest grade in magnetic fraction when the size was less than 53 µm. The separator then removed 6.7 % of the aluminium, 10.8 % of the iron, 14.1 % of the calcium and 13.6 % of the titanium. The downside of the -53 µm fraction is that the small particles introduce more surface area, which again can introduce more oxygen in the material. Also a small particle size would not be an option if the silicon is to be remelted in an aluminium alloy as described in Section 2.7.4.1.

For the Permroll experiment the recovery of alloying elements were large for the -53 micron, Figure 7.3. However in this case there was a large silicon loss since 63 % of the silicon ends up in the magnetic fraction compared to only 1.4 % for the SLon separation. The reason for the increased amount of silicon in the – 53 µm was probably due to electrostatic forces between the small particles. For the larger fractions of the Permroll experiments, -300 + 150 µm and + 300 µm the increase of iron was higher in the magnetic fraction than the increase of Al, Ca and Ti. This might have been caused by a reduction of inter particle forces when particles were larger and only particles that were magnetic susceptible was separated (in addition to particles stuck on magnetic susceptible particles). If this was the case, it is probable that the HT-(Al)FeSi$_2$ was responsible for the magnetic properties of the material.

The bulk part of all samples was silicon, which is a diamagnetic material (**Lide,** 2005) and in theory should be repelled by the magnetic matrix. This indicated that inter particle forces were present and strong.

Brinson et al. (2002) did not obtain magnetic separation of MG-Si when a High Grade Magnetic separator was applied. However when the silicon reacted with methyl chloride it was possible to separator the residue. A similar effect was observed by **Rong et al.** (2002) who were able to separate the residue when silicon tetrachloride had been reacted with silicon in a fluidized bed reactor.

Chen et al. (2013) investigated the magnetic separation of a material containing 29 wt % iron, mainly as hematite, and quartz. They achieved a better magnetic separation using the 1mm matrix for the SLon 100 separator. The size of the material to be separated was + 30 µm, 20-30 µm, 10-20 µm and -10 µm. When utilizing the 1 mm matrix both the recovery and the grade of iron was increased for the 20-30 µm and 10-20 µm fractions. For the fraction -10 µm the hydrodynamic drag force increased so the recovery was reduced. For the + 30 µm fraction the 2 mm gave the best result. This illustrate that the separation is dependent on the matrix used, and if new experiments were to be done a 1 mm matrix should be tested at least for the -53 µm fraction.

Alternatives for further optimization of the SLon separation would be to change experimental settings such as the pulse in the water stream, size of the matrix used or the field strength. The chemistry could also be changed to gain more knowledge about the susceptibility of the different phases.

8 Conclusions

The results from the COMSOL heat transfer model were in good agreement with the experimental measurements. The model and the parameters may be utilized for future work in order to optimize existing or design new silicon casting methods. The developed COMSOL model was used to understand the resulting microstructure of the cast.

The experiments illustrated that several factors contributed to the final grain size, not only the cooling rate. Other factors were: inclusions in the melt, by reducing the barrier to heterogeneous nucleation; amount of alloying elements in the melt, causing constitutionally undercooled regions which facilitated equiaxed growth; temperature in the melt, which also could have facilitated equiaxed growth but also the formation of solidification layers during casting.

It was observed that silicon extremely quick formed a solidified skin/layer during the casting process. These layers acted as a boundary for the alloying/trace elements in the enriched melt. A new enrichment of the liquid started below the layer (or above depending on the direction of the heat flow). The result was that one side of the layer was enriched in alloying/trace elements, and the other side was deficient in alloying/trace elements. This influenced the segregation pattern and the silicon grain size.

For the industrial MG-Si2 experiment it was observed that small silicon grains were often accompanied by an uneven distribution of intermetallic phases, while large silicon grains were found in combination with a more even, “sheet” formed distribution of intermetallic phases. This work supports that the cooling rate after the solidification of primary silicon had an effect on the size and form of the intermetallic phases. This may be utilized industrially to achieve a wanted intermetallic structure.

It was observed that all intermetallic phases contained a large amount of cracks. The size and shape after crushing may be defined by the crack pattern and the original size of the intermetallic phases.

A consequent handling of the casted silicon may be important to influence the intermetallic phases. I.e. a pile storage of silicon casts may retain the heat longer in the cast and result in larger intermetallic phases with a lower probability to break-up into small pieces.

A higher cooling rate on the contrary seemed to give more “sheet”-formed intermetallic phases due to a higher surface area/volume ratio. This may cause the intermetallic phases to break into smaller pieces.

The distribution of the intermetallic phases also depended on solidification layers, available space between the silicon grains and the amount of alloying elements.

An optimized shape and size of the intermetallic phases may be significant for the usage of the silicon in the different downstream processes.

The segregation depended on the distance the solidifying fronts travelled. The longer the distance the higher the enrichment in the melt. Macro segregation was observed in all cast, but it was less in the 1.5 cm cast since the fronts travelled a shorter distance.

Cu, Mn and V followed the segregation pattern of the main alloying elements Al, Ca, Fe and Ti, while the pattern for Mg, Sn and P was not as pronounced. This was in agreement with their respective distribution coefficients. Tin hardly segregated and often followed the pattern of silicon rather than the main alloying elements.

Over 700 intermetallic phases from the different experiments were investigated by EPMA. It was seen that the main phases in the metallurgical grade silicon were HT-(Al)$FeSi_2$ Al_3FeSi_2, $Al_6Fe_4Si_6$, $Al_6CaFe_4Si_8$, and (Al)$FeSi_2Ti$. In addition Al_2CaSi_2 was observed. This was consistent to earlier findings in literature. A few analyses of the silicon matrix indicated that an increased cooling rate, such as in the copper plate experiments, increased the incorporation of alloying and trace elements into the silicon matrix. This suggests that the trade off to obtain a smaller grain size due to an increased cooling rate was a less pure silicon matrix.

The transition elements close to titanium in the periodic table were found in the highest concentration in the titanium rich phases, $(Al)FeSi_2Ti$ or Si_2Ti. This was true for vanadium, chromium and zircon. Large elements like barium and wolfram were also found in connection with these phases.

The highest amount of copper was found in combination with the highest amount of aluminium, which was the Al_3FeSi_2 phase for MG-Si type silicon and a Al-Si phase for alloy A.

The highest amount of phosphorus was found in combination with the Al_2CaSi_2 phase, when this phase was not present the $Al_6CaFe_4Si_8$ and the $(Al)FeSi_2Ti$ phases were preferred.

A mass balance was done for a metallurgical grade silicon with analysis Al = 0.18 wt %, Ca = 0.03 wt %, Fe = 0.4 wt % and Ti = 0.02 wt %. Usually the intermetallic phases contained several hundred times more trace elements than the bulk analysis and it was seen that most elements with a low distribution coefficient were found in the intermetallic phases. The mass balance indicated that some transition elements, such as nickel and copper, could diffuse in solid state into the silicon grain boundaries or silicon matrix.

It was not possible to find a general expression describing the abrasion strength of the material. A higher cooling rate increased the abrasion strength, but the material in question was too inhomogeneous to obtain a value suitable for the bulk properties. The micro hardness of the intermetallic phases was measured and it depended on the amount of cracks present in the phases before the measurement since the cracks influenced the length of the measured diagonals. Analyses from several fractions of MG-Si revealed that fractions -180 µm and especially the -53 µm fraction was enriched in alloying/trace elements. This was in accordance with the cracks that divided the intermetallic phases into smaller pieces and thus created weak zones in the material.

The initial test to separate the intermetallic phases from the matrix showed promising results for the -53 µm and 53-150 µm size fractions for the SLon 100 separator. The magnetic fractions were enriched in all alloying and trace elements and it was not possible to conclude what intermetallic phases were responsible for the separation.

9 Future work

There are several subjects that could have been studied in more detail and in the following some of these will be listed.

There are numerous effects that can contribute to the silicon grain size and a natural step would be to determine the effect of the individual factors. Variables for new casting experiments could be: amount of SiC present, solidification layers in the cast, temperature in the melt, cooling rate in the area where the silicon grain size is determined, cooling rate in the temperature region where the remaining melt/ intermetallic phases can rearrange.

It was assumed that the silicon grain size was determined in a smaller temperature region than the region remaining melt/intermetallic phases can rearrange to reduce the surface area. The rearrangement was assumed to occur between 1396-600 °C for metallurgical grade silicon. This should be validated by new experiments.

It has been assumed that transition elements can diffuse back into the silicon matrix or the grain boundaries, but this was not confirmed. SIMS was mentioned as an alternative to test this. Another alternative could be a concentration profile with the EPMA.

More work should be done to get a better value for the silicon grain size. The value could include issues such as a shape factor and grain size distribution. A small part of sample B was investigated with EBSD, and the linear intercept method gave a smaller average grain size than with the circular intercept method. More tests should be performed to compare the two methods.

The 1D model by **Mjøs** (2006), adapted by **Dalaker et. al** (2013), Cyberstar, could be used to calculate the breakdown of the plane front during directional solidification. This could be compared to the extracted samples. To investigate the segregation in more detail samples from different parts of the furnace could be examined.

For the magnetic separation more tests should be done in order to learn about the magnetic susceptibilities of the intermetallic phases present.

An optimization varying factors such as chemistry, silicon grain size, field strength, water pulse and matrix used could be tested.

The COMSOL model could be improved to better simulate the water cooling and the filling of the mould.

One of the key issues regarding the casting of silicon, is how does the quality effect the downstream processes such as the leaching process, the direct synthesis or as an additive to an aluminium alloy. It was seen that the solidification process combined with the composition affected the silicon grain size, the type and distribution of intermetallic phases and the concentration of trace elements in the silicon matrix and the intermetallic phases. These are parameters that can have an impact in the further processing. A natural step in this work would be to connect the solidification with a downstream process such as leaching or the direct synthesis.

Bibliography

Abe, T. "The Growth of Si Single Crystals from the Melt and Impurity Incorporation Mechanisms." *Journal of Crystal Growth* 24–25, (1974): 463-467.

Anglezio, J. C., et al. "Characterization of Metallurgical Grade Silicon." *Journal of Materials Research* 5, (1990): 1894-1899.

Anglezio, J. C., et al. "Contribution to the Experimental and Thermodynamic Assessment of the AlCaFeSi System-I. AlCaFe, AlCaSi, AlFeSi and CaFeSi Systems." *Calphad* 18, (1994**a**): 273-309.

Anglezio, J. C., et al. "A Study of the Si-Rich Domain of the AlCaFeSi Quaternary System." *Calphad* 18, (1994**b**): 311-318.

ASTM-E112-96. "Standard Test Methods for Determining Average Grain Size ", (2004).

ASTM-E230/E230M:12. "Standard Specification and Temperature-Electromotive Force (emf) Tables for Standardized Thermocouples" (2012).

Aylward, G. H. and Findlay, T. J. V. *Si Chemical Data*. Milton: Wiley, (2008).

Baker, J. C. and Cahn, J. W. "Thermodynamics of Solidification." In *Solidification: Papers Presented at a Seminar of the American Society for Metals Oct. 11 and 12, 1969,* American Society for Metals, (1971).

Bakken, J. A. *Varme- Og Masseoverføring, Grunnkurs*. Trondheim: Institutt for materialteknologi og elektrokjemi, NTNU, (2000):44.

Baud, L. and Margaria, T. "Silicon for Silicones: A Developing Route for P.E.M." In *INFACON 7*. Trondheim, (1995): 655-664.

Beatty, K. M. and Jackson, K. A. "Monte Carlo Modelling of Silicon Crystal Growth." *Journal of Crystal Growth* 211, (2000): 13-17.

"Bluestar Silicones" http://www.bluestarsilicones.com, (2013).

Boisvert, R., et al. "Casting and Cooling/Crushing of Silicon Metal and Silicon Alloy at Bécancour Silicon Inc." In *INFACON X, 2004*, South Africa, (2004): 138-146.

Brinson J. A., et al. "Magnetic Separation for Silicon Containing Materials." Dow Corning Corporation, (2002).

Bullón, J., et al. "The Improvements to Copper Casting Machine for Ferroalloys.", (2007): 539-547.

Burton, J., et al. *Journal of Chem. Phys.* 21, (1953): 1987.

Callister, W. D. and Rethwisch, D. G. *Materials Science and Engineering: An Introduction.* New York: Wiley, (2007).

Cantor, B. and Nabarro, F. R. N. "Heterogeneous Nucleation and Adsorption." *Philosophical Transactions of the Royal Society A: Mathematical, Physical and Engineering Sciences* 361, (2003): 409-417.

Ceccaroli, B. and Lohne, O. "Solar Grade Silicon Feedstock." In *Handbook of Photovoltaic Science and Engineering*: John Wiley & Sons, (2003).

Chen, L., et al. "High-Gradient Magnetic Separation of Ultrafine Particles with Rod Matrix." *Mineral Processing and Extractive Metallurgy Review* 34, (2013): 340-347.

Chikawa, J. and Sato, F. "In Situ X-Ray Study of Dislocations in Silicon Crystals Growing from the Melt." *Journal of Physics: Conference Series* 59, (1980): 95-109.

Ciftja, A. *Solar Silicon Refining: Inclusions, Settling, Filtration, Wetting.* Vol. 2009:103. Trondheim: NTNU, (2009).

"COMSOL Multiphysics 4.3a" http://www.comsol.no, (2012)

Dalaker, H. ”Foreløpige resultater fra støp av fire ingoter med forskjellige Si-legeringer i Cyberstar- ovnen”.: SINTEF Materials and Chemistry, (2009).

Dalaker, H., et al. "An Investigation of the Thermal Gradients in Silicon During Multicrystalline Ingot Casting." In *35th IEEE PVSC,* Honolulu, (2010): 2157-2161.

Dalaker, H. and Syvertsen, M. "Validation and Refining of 1D Model for Crystallisation of Multicrystalline Silicon Ingots." (2013).

deHuff, J. A. "The Structure of Ferrosilicon." In *Electric Furnace Proceedings*, (1969):167-174.

deLinde, J. "Global Demand for Silicon." CRU, (2013).

Dons, A. L., et al. *Final Report SiStruck-SINTEF F9400*. SINTEF Materials and Chemistry, (2009).

Dubrous, F. and Anglezio, J. C. "Structure and Behaviour of Metallurgical Silicon." In *Electric Furnace Conference*, edited by Iron and Steel Society USA, New Orleans, USA, (1990): 241-247.

Flemings, M. C. *Solidification Processing*. New York: McGraw-Hill, (1974).

Forwald, K. *Properties of Some Silicon Rich Alloys*. Vol. 1997:127. Trondheim: NTNU, (1997).

Fujiwara, K. "Crystal Growth Behaviours of Silicon During Melt Growth Processes." *International Journal of Photoenergy*, (2012).

Gabrielsen, R. H. and Grue, J. *Norwegian Energy Policy in Context of the Global Energy Situation*. Oslo: Novus, (2012): pp 85-102.

Gaskell, D. R. *Introduction to the Thermodynamics of Materials*. New York: Taylor & Francis, (2008).

Geankoplis, C. J. *Transport Processes and Separation Process Principles (Includes Unit Operations)*. Prentice Hall, (2003).

Goldstein, J. I. et al. *Scanning Electron Microscopy and X-Ray Microanalysis*. New York: Kluwer Academic/Plenum Publishers, (2003):pp 256-269.

Gueneau, C., et al. "$FeAl_3Si_2$." *Acta Crystallographica Section C* 51, (1995**a**): 177-9.

Gueneau, C., et al. "$Fe_2Al_3Si_3$." *Acta Crystallographica Section C* 51, (1995**b**): 2461-2464.

Gueneau, C., et al. "Relationships between the Grinding Behavior and the Microstructure of Ferro-Silicon Alloys with 65 Wt% Silicon." In *INFACON 7*. Trondheim, (1995**c**).

Hamilton, D. R. and Seidensticker, R. G. "Propagation Mechanism of Germanium Dendrites." *Journal of Applied Physics* 31, (1960): 1165-1168.

Hjelen, J. *Scanning Electron Microscopy*. Trondheim: Department of Materials Science and Engineering, NTNU, (1989).

Hopkins, R. H. In *Proceedings of the Flat-Plate Solar Array Project Workshop on Low Cost Polysilicon for Terestrial Photovoltaic Solar-Cell Applications*. Las Vegas, (1985):15-36.

Hull, R. *Properties of Crystalline Silicon*. London: INSPEC, the Institution of Electrical Engineers, (1999).

Hunt, J. D. "Steady State Columnar and Equiaxed Growth of Dendrites and Eutectic." *Materials Science and Engineering* 65, (1984):75-83.

"Image J 1.46r" http://rsbweb.nih.gov/ij/ (2013).

"Image- Pro Analyzer“, Version 7.01.658, Media-Cybernetics© (2005-2009).

Incropera, F. P. and DeWitt, D. P. *Fundamentals of Heat and Mass Transfer*. New York: Wiley, (2002).

ISO-6507-1. "Metallic Materials- Vickers Hardness Test- Part 1: Test Method." (2005).

Kamfjord, N. E. *Mass and Energy Balances of the Silicon Process: - Improved Emission Standards*. Vol. 2012:162. Trondheim: NTNU, (2012).

Kattamis, T. Z., et al. "Influence of Coarsening on Dendrite Arm Spacing of Aluminium-Copper Alloys." *Transactions of the Metallurgical Society of AIME*, (1967): 239.

Kinoshita, M. and Champier, G. "Recrystallization of Cast Polycrystalline Silicon." *Materials Science and Engineering* 47, (1981): 29-35.

Klevan, O. S. *Removal of C and Sic from Si and FeSi During Ladle Refining and Solidification*. Vol. 1997:11. NTNU, (1997).

Kloc, C., et al. "Preparation and Properties of Fesi, A-Fesi2 and B-Fesi2 Single Crystals." *Journal of Alloys and Compounds* 219, (1995): 93-96.

Krendelsberger, N., et al. "On the Reaction Scheme and Liquidus Surface in the Ternary System Al-Fe-Si." *Metallurgical and Materials Transactions A: Physical Metallurgy and Materials Science* 38, (2007): 1681-1691.

Krogh, S. "Crushing and Screening." Elkem University, (1999).

Ksiazek, M. *The Thermophysical Properties of Raw Materials for Ferromanganese Production*. Vol. 2012:47. NTNU, (2012)

Kurz, W. and Fisher, D. J. *Fundamentals of Solidification*. Uetikon-Zuerich: Trans Tech Publications, (1998).

Liaw, H. M. "Crystal Growth of Silicon." In *Handbook of Semiconductor Silicon Technology*, (1990).

Lide, D. R. "Magnetic Susceptibility of the Elements and Inorganic Compounds." In *Crc Handbook of Chemistry and Physics*, (2005).

Liu, X., et al. "EPMA Analysis of Calcium-Rich Compounds in near Eutectic Al–Si Alloys." *Journal of Alloys and Compounds* 388, (2005): 83-90.

Liu, Z. K. and Chang, Y. A. "Thermodynamic Assessment of the Al-Fe-Si System." *Metallurgical and Materials Transactions A: Physical Metallurgy and Materials Science* 30, (1999): 1081-1095.

Ludwig, T. H., et al. *Metallurgical and Materials Transactions A: Physical Metallurgy and Materials Science* 44, (2013): 3783-3796.

Maex, K. and van Rossum, M. *Properties of Metal Silicides*. INSPEC, (1995).

Mangelinck-Noël, N. and Duffar, T. "Modelling of the Transition from a Planar Faceted Front to Equiaxed Growth: Application to Photovoltaic Polycrystalline Silicon." *Journal of Crystal Growth* 311, (2008): 20-25.

Margaria, T., et al. "Intermetallic Compounds in Metallurgical Grade Silicon." In *INFACON 6*, Cape Town, (1992): 209-214.

Margaria, T. "Identification and Control of the Characteristics of Silicon Used in Direct Synthesis." In *Silicon for the Chemical Industry,* (1994): 69-80.

Margaria, T., et al. "Silicon Refining: Experimental Studies and Industrial Means to Control Silicon Quality." In *Silicon for the Chemical Industry,* (1996): 21-31.

Martin, C., et al. "Detrimental Effect of Alkaline Impurities on Fused Silica Crucibles During Multi-Crystalline Ingot Growth." *CSSC3-workshop, Trondheim,* (2009).

Massalski, T. B. *Binary Alloy Phase Diagrams.* Materials Park, Ohio: ASM International, (1990).

Meteleva-Fischer, Y., et al. "Microstructure of Metallurgical Grade Silicon During Alloying Refining with Calcium." *Intermetallics* 25, (2012): 9-17.

Meteleva-Fischer, Y., et al. "Alloying Refining of Metallurgical Grade Silicon with Rare Earth Elements." (2013): 201-209.

Mills, K. C. and Courtney, L. "Thermophysical Properties of Silicon." *ISIJ International* 40, (2000): S130-S138.

Mjøs, Ø. *Directional Solidification of Silicon for Solar Cells.* Vol. 2006:109. Trondheim: NTNU, (2006).

Momma, K. and Izumi, F. "VESTA 3 for Three-Dimensional Visualization of Crystal, Volumetric and Morphology Data." *J. Appl. Crystallogr.* 44, (2011): 1272-1276.

Myrhaug, E. H. *Non-Fossil Reduction Materials in the Silicon Process: Properties and Behaviour.* Vol. 2003:67, NTNU, (2003).

Myrhaug, E. H. and Tveit, H. "Material Balances of Trace Elements in the Ferrosilicon and Silicon Processes." In *58th Electric Furnace Conference (*2000).

Møll, M. F., et al. "Study of the Solidification in a Silicon Alloy-Cooling Rate Vs. Microstructure." In *Silicon for the Chemical and Solar Industry XI*, Bergen -Ulvik, (2012).

Møll, M. F., et al. "The Main Reasons to Develop an Improved Casting Process for Silicon." In *INFACON XIII.* Kazakhstan, (2013).

Mørk, P. C. *Overflate Og Kolloidkjemi: Grunnleggende Prinsipper Og Teorier*. [Trondheim]: Norges teknisk-naturvitenskapelige universitet, Institutt for industriell kjemi, (1997).

Nygaard, L. "Silicon Solidification Techniques for the Chemical Industry." In *Silicon for the Chemical Industry* (2006): 71-78.

Nkosibomvu, Z. L., et al. "Mössbauer Spectroscopy and SEM Characterisation of Commercial Ferrosilicon Powders." *Hyperfine Interactions* 112, (1998): 261-265.

Næss, M. K. *Mechanisms and Kinetics of Liquid Silicon Oxidation*. Vol. 2013:145. Trondheim: NTNU, (2013).

Oberteuffer, J. "Magnetic Separation: A Review of Principles, Devices, and Applications." *Magnetics, IEEE Transactions on* 10, (1974): 223-238.

Ott, E. *Solidification of Two Ferroalloys, FeSi 75wt%Si and MC-FeMn: Formation of Microstructure and Cracks*, NTNU, (2003).

Queiroz, A. M., et al. "Acid Refining of Synthesised Alloys within the Quaternary System Fe-Si-Ca-Al: Effect of Ferric Ions." *Mineral Processing and Extractive Metallurgy Review* 22, SCPEC. ISS (2001): 303-322.

Raghavan, V. "Al-Fe-Si (Aluminum-Iron-Silicon)." *Journal of Phase Equilibria and Diffusion* 30, (2009): 184-188.

Raghavan, V. "Al-Fe-Si (Aluminum-Iron-Silicon)." *Journal of Phase Equilibria and Diffusion*, (2010): 1-3.

Rivlin, V. G. and Raynor, G. V. "Phase Equilibria in Iron Ternary Alloys - 4. Critical Evaluation of Constitution of Aluminium-Iron-Silicon System." *International metals reviews* 26, (1981): 133-152.

Rong, H. "*Silicon for the Direct Process to Methylchlorosilanes*." NTNU, (1992).

Rong, H., et al. "Fremgangsmåte for å fjerne forurensinger fra silisium-innholdende residue." edited by Elkem ASA, (2002).

Safarian, J. and Tangstad, M. "Vacuum Refining of Molten Silicon." *Metallurgical and Materials Transactions B: Process Metallurgy and Materials Processing Science*, (2012): 1-19.

Sandvik, K. L., et al. *Oppredning Av Primære Og Sekundære Råstoffer*. Trondheim: Tapir, (1999).

Schei, A., et al. "Impurity Distribution in Silicon." In *Silicon for the Chemical Industry*, (1992): 11-23.

Schei, A., et al. *Production of High Silicon Alloys*. Trondheim: Tapir forlag, (1998).

SIMS, "Secondary Ion Mass Spectrometry, Sims Analysis", http://www.eaglabs.com/mc/secondary-ion-mass-spectrometry.html. (2013)

Shimpo, T., et al. "Thermodynamic Study of the Effect of Calcium on Removal of Phosphorus from Silicon by Acid Leaching Treatment." *Metallurgical and Materials Transactions B: Process Metallurgy and Materials Processing Science* 35, (2004): 277-284.

Schussler, G., et al. "Intermetallic Silicides in Refined Metallurgical Grade Silicon."In *Silicon for the Chemical Industry,* (1992):25-37.

Sherrell, I. and Dunn, P. "Recent Advances in High Gradient Magnetic Separators.", (2012): 241-248.

Sigmund, H. "Solubilities of Magnesium and Calcium in Silicon." *Journal of the Electrochemical Society* 129, (1982): 2809-2812.

Stølen, S., et al. *Chemical Thermodynamics of Materials : Macroscopic and Microscopic Aspects*. Chichester: Wiley, (2004).

Sverdlin, A. ""Chips"- Process for Cast Iron Inoculation." *Foundary Management and Technology,* (1994).

Takeda, S. and Mutuzaki, K. *Tetsu-to Hagane* 26, (1940): 335-361.

Tang, K. "FactSage Modelling MG-Si.", Personal Communication, (2013).

Tangstad, M. *Metal Production in Norway*. Akademika Forlag, (2013):pp 181-200.

Tangstad, M., et al. "Behavior of Agglomerates in Ferromanganese Production." In *12th International Ferroalloys Congress, INFACON.* Helsinki, Finland, (2010): 457-465.

Tranell, G., et al. "Silicon Feedstock for Solar Cells – Availability, Quality Criteria and Future Production Routes." In *Proceedings of the 4th*

International Workshop on Science and Technology of Crystalline Silicon Solar Cells, CSSC4. , (2012).

ThermoCAM™ Researcher Pro 2.10, Copyright© (2007-2010) FLIR Systems AB

Trumbore, F. A. "Solid Solubilities of Impurity Elements in Germanium and Silicon." *Bell System Technical Journal* 39, (1960): 205-233.

Tveit, H. *Størkning Av 75% Ferrosilisium : Forløp, Struktur Og Styrke*. Vol. 1988:53. NTNU,(1988).

Tveit, H., Personal Communication, (2013.)

Wagner, R. S. "On the Growth of Germanium Dendrites." *Acta Metallurgica* 8, (1960): 57-60.

Weitzer, F., et al. "On the Reaction Scheme and Liquidus Surface in the Ternary System Fe–Si–Ti." *Intermetallics* 16, (2008): 273-282.

Xiong, D., et al. "New Technology of Pulsating High Gradient Magnetic Separation." *International Journal of Mineral Processing* 54, (1998): 111-127.

Zulehner, W. and Huber, D. "Czochralski Grown Silicon." *Crystals* 8, (1982).

Zumdahl, S. S. *Chemical Principles*. Boston: Houghton Mifflin Company, (1998).

Aas, H. "Silgrain Process Silicon Metal from 90% Ferrosilicon." *Met Soc AIME, TMS,* (1971).

Appendix A- Chemical analysis

In the following chemical analysis from a selection of experiments are given. Sample D, G, H, 2.1-2.3, Ingot 1-3, were analysed at Elkem Thamshavn and sample 3.1-3.5 and bulk analysis Cyberstar were analysed at Elkem Technology. Values marked with a star are below the detection limit of the XRF at Thamshavn.

Table A.1: Average chemical analysis sample D, MG-Si2 Industrial..

Position from top [cm]	wt %				ppmw					
	Al	Ca	Fe	Ti	Mg	Cu	Mn	V	Sn	P
0-2.5	0.22	0.03	0.44	0.03	22	21	59	10	17	31
2.5-5	0.17	0.03	0.34	0.02	24	12	45	9	14	25
5-7.5	0.20	0.04	0.37	0.02	22	14	50	9	15	27
7.5-10	0.27	0.05	0.54	0.03	23	20	72	14	14	31
10-11.5	0.13	0.03	0.25	0.02	20	12	33	7	16	23

Table A.2: Average chemical analysis sample G, MG-Si2 Industrial.

Position from top [cm]	wt %				ppmw					
	Al	Ca	Fe	Ti	Mg	Cu	Mn	V	Sn	P
0-2	0.12	0.02	0.25	0.02	22	12	36	8	14	25
2-4	0.24	0.04	0.48	0.03	27	17	66	13	14	29
4-6	0.23	0.04	0.44	0.03	24	19	59	12	12	27
6-8	0.14	0.04	0.35	0.02	23	16	47	10	14	26
8-10	0.14	0.02	0.52	0.02	22	44	60	10	13	31

Table A.3: Average chemical analysis sample H, MG-Si2 quality cast on another day.

Position from top [cm]	wt %				ppmw					
	Al	Ca	Fe	Ti	Mg	Cu	Mn	V	Sn	P
0-2.5	0.11	0.02	0.17	0.01	19*	9*	22	6	15	14
2.5-5	0.25	0.12	0.26	0.02	26	15	31	6	15	17
5-7.5	0.24	0.04	0.37	0.02	22	19	45	10	16	19
7.5-10	0.16	0.03	0.27	0.02	24	13	31	8	16	16
10-13.5	0.12	0.02	0.20	0.01	19	8*	30	4*	14	15

Table A.4: Chemical analysis sample 2.1, Copper plate experiment, MG-Si1.

Position from top [cm]	**wt %**				**ppmw**					
	Al	**Ca**	**Fe**	**Ti**	**Mg**	**Cu**	**Mn**	**V**	**Sn**	**P**
0-0.75	0.08	0.01	0.33	0.02	34	38	43	8	13	19
0.75-1.5	0.09	0.01	0.22	0.02	43	23	29	5	14	25

Table A.5: Chemical analysis sample 2.2, Copper plate experiment, MG-Si1.

Position from top [cm]	**wt %**				**ppmw**					
	Al	**Ca**	**Fe**	**Ti**	**Mg**	**Cu**	**Mn**	**V**	**Sn**	**P**
0-1.0	0.03	0.00	0.19	0.01	26	21	26	5	14	13
1.0-2.0	0.06	0.01	0.32	0.02	30	39	44	9	15	17
2.0-3.0	0.04	0.01	0.19	0.01	29	20	22	6	15	15

Table A.6: Chemical analysis sample 2.3, Copper plate experiment, MG-Si1.

Position from top [cm]	**wt %**				**ppmw**					
	Al	**Ca**	**Fe**	**Ti**	**Mg**	**Cu**	**Mn**	**V**	**Sn**	**P**
0-1.0	0.03	0.01	0.19	0.01	28	20	26	5	16	14
1.0-2.0	0.07	0.01	0.42	0.03	33	69	57	12	12	17
2.0-3.0	0.03	0.00	0.19	0.01	26	23	25	6	15	15

Table A.7: Average chemical analysis sample 3.1, Copper plate experiment, MG-Si2.

Position from top [cm]	**wt %**				**ppmw**					
	Al	**Ca**	**Fe**	**Ti**	**V**	**Cr**	**Mn**	**Ni**	**Cu**	**Zr**
0-0.75	0.15	0.00	0.48	0.03	21	21	56	12	15	24
0-75-1.5	0.12	0.00	0.40	0.03	18	17	45		13	20

Table A.8: Average chemical analysis sample 3.2, Copper plate experiment, MG-Si2.

Position from top [cm]	**wt %**				**ppmw**					
	Al	**Ca**	**Fe**	**Ti**	**V**	**Cr**	**Mn**	**Ni**	**Cu**	**Zr**
0-1.0	0.10		0.35	0.02	17		39		13	18
1.0-2.0	0.16		0.54	0.03	21	21	65	12	16	29
2.0-3.0	0.09		0.35	0.02	16		39		11	19

Table A.9: Average chemical analysis sample 3.3, Copper plate experiment, MG-Si2..

Position from top [cm]	**wt %**				**ppmw**					
	Al	**Ca**	**Fe**	**Ti**	**V**	**Cr**	**Mn**	**Ni**	**Cu**	**Zr**
0-1.0	0.09		0.28	0.02	13.5		29		10	13
1.0-2.0	0.18		0.55	0.03	23	18	65	10	18	29
2.0-3.0	0.10		0.32	0.02	16		35		12	16

Table A.10: Average chemical analysis sample 3.4, Copper plate experiment, MG-Si2..

Position from top [cm]	**wt %**				**ppmw**					
	Al	**Ca**	**Fe**	**Ti**	**V**	**Cr**	**Mn**	**Ni**	**Cu**	**Zr**
0-1.0	0.09		0.32	0.02	18		34		12	16
1.0-2.0	0.17		0.49	0.03	21		58		15	26
2.0-3.0	0.12		0.36	0.02	16		41		14	18
3.0-4.0	0.10		0.32	0.02	16		35		12	16
4.0-5.0	0.11		0.35	0.02	17		40		11	18

Table A.11: Average chemical analysis sample 3.5, Copper plate experiment, MG-Si2..

Position from top [cm]	**wt %**				**ppmw**					
	Al	**Ca**	**Fe**	**Ti**	**V**	**Cr**	**Mn**	**Ni**	**Cu**	**Zr**
0-1.0	0.08		0.28	0.02	14		32		11	15
1.0-2.0	0.17		0.49	0.03	22		58		16	26
2.0-3.0	0.13		0.37	0.02	17		43		13	19
3.0-4.0	0.12		0.38	0.02	18		44		14	20
4.0-5.0	0.11		0.33	0.02	15		38		12	18

Table A.12: Average chemical analysis Ingot 1, Cyberstar, MG-Si2.

	wt %				**ppmw**								
fs	**Al**	**Ca**	**Fe**	**Ti**	**Mg**	**Zr**	**Cu**	**Ni**	**Mn**	**Cr**	**V**	**Sn**	**P**
0-0.2	0.03	0.01	0.00	0.00	23	0*	3*	1*	1*	0*	0*	14	19
0.2-0.4	0.07	0.00	0.31	0.02	31	19*	10	6	37	5	7	13	34
0.4-0.6	0.13	0.00	0.60	0.03	32	34	17	10	73	16	11	12	39
0.6-0.8	0.21	0.01	0.94	0.05	33	51	27	14	113	29	16	15	46
0.8-1	0.95	0.02	3.03	0.16	30	134	120	52	421	106	19	15	71

Table A.13: Average chemical analysis Ingot 2, Cyberstar, MG-Si1.

	wt %				**ppmw**								
fs	**Al**	**Ca**	**Fe**	**Ti**	**Mg**	**Zr**	**Cu**	**Ni**	**Mn**	**Cr**	**V**	**Sn**	**P**
0-0.2	0.01	0.01	0.00	0.00	26	1*	2*	2*	2*	0*	0*	14	12
0.2-0.4	0.07	0.01	0.46	0.03	41	21	26	9	56	14	15	14	28
0.4-0.6	0.10	0.01	0.67	0.04	59	30	43	13	81	26	21	14	32
0.6-0.8	0.15	0.02	0.91	0.06	73	39	72	20	114	37	28	14	35
0.8-1	0.62	0.05	2.56	0.15	53	89	287	59	383	107	75	12	58

Table A.14: Average chemical analysis Ingot 3, Cyberstar, MG-Si2.

fs	wt %				ppmw								
	Al	**Ca**	**Fe**	**Ti**	**Mg**	**Zr**	**Cu**	**Ni**	**Mn**	**Cr**	**V**	**Sn**	**P**
0-0.2	0.07	0.02	0.13	0.01	22	7*	8*	3*	16	1*	3*	14	28
0.2-0.4	0.25	0.01	1.17	0.06	23	64	27	18	132	38	27	15	47
0.4-0.6	0.28	0.01	1.19	0.06	27	64	28	18	139	36	27	14	47
0.6-0.8	0.34	0.01	1.29	0.07	25	68	37	21	158	41	32	14	52
0.8-1	1.24	0.03	3.24	0.17	17	142	127	58	448	109	70	13	76

Table A.15: Sample cut from top to bottom Cyberstar ingots. The samples have been extracted as illustrated in Figure 3.13

Sample	wt %				ppmw				
	Al	**Ca**	**Fe**	**Ti**	**V**	**Cr**	**Mn**	**Zr**	**P**
Ingot 1	0.26	0.01	0.69	0.04	24	15	85	34	45
Ingot 2	0.02	<0.002	0.04	0.00	<10	<15	<10	<10	25
Ingot 3	0.11	0.00	0.25	0.01	12	<15	27	11	62*

Appendix B

B.1 Grain distribution in the samples

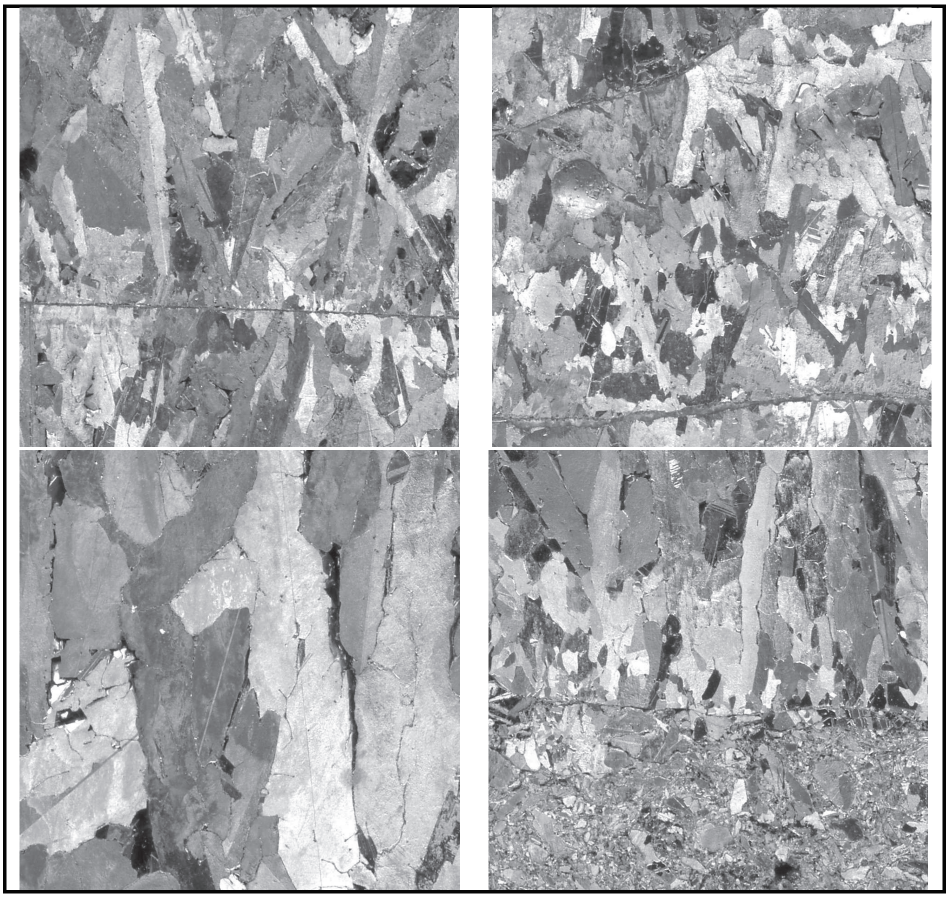

Figure B.1: Examples of grain size from sample A1, alloy A- Upper left is from top, lower right from bottom. Each square equals an area of 1cm x 1cm. The area where the magnification is from is illustrated as squares in Figure 5.11.

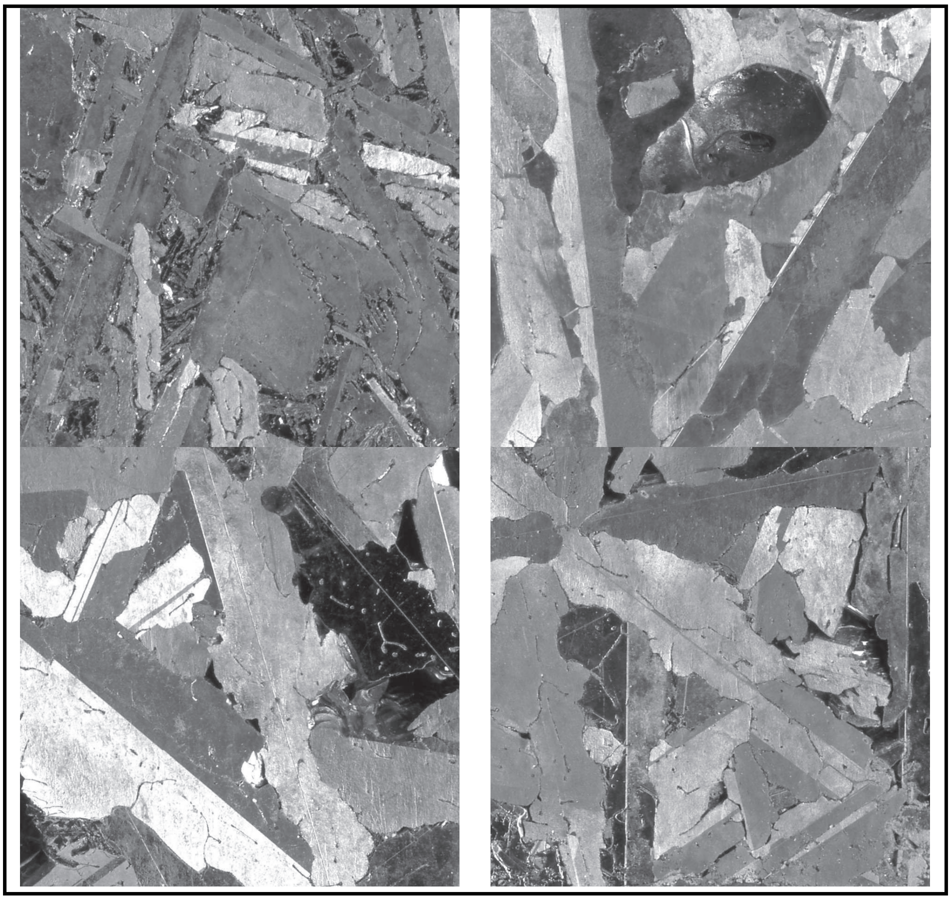

Figure B.2 : Examples of grain size from sample A2, alloy A. Each square equals an area of 1cm x 1cm.

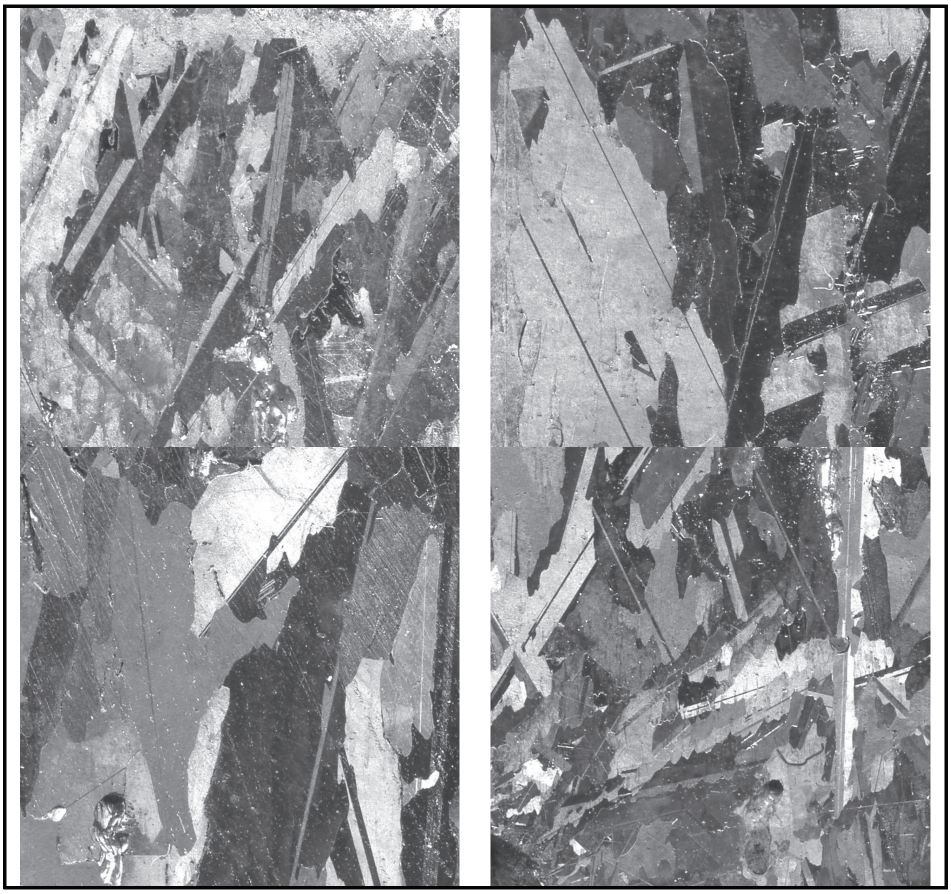

Figure B.3: Examples of grain size from sample B, MG-Si2 industrial. Each square equals an area of 1cm x 1cm. From upper left to lower right the samples have been collected, 0-1 cm from top, 5 cm from top, 7-8 cm from top, and 9-10 cm from top (close to mould/fines layer).

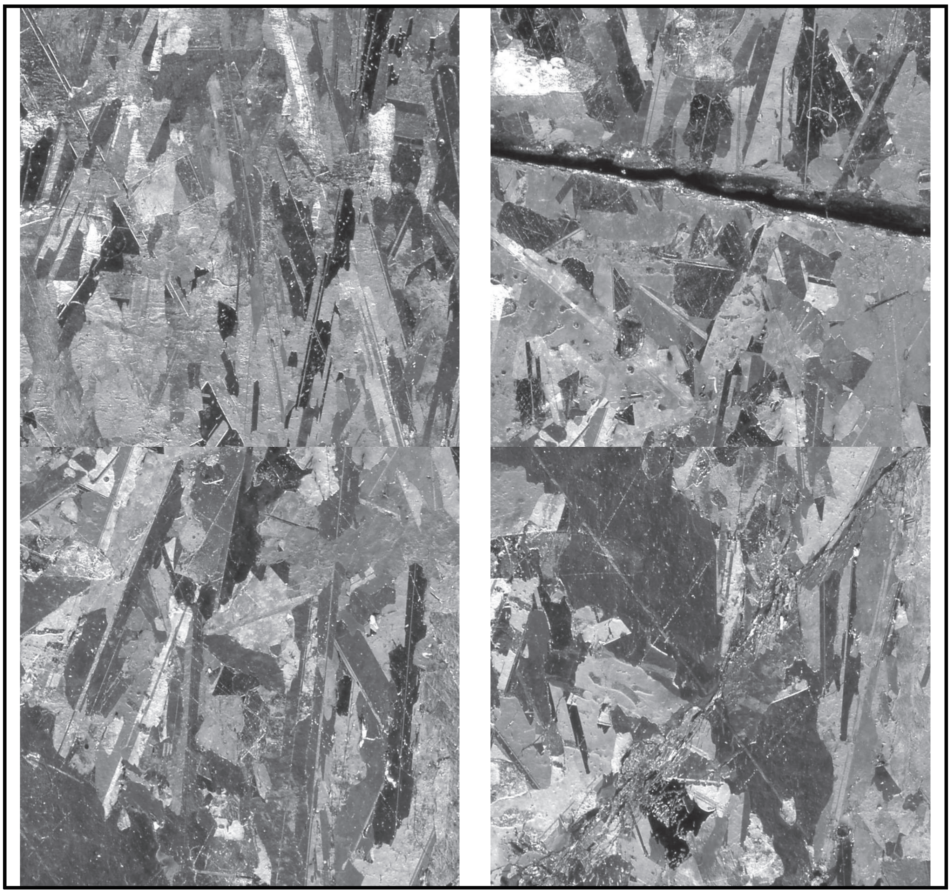

Figure B.4: Examples of grain size from sample 3.5 (5 cm) - copper plate, MG-Si2. Each square equals an area of 1cm x 1cm.

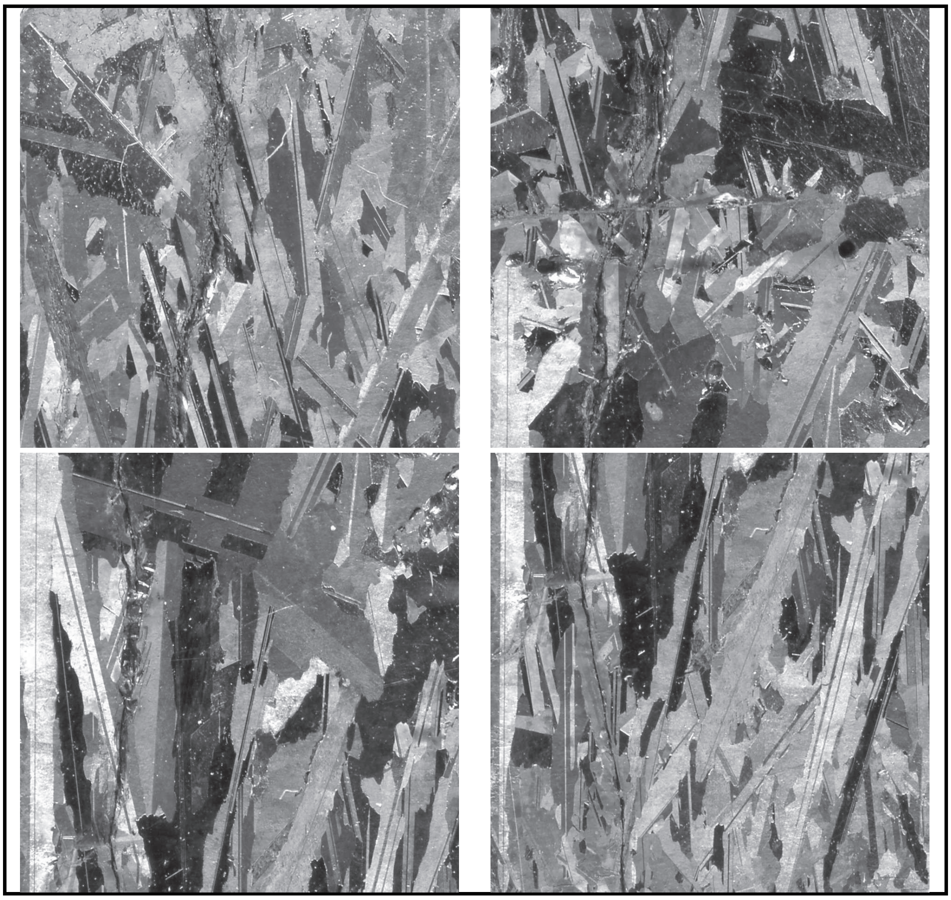

Figure B.5: Examples of grain size from sample 2.3 (3 cm) - copper plate, MG-Si1. Each square equals an area of 1cm x 1cm.

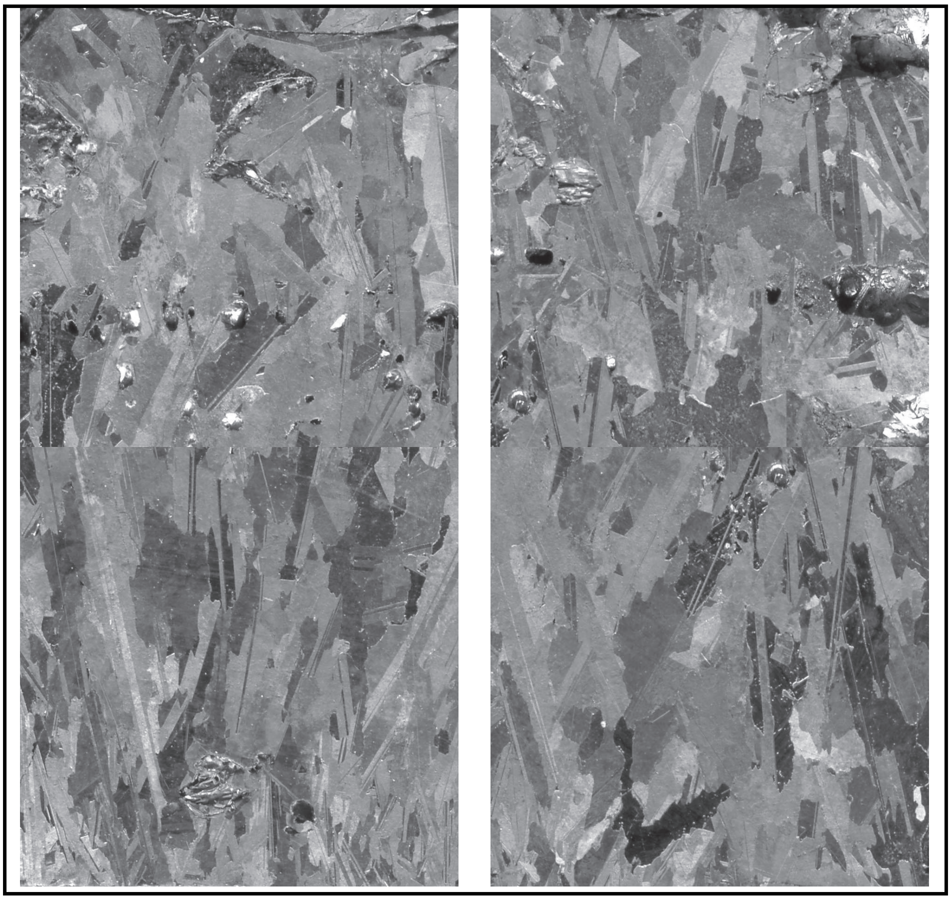

Figure B.6: Examples of grain size from sample 2.1 (1.5 cm) – copper plate, MG-Si1. Each square equals an area of 1cm x 1cm.

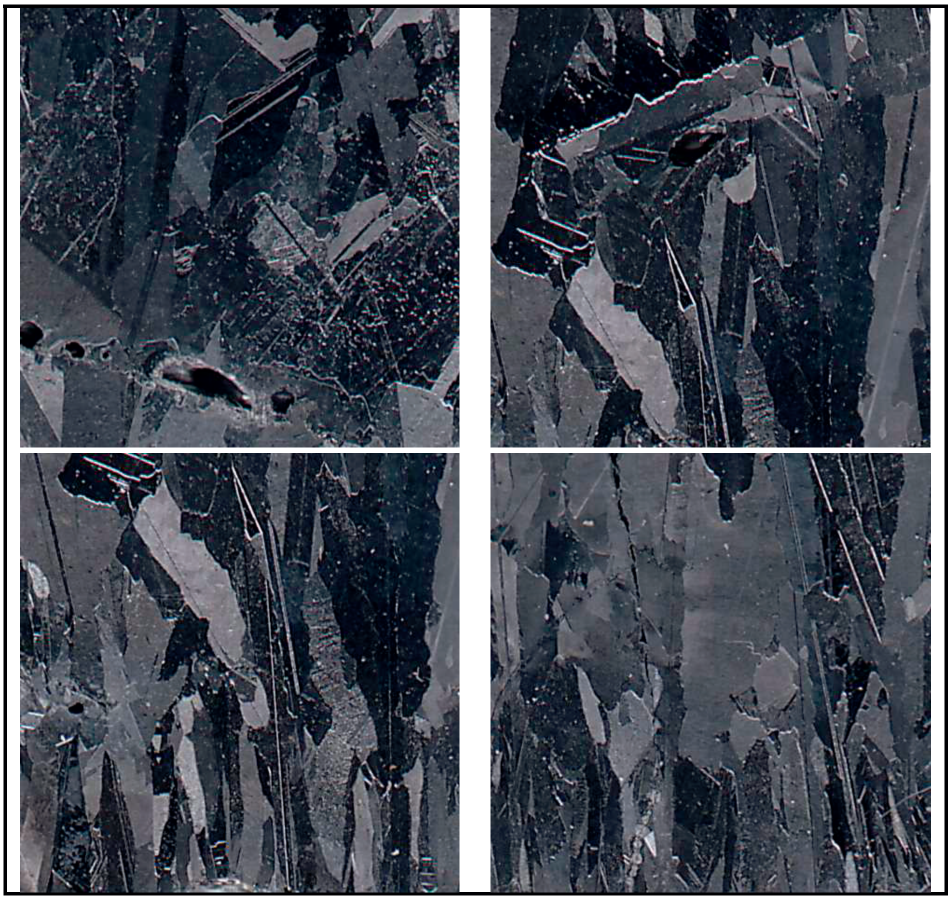

Figure B.7: Examples of grain size from sample 1.1 (3 cm) – copper plate, SoG-Si. Each square equals an area of 1cm x 1cm.

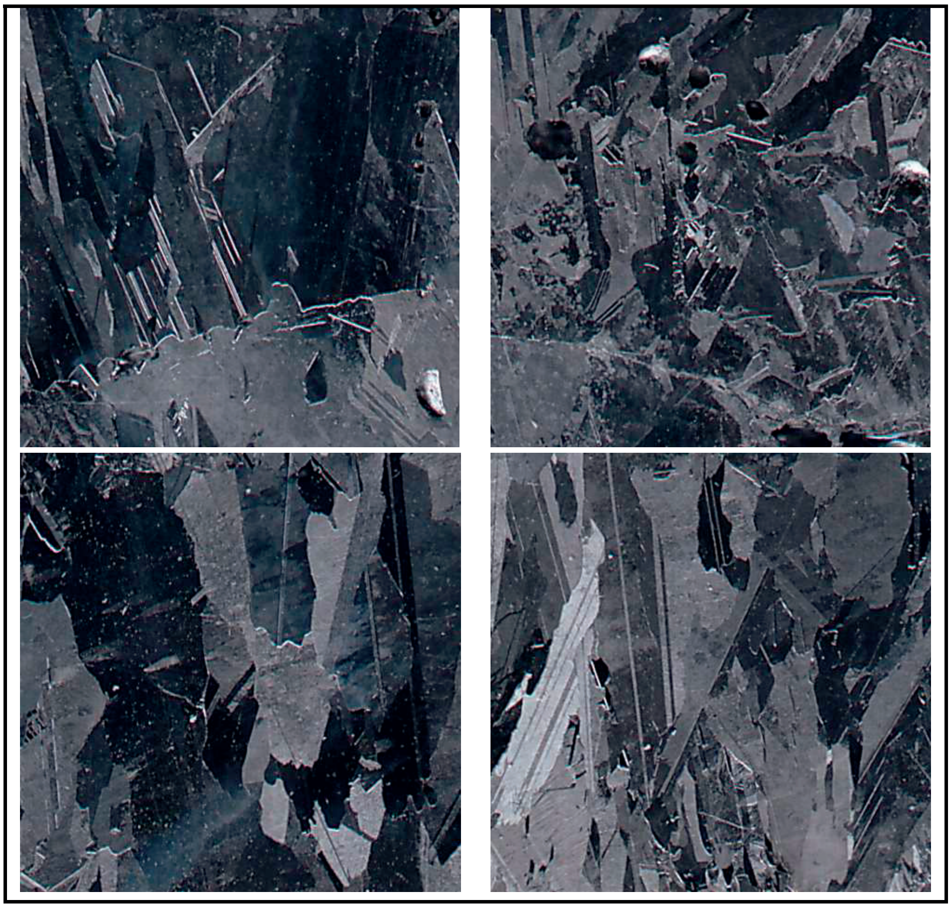

Figure B.8: Examples of grain size from sample 1.2 (5 cm) – copper plate, SoG-Si. Each square equals an area of 1cmx1cm.

B.2 Distribution of intermetallic phases

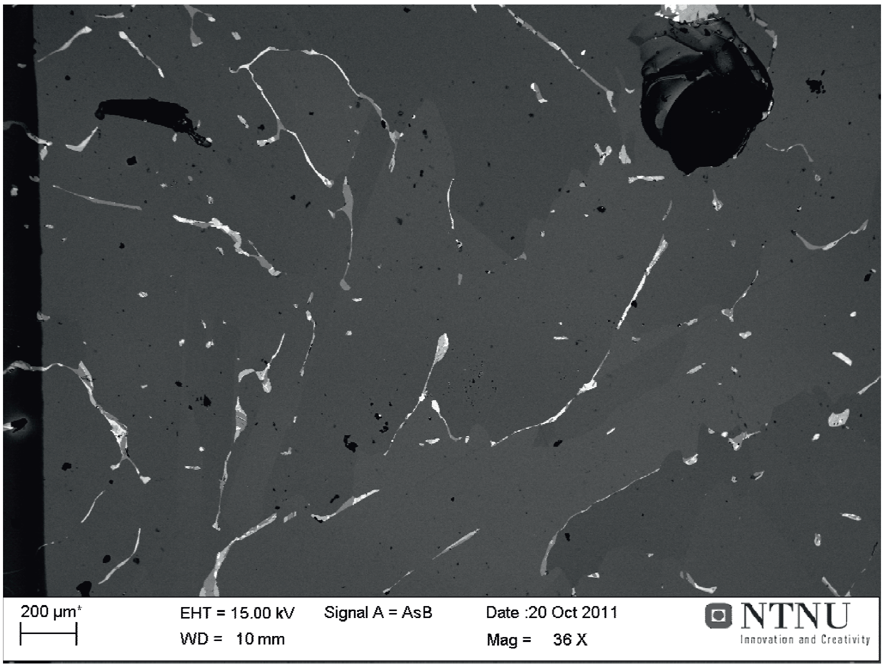

Figure B.9: SEM micrograph close to the top, sample A1, experiment A1.

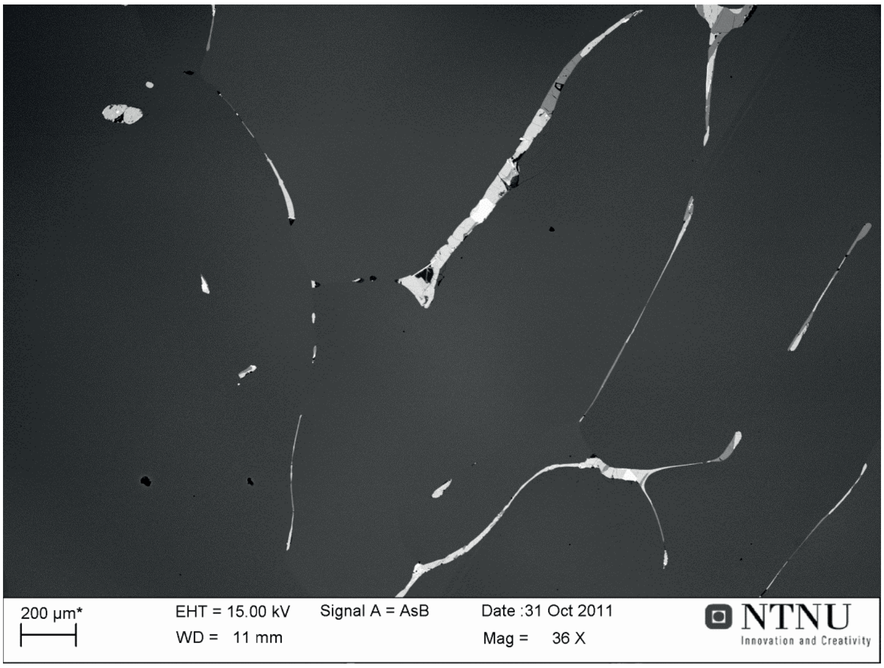

Figure B.10 SEM micrograph, sample 2.2, experiment A2.

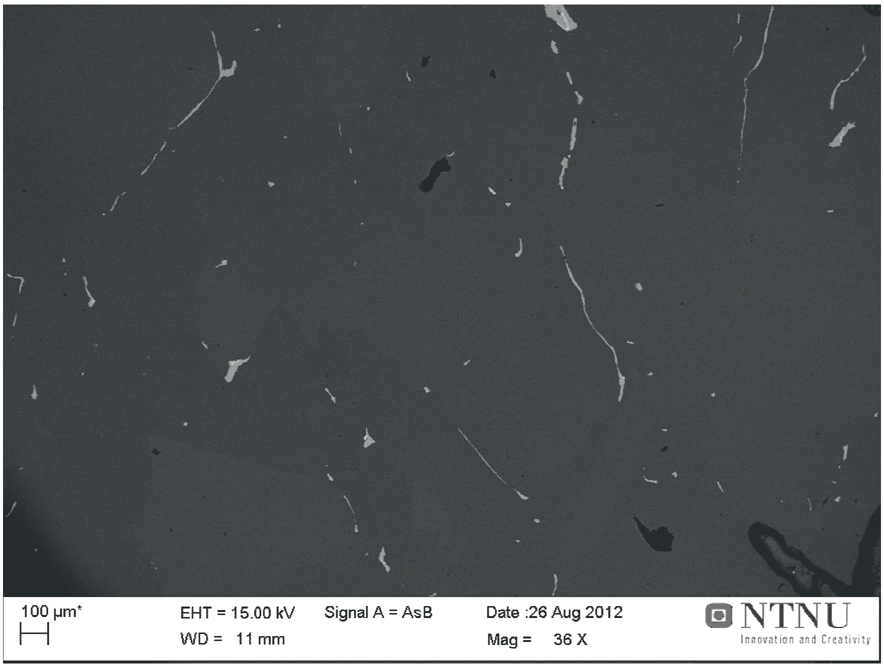

Figure B.11: SEM micrograph close to the top, sample B, experiment MG-Si2.

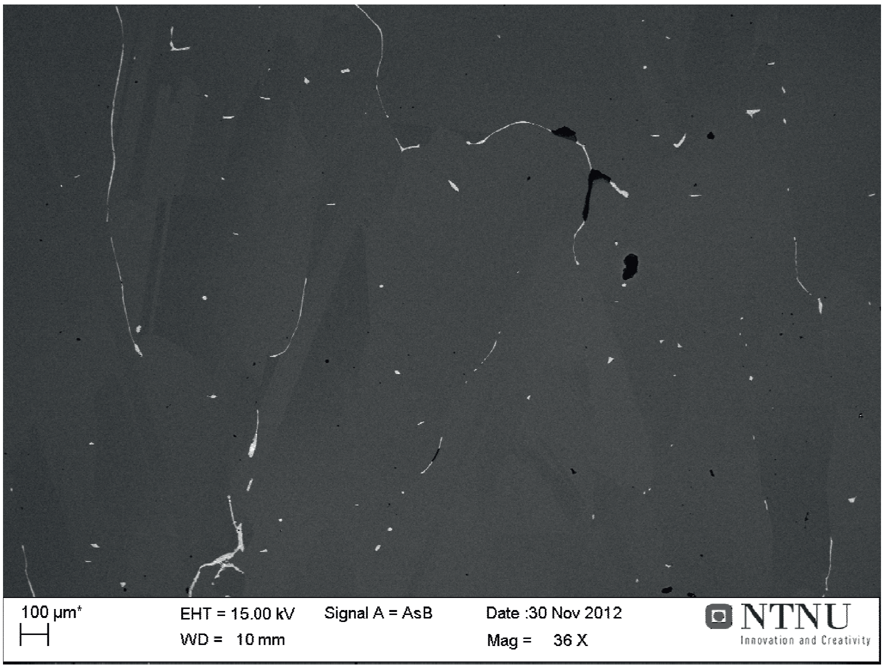

Figure B.12: SEM micrograph close to the top, sample 3.5- copper plate experiment.

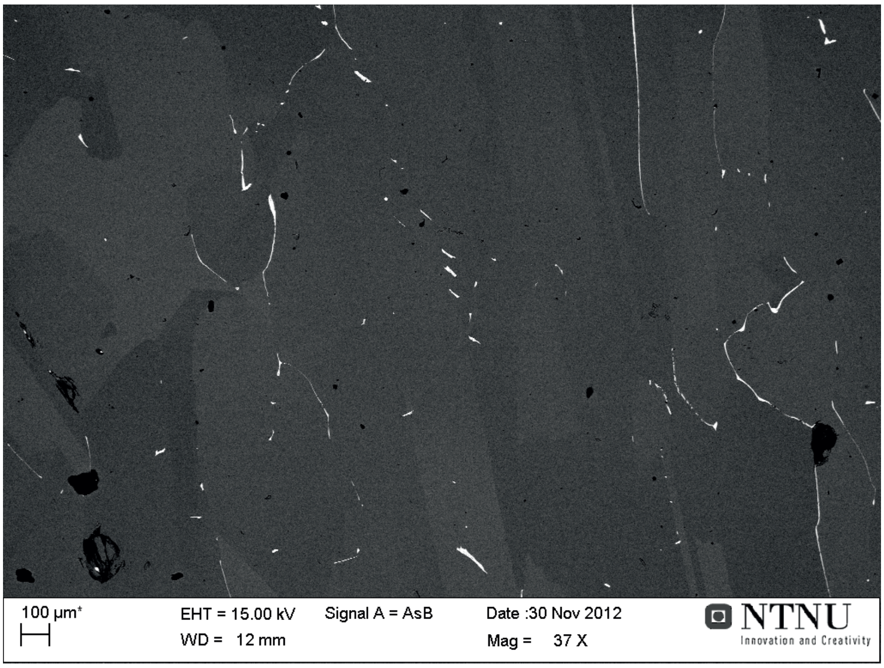

Figure B.13: SEM micrograph close to the top, sample 3.3- copper plate experiment.

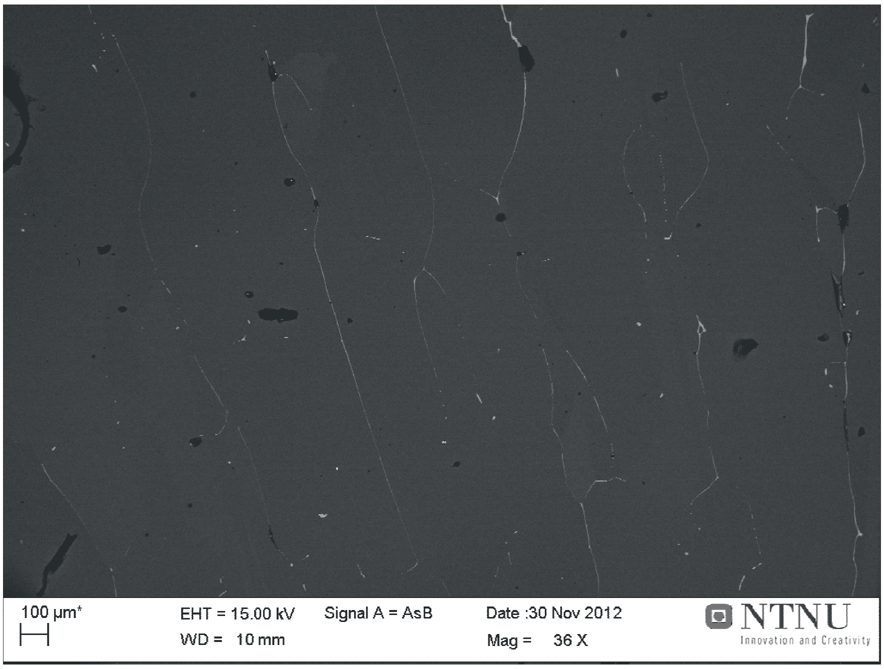

Figure B.14: SEM micrograph close to the top, sample 3.1- copper plate experiment.

B.3 EBSD grain size measurement

Table B. 1: Grain size of a section sample B, top part.

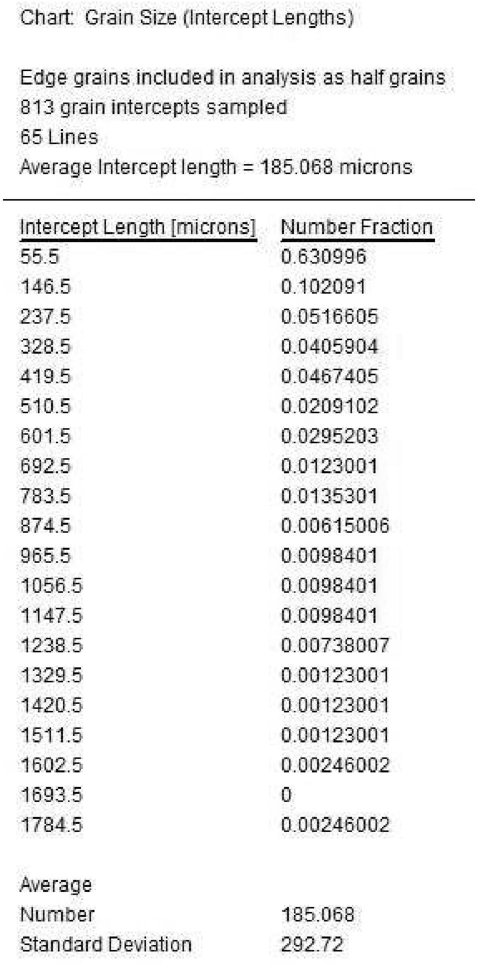

Chart: Grain Size (Intercept Lengths)

Edge grains included in analysis as half grains
813 grain intercepts sampled
65 Lines
Average Intercept length = 185.068 microns

Intercept Length [microns]	Number Fraction
55.5	0.630996
146.5	0.102091
237.5	0.0516605
328.5	0.0405904
419.5	0.0467405
510.5	0.0209102
601.5	0.0295203
692.5	0.0123001
783.5	0.0135301
874.5	0.00615006
965.5	0.0098401
1056.5	0.0098401
1147.5	0.0098401
1238.5	0.00738007
1329.5	0.00123001
1420.5	0.00123001
1511.5	0.00123001
1602.5	0.00246002
1693.5	0
1784.5	0.00246002

Average	
Number	185.068
Standard Deviation	292.72

Appendix C

C.1 Results from EPMA

In the following the results from the EPMA of the most frequently observed intermetallic phases in each the experiments are presented. Each phase is represented with a **mean atomic %,** the standard deviation (STD) and the number of point analysis of an element in a given phase (#).

For the first EPMA analysis performed on MG-Si2 industrial, only elements Al, O, C, P, Si, Ca, Ti and Fe were searched for. For the second run also V, Cr, Mn, Zr, Ni, Ba, Cu, Pb and Zn were analysed in addition to Ba, La, Ce, Nd, W and Mg for A1 and A2, and W and Mg for the copper plate and Cyberstar experiments.

Al_3FeSi_2

A1

	Al	V	P	Si	Cr	Ca	Mn	Ti	Fe	Zr	Ni	Ba	Cu	Pb	Zn	Mg	W
Mean	48.87	0.02	0.00	34.79	0.04	0.09	0.21	0.01	15.82	0.00	0.01	0.09	0.00	0.00	0.01	0.01	0.01
STD	3.62	0.03	0.01	1.96	0.02	0.09	0.03	0.02	1.44	0.00	0.01	0.35	0.01	0.00	0.01	0.01	0.01
#	15	15	15	15	15	15	15	15	15	15	15	15	15	15	15	15	15

A2

	Al	V	P	Si	Cr	Ca	Mn	Ti	Fe	Zr	Ni	Ba	Cu	Pb	Zn	Mg	W
Mean	51.69	0.03	0.00	32.29	0.01	0.09	0.13	0.01	15.70	0.00	0.01	0.00	0.01	0.01	0.00	0.01	0.01
STD	1.27	0.03	0.01	1.18	0.01	0.11	0.04	0.01	0.31	0.00	0.01	0.00	0.02	0.01	0.01	0.01	0.01
#	17	17	17	17	17	17	17	17	17	17	17	17	17	17	17	17	17

MG-Si2 Industrial

	Al	V	P	Si	Cr	Ca	Mn	Ti	Fe	Zr	Ni	Ba	Cu	Pb	Zn
Mean	44.56	0.05	0.01	39.88	0.09	0.04	0.48	0.11	14.97	0.02	0.02	0.01	0.10	0.00	0.01
STD	2.12	0.06	0.01	2.00	0.06	0.14	0.12	0.23	0.68	0.06	0.02	0.01	0.04	0.00	0.01
#	25	14	25	25	14	25	14	25	25	14	14	14	14	14	14

Copper plate MG-Si1

	Al	V	P	Si	Cr	Ca	Mn	Ti	Fe	Zr	Ni	Ba	Cu	Pb	Zn
Mean	46.97	0.03	0.00	37.72	0.08	0.00	0.54	0.04	14.19	0.00	0.19	0.00	0.21	0.00	0.02
STD	2.25	0.03	0.00	2.44	0.08	0.00	0.17	0.03	0.37	0.01	0.17	0.00	0.08	0.01	0.01
#	4	4	4	4	4	4	4	4	4	4	4	4	4	4	4

Copper plate MG-Si2

	Al	V	P	Si	Cr	Ca	Mn	Ti	Fe	Zr	Ni	Ba	Cu	Pb	Zn
Mean	46.68	0.02	0.00	37.83	0.08	0.00	0.58	0.10	14.54	0.00	0.08	0.00	0.07	0.00	0.01
STD	4.64	0.03	0.00	4.30	0.04	0.00	0.36	0.16	0.70	0.01	0.06	0.00	0.04	0.00	0.01
#	18	18	18	18	18	18	18	18	18	18	18	18	18	18	18

Cyberstar MG-Si1

	Al	V	P	Si	Cr	Ca	Mn	Ti	Fe	Zr	Ni	Ba	Cu	Pb	Zn	Mg	W
Mean	46.14	0.02	0.00	37.98	0.06	0.00	0.69	0.03	14.88	0.00	0.04	0.00	0.15	0.00	0.01	0.00	0.00
STD	0.18	0.03	0.01	0.16	0.03	0.00	0.33	0.05	0.25	0.00	0.01	0.00	0.06	0.00	0.02	0.00	0.00
#	4	4	4	4	4	4	4	4	4	4	4	4	4	4	4	4	4

Cyberstar MG-Si2

	Al	V	P	Si	Cr	Ca	Mn	Ti	Fe	Zr	Ni	Ba	Cu	Pb	Zn	Mg	W
Mean	44.92	0.01	0.00	39.03	0.12	0.00	0.59	0.06	14.97	0.01	0.01	0.00	0.23	0.00	0.02	0.01	0.00
STD	1.31	0.02	0.00	1.21	0.05	0.00	0.18	0.08	0.32	0.02	0.02	0.00	0.10	0.00	0.03	0.02	0.00
#	10	10	10	10	10	10	10	10	10	10	10	10	10	10	10	10	10

$Al_6CaFe_4Si_8$

A1

	Al	V	P	Si	Cr	Ca	Mn	Ti	Fe	Zr	Ni	Ba	Cu	Pb	Zn	Mg	W
Mean	35.66	0.02	0.01	38.88	0.01	5.32	0.09	0.02	19.78	0.01	0.01	0.01	0.01	0.00	0.01	0.17	0.01
STD	4.20	0.03	0.01	1.79	0.01	0.44	0.03	0.02	2.10	0.01	0.01	0.01	0.01	0.00	0.02	0.07	0.02
#	15	15	15	15	15	15	15	15	15	15	15	15	15	15	15	15	15

MG-Si2 Industrial

	Al	V	P	Si	Cr	Ca	Mn	Ti	Fe	Zr	Ni	Ba	Cu	Pb	Zn
Mean	30.95	0.02	0.02	43.06	0.02	5.34	0.18	0.03	20.50	0.01	0.03	0.00	0.01	0.00	0.01
STD	0.84	0.03	0.02	0.72	0.02	0.26	0.03	0.04	0.72	0.01	0.02	0.00	0.01	0.00	0.01
#	66	24	66	66	24	66	24	66	66	24	24	24	24	24	24

Copper plate MG-Si1

	Al	V	P	Si	Cr	Ca	Mn	Ti	Fe	Zr	Ni	Ba	Cu	Pb	Zn
Mean	31.87	0.04	0.03	43.04	0.04	4.80	0.23	0.09	19.69	0.04	0.09	0.00	0.03	0.00	0.00
STD	0.49	0.04	0.01	0.32	0.00	0.13	0.02	0.11	0.15	0.02	0.01	0.00	0.01	0.00	0.01
#	3	3	3	3	3	3	3	3	3	3	3	3	3	3	3

Copper plate MG-Si2

	Al	V	P	Si	Cr	Ca	Mn	Ti	Fe	Zr	Ni	Ba	Cu	Pb	Zn
Mean	34.76	0.00	0.03	40.85	0.06	3.71	0.39	0.05	19.55	0.04	0.48	0.00	0.07	0.00	0.01
STD	15.59	0.00	0.02	18.30	0.05	1.68	0.19	0.03	8.80	0.03	0.67	0.00	0.11	0.00	0.01
#	4	4	4	4	4	4	4	4	4	4	4	4	4	4	4

Cyberstar MG-Si1

	Al	V	P	Si	Cr	Ca	Mn	Ti	Fe	Zr	Ni	Ba	Cu	Pb	Zn	W	Mg
Mean	31.72	0.00	0.02	41.55	0.02	5.11	0.21	0.30	20.32	0.03	0.07	0.00	0.11	0.00	0.01	0.52	0.01
STD	1.38	0.01	0.03	0.83	0.02	0.22	0.04	0.44	0.19	0.05	0.06	0.00	0.04	0.00	0.02	0.40	0.01
#	6	6	6	6	6	6	6	6	6	6	6	6	6	6	6	6	6

Cyberstar MG-Si2

	Al	V	P	Si	Cr	Ca	Mn	Ti	Fe	Zr	Ni	Ba	Cu	Pb	Zn	W	Mg
Mean	33.24	0.05	0.07	40.76	0.01	4.86	0.19	0.01	20.56	0.01	0.05	0.00	0.05	0.00	0.01	0.04	0.08
STD	0.69	0.05	0.03	0.86	0.02	0.14	0.08	0.01	0.37	0.02	0.03	0.00	0.05	0.00	0.02	0.11	0.13
#	9	9	9	9	9	9	9	9	9	9	9	9	9	9	9	9	9

Al_2CaSi_2

A1

	Al	V	P	Si	Cr	Ca	Mn	Ti	Fe	Zr	Ni	Ba	Cu	Pb	Zn	Mg	W
Mean	41.68	0.01	0.15	38.43	0.01	19.42	0.01	0.01	0.19	0.00	0.00	0.02	0.01	0.00	0.01	0.04	0.01
STD	0.69	0.02	0.11	0.79	0.01	0.26	0.01	0.01	0.10	0.01	0.01	0.02	0.01	0.00	0.01	0.02	0.01
#	14	14	14	14	14	14	14	14	14	14	14	14	14	14	14	14	14

A2

	Al	V	P	Si	Cr	Ca	Mn	Ti	Fe	Zr	Ni	Ba	Cu	Pb	Zn	Mg	W
Mean	42.94	0.01	0.07	37.06	0.00	19.68	0.01	0.01	0.13	0.00	0.01	0.01	0.01	0.00	0.01	0.04	0.01
STD	0.39	0.02	0.11	0.31	0.01	0.36	0.01	0.01	0.11	0.00	0.01	0.01	0.02	0.00	0.01	0.03	0.01
#	18	18	18	18	18	18	18	18	18	18	18	18	18	18	18	18	18

MG-Si2 Industrial

	Al	V	P	Si	Cr	Ca	Mn	Ti	Fe	Zr	Ni	Ba	Cu	Pb	Zn
Mean	40.25	0.05	0.17	40.82	0.03	17.63	0.01	0.01	0.90	0.00	0.00	0.13	0.00	0.00	0.00
STD															
#	1	1	1	1	1	1	1	1	1	1	1	1	1	1	1

HT-(Al)FeSi$_2$

MG-Si2 Industrial

	Al	V	P	Si	Cr	Ca	Mn	Ti	Fe	Zr	Ni	Ba	Cu	Pb	Zn
Mean	6.81	0.02	0.01	64.03	0.04	0.01	0.30	0.04	28.95	0.00	0.01	0.00	0.02	0.01	0.01
STD	1.74	0.02	0.01	2.13	0.03	0.04	0.10	0.05	0.89	0.01	0.02	0.00	0.02	0.01	0.02
#	60	21	60	60	21	60	21	60	60	21	21	21	21	21	21

Copper plate MG-Si1

	Al	V	P	Si	Cr	Ca	Mn	Ti	Fe	Zr	Ni	Ba	Cu	Pb	Zn
Mean	6.05	0.02	0.00	66.15	0.06	0.00	0.30	0.05	27.30	0.00	0.02	0.00	0.02	0.01	0.01
STD	2.11	0.03	0.00	2.49	0.02	0.03	0.07	0.05	0.53	0.00	0.02	0.00	0.05	0.01	0.01
#	43	43	43	43	43	43	43	43	43	43	43	43	43	43	43

Copper plate MG-Si2

	Al	V	P	Si	Cr	Ca	Mn	Ti	Fe	Zr	Ni	Ba	Cu	Pb	Zn
Mean	7.11	0.02	0.00	64.93	0.04	0.02	0.24	0.06	27.54	0.00	0.01	0.00	0.01	0.00	0.01
STD	2.32	0.03	0.00	2.43	0.02	0.09	0.05	0.06	0.50	0.01	0.01	0.00	0.02	0.00	0.02
#	61	61	61	61	61	61	61	61	61	61	61	61	61	61	61

Cyberstar MG-Si1

	Al	V	P	Si	Cr	Ca	Mn	Ti	Fe	Zr	Ni	Ba	Cu	Pb	Zn	W	Mg
Mean	6.79	0.02	0.00	63.88	0.05	0.01	0.37	0.09	28.72	0.01	0.01	0.00	0.01	0.00	0.02	0.01	0.01
STD	1.52	0.03	0.01	1.88	0.03	0.04	0.09	0.10	0.57	0.01	0.01	0.01	0.02	0.00	0.02	0.02	0.02
#	10	10	10	10	10	10	10	10	10	10	10	10	10	10	10	10	10

Cyberstar MG-Si2

	Al	V	P	Si	Cr	Ca	Mn	Ti	Fe	Zr	Ni	Ba	Cu	Pb	Zn	W	Mg
Mean	9.54	0.02	0.01	60.78	0.03	0.00	0.33	0.03	29.20	0.00	0.01	0.00	0.02	0.00	0.01	0.01	0.01
STD	0.71	0.03	0.01	0.77	0.02	0.00	0.03	0.04	0.26	0.01	0.01	0.00	0.02	0.00	0.01	0.01	0.01
#	11	11	11	11	11	11	11	11	11	11	11	11	11	11	11	11	11

$Al_6Fe_4Si_6$

MG-Si2 Industrial

	Al	V	P	Si	Cr	Ca	Mn	Ti	Fe	Zr	Ni	Ba	Cu	Pb	Zn
Mean	40.28	0.05	0.00	36.37	0.05	0.02	0.37	0.10	23.01	0.00	0.04	0.00	0.02	0.00	0.00
STD	1.56	0.08	0.01	1.66	0.04	0.06	0.09	0.15	0.81	0.00	0.03	0.00	0.02	0.00	0.00
#	15	6	15	15	6	15	6	15	15	6	6	6	6	6	6

Copper plate MG-Si1

	Al	V	P	Si	Cr	Ca	Mn	Ti	Fe	Zr	Ni	Ba	Cu	Pb	Zn
Mean	40.67	0.01	0.00	36.36	0.06	0.00	0.42	0.18	22.09	0.00	0.11	0.00	0.09	0.00	0.00
STD	0.71	0.01	0.01	0.43	0.03	0.01	0.09	0.12	0.44	0.01	0.04	0.00	0.07	0.00	0.00
#	6	6	6	6	6	6	6	6	6	6	6	6	6	6	6

Copper plate MG-Si2

	Al	V	P	Si	Cr	Ca	Mn	Ti	Fe	Zr	Ni	Ba	Cu	Pb	Zn
Mean	40.70	0.03	0.00	36.38	0.05	0.00	0.30	0.11	22.33	0.01	0.05	0.00	0.02	0.00	0.00
STD	0.87	0.03	0.00	0.89	0.02	0.00	0.04	0.28	0.31	0.02	0.02	0.00	0.02	0.00	0.01
#	28	28	28	28	28	28	28	28	28	28	28	28	28	28	28

Cyberstar MG-Si1

	Al	V	P	Si	Cr	Ca	Mn	Ti	Fe	Zr	Ni	Ba	Cu	Pb	Zn	W	Mg
Mean	41.92	0.01	0.00	34.45	0.03	0.00	0.35	0.17	22.88	0.00	0.05	0.00	0.11	0.00	0.01	0.00	0.01
STD	1.09	0.03	0.00	0.92	0.03	0.00	0.05	0.10	0.24	0.01	0.03	0.00	0.04	0.00	0.01	0.01	0.02
#	6	6	6	6	6	6	6	6	6	6	6	6	6	6	6	6	6

Cyberstar MG-Si2

	Al	V	P	Si	Cr	Ca	Mn	Ti	Fe	Zr	Ni	Ba	Cu	Pb	Zn	W	Mg
Mean	41.03	0.01	0.00	35.28	0.02	0.00	0.27	0.07	23.17	0.00	0.04	0.00	0.04	0.00	0.02	0.01	0.02
STD	1.12	0.02	0.01	1.26	0.01	0.01	0.06	0.15	0.41	0.01	0.04	0.00	0.04	0.00	0.03	0.02	0.02
#	21	21	21	21	21	21	21	21	21	21	21	21	21	21	21	21	21

(Al)FeSi$_2$Ti

MG-Si2 Industrial

	Al	V	P	Si	Cr	Ca	Mn	Ti	Fe	Zr	Ni	Ba	Cu	Pb	Zn
Mean	3.44	0.62	0.01	49.22	0.12	0.01	0.39	23.32	22.89	0.54	0.02	0.11	0.02	0.00	0.01
STD	1.23	0.13	0.02	1.17	0.04	0.03	0.08	0.64	1.00	0.11	0.02	0.01	0.02	0.00	0.01
#	25	15	25	25	15	25	15	25	25	15	15	15	15	15	15

Copper plate MG-Si1

	Al	**V**	**P**	**Si**	**Cr**	**Ca**	**Mn**	**Ti**	**Fe**	**Zr**	**Ni**	**Ba**	**Cu**	**Pb**	**Zn**
Mean	2.34	0.73	0.06	50.26	0.15	0.00	0.43	23.46	21.97	0.41	0.02	0.13	0.03	0.00	0.01
STD	1.46	0.13	0.03	0.77	0.03	0.00	0.05	1.72	0.37	0.05	0.02	0.02	0.02	0.01	0.01
#	24	24	24	24	24	24	24	24	24	24	24	24	24	24	24

Copper plate MG-Si2

	Al	**V**	**P**	**Si**	**Cr**	**Ca**	**Mn**	**Ti**	**Fe**	**Zr**	**Ni**	**Ba**	**Cu**	**Pb**	**Zn**
Mean	3.98	0.62	0.07	48.89	0.16	0.00	0.42	23.19	21.99	0.54	0.02	0.11	0.01	0.00	0.01
STD	0.90	0.07	0.03	1.02	0.04	0.00	0.05	1.13	0.42	0.07	0.02	0.01	0.02	0.00	0.01
#	35	35	35	35	35	35	35	35	35	35	35	35	35	35	35

Cyberstar MG-Si1

	Al	**V**	**P**	**Si**	**Cr**	**Ca**	**Mn**	**Ti**	**Fe**	**Zr**	**Ni**	**Ba**	**Cu**	**Pb**	**Zn**	**W**	**Mg**
Mean	2.32	0.44	0.02	48.15	0.12	0.01	0.45	25.04	22.65	0.50	0.01	0.14	0.01	0.01	0.02	0.03	0.10
STD	0.84	0.10	0.01	1.19	0.03	0.01	0.09	0.56	0.34	0.12	0.01	0.01	0.02	0.01	0.02	0.03	0.11
#	11	11	11	11	11	11	11	11	11	11	11	11	11	11	11	11	11

Cyberstar MG-Si2

	Al	**V**	**P**	**Si**	**Cr**	**Ca**	**Mn**	**Ti**	**Fe**	**Zr**	**Ni**	**Ba**	**Cu**	**Pb**	**Zn**	**W**	**Mg**
Mean	4.44	0.39	0.01	46.89	0.13	0.01	0.57	24.22	22.51	0.61	0.01	0.14	0.01	0.00	0.02	0.00	0.02
STD	2.97	0.10	0.01	1.80	0.08	0.04	0.27	1.22	0.94	0.34	0.02	0.02	0.02	0.00	0.02	0.01	0.03
#	17	17	17	17	17	17	17	17	17	17	17	17	17	17	17	17	17

Al-Fe-Si-Ti

A1/A2

	Al	V	P	Si	Cr	Ca	Mn	Ti	Fe	Zr	Ni	Ba	Cu	Pb	Zn	Mg	W
Mean	25.57	0.28	0.01	37.28	0.01	0.18	0.08	16.63	18.13	0.32	0.01	1.48	0.00	0.00	0.02	0.01	0.01
STD	1.08	0.10	0.01	8.35	0.01	0.20	0.04	6.19	6.68	0.24	0.02	4.15	0.01	0.01	0.02	0.01	0.01
#	9	9	9	9	9	9	9	9	9	9	9	9	9	9	9	9	9

Cyberstar MG-Si2

	Al	V	P	Si	Cr	Ca	Mn	Ti	Fe	Zr	Ni	Ba	Cu	Pb	Zn	W	Mg
Mean	24.18	0.32	0.02	34.33	0.05	0.00	0.24	19.92	20.51	0.21	0.08	0.11	0.00	0.01	0.01	0.01	0.02
STD	0.96	0.08	0.03	2.51	0.06	0.00	0.08	2.46	0.55	0.06	0.07	0.00	0.00	0.01	0.01	0.01	0.00
#	2	2	2	2	2	2	2	2	2	2	2	2	2	2	2	2	2

(Al,Fe)Si_2Ti

Cyberstar MG-Si1/MG-Si2

	Al	V	P	Si	Cr	Ca	Mn	Ti	Fe	Zr	Ni	Ba	Cu	Pb	Zn	W	Mg
Mean	1.47	2.01	0.01	63.80	0.72	0.02	0.20	22.63	5.54	0.16	0.01	0.13	0.00	0.00	0.20	1.77	1.33
STD	0.70	1.14	0.01	1.69	0.57	0.02	0.14	2.24	2.53	0.09	0.01	0.02	0.01	0.00	0.15	2.84	1.71
#	9	9	9	9	9	9	9	9	9	9	9	9	9	9	9	9	9

(Al,Zr)Si_2Ti

A2/A1

	Al	V	P	Si	Cr	Ca	Mn	Ti	Fe	Zr	Ni	Ba	Cu	Pb	Zn	W	Mg
Mean	9.08	0.76	0.00	56.23	0.01	0.16	0.00	30.01	0.40	3.11	0.01	0.17	0.02	0.00	0.00	0.01	0.01
STD	0.63	0.20	0.00	0.89	0.01	0.15	0.01	1.40	0.19	1.01	0.01	0.03	0.02	0.01	0.00	0.01	0.01
#	9	9	9	9	9	9	9	9	9	9	9	9	9	9	9	9	9

Al-Si-Ba

A1/A2

	Al	V	P	Si	Cr	Ca	Mn	Ti	Fe	Zr	Ni	Ba	Cu	Pb	Zn	W	Mg
Mean	29.97	0.03	0.00	55.71	0.01	0.66	0.01	0.16	0.48	0.01	0.01	12.89	0.02	0.00	0.03	0.02	0.01
STD	2.89	0.04	0.01	3.22	0.02	0.15	0.01	0.02	0.32	0.01	0.02	0.35	0.02	0.00	0.04	0.02	0.01
#	5	5	5	5	5	5	5	5	5	5	5	5	5	5	5	5	5

Al-Si

A1/A2

	Al	V	P	Si	Cr	Ca	Mn	Ti	Fe	Zr	Ni	Ba	Cu	Pb	Zn	Mg	W
Mean	94.09	0.08	0.00	3.02	0.05	0.06	0.00	1.21	0.09	0.01	0.00	0.01	0.19	0.00	0.02	0.69	0.01
STD	7.07	0.16	0.01	5.25	0.09	0.08	0.01	2.97	0.08	0.01	0.01	0.02	0.06	0.00	0.02	0.92	0.02
#	14	14	14	14	14	14	14	14	14	14	14	14	14	14	14	14	14

Al-Si-Ce-La-Nd

A1/A2

	Al	V	P	Si	Cr	Ca	Mn	Ti	Fe	Zn	Mg	W	Ce,La,Nd
Mean	44.13	0.00	0.00	38.70	0.00	4.05	0.00	0.00	0.11	0.00	2.29	0.11	10.6
STD	1.07	0.00	0.00	0.34	0.00	0.85	0.00	0.00	0.04	0.00	1.25	0.09	0.37
#	3	3	3	3	3	3	3	3	3	3	3	3	3

C.2 Distribution of trace elements between the intermetallic phases

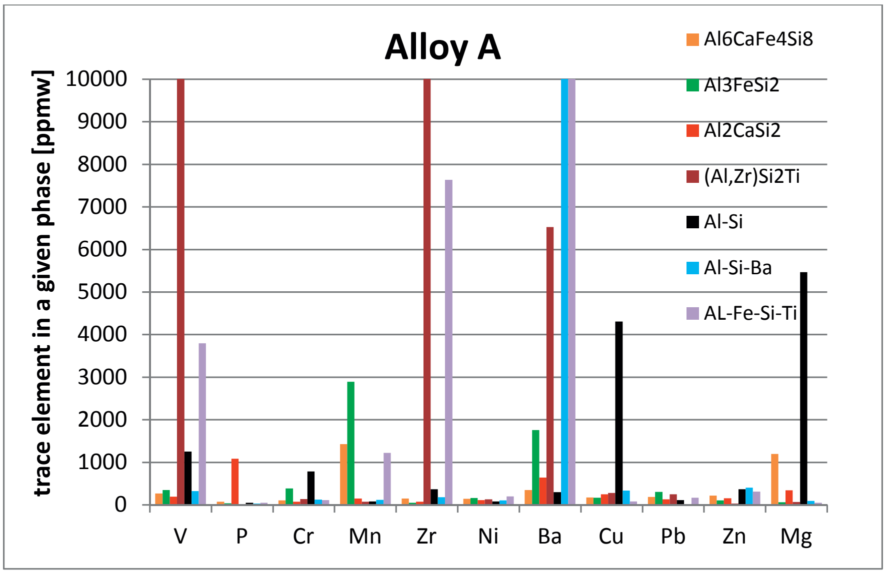

Figure C.1: Average content, ppmw, of a selection of trace elements in the intermetallic phases of alloy A. Peaks not shown, (Al,Zr)Si_2Ti phase contain 1.1 and 7.8 wt % V and Zr. 4.9 and 42 wt % Ba is found in the Al-Fe-Si-Ti and the Al-Si-Ba phases respectively.

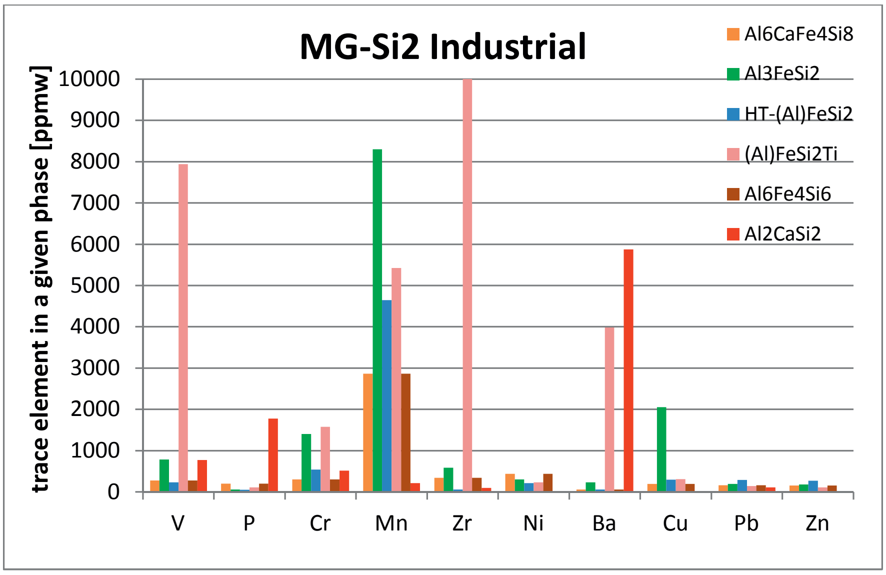

Figure C.2: Average content, ppmw, of a selection of trace elements in the intermetallic phases, MG-Si2 industrial. Peak not shown, (Al)$FeSi_2Ti$ phase contain 1.24 wt % Zr.

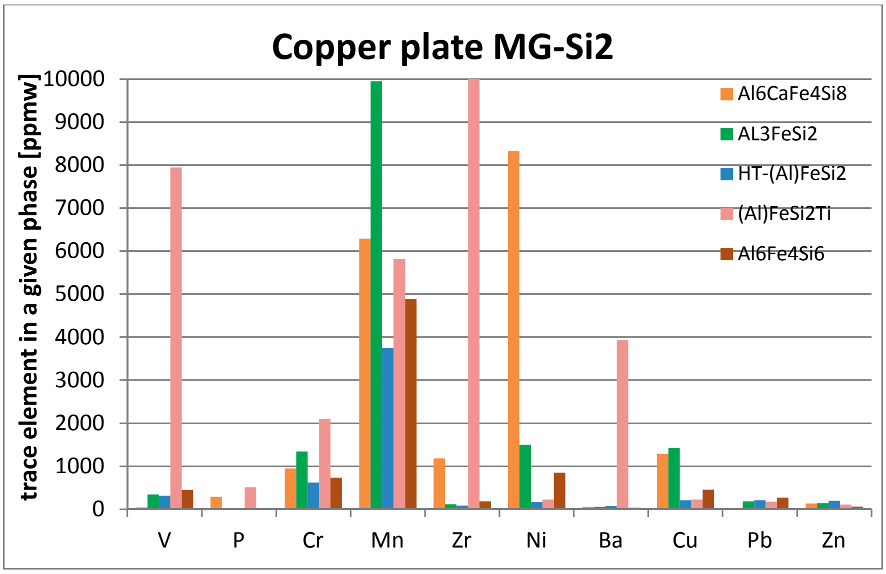

Figure C.3: Average content, ppmw, of a selection of trace elements in the intermetallic phases, Copper plate, MG-Si2. Peak not shown, (Al)$FeSi_2Ti$ phase contain 1.25 wt % Zr.

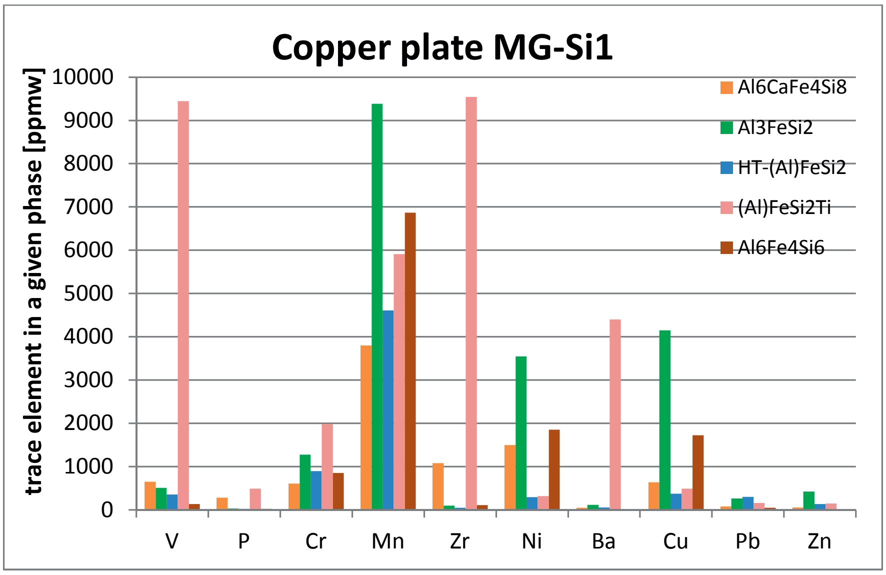

Figure C.4: Average content, ppmw, of a selection of trace elements in the intermetallic phases, Copper plate, MG-Si1.

For the Cyberstar experiments the content in the (Al,Fe)Si_2Ti phase is an average of the observations in MG-Si1 and MG-Si2.

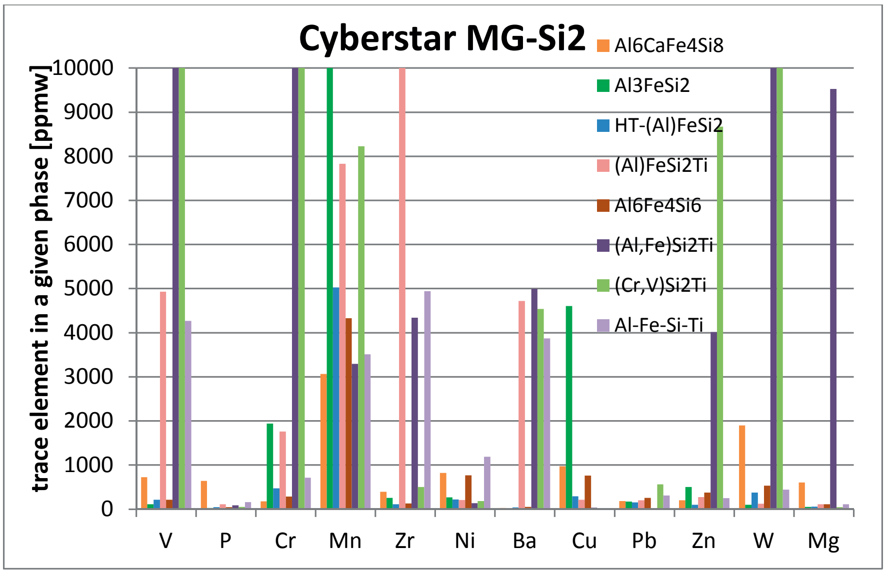

Figure C.5 Average content, ppmw, of a selection of trace elements in the intermetallic phases, Cyberstar MG-Si2. Peaks not shown, (Al,Fe)Si_2Ti phase contain 3, 1.1 and 10 wt % V, Cr and W. (Cr,V)Si_2Ti phase contain 4.9, 6.7 and 2.1 wt % V, Cr and W. (Al)FeSi_2Ti phase contain 1.4 wt % Zr and Al_3FeSi_2 phase contain 1.01 wt% Mn.

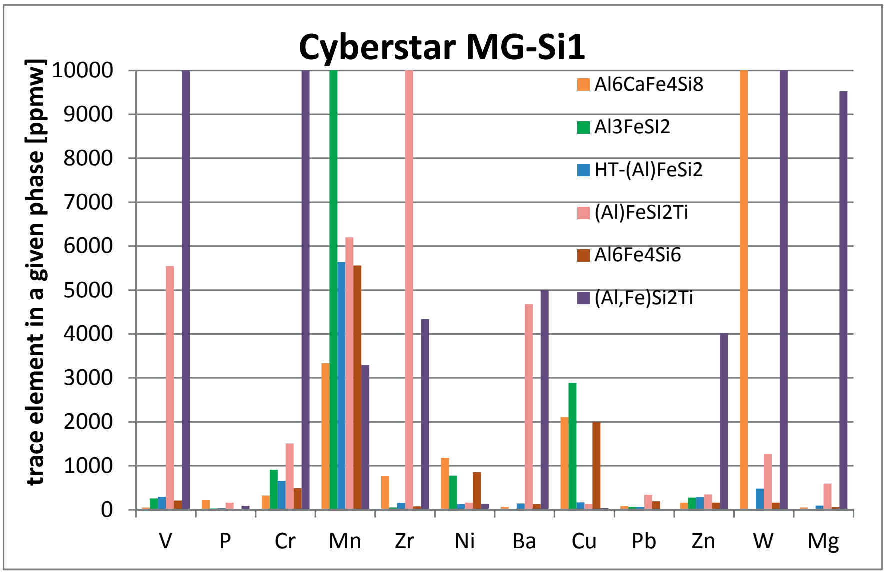

Figure C.6: Average content, ppmw, of a selection of trace elements in the intermetallic phases, Cyberstar, MG-Si1. Peaks not shown, (Al,Fe)Si_2Ti phase contain 3, 1.1 and 10 wt % V, Cr and W. (Al)FeSi_2Ti phase contain 1.1 wt % Zr and Al_3FeSi_2 phase contain 1.2 wt% Mn and $Al_6CaFe_4Si_8$ contain 2.7 wt % W.